Design and synthesis of organic luminescent materials with a 2,2'-bipyrimidine scaffold for hybrid LED lighting.

Shenming Wang

To cite this version:

Shenming Wang. Design and synthesis of organic luminescent materials with a 2,2'-bipyrimidine scaffold for hybrid LED lighting.. Chemical Sciences. Institut Polytechnique de Paris, 2024. English. ⟨NNT : 2024IPPAX016⟩. ⟨tel-05436824⟩

HAL Id: tel-05436824
https://theses.hal.science/tel-05436824v1

Submitted on 1 Jan 2026

INSTITUT
POLYTECHNIQUE
DE PARIS

NNT: 2024IPPAX016

Thèse de doctorat

Design and synthesis of organic luminescent materials with a 2,2′-bipyrimidine scaffold for hybrid LED lighting

Thèse de doctorat de l'Institut Polytechnique de Paris
préparée à l'École Polytechnique

École doctorale n°626 École Doctorale de l'Institut Polytechnique de Paris (ED IP Paris)
Spécialité de doctorat: Chimie

Thèse présentée et soutenue à Palaiseau, le 30 avril 2024, par

Shenming WANG
王申鸣

Composition du Jury:

Cédric Tard Directeur de recherche, CNRS, IP Paris (UMR 8238)	Président
Rachel Méallet Professeure, Université Paris-Saclay (UMR 8214)	Rapporteur
Gilles Clavie Directeur de recherche, CNRS, ENS Paris Saclay (UMR 8531)	Rapporteur
Geneviève Chadeyron Professeure, Université Clermont Auvergne (UMR 6296)	Examinateur
Gaël Zucchi Chargé de Recherche, CNRS (UMR 7647)	Directeur de thèse

Acknowledgement

Time flies. I have spent more than 3 years in LPICM where I have enjoyed doing my research and have learned a lot. First of all, I want to deeply thank my supervisor, Dr. Gaël Zucchi. He gave me a lot of help in research with good patience and kind considerations. Whenever I have questions, he always provides me constructive suggestions. Thanks to him, the project is going on the right way with cheering progress. With his encouragement, I can enter the last stage of my doctoral life and finish this manuscript.

Then I want to express my great appreciations to all the members in LPICM. I really enjoy the relaxing and positive research atmosphere, which is helpful for all the junior researchers to study and develop their own project. Thanks to Prof. Yvan Bonnassieux for creating the fascinating atmosphere and organizing all the activities in the lab. Thanks to Dr. Pere Roca for organizing the monthly Prom meeting and his great sense of humor. Thanks to other members in the lab, Dr. Abderrahiem Yassar, Dr. Jean-charles Vanel, Mme. Gabreilla Medina, Mme. Laurance Gérot and other members for their helps. Thanks to all my colleagues and friends who work in Chimorga, particularly to Christian Murga, Pingping Ni and Camilla Noè. It is a pleasure to work with you. I will remember the conversation we made to discuss researches and random interesting things in life. Thanks to Aram Nasiri, Martina Papa, Guili Zhao, Xinlei Yao , Deyan Ivanov, Aymeric Courilleau, Elmehdi Ould-maina, Hindia Nahdi, Lakshman Srinivasan, Weixi Wang, Shuang Li, Lunnet Newman, and other friends in LPICM. I am sorry that I could list all of their names.

Also, I want to thank all the people who have helped me in the past 3 years. Thanks to Prof. Cédric Tard, for his interesting classes and his kind supports in both researches and planning of my doctoral life. Thanks to Dr. Sophie Bourcier for measuring and analyzing the Mass spectra. Thanks to Dr. Nicolas Casaretto for measuring and analyzing the single-crystals XRD results. Thanks to Dr. Rabei Mohammedi for the DLS measurements and the relevant training. Thanks to Sami Laroui for training me for the access to Platine and the spin-coater.

I want to thank *Les Clermontois*, especially Prof. Geneviève Chadeyron, Prof. Jean-Philippe Roblin and Dr. Anthony Barros, for their hard works and important contributions on this project for measuring the photophysical properties and photostabilities of the films. Thanks to Romain and other students in Clermont-Ferrand for treating me well during my short stay.

I want to thank my Chinese friends in France, Yang Ye, Fusi Lin, Heng Zhang, Zheyi Yang, Lihao Guan, Shihao Bian, etc. Thanks to Yihan Xiong, who has offered me a lot of emotional supports and shared good memories.

Great thanks also to all members of my jury committee for making the time to review my thesis. I thank you in advance for the precious suggestions and advices concerning this work.

In the end, I want to thank my family members who always support me, from the beginning of my life to today. Without you, there is no me.

谨以此纪念我逝去的叔叔王文，是你的鼓励让我开启海外求学之路。

Shenming WANG 王申鸣
05/03/2024, Paris

Abstract

Luminescence is a process of emitting photons after absorbing energy. Luminescent materials are widely applied in our daily life. One of the most application is the white light-emitting diodes (LEDs) for lighting system. It is made up of a blue-emitting LED based on InGaN and covered with yellow-emitting phosphor YAG:Ce, both are inorganic materials. Nevertheless, the light is not of perfect quality: it lacks red component and have an excess of blue light.

To solve the existing problems, we tried to develop organic down-converters to replace YAG:Ce, which can be embedded with near-UV or blue LEDs based on inorganic semiconductors, to fabricate hybrid white LEDs with better quality of light. Organic luminescent materials possess a lot advantages over the inorganic analogues. By carefully designing, they can exhibit efficiency fluorescence in visible area with tunable emission and strong absorption in near-UV and blue region. Due to this, they can be made in thin films for light-weight optoelectronic devices. They can be highly soluble in organic solvent which provide the possibility for the solution-processing techniques, such as spin-coating and slot-die coating. They are metal-free, which is desired for the sustainable development. These various merits make them promising alternatives to the inorganic phosphors.

There are two methods to realize white light. One is to use a yellow emitter to cover a blue-emitting LED. The other one involves several organic molecules which emit in three principal color, blue, green, red and can fully absorb the emission of near-UV LED. The second method can enable us to obtain better quality of white light by fine-tuning the ratio between three components.

In this work, we have employed different molecular design strategies including: (1) the donor-acceptor (D-A) approach, which can adjust the bandgap in order to tune the absorption and emission wavelength; (2) to control the inter- and intramolecular

interaction to improve the absorption and emission efficiency in solid state.

Herein, we designed and synthesized a series of D-A molecules **M1-M7** implementing new acceptors 2,2′-bipyrimidine derivatives as building block. They were fully purified and characterized. The photophysical investigations were conducted in both diluted solutions and solid state. They showed tunable emission which can cover the whole visible spectrum, highly-efficient fluorescence and absorption, more importantly, high conversion rate from near -UV or blue external source to visible light. **M4** is the most emissive molecule in solid state and very sensitive to the surrounding, thus can be tuned by multiple approaches. The 10wt% doped film of **M4** in PMMA exhibits yellow emission at around 560 nm with a high photoluminescence quantum yield (PLQY) of 82%. **M4** in microcrystalline powder emits in orange region while its neat film is red-emissive.

In order to apply them, we also inspected their photostabilities to estimate the lifespans of the possible devices. The photostability of **M4** can be hugely enhanced in less-powerful scenario. The blenders of different emitters are made for generating white light. At last, the hybrid LEDs were fabricated based on a blue inorganic LED and **M4,** one of which shows a white light with CIE coordinates of (0.33, 0.37) and a color temperature of 5450K.

Additionally, there are still some works remaining unfinished. I have proposed several perspectives for the future studies. It will be interesting to investigate the photodegradation and reveal the mechanism. Some new synthetic designs are proposed to have better blue- and red-emitters. Their thermal stabilities are needed to be inspected. As the final goal of the project, the hybrid LED based on a near-UV core deserved more efforts to be accomplished.

Résumé

La luminescence est un processus d'émission de photons après absorption d'énergie. Les matériaux luminescents sont largement utilisés dans notre vie quotidienne. L'une des applications les plus courantes est celle des diodes électroluminescentes (LED) blanches pour les systèmes d'éclairage. Celles-ci sont composées d'une LED émettant en bleu à base d'InGaN, recouverte d'un phosphore émettant en jaune, YAG:Ce, tous deux des matériaux inorganiques. Cependant, la qualité de la lumière produite n'est pas optimale : elle manque de composante rouge et présente un excès de lumière bleue.

Pour résoudre ces problèmes, nous avons entrepris de développer des convertisseurs descendantes organiques pour remplacer le YAG:Ce. Ces convertisseurs peuvent être intégrés avec des LED proches-UV ou bleues à base de semi-conducteurs inorganiques, afin de fabriquer des LED blanches hybrides avec une meilleure qualité de lumière. Les matériaux luminescents organiques présentent de nombreux avantages par rapport à leurs homologues inorganiques. En les concevant soigneusement, ils peuvent produire une fluorescence efficace dans la région visible, avec une émission modulable et une forte absorption dans la région proche-UV et bleue. De ce fait, ils peuvent être fabriqués sous forme de films minces pour des dispositifs optoélectroniques légers. Ils sont également hautement solubles dans des solvants organiques, ce qui permet d'utiliser des techniques de traitement en solution telles que le dépôt par rotation et le revêtement par fente. Ils sont exempts de métaux, ce qui est souhaitable pour le développement durable. Ces divers avantages font d'eux des alternatives prometteuses aux phosphores inorganiques.

Il existe deux méthodes pour produire de la lumière blanche. La première consiste à utiliser un émetteur jaune pour couvrir une LED émettant en bleu. La seconde implique l'utilisation de plusieurs molécules organiques émettant dans les trois couleurs

principales – bleu, vert et rouge – et capables d'absorber entièrement l'émission d'une LED proche-UV. Cette seconde méthode permet d'obtenir une meilleure qualité de lumière blanche en ajustant finement le ratio entre les trois composants.

Dans ce travail, nous avons employé différentes stratégies de conception moléculaire, notamment : (1) l'approche donneur-accepteur (D-A), qui permet d'ajuster la bande interdite afin de moduler les longueurs d'onde d'absorption et d'émission ; (2) le contrôle des interactions inter- et intramoléculaires pour améliorer l'efficacité de l'absorption et de l'émission à l'état solide.

Nous avons conçu et synthétisé une série de molécules D-A, **M1-M7**, en utilisant de nouveaux accepteurs dérivés de la 2,2′-bipyrimidine comme blocs de construction. Elles ont été entièrement purifiées et caractérisées. Les investigations photophysiques ont été menées à la fois en solutions diluées et à l'état solide. Ces molécules ont montré une émission modulable couvrant tout le spectre visible, une fluorescence et une absorption hautement efficaces et, plus important encore, un taux de conversion élevé d'une source externe proche-UV ou bleue vers la lumière visible. Parmi elles, **M4** s'est révélée être la molécule la plus émissive à l'état solide et très sensible à l'environnement, pouvant ainsi être modulée par de multiples approches. Le film dopé à 10 % de **M4** dans le PMMA présente une émission jaune autour de 560 nm avec un rendement quantique photoluminescent (PLQY) élevé de 82 %. **M4** en poudre microcristalline émet dans la région orange, tandis que son film pur est émissif en rouge.

Pour évaluer leur applicabilité, nous avons également examiné leur photostabilité afin d'estimer la durée de vie des dispositifs potentiels. La photostabilité de **M4** peut être grandement améliorée dans des scénarios moins énergivores. Des mélanges de différents émetteurs ont été réalisés pour générer de la lumière blanche. Enfin, des LED hybrides ont été fabriquées à partir d'une LED inorganique bleue et de **M4**, l'une d'elles montrant une lumière blanche avec des coordonnées CIE de (0,33, 0,37) et une température de couleur de 5450K.

De plus, il reste encore quelques travaux à achever. J'ai proposé plusieurs perspectives pour les études futures. Il serait intéressant d'étudier la photodégradation et de révéler les mécanismes sous-jacents. De nouveaux designs synthétiques sont proposés pour obtenir de meilleurs émetteurs bleus et rouges. Leurs stabilités thermiques devront également être inspectées. L'objectif final du projet, à savoir la fabrication d'une LED hybride basée sur un noyau proche-UV, mérite davantage d'efforts pour être accompli.

Contents

Chapter I Introduction

In this initial chapter, we will briefly introduce the luminescence phenomenon and luminescent materials and some applications, especially light-emitting diodes (LEDs). The pros and cons of the commercial white light-emitting diodes (WLEDs) will be illustrated to introduce the objective of this thesis: to design and synthesize the proper organic luminophores which could be suitable to replace the inorganic phosphors in WLEDs. All the information is significant to help us present our entire work for this thesis.

In **Chapter II**, we will present the design concepts of our organic luminophores, the selection of their chemical skeletons, substituted units and the connecting ways between them. The synthetic procedures will be shown step by step, following with characterizations by the means of ^{1}H and ^{13}C NMR, HRMS and single-crystal XRD. The experimental procedures about photophysical measurements and fabrications of films will also be demonstrated. In the end, we will discuss about the synthesis.

In **Chapter III**, photophysical measurements on these new molecules in diluted solutions will be exhibited to profile their basic features. To prove the design concepts we have adopted, comparisons between molecules will be made to clearly illustrate similarities and differences. The solvent effect on their photophysical performances will be explained. In the end, we will try to construct their electronic structures by photoluminescent experiments and establish their structure-property relationships.

In order to apply the newly-synthesized organic luminophores in WLEDs, the photophysical properties in the aggregates and solid states have been carried out, especially on films. These studies will be described in **Chapter IV**, as well as the photo-stability studies and white-light applications.

Finally, general conclusions and perspectives will be given in the last chapter following to show the achievements and absence in this thesis. Some additional information will be listed following the **Chapter V**.

1.1 Luminescence and luminescent materials

Light, and more specifically, visible light, is the electromagnetic radiation having wavelength in the range of 400-750 nm (**Figure 1-1**). On Earth, the natural light is mainly coming from the sun, but also from fire and emissive creatures. In modern society, the primary artificial light is the electric light generated with the help of luminescent materials.

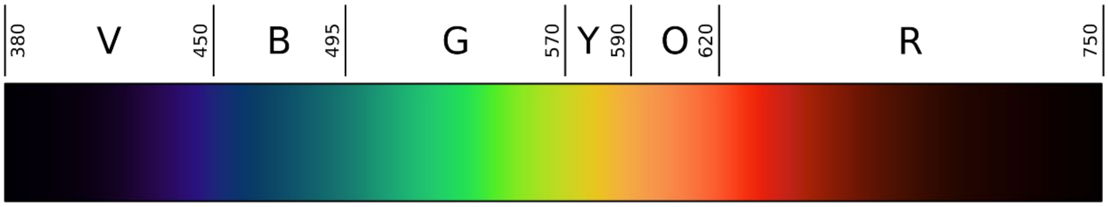

Figure 1-1 Spectrum of visible light.

In the process of luminescence, the material is excited by absorbing external energy, then deactivates by releasing the excess of energy in form of photons and goes back to the ground state[1], which is shown in **Figure 1-2** by Jablonski diagram. The relaxation of excited states involves two pathways: the radiative decay and the non-radiative decay. The radiative decay can lead to the emission of photons. They are formally classified as fluorescence and phosphorescence, depending on whether the spin multiplicity changes during the transition. Fluorescence, as a parity-allowed transition where the multiplicity keeps the same, is fast and usually possesses a decay lifetime of less than 10^{-8} seconds[2]. Phosphorescence has a lifetime longer than 10^{-8} seconds, and up to a few seconds, which is “forbidden” for involving the changes of multiplicity. The non-radiative decays including vibrational relaxation, internal conversion, intersystem crossing and reverse intersystem crossing. Vibrational relaxation, which is lost as kinetic energy to other vibrational modes intra- or intermolecularly and often measured by Raman or Infrared spectroscopy. Internal conversion is an electron movement from a higher to a lower excited state, where the electron spin remains the same. For example, the transition from singlet excited states S2 to S1 in **Figure 1-2**. Intersystem crossing is another non-radiative transition where the spin state changes, as the electron moving from the singlet excited state S1 to triplet excited state T1. Intersystem crossing often results in phosphorescence.

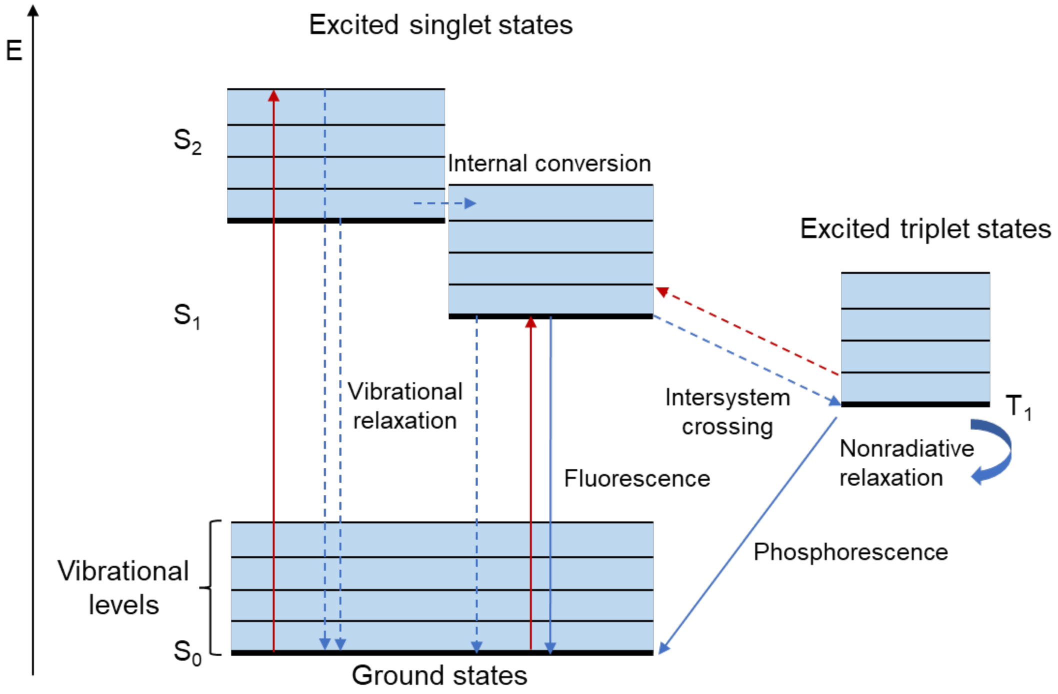

Figure 1-2 Jablonski-Perrin diagram to illustrate mechanism of luminescence.

Depending on the type of stimulation, luminescence can be classified as: electroluminescence (by electric flow or strong electric filed), photoluminescence (by absorption of photons), chemiluminescence (chemical reactions), mechanoluminescence (induced by a stress on a material) and other infrequent types. The most widely applied luminescent materials are mainly two kinds: electroluminescent and photoluminescent materials, which are attached importance in this brief review.

1.1.1 Electroluminescence (EL)

An electroluminescent material emits light either during the passage of an electric flow with the radiative recombination of holes and electrons (low-field EL), or in a strong electric field (high-field EL)[3]. Low field EL takes place more commonly in p-n junction semiconductors, wherein the electrons and holes are well separated before the recombination. A representative material like gallium nitride is widely applied in LEDs with low-energy consumption[4]. On the other hand, high field EL materials, like doped zinc sulfide[3], occurs in devices like phosphor-based EL panels. EL panels are capacitors where the luminescent material is in between the two outside plates of dielectric layers (**Figure1-3**). When the capacitor is fully charged, the phosphor gives off photons. One of the electrodes is made transparent to allow the emitted photons go through the surface. EL panels are frequently used as backlights for liquid crystal displays (LCD)[5].

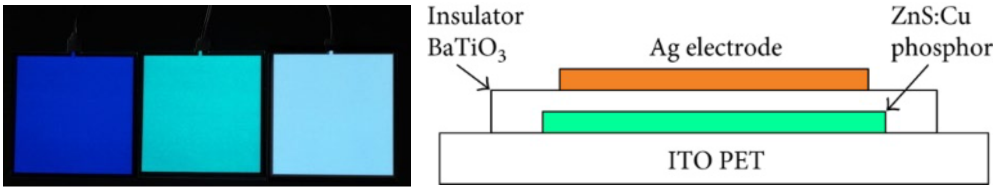

Figure 1-3 Electroluminescent panels and their structure.

1.1.2 Photoluminescence (PL)

Photoluminescence is an optical process in which a material after absorbing light and then getting excited, returns to the ground state by emitting photons in a radiative way.

A particular case in which the PL process is observed is the charge-transfer (CT) transition[1]. In general, a CT transition could occur due to the electron transfer between ligands and metal ions[6]. For instance, in host lattice comprising WO_4^{2-} or MO_4^{2-}, the photo energy is absorbed by the host due to the electron transfer from O^{2-} to W^{6+} or M^{6+}, exhibiting a charge-transfer band in the absorption spectrum[7]. The doping of rare-earth ions like Eu^{3+} gives rise to this phenomenon[8]. In these cases, the host lattice only plays the role to provide the proper environment for the activator ions to emit.

The second main deactivation process is a non-radiative one. For examples, an activator ion, which absorbs light from external source, part of the energy is dissipated through bond vibrations, collisions between molecules, and other non-radiative route without any emission. The energy is transferred through an inefficient way among the other ions in the lattice (**Figure 1-4 left**). Also, sometimes the absorption is too low to lead to emission. In this circumstance, the introduction of sensitizer is necessary to act as a bridge for activator ions to absorb energy[1]. As the name suggests, sensitizer ions produce a sensitizing action in the luminescence process by efficiently absorbing the external energy and transfer it to the activator ions (shown in **Figure 1-4 right**). This is called the antenna effect. For instance, lanthanide ions (Ln^{3+}, such as Eu^{3+}, Tb^{3+}, Dy^{3+}, etc.) exhibit weak absorption in the UV region (the extinction coefficient for such trivalent cations is $\varepsilon \approx 1–10\ M^{-1}\cdot cm^{-1}$)[9], due to the parity forbidden 4f–4f transition. Ce^{3+} and Eu^{2+} work as an efficient sensitizer for them because of the transition from 4f orbital to downshifted 5d orbital while doped into certain host matrix[8,10]. These phosphors containing rare-earth and transition metals ions are the most frequently used materials which are applied in marketed phosphor converted white light-emitting diodes (pc-WLEDs)[11].

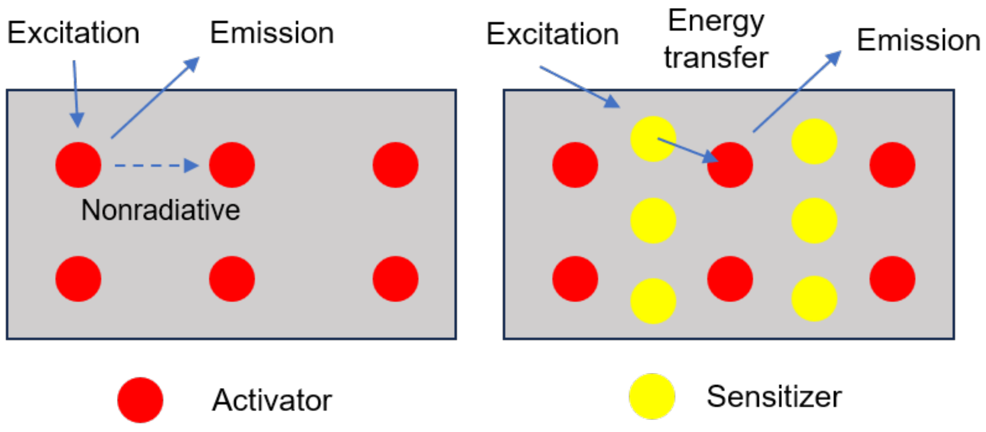

Figure 1-4 Energy transfer between the sensitizer and activator ions.

Besides of sensitizer ions, organic chromophores are also efficient for sensitizing the luminescence of lanthanide ions[12]. For most organic chromophores, they show high absorption coefficient ($\varepsilon \approx 10^4–10^5\ M^{-1}\cdot cm^{-1}$) in the UV region[13]. In general, the ligand can be highly π-conjugated aromatic or hetero-aromatic compounds with a triplet excited state showing at least 1850 cm^{-1} higher energy level than the lowest emitting levels of the Ln^{3+} cation[14], such as 2,2'-bipyridine[15], 1,10-phenanthroline[16] and 2,2':6',2''-terpyridine[17].

PL process can be also observed in pure organic system, the mechanism of which is vital to this thesis. Light-absorption of organic chromophores depends on the bandgap, which is the energy difference between the Highest Occupied Molecular Orbital (HOMO) and the Lowest Unoccupied Molecular Orbital (LUMO). Thinking about isolated molecules in diluted solution, those who have extended π-conjugated system, which gives rise to energetically low-lying LUMO and/or high-lying HOMO, can absorb in lower-energy area[18]. The molecular geometry change will take place accompanying with the S_0-S_1 transition, where one electron is promoted from the doubly-occupied HOMO to the LUMO. As shown in **Figure 1-5** for stilbene, the single and double bonds in S_0 are equalized in S_1 through this geometry change[19], giving rise to the broadening of the spectrum[20]. After light absorption to an excited state S_n, the molecule rapidly deactivates by vibrational relaxation, in a way of heat dissipation to the solvent. Internal conversion from S_n-S_{n-1} is usually fast due to the normally small energy separations when $n > 1$. From S1, due to the much larger S_1-S_0 gap, the radiative decay, in particular, fluorescence, can take place. In solution, the emission from higher excited state usually cannot be observed for the ultra-fast internal conversion, also known as Kasha's rule[21].

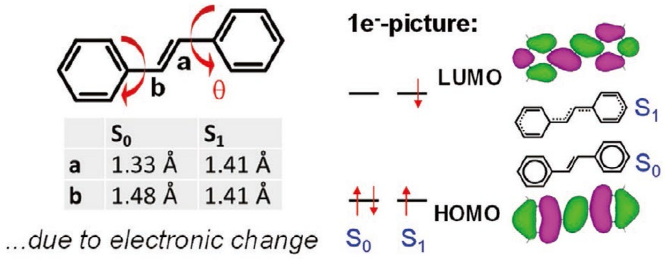

Figure 1-5 Electronic structure and geometry of stilbene in S0 and S1, with (DFT calculated) bond lengths *a*, *b* and torsional angle *θ*, reproduced from literature[19].

For organic chromophores in solid state, the intermolecular arrangement is a decisive parameter for their PL properties. As shown in **Figure 1-6**, for distyrylbenzene (DSB) derivatives, their absorption and PL spectra in solution (blue lines) are also slightly different due to the various substitutions[22-24]. On the other hand, the optical properties of their nanoparticles in suspensions show strongly distinct features. In amorphous solids, only a small hypochromic shift in absorption and a small bathochromic shift in emission against solution is observed (see **Figure 1-6 a**). For molecules with side-by-side arrangement (see **Figure 1-6 b** and **c**), strong hypochromic shift occurs in absorption due to the H-aggregation, which usually leads to the hypochromic shift in absorption. Emission spectra can be vibronically structured (**Figure 1-6 b**), exhibiting the signatures of "relaxed excitons" (see **Figure 1-y c**) or showing strongly red-shifted, unstructured spectra reminiscent of excimers. For slipped stacks, moderate bathochromic shifts of absorption band due to J-aggregation can be observed.

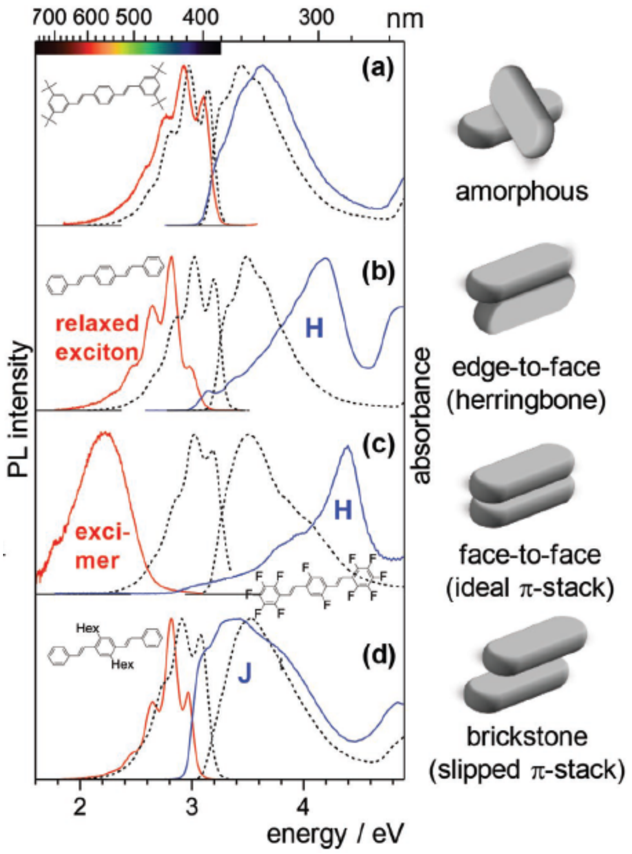

Figure 1-6 Absorption (right) and emission (left) features of nanoparticle suspensions for substituted DSB materials, reproduced from literature[19].

1.1.3 Characterization of the light quality

Photometric units are used to characterize the perception of light by human eyes, such as luminance representing the light intensity per unit area which is perceived by human eyes in the units of candela/m^2 (cd/m^2), and illuminance expressing the measure of how much the incident light illuminates the surface in the units of lumen/m^2 (lm/m^2).

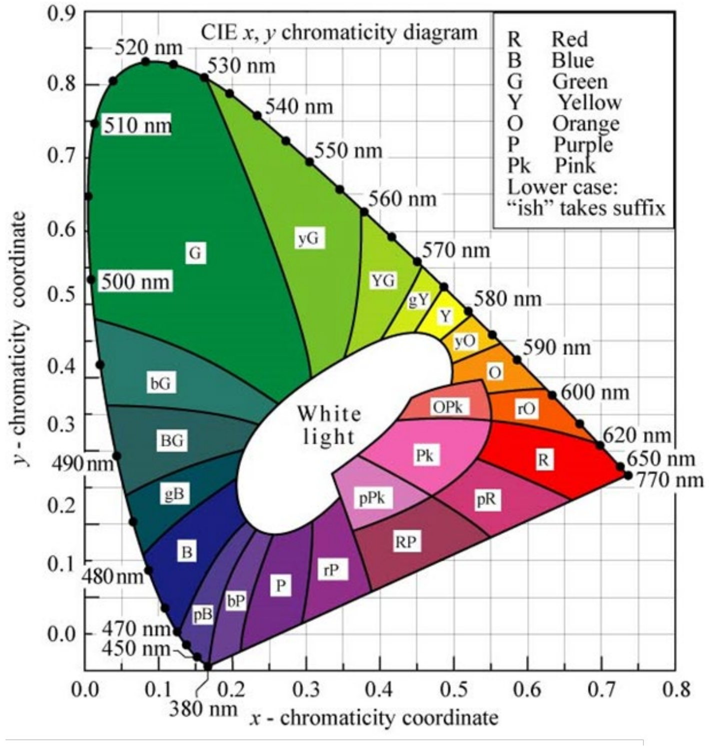

Figure 1-7 CIE 1931 chromaticity diagram with color regions, reproduced from http://hyperphysics.phy-astr.gsu.edu/hbase/vision/cie.html.

To characterize the color of light, the concepts of chromaticity, calculated color temperature (CCT) and color rendering index (CRI), are introduced. Chromaticity is the characterization of light quality regardless of luminance, commonly specified by the Commission Internationale de L'éclairage (CIE) 1931 color spaces[25]. It consists of two parameters hue and colorfulness to locate each color, as it is shown in **Figure 1-7**. In particular, perfect white, that mimics natural light, is highly desired for lighting applications. It is considered to be in the center of the diagram (0.33, 0.33). Then, CCT is a parameter used to describe the color of light by comparing it to the black body. The color temperature is measured in kelvins (K). It is especially important in lighting and photography to distinguish between cold colors (2700-3000 K) and warm colors (**Figure 1-8**). The other parameter, a CRI, is a quantitative measure of the ability of a light source to reveal the colors of various objects faithfully in comparison with a natural or standard light source. For instance, an incandescent bulb with a CRI above 99 (the natural sunlight is 100), indicates emission of a light very close to the standard light source.

Figure 1-8 Indication of light with different CCT, adopted from http://www.inlineelectric.com.

1.2 Light-emitting diodes

Among applications of luminescent materials, lighting systems are important ones. From prehistorical era to modern society, it is always a crucial subject for human beings to find or create the light sources. Lighting systems have evolved from candles to gas lighting and incandescent bulbs, to fluorescent lamps and finally to LEDs. Nowadays, LEDs are considered as the most important lighting and displaying technology, as they can be found in domestic lights, traffic lights, backlighting, display materials and visible-light communication system. The development of LEDs and materials used to elaborate them will be highlighted hereafter.

1.2.1 Development of LEDs

A LED is a semiconductor device carrying a heavily doped p-n junction. For instance, the doping concentration is 10^{16} cm^{-3} to 10^{19} cm^{-3} for p and n-type AlGaN to elaborate effectively in LEDs[26]. This high doping level ensures that there is a large number of charge carriers (electrons and holes) available to participate in the conduction process, which allows for efficient light emission. The general structure of LEDs is shown in **Figure 1-9**. The emissive layer composed by the semiconductor is installed between the anode and cathode. When the current flows through a LED, electrons recombine with the holes and the energy is released in the form of photons. Comparing to conventional lighting devices like incandescent lamps and fluorescent bulbs, LEDs possess many advantages: smaller size, lower energy consumption (90-100 lm/W for LEDs), longer lifetimes (tens of thousands of hours), lower turn-on voltage (1-5 V while 220V for incandescent lamps and fluorescent bulbs)[27], and immediate switching without warm-up and cool-down.

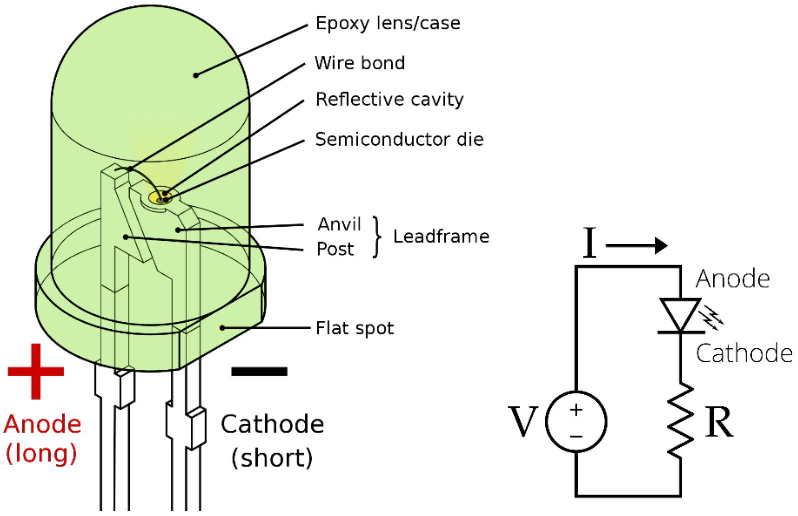

Figure 1-9 Basic structure of light-emitting diodes.

The first observation of electroluminescence can be tracked back to 1907, in a silicon carbide junction diode by H. J. Round[28]. However, the first practical visible LED was fabricated by Nick Holonyak in 1962[29]. Then the most important blue LED with high brightness was developed by Shuji Nakamura (Nichia company) based on InGaN/AlGaN[4,30], which offered the possibilities to further develop highly efficient white light sources. In 1996, a WLED was produced by Nichia with this blue-emitting LED covered with yellow emitting phosphors[31]. Nakamura won the Noble prize in 2014 for “the invention of efficient blue light-emitting diodes, which has enabled bright and energy-saving white light sources”. Moreover, the LEDs will emit colored light at a specific wavelength decided by the energy band gap of the semiconductor. By selecting different electroluminescent semiconductors, LEDs can be made to emit a narrow band ranging from near-infrared to ultraviolet[32-34].

When the emissive layer is composed by organic electroluminescent molecules, it is called organic light-emitting diode (OLED). These organic compounds are semiconductive due the π-electrons in delocalized orbital caused by the conjugation system over the molecules. The first practical OLED was built in 1987 by Ching Wan Tang and Steven Van Slyke[35]. There have been many researches concerning OLED afterwards[36-38]. Until now, OLEDs have become the main-stream technic in high-performance and ecofriendly display devices such as screens for mobile phones and televisions[39]. It can work without backlight since it emits its own light. The simple OLEDs are normally constituted of cathode, anode, and emissive layers in between. Modern OLEDs contain more conducting layers, including hole and electron transport materials (HTM and ETM) (see **Figure 1-10**).

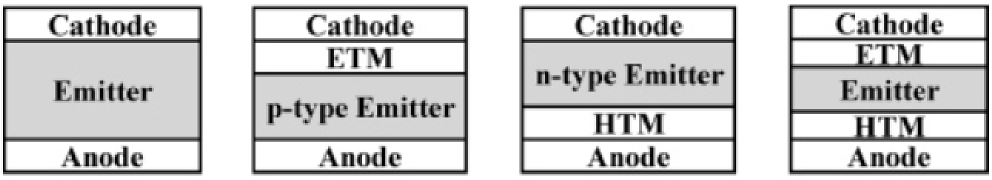

Figure 1-10 Device architectures of OLEDs, reproduced from literature[40].

Conducting layers, are crucial to manage and control carrier density and tuning the transport pathway[41]. To transport holes, HTM should be electron-rich compounds. Triphenylamine derivatives are often used as hole transport layers in OLEDs[42]. In contrast, ETM should be electron-deficient materials. For examples, triazole and triazine derivatives constitute a class of azole-based materials that have been used as ETMs in OLEDs[40,43,44].

The emissive layer, where the organic EL molecules are doped in the host material, is the heart of the devices. The electrical energy is directly converted into light in this layer. The suitable organic EL molecules for OLEDs usually contain large π-electron conjugated systems (**Figure 1-11**). Conventional choices are small molecules, like aluminum complexes Alq_3[35], anthracene and coumarin derivatives[45,46]. Polymers, such as polyfluorene derivatives, also have been used as emitting materials in polymer light-emitting diodes (PLEDs)[47].

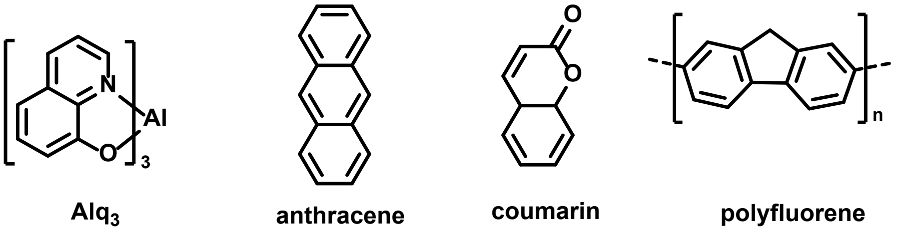

Figure 1-11 Organic EL molecules used in emissive layers in OLEDs.

Even though OLEDs possess many advantages over conventional inorganic LEDs, such as they have lighter weight and can be embedded with flexible subtract, they have better picture quality, faster response and power efficiency, etc. However, they also suffer from the nature of organic compounds. Firstly, conventional OLEDs show relatively low quantum efficiency, especially for blue OLEDs. The maximum internal quantum efficiency of the conventional fluorescence-based OLED is 25%, limited by the probability of 0.25 for the occurrence of the singlet excitons. The 75% triplet excitons are forbidden in the radiative transition and are wasted. The external quantum efficiency (EQE) is around 5% at most. From 2009 to 2012, Adachi and coworkers published a series of papers reporting effective thermal activated delayed fluorescence (TADF) molecular design strategies and competitive EQE for OLEDs[38,48,49]. The TADF process usually involves an excited molecular species in a triplet state, which undergo a reverse intersystem crossing to singlet state by absorbing thermal energy, resulting in a harvest of triplet excitons. In 2022, Han *et al.* synthesized a new D-A type luminescent material, TDBA-Cz (Shown in **Figure 1-12**), which can elaborate with non-doped blue OLEDs with a narrow emission at 467 nm and an EQE up to 21.4%[50]. The other main disadvantage of OLED is the limited lifespan caused by the degradation of organic semiconductors[51]. In particular, blue OLEDs at that time had a lifetime of around 14,000 hours to half original brightness (five years at eight hours per day) when used for flat-panel displays. This is lower than the typical lifetime of LCD, LED or PDP technology; each rated for about 25,000–40,000 hours to half brightness[52]. There are some researches concerning the improvement of their stabilities[53,54]. As far as today, it is still difficult to completely replace the InGaN-based LEDs with OLEDs.

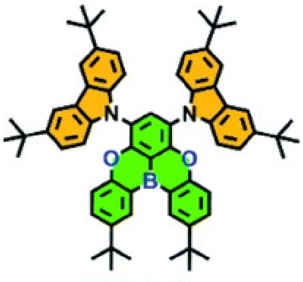

TDBA-Cz

Figure 1-12 TADF emitter TDBA-Cz.

Besides OLEDs, there are some potential technologies of new family of LEDs. Perovskites semiconductors, are a class of materials with crystal structures following the formula ABX3. The name is originating from $CaTiO_3$. The have potential to be made at low cost via facile solution processing, and could provide tunable colors and narrow emission line widths at high photoluminescence quantum yields (PLQY)[55,56]. In 2018, Wei and coworkers reported a perovskite LEDs with EQE of more than 20%[57], which is already rivaled those of the best performing OLEDs.

1.2.2 White light-emitting diode

There are two primary approaches to produce WLEDs. One is to mix single-color LEDs that emit three primary colors, red, green and blue[58]. But this method cannot provide white light with good color rendering because it is composed by three narrow bands. The other one is to use down-converting phosphors to convert the blue or UV light to a broad white light. In 1996, the first pc-WLED was produced by Nichia with a blue InGaN LED chips covered with yellow emitting phosphors[31]. It has been commercialized massively afterwards[59]. The most commonly used phosphor in white LEDs is the Ce^{3+}-doped lattice of yttrium aluminum garnet (YAG), with the general formula: $Y_{3-x}Al_5O_{12}:Ce_x$, abbreviated YAG:Ce[60], shown in **Figure 1-13**. As we can see in **Figure 1-14**, this yellow phosphor exhibits two excitation band at 340 nm and 460 nm attributed to the 4f-5d^2 and 4f-5d^1 transitions of Ce^{3+}, respectively, and the emission band around 540 nm (red shifts with increasing of Ce^{3+} concentration)[61]. YAG:Ce shows an extremely high PLQY of 97%[62], and a very high quenching temperature of its luminescence, which is more than 700K[63]. Those excellent performances make it an outstanding option as a phosphor in WLED.

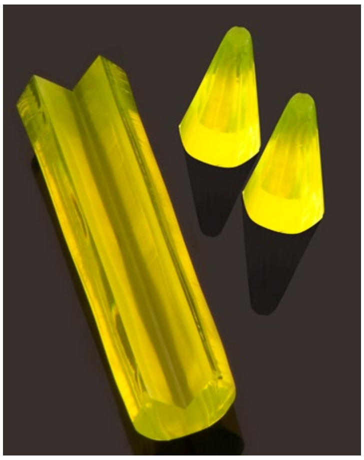

Figure 1-13 Yellow phosphor YAG:Ce crystals, reproduced from https://www.scientificmaterials.com/products/ce-yag.php.

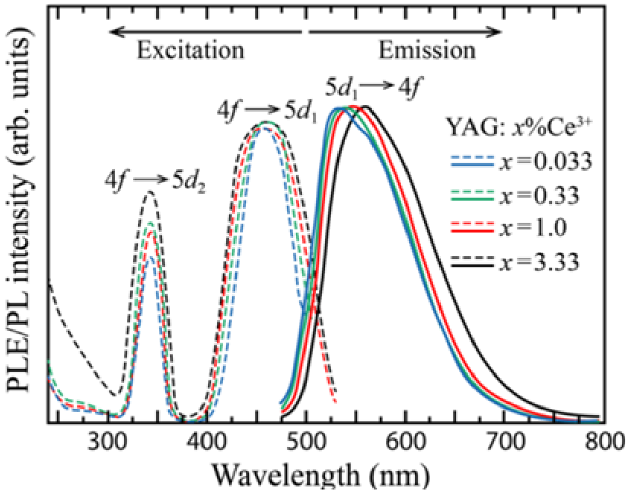

Figure 1-14 PL excitation and emission spectra of YAG:Ce with different Ce^{3+} concentration, reproduced from literature[63].

However, due to the lack of red component, YAG:Ce is considered as a cold-color phosphor, showing high color temperature and low CRI (71)[31,64]. In order to enhance the red emission of YAG:Ce, there are two main approaches that can be applied. Firstly, by co-doping with lanthanide ions (Eu^{3+}, Pr^{3+}, Sm^{3+}), a secondary peak could occur in the red spectral range. For example, the co-doped phosphor YAG:Ce,Pr shows a yellow emission band around 540 nm with an additional red emission band at 610 nm, under a 460 nm excitation wavelength[65], as shown in **Figure 1-15** left. The other approach is substituting Y^{3+} with larger ions (e.g., Tb^{3+}, Gd^{3+}, La^{3+}) to augment the crystal field splitting and regulate the Ce^{3+} emission to the long wavelength regions[64,66]. Kim *et al.* reported WLEDs using Tb^{3+} substituted YAG:Ce with red-shifted emission and improved CRI to 80 (**Figure 1-15** right)[64].

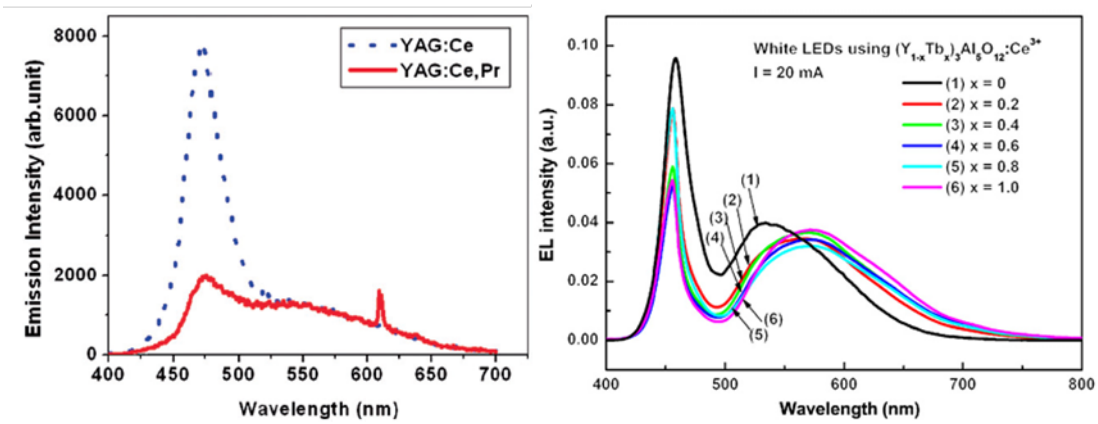

Figure 1-15 Emission spectra of WLED with Pr^{3+} doping (left) and Ce^{3+} substituting (right) YAG:Ce phosphor.

Although inorganic phosphors (IPs), especially YAG:Ce, have plenty of merits when applied as converting emitters, they are all limited by the inorganic nature: (1) they are based on rare-earth elements which are very limited source on our planet, with very polluting process of mining and harsh fabricating conditions[67]; (2) they have low absorption coefficient (~ 15 cm^{-1} for YAG:Ce)[68], thus leave an excess of blue component from the light pump, which is a menace to eye photoreceptors and disorder the circadian rhythm; (3) the resulting devices emit a light that is not of perfect quality due to the lack of red component. Therefore, IPs are considered as the principal concern to be solved heading to the next generation of artificial LED lighting system. In this context, hybrid LEDs are attracting researchers' attentions[69-71]: to keep the high performing near-UV or blue-emitting LED core based on InGaN, and to replace the IPs by organic or hybrid luminophores with tunable colors.

Comparing to the conventional inorganic phosphors, organic luminophores are considered to have many merits: (1) Thanks to the high absorption coefficient of organic π-conjugated compounds ($\varepsilon \approx 10^4$–10^5 $M^{-1}\cdot cm^{-1}$)[13], it is possible to fabricate their thin films (thickness is less than 100 micrometers) and elaborate light-weight devices. (2) they have the easy tunability of the emitting color by simple modification of chemical structures, and some of them can show high emission efficiency by careful chemical design; (3) they are metal-free, basically consist of carbon, hydrogen and some heteroatoms like nitrogen, sulfur; (4) the synthetic conditions are relatively mild and they can be processed through solution procedure, such as spin-coating, slot-die coating, etc.

In this thesis, we are aiming at designing and synthesizing a new family of organic luminescent molecules which could be applied as luminophores in WLED. Notably, to replaces IPs, we should attach importance on the PL properties of these organic down-converters. Even though there are massive examples of organic luminescent molecules from literatures, most of them are focus on the applications as the EL emitters in OLEDs, while not many articles concern the topics of organic/hybrid PL materials in hybrid WLEDs. Nevertheless, it is still crucial to understand the general approaches to design organic emissive molecules. In the next section, we will review the different design concepts suitable for the design of organic emissive compounds and define the suitable strategy for the present project in PL applications.

1.3 Organic luminescent materials

Organic luminescent materials are usually composed of a large π-conjugated system[72] as the bandgap falls into a range from the near UV to the near IR. These compounds have been studied and applied in optoelectronic devices for decades. In this brief review, we will introduce the strategy to tune the emission color of such organic luminescent compounds. Then, we will discuss some other tactics to further improve the PL performance in solid state since we wish to apply them in thin films. Some successful examples will be presented in the end.

1.3.1 Towards controlling emission color: donor-acceptor strategy and others

To design organic luminescent molecules, it is of primary importance to control the optical bandgap. In particular, building molecules in which an electron donor (D) is linked to an acceptor (A), labelled as (D-A), is a strategy that has been widely used to lower the band gaps of organic materials. It was introduced by Wynberg and co-workers in 1992 and has been an effective method for preparing conjugated molecules with bandgaps down to the near-IR[73]. This approach involves the synthesis of a molecule with a delocalized π-conjugated system comprising an electron-rich unit connected to an electron-deficient one, thus leading to a resulting system showing a high-lying HOMO and a low-lying LUMO, with respect to the position of the corresponding levels of the donor and the acceptor taken separately (**Figure 1-16**).

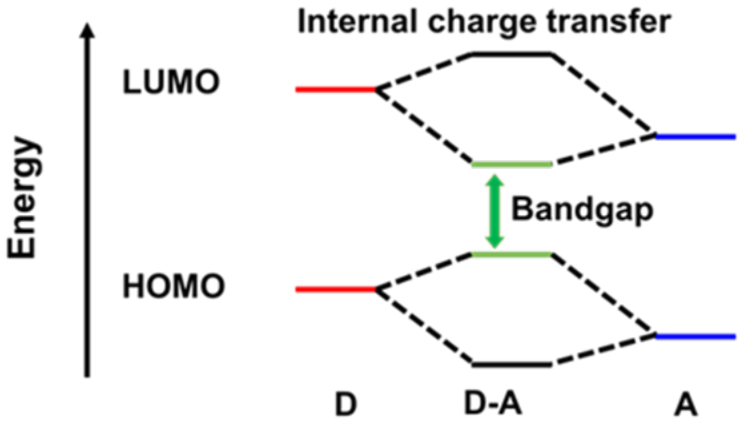

Figure 1-16 Schematic representation of the energy diagram for a D-A system.

In fact, the connection between the D and A units generates an internal charge transfer (ICT) that lowers the bandgap[74]. By careful selection of the D and A units, the value of the bandgap can be tuned[75], so the emission[76-78]. A recent example is that, Park's group reported a series of D-A molecules with a bis-lactam scaffold grafting with different donor groups, named NTD fluorophores, exhibiting tunable emission color from blue to red (**Figure 1-17**)[79]. As shown in **Figure 1-18**, Steinberg *et al.* synthesized a family of benzimidazole-based Schiff bases with different D and A units and emit in green, yellow and red in solid state[80].

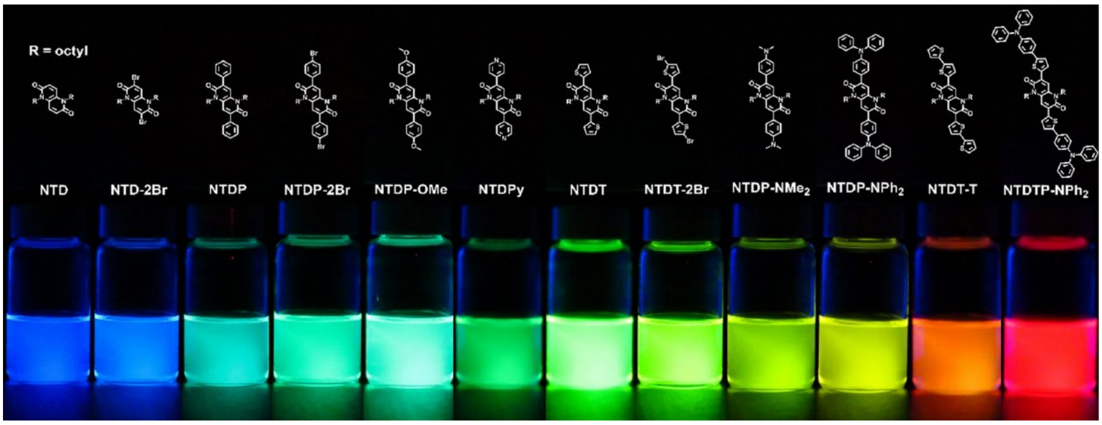

Figure 1-17 Photographs of NTD fluorophores under 365 nm UV irradiation, reproduced from literature[79].

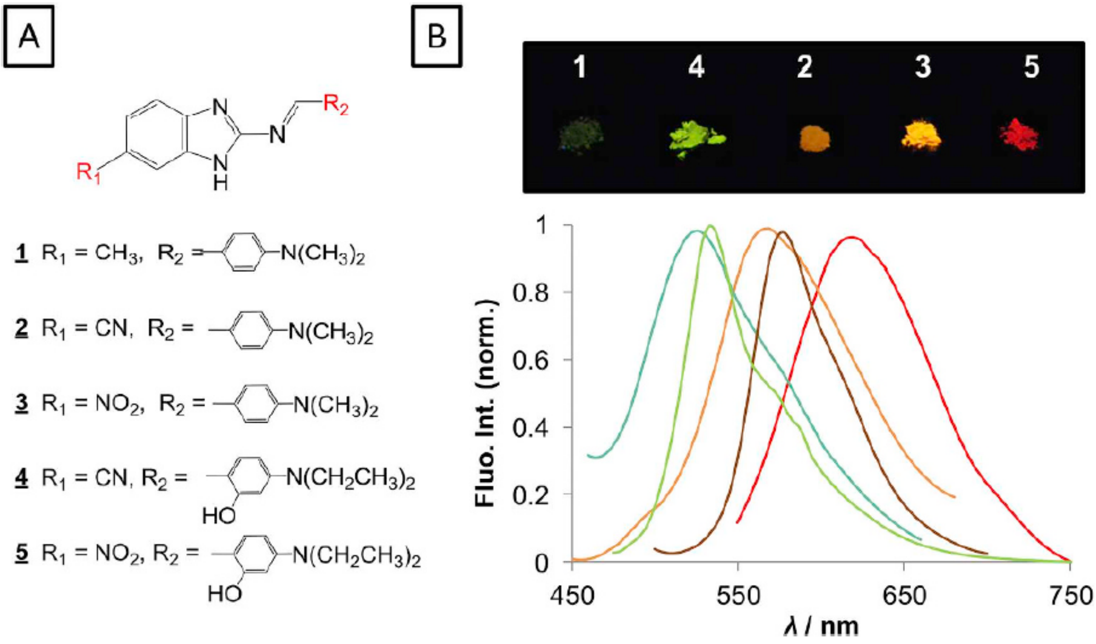

Figure 1-18 A) Benzimidazole-based Schiff bases 1–5; B) Solid-state emission spectra and photographs taken under 365-nm UV lamp, reproduced from literature[80].

There are also many successful precedents of highly efficient D-A fluorophores (shown in **Figure 1-19**). Ma and coworkers reported deep-blue emitter TPA-PPI with high PLQY (90%) both in solution and in the solid state[81]. Zhang *et al.* synthesized an orange-red emitter SNF-2AP, showing high PLQY of 99% in a doped film[82]. Tang's group reported a red fluorophores DCPPr-α-NDPA with 82% PLQY in toluene, and 90% in doped film[83]. Herein, the D-A strategy is proved to be an effective approach to construct highly emissive luminophores with tunable emission colors.

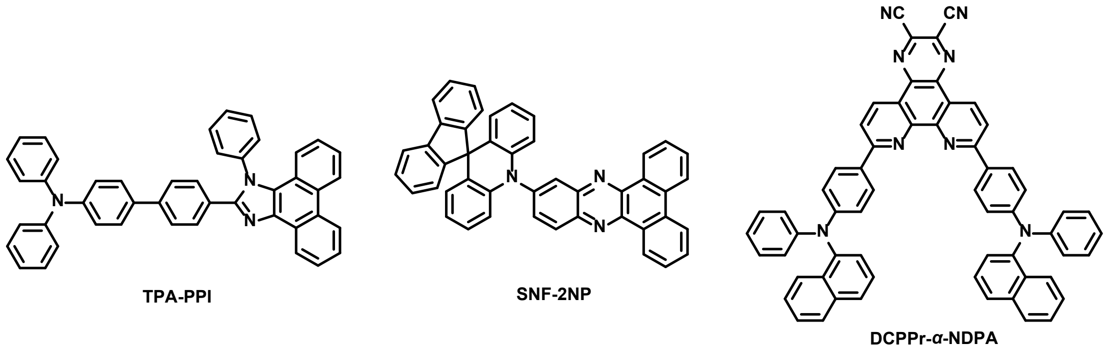

Figure 1-19 Highly emissive D-A fluorophores.

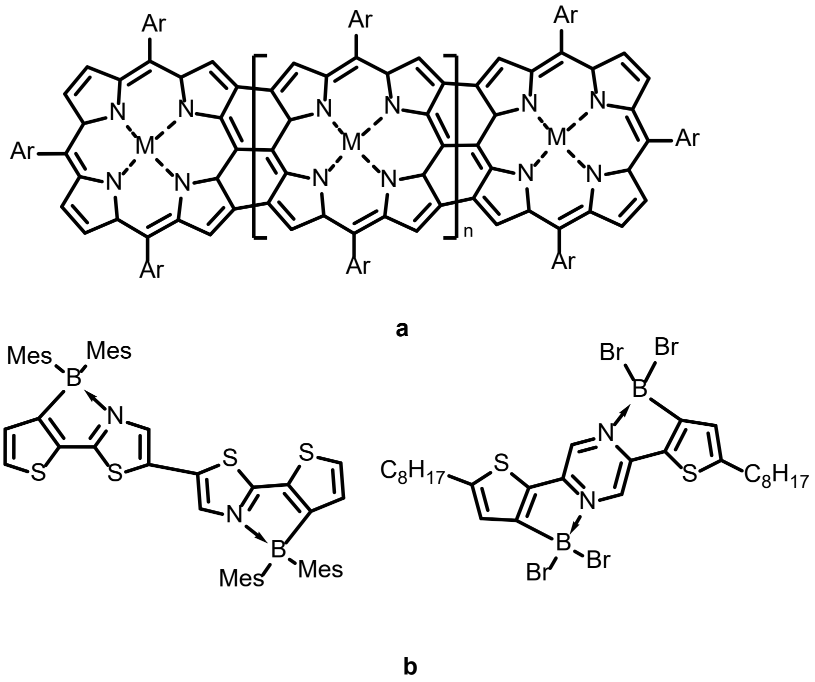

Figure 1-20 Examples of coplanar system in organic conjugated molecules.

Besides the D-A strategy, there are some ways that allow to tune the bandgap through the extension of the coherent π-conjugated delocalization. Conjugated polymers have more often been preferred compared to small molecules because of their longer possible conjugation length[84]. Their potentially overlapping orbitals create expanded system of delocalized π-electrons along the backbone, resulting in a lower bandgap[85]. In the same idea, π-bridge was introduced in conjugated molecules to enhance π-delocalization for lowering the band-gap[86]. However, the effective coherent conjugated length is severely limited by the torsional motion between the units. Thus, constraining the π-conjugation into a coplanar system by chemical means has been developed. The Osuka group has synthesized fully planar oligoporphyrins **(Figure 1-20 a**) to produce infrared absorption and emission[87]. Yamaguchi and Fang groups constructed B-N bonds in thienyl thiazole and thienyl pyrimidine derivatives (**Figure 1-20 b**) to fix the π-conjugated framework into a planar fashion to obtain a lower bandgap[88,89].

1.3.2 Aggregation-induced emission (AIE)

The conventional organic emissive molecules usually contain polycyclic aromatic hydrocarbon like anthracene and perylene[72]. They can show high PLQY in solution, but the efficiency is generally low in thin film and solid state as a consequence of aggregation caused quenching (ACQ). Indeed, the emission intensity is quenched by intermolecular interactions like π-π stacking between the large aromatic groups. Therefore, in practice, conventional organic emitters have to be doped at a low concentration in a matrix to improve the performance and avoid detrimental intermolecular interaction.

The discovery of the AIE phenomenon, described hereafter, has provided a valuable solution to solve this problem. In 2001, Tang and his co-workers found that hexaphenylsilole and a series of silole derivatives (**Figure 1-21**) were non-emissive in diluted solutions but became emissive in casted films[90,91]. Silole molecules cannot pack through π-π stacking because of their shape, but the strict restriction of intramolecular rotations (RIR) blocks the non-radiative pathways and gives the emissive property in aggregation-state[92]. Silole derivatives have been applied in optoelectronic devices due to the advantage of high efficiency in aggregation and solid state[93,94]. Inspired by silole derivatives, many AIE luminophores were developed (**Figure 1-21**). Tian *et al.* reported several AIE fluorophores building on triphenylamine core, which can be used in non-doped red emitters, among which SBCHO shows a sharply increased PLQY of 31% in aggregates, while it is virtually non-emissive in solution[95]. Moreover, many researches start to incorporate the AIE with ICT by employing D-A strategy. In 2008, two fluorenonearylamine derivatives, 1DPAFO and 2DPAFO with triphenylamine as D moieties are synthesized in Jiang's group[96]. Their PL intensities were boosted up about 100 times in aggregates comparing to ethanol solutions. Recently, Zhang's group designed an AIE-active D-A luminophore BPMT, with emission in deep-red to near-infrared and a PLQY of 8.4% in aggregates (0.4% in THF solution)[97].

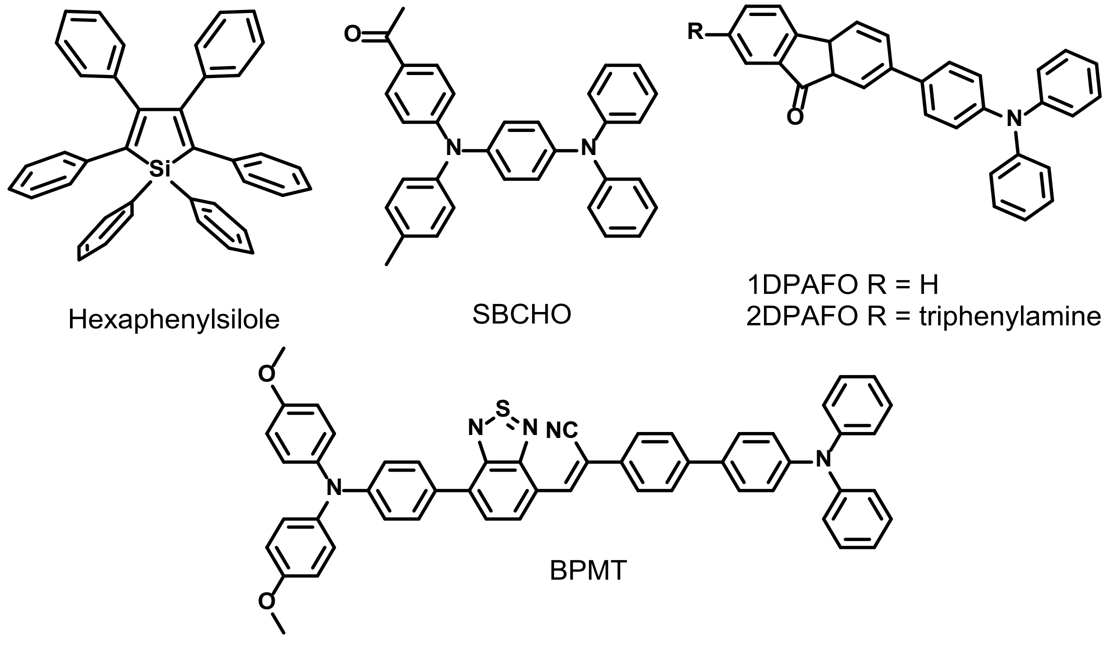

Figure 1-21 Reported AIE luminophores.

1.3.3 Organic down-converters for hybrid LEDs

Following the design methods described in **§1.3.1**, below are some examples of reported organic down-converters for hybrid WLEDs. Before heading to the literature review, some important concepts for down-converters are needed to be defined. As we mentioned before, PLQY is an important value to estimate the efficiency of the emitter, as known as internal quantum yield, which can be defined as

$$PLQY = \frac{Number\ of\ the\ emitted\ photons\ by\ converter}{Number\ of\ the\ absorbed\ photons\ by\ converter}$$

The absorptance is

$$Absorptance = \frac{Number\ of\ the\ absorbed\ photons}{Number\ of\ the\ photons\ from\ external\ source}$$

And the external quantum yield (Φ_{ex}), representing the conversion efficiencies of the down-converters from the external light source to the visible light, is defined as

$$\Phi ex = \frac{Number\ of\ the\ emitted\ photons\ by\ converter}{Number\ of\ the\ photons\ from\ external\ source}$$

Which is equal to

$$\Phi ex = PLQY \times A$$

As early as in 1997, Heeger *et al.* reported a hybrid LED where the InGaN based blue-emitting chip serves as pump to excite the film of mixed conjugated polymers, the red-emitting MEH–PPV and the green-emitting BuEH-PPV, to generate bright white light[71]. The structures of these polymers are shown in **Figure 1-22**. The conversion efficiency from the photons emitted by the blue emitters to the photons emitted by the hybrid reached up to 60%[71]. In Turnbull's group, a hybrid WLED that comprised a blend of the conjugated polymers MEH-PPV (orange-red) and BBEHP-PPV (green), was described as an interesting candidate for visible light communication[98]. The new devices show overall PLQYs from blue-emitters to hybrid LEDs varying from 25% to 28% depending on the ratio of different polymers, good CRI (76), and fast response due to the much-shorter fluorescence lifetimes (~ 1 ns) compare to LEDs embedded with inorganic phosphors (~ 600 ns).

The polyfluorene family is also competitive for hybrid WLEDs[69,99,100]. The Bradely group reported hybrid LEDs with the InGaN ultraviolet-emitting core converted by red-, green-, blue-, and white-light-emitting films respectively. These films are based on polyfluorene derivatives. They achieved white light at (0.30, 0.34) by blending different polymers[100]. In 2008, Tuncel and coworkers fabricated a hybrid WLED with PFA (PLQY = 0.86) serving as luminophore pumped by 378-nm near-UV emitter (**Figure 1-22**)[69]. This device emitted a white light at around (0.3, 0.3) with a

CRI reaching 91. The Φ_{ex} of near-UV source to visible light are not reported for the polyfluorene derivatives.

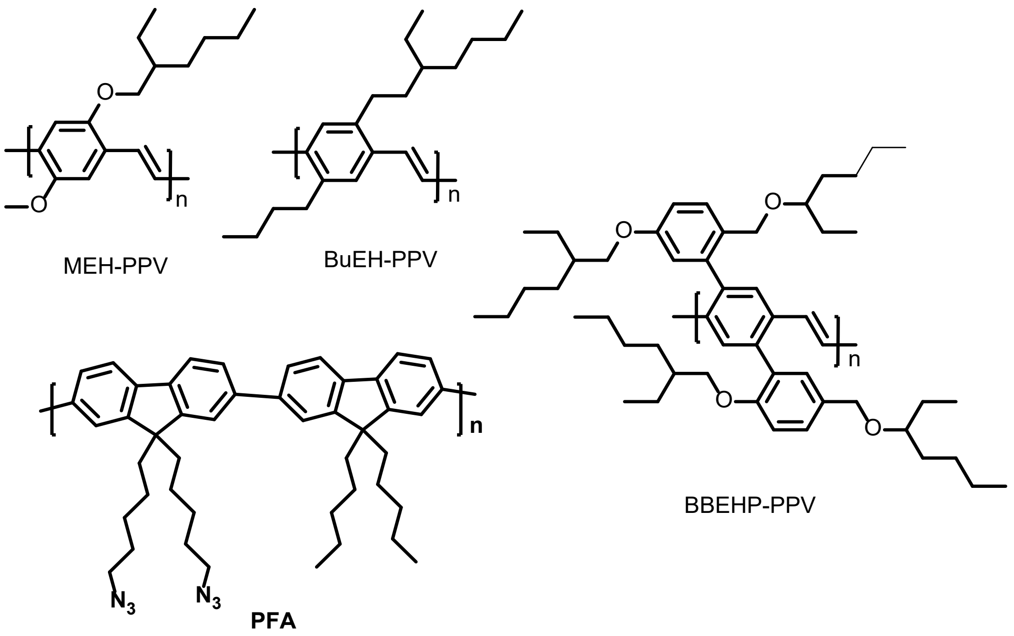

Figure 1-22 Polymers applied as organic down-converting materials for hybrid LEDs.

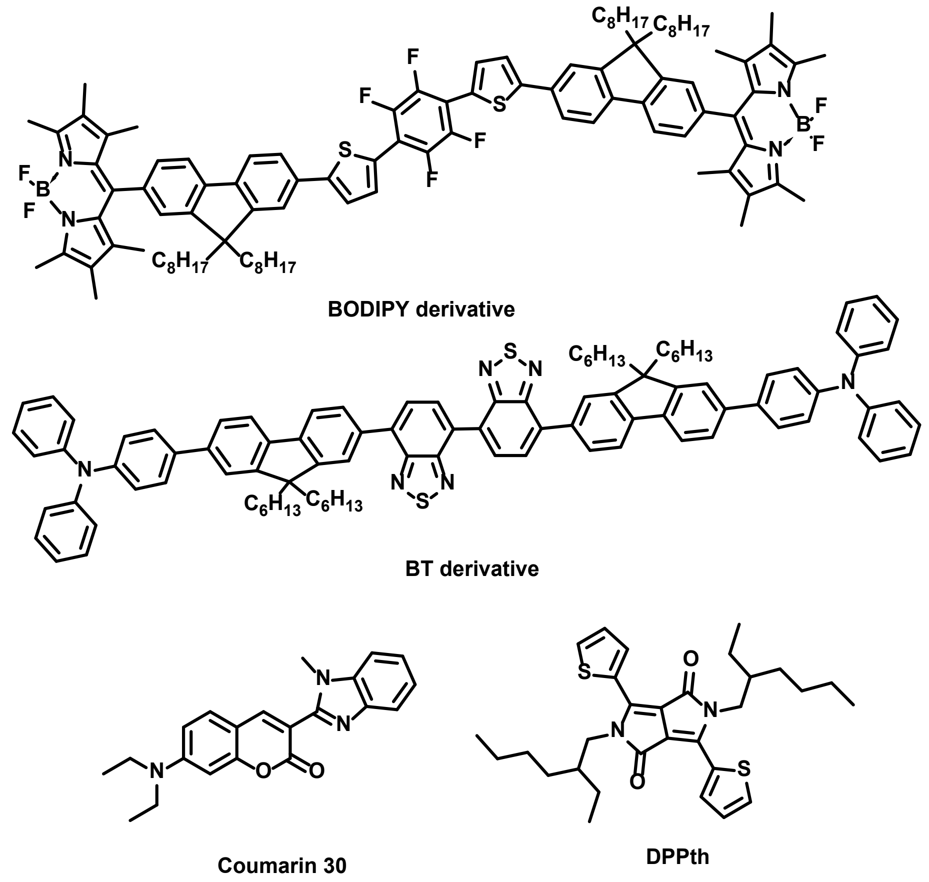

Figure 1-23 Small molecules used as organic down-converting materials for hybrid LEDs.

Besides conjugated polymers, there are some small molecules implemented as down-converters for hybrid WLEDs, as shown in **Figure 1-23**. the Martin and Skabara group has developed a series of near-UV and blue-absorbing molecules comprising 4,4-difluoro-4-borata-3*a*-azonia-4*a*-aza-*s*-indacene (BODIPY) and 2,1,3-benzothiadiazole (BT) units suitable for hybrid inorganic/organic LEDs and achieved white light[101-103]. A hybrid WLEDs with a blue chips covered by yellow-emitting films of BODIPY derivative was reported by them in 2014 with CIE coordinates of (0.34, 0.31), converted from blue light (0.16, 0.02)[102]. Also in 2014, a blender of green-emitting Coumarin 30 and red-emitting DPP-th in bulky PMMA doped films was used in hybrid WLEDs[104]. It exhibited a nearly perfect white light at (0.32,0.33) with a CRI of 80. An excellent short-term photostability was found: the emission intensity remained over 90% by continuous operation for 72 hours.

The state of art reveals that there are two main pathways to fabricate hybrid WLEDs. One way is to embed one yellow down-converter with a blue-emitting LED; the other way is to cover a near-UV LED with phosphors emitting in three principal colors, blue, green and red, to generate the white light by tuning the ratio between these three components.

1.4 Summary

In this initial chapter, we briefly introduced the luminescence and luminescent materials, including the process, mechanism and applications. Especially we reviewed the development of LEDs, which is evolving from inorganic to organic materials, owing to their light weight, flexibility, excellent PL performance and eco-friendly property. The fact that, it is still difficult to completely replace the inorganic near-UV and blue LEDs with organic ones, is highlighted.

Then the commercial pc-WLEDs based on the blue LEDs covered with yellow inorganic phosphor YAG:Ce are described. The main disadvantage of this devices is the imperfect quality of the white light, due to the excess of blue component and lack of red component. Meanwhile, the organic PL materials show plenty of merits, particularly the facile tunability of emission color. Herein, the goal of this thesis is proposed, which is to use the combination of organic near-UV or blue LEDs and tunable organic down-converters for constructing the highly efficient hybrid WLEDs with perfect quality of white light.

The following part is a state of the art for the organic down-converters employed in the hybrid LEDs. Starting with the frequently adopted strategies, we illustrate the general ideas on how to design these organic luminophores. Then some successful precedents are presented to give a picture on how the domain is developed. For such application, there are some common characters for emissive molecules and polymers: (1) strong absorption in the near-UV and/or blue; (2) high PLQY; (3) usually broad emission band is preferable for a better CRI hence white light is targeted; (4) good processing property for the film fabrications; (5) thermal and photo-stabilities are also important.

With the design ideas and accomplished examples in mind, we will introduce the design of a new family of emissive D-A molecules which are able to work as efficient organic down-converters in hybrid white LEDs. There are two methods to achieve white light in hybrid WLEDs: one is to cover a blue-emitting LED by yellow-emitting organic down-converter, the other one is to use more than one phosphors to convert the near-UV source by complete absorption.

Chapter II Design and synthesis

In this chapter, we will overview the general strategy we adopted for the design of donor-acceptor (D-A) molecules, especially the selection of donor and acceptor groups. Then we will present the experimental section, including the general information of materials and instruments, the synthetic procedures and characterizations, the method for the photophysical measurements and film fabrications.

2.1 General design for the D-A molecules

As we mentioned in **Chapter I**, the selections of electron-donors and acceptors are vital for the emissive properties as they influence the photoluminescent performance of the whole molecule profoundly. Regarding the common donors, polycyclic aromatic hydrocarbons like anthracene and pyrene have been widely used. They are very rigid and planar, usually leading to aggregation-caused quenching (ACQ) in the solid state and, consequently, difficult processing due to poor solubility[72]. Aromatic amines (**Figure 2-1)**, such as carbazole, triphenylamine, indoline and julolidine derivatives, are more suitable candidates due to their richness in electrons[105] and better solubilities[106]. They were extensively utilized in the design of dyes and for electronic applications[107-110]. Aromatic amine groups usually show strong absorption in the middle or near-UV region[111], with molar absorption coefficients (ε) more than 1×10^4 L·mol^{-1}·cm^{-1}. For example, triphenylamine exhibits a sharp absorption at 303 nm in cyclohexane solution, and dual absorptions at 323 and 335 nm are obtained with carbazole in ethanol solution. This near-UV absorption is of great interest to design visible-emissive compounds. Additionally, triphenylamine is often used to construct D-A molecules with aggregation-induced emission (AIE) to improve the solid-state luminescence. Tang's group reported two D-A compounds comprising triphenylamine as donor, which showed intense yellow emission in solid with quantum efficiencies of 33.2% and 38.2%, thanks to the AIE nature[112]. The propeller-like structure of triphenylamine can prevent

π-π stacking and the following ACQ, and restrict intramolecular rotations in aggregate state to open up the radiative channel[113]. Therefore, triphenylamine derivatives are primarily chosen as the electron donors. Carbazole derivatives are also chosen for their similarities in structure to triphenylamines, which gives the possibility to conduct the comparative studies.

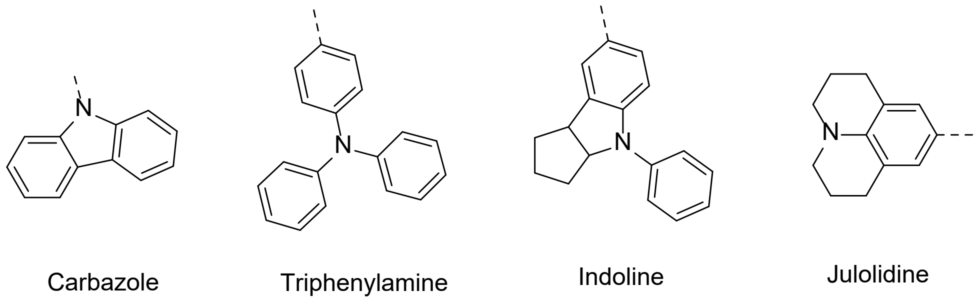

Figure 2-1. Examples of aromatic amines.

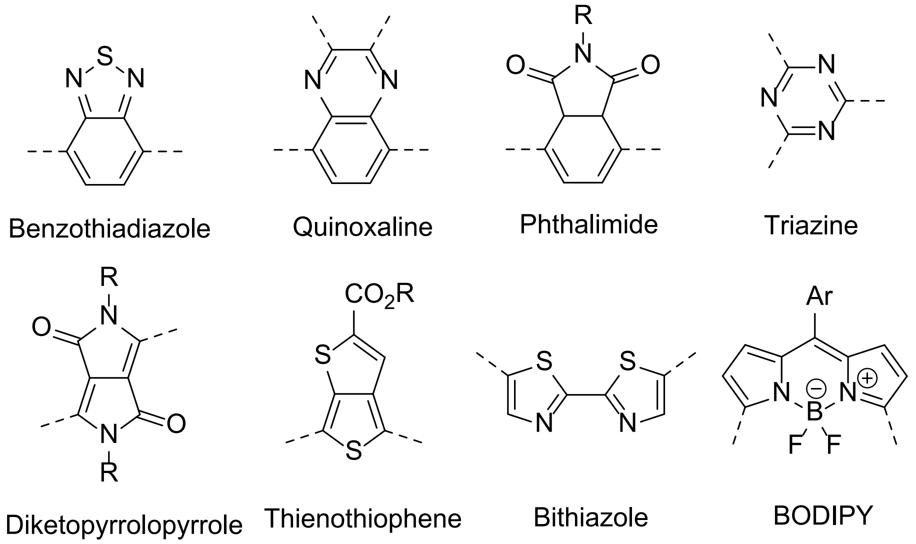

Figure 2-2. Frequently reported electron-accepter units in D-A molecules.

Concerning the acceptor part, the frequently electron-deficient moieties are benzothiadiazole, quinoxaline, phthalimide, thienothiophene and boron-dipyrromethene (BODIPY) [114-118]. Their structures are shown in **Figure 2-2**. Besides them, some other heterocyclics like pyridine, pyrimidine and benzimidazole have also been utilized as electron-acceptors[80,119,120]. We could summarize some common features from them as follows: (1) they comprise large conjugated systems, in other words, they are rather planar. The better planarity expands the conjugation and enhance the photophysical properties; (2) hetero atoms like nitrogen and sulfur are important to boost the electron-deficient properties.

Particularly, bipyrimidine derivatives have attracted our attention. We found it an interesting novel candidate of acceptor in D-A molecules because of its high electron affinity[121]. As it is shown in **Figure 2-3**, taking 2,2'-bipyrimidine as an example, in the pyrimidine ring, the lone pair of each nitrogen resides in a perpendicular orbital towards the π-conjugated system, while only one electron participates in the delocalized system. In the meantime, the stronger electronegativity of nitrogen over carbon gives rise to the electron deficiency of the whole compound[122]. Therefore, the pyrimidine ring shows a higher electron affinity than some other *N*-hetero rings like pyridine.

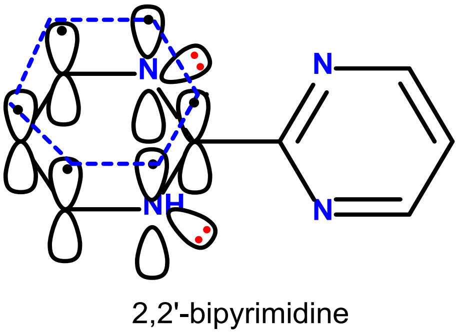

Figure 2-3 Electron distribution in 2,2'-bipyrimidine.

In the past few decades, bipyrimidine derivatives have been used as chelating ligands in transition-metals and lanthanides complexes[123-125]. Recently, there are few studies have reported their usages in the buildings of conjugated molecules for optical and electronic applications, and even fewer reports on their uses on building D-A molecules. Singman's group has synthesized a series of low-potential two-electron organic anolytes based on 2,2'-bipyrimidines derivatives[126]. Some of them showed high degree of stabilities in electrochemical cycling. Zhu et al. reported two hole transport materials for conventional solar cells (shown in **Figure 2-4 a**) based on the building blocks of 2,2'-diphenyl-5,5'-bipyrimidine associated with carbazole and diphenylamine derivatives[127]. The introduction of the electron-withdrawing bipyrimidine group increases molecular dipole moment, thus leading to an enhanced dipole-dipole interaction, which promotes charge transfer and affords a high hole mobility. Camerel and coworkers have reported 2,2'-bipyrimidine-based chromophores (**Figure 2-4 b**) with chiral side groups works as non-linear optical (NLO) organic liquid crystals and thin films[128,129]. One example focusing on their luminescent properties is reported by Lee and his coworkers[130,131]. They designed some D-A emitters using bipyrimidines as acceptors (**Figure 2-4 c**), which showed thermally activated delayed fluorescence (TADF) and high photoluminescence quantum yield (PLQY).

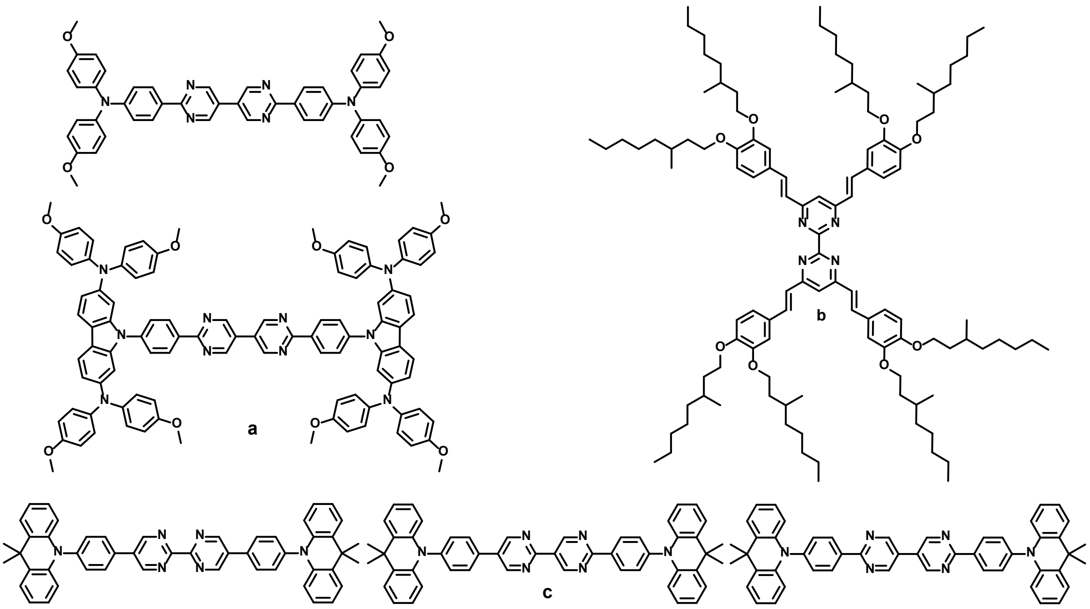

Figure 2-4 Examples of bipyrimidine based D-A molecules.

This short review illustrates that bipyrimidine derivatives could work extraordinarily in conjugated molecules, especially in electron push-pull system, thanks to the electron-deficient nature. Also, bipyrimidine shows high absorption in middle-UV, for example, the absorption band of 2,2'-bipyrimidine appears at 290 nm in THF ($\varepsilon = 1.7\times10^6$)[132]. Moreover, conjugated molecules containing bipyrimidine have been reported to show high photo- and thermal stabilities[133]. The other advantage is that their electron-deficient properties could be tuned by the introduction of additional electron-withdrawing or electron-donating groups, to achieve the desired photoluminescent properties. In this thesis, 2,2'-bipyrimidine (BPM) is selected particularly from the bipyrimidine family due to an interesting fact. In solution, the two pyrimidine rings are free to rotate, which increases the solubility and facilitates the fabrication of films in solution processes. On the other hand, as reported by Lee's group[131], the two pyrimidine rings of BPM tend to be coplanar in a D-A-D molecule. The single-crystal structure of BPM reveals that the inter-ring torsion angles is zero and it exists in a planar model in solid[134]. This could improve the conjugation of the acceptor segment in solid state with proper design.

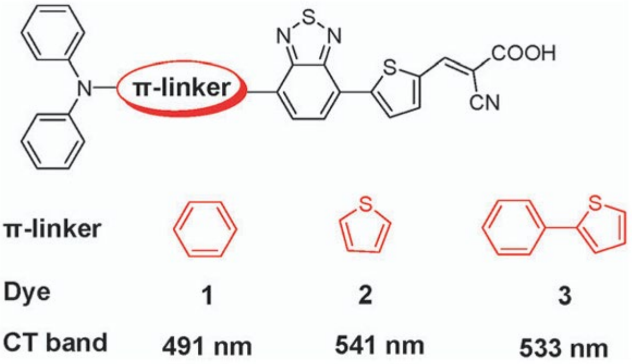

Figure 2-5 Effect of the π-linkers in D-π-A system, reproduced from literature[135].

Besides the selections of donors and acceptors, it is also of importance to adjust the way to attach the two parts with each other. The direct connection is one way, while another other way is to insert π-spacers in-between. In general, π-spacers can promote and control electron transfer in long distance and extend the conjugation length[86,136]. For example, Zhu et al reported the internal charge-transfer (ICT) absorption band can be tuned in a D-π-A system[135]. As shown in **Figure 2-5**, by changing the π-linker among phenyl, thiophene and phenyl thiophene, the ICT absorption band varies from 497 to 541 to 533 nm. The common options of conjugated π-linkers could be phenyl, thienyl, vinyl, ethynyl linkers and other conjugated system, and their repetitions or combinations, as they are shown in **Figure 2-6**.

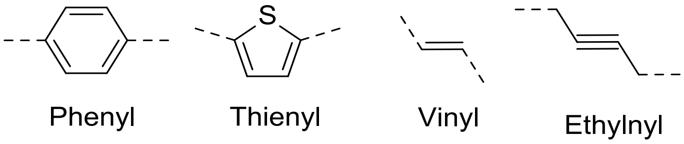

Figure 2-6 Common π-linkers used in D-A molecules.

In a previous work of our group, Lin has developed a series of D-A copolymer with BPM as the acceptor unit[137]. He has achieved tunable emission color from blue to green with interesting emissive properties and photo-stabilities. Continuing the established work, in this thesis, we well keep the building block of electron-deficient BPM to construct D-A small molecules. Comparing to polymers, small molecules are easier to be characterized, their behaviors can be understood more conveniently and precisely[72]. The synthesis of small molecules is reproducible, while it is very difficult for polymers. By modifying the electron push-pull strength, we aim at further tuning the emission color of different compounds from blue, green to red to cover the whole visible spectrum. Then, conditions are, *a priori*, met to obtain luminophores that emit white light by combining them.

2.2 Experimental section

In this section, we will show the synthetic procedures and characterization means taken to characterize the molecules. The method for photophysical measurements and fabrication of films are also presented.

2.2.1 Materials and instruments

2-chloropyrimidine, 2-chloro-4-(trifluoromethyl)pyrimidine, nickel chloride, triphenyl phosphine, bromine, sodium cyanide, sodium ethoxide, 1,4-diazabicyclo[2.2.2]octane (DABCO), diethyl malonate, ammonium chloride, potassium carbonate, sodium sulfite, sodium sulphate, ammonia, Tetrasodium 2,2′,2″,2‴-(Ethane-1,2-diyldinitrilo)tetraacetate (EDTA tetrasodium salt), cupper iodide, carbazole, hydrochloride were purchased from VWR. Tetrakis(triphenylphosphine)palladium, 9H-Carbazole-9-(4-phenyl) boronic acid pinacol ester, 4-(diphenylamino)phenyl boronic acid, 4-(bis(4-methoxyphenyl)amino)phenyl boronic acid, dicyclohexyl(2′,6′-dimethoxy[1,1′-biphenyl]-2-yl)phosphane (SPhos), palladium diacetate, [1,1′-

bis(diphenylphosphino)ferrocene]dichloropalladium(II), tetrahydrofuran (THF), dichloromethane (DCM), chloroform, bis(triphenylphosphine)palladium(II) dichloride tetrakis(triphenylphosphine)palladium(0), *N,N'*-dimethylpropyleneurea (DMPU) were purchased from Sigma-Aldrich and used as received unless otherwise specified. All solvents were carefully dried and purified before use when necessary. All manipulations involving air-sensitive reagents were performed under a dry argon atmosphere by using glovebox and Schlenk techniques.

NMR spectra have been recorded on Bruker Avance 300 or 400 spectrometers using $CDCl_3$ or CD_2Cl_2 as solvents; chemical shifts are given with respect to TMS ($\delta = 0$). The mass spectra were measured with TimsTOF Bruker ESI-Pos High resolution mass spectrometry (HRMS). The single crystals suitable for X-ray diffraction (XRD) were grown in solutions and selected. Measurements were done with a Stoe STADIVARI diffractometer, a Molybdenum X-ray microsource (from Xenocs) and a EIGER2 CdTe hybrid-photon-counting detector at 150K on suitable single crystals.

The UV-Vis absorption spectra were recorded using an Agilent Technologies Cary 60 UV–vis spectrophotometer. The photoluminescence spectra were measured with an Edinburgh Instruments spectrofluorometer FS5.

2.2.2 Synthetic procedures

2.2.2.1 Synthesis of BPM building blocks

The synthetic routes towards the desired compounds are exhibited in **Scheme 2-1**. Route **1** summarizes the syntheses of BPM (**1a**) and its dibromo (**1b**) and mono-bromo (**1c**) derivatives that have been previously reported[138,139]. Trifluoromethyl-substituted BPM (**2a**) and its dibromo (**1b**) and mono-bromo (**1c**) derivatives are newly synthesized following the same procedure. Synthetic route **3** is another pathway to obtain di-halogenated BPM[140,141]. Unfortunately, limited by the time, we have not carried out the last two steps to acquire **3c** and **3d**. For new compounds, both ^{1}H and ^{13}C NMR spectra will be presented as well as mass spectra in **§2.2.2.3**.

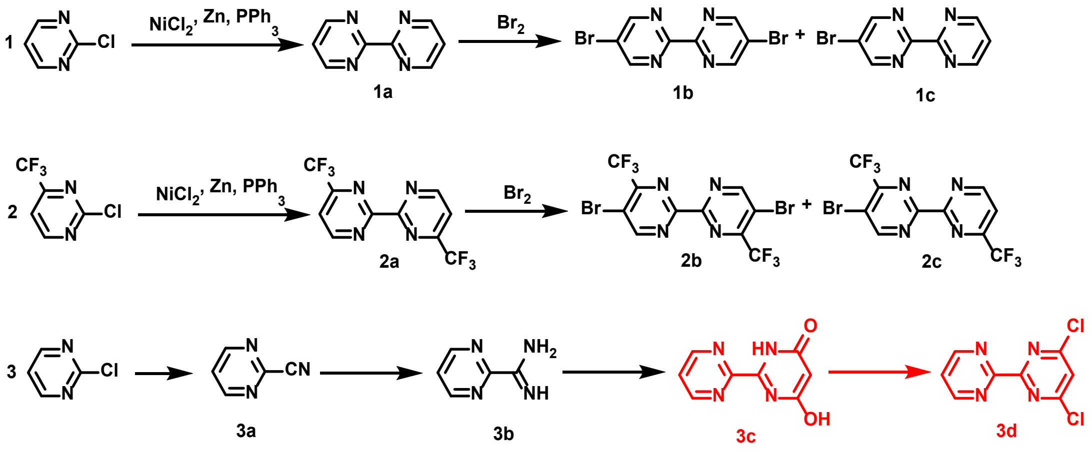

Scheme 2-1 Synthetic routes for BPM-based building blocks.

Synthesis of 2,2'-bipyrimidine (1a)

To a 100 mL dried two-neck flask charged with 4.58 g (17.46 mmol) of triphenyl phosphine, 0.75 g (5.82 mmol) of nickel chloride, and 0.57 g (8.73 mmol) of zinc powder, 170 mL of dry DMF (bubbled with argon for 30 minutes) was added under argon and stirred vigorously at room temperature for 1 h. Then, 2.00 g (17.46 mmol) of 2-chloropyrimidine was added under Argon and stirred at room temperature. After 1 h, the temperature was increased to 80˚C for 70 h. Then, the reaction mixture was cooled down to room temperature and filtered with Celite. The filtered cake was washed with chloroform until the filtrate is colorless. The solution was concentrated under vacuum. To the green-grey residue, an aqueous solution of EDTA tetrasodium salt was added (7.27 g, 30 mL). After stirring for 3 h, 30 mL of an 1M NH_3 aqueous solution was added. Then, the mixture was extracted by 30 mL of diethyl ether (3 times) and 30 mL of chloroform (8 times). The chloroform part was washed by 30 mL of deionized water (3 times) water and 30 mL brine (3 times), dried with Na_2SO_4 and the solvent was removed under vacuum. The crude product was purified by column chromatography (dichloromethane as eluent) and the product was obtained as a white solid (3.30g, yield: 52%).

^{1}H NMR (300 MHz in CDCl3, δ): 9.03 (d, J = 4.9 Hz, 4H), 7.44 (t, J = 4.8 Hz, 2H).

^{13}C NMR (75 MHz in CDCl3, *δ*): 161.8, 157.6, 121.2.

Synthesis of 5,5'-dibromo-2,2'-bipyrimidine (1b)

In a sealed tube, **1a** (542 mg, 3.43 mmol) and bromine (0.71 mL) were added under Argon and heated at 150°C for 72 h. Then the mixture was cooled down to room temperature. The hard solid was powdered and treated with a Na_2SO_3 solution (1.8 g, in 25 mL DI H_2O) to remove the excess of bromine. Then, the mixture was treated with an NaOH aqueous solution to adjust the pH to 14. The mixture was extracted with 30 mL of chloroform for 3 times, then the organic part was washed with deionized water (20 mL for 3 times) and brine (20 mL for 3 times), and dried with Na_2SO_4 and concentrated under vacuum. The crude product was purified by column chromatography (dichloromethane as eluent) and the product was obtained as a white solid (575 mg, yield: 53%).

^{1}H NMR (300 MHz in CDCl3, *δ*): 9.05 (s, 4H).

^{13}C NMR (75 MHz in CDCl3, *δ*): 159.7, 158.9, 121.9.

Synthesis of 5-bromo-2,2'-bipyrimidine (1c)

The product **1c** was obtained as a white solid (130 mg, yield: 16%) with the same reaction as for **1b**.

^{1}H NMR (400 MHz in CDCl3, *δ*): 9.04 (s, 2H), 9.00 (d, *J* = 4.8 Hz, 2H), 7.45 (t, *J* = 4.8 Hz, 1H).

^{13}C NMR (100 MHz in CDCl3, *δ*): 161.63, 160.26, 158.71, 158.11, 121.68, 121.62.

Synthesis of 4,4'-bis(trifluoromethyl)-2,2'-bipyrimidine (2a)

The synthesis of **2a** is the same as that of **1a** except using 2-chloro-4-(trifluoromethyl)pyrimidine instead of 2-chloropyrimidine. The product **2a** was obtained as a white solid (425 mg, yield: 49%).

^{1}H NMR (400 MHz in CDCl3, *δ*): 9.32 (d, *J* = 4.0 Hz, P1, 2H), 7.83 (d, *J* = 4.0 Hz, P2 2H).

^{13}C NMR (100 MHz in CDCl3, *δ*): 162.32 (s, C4), 160.69 (s, C1), 157.06 (q, *J* = 37.0

Hz, C3), 120.25 (q, *J* = 274 Hz, C5), 117.58 (q, *J* = 3.0 Hz, C2).

ESM-Pos Ms (m/z): $C_{10}H_5F_6N_4$ for $[MH^+]$, calculated 295.0413, found 295.0415.

Synthesis of 5,5'-dibromo-4,4'-bis(trifluoromethyl)-2,2'-bipyrimidine (2b)

The synthesis of **2b** is the same as for **1b** except using **2a** instead of **1a**, and the reaction mixture in the sealed tube was heated at 150 ˚C for 7 days. The product **2b** was obtained as a white solid (12 mg, yield: 2%). It is too few for taking ^{13}C NMR.

^{1}H NMR (400 MHz in CDCl3, δ): 9.32 (s, 2H).

Synthesis of 5-bromo-4,4'-bis(trifluoromethyl)-2,2'-bipyrimidine (2c)

The product **2c** was obtained as a white solid (60 mg, yield: 12%) with the same reaction as for **2b**.

^{1}H NMR (400 MHz in CDCl3, *δ*): 9.32 (s, 1H, P3), 9.31 (d, *J* = 8.0 Hz, 1H, P1), 7.83 (d, *J* = 4.1 Hz, P2).

^{13}C NMR (100 MHz in CDCl3, *δ*): 163.51 (s, C1'), 161.78 (s, C5), 160.74 (s, C1), 159.61 (s, C5'), 157.10, (q, *J* = 37.0 Hz, C3), 154.35 (q, *J* = 37.0 Hz, C3'), 120.18 (q, *J* = 274 Hz, C4') 119.95 (q, *J* = 275 Hz, C4), 118.55 (s, C2') 117.66 (q, *J* = 3.0 Hz, C2).

Synthesis of pyrimidine-2-carbonitrile (3a)

To a 200 mL flask charged with a solution of 2.7 g (55.0 mmol) of sodium cyanide and 0.59 g (5.24 mmol) of DABCO in DMSO (30 mL) and deionized water (15 mL), 2-chloropyrimidine (6 g, 52.4 mmol) in DMSO (20 mL) was added dropwise during 15 min, and the reaction mixture was stirred overnight. The mixture was extracted with 100 mL of diethyl ether (3 times). The combined organic layers were washed with 50 mL of water and brine for 3 times, dried with sodium sulfate, concentrated in vacuum and purified with column chromatography (dichloromethane as eluent). The product was obtained as a beige solid (4.50 g, 82%).

^{1}H NMR (400 MHz in $CDCl_3$, *δ*): 8.86 (d, *J* = 5.0 Hz, 2H), 7.56 (t, *J* = 5.0 Hz, 1H).

^{13}C NMR (100 MHz in $CDCl_3$, *δ*): 158.2, 145.4, 123.8, 115.7

Synthesis of pyrimidine-2-carboximidamide (3b)

To a solution of **3a** (1 g, 9.51 mmol) in 50 mL of methanol, sodium ethoxide (129 mg, 1.90 mmol) was added and stirred at room temperature for 12 hours. Then, 559 mg (10.46 mmol) of ammonium chloride was added. The mixture was heated and refluxed for 4 hours and then the solvent was evaporated under vacuum. The residue was suspended in ethanol, heated and refluxed for 1 hour and filtered after cooling down. The product was obtained after recrystallization from a propanol/hexane (5:1) solution as colorless needle-like crystals in a yield of 0.83 g (71%).

^{1}H NMR (400 MHz in CDCl3, *δ*): 8.95 (d, *J* = 4.9 Hz, 2H) 7.63 (t, *J* = 4.9 Hz, 1H), 7.12 (br. s, 3H).

^{13}C NMR (100 MHz in CDCl3, *δ*): 159.64, 157.52, 156.16, 121.81.

2.2.2.2 Synthesis of D-A molecules

Obtaining **1b** as the main product, we decided to construct D-A-D type molecules to extend the π-conjugated system.

Synthesis of 5,5'-di(9H-carbazol-9-yl)-2,2'-bipyrimidine (M1).

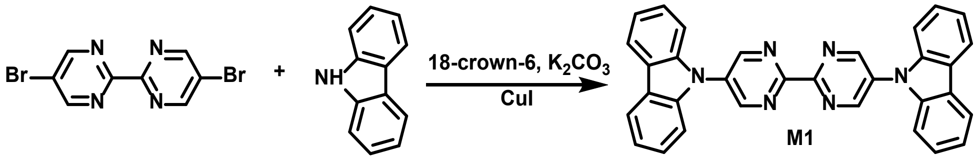

To a 50 mL two-neck flask charged with 200 mg (0.63 mmol) of 5,5’-dibromo-2,2’-bipyrimidine and 265 mg (1.58 mmol) of carbazole, 24 mg (0.13 mmol) of copper iodide, 33 mg (0.13 mmol) of 18-crown-6, 261 mg (1.89 mmol) of potassium carbonate and 1 mL of DMPU were added under Argon. Then, the temperature was increased to 200˚C and the mixture was stirred for 24 hours. The reaction mixture was then cooled and quenched with 2 M HCl (100 mL). The solution was extracted with chloroform, washed with ammonia and water, dried over Na_2SO_4, and the solvent was removed under vacuum. The crude product was purified by column chromatography using dichloromethane as eluent to yield the pure compound as a light-yellow powder (173 mg, 56% yield). Light yellow crystals suitable for X-ray diffraction were grown from a slow diffusion in chloroform/hexane mixed solution.

^{1}H NMR (400 MHz in $CDCl_3$, δ): 9.40 (s, 4H, P1), 8.19 (dt, 4H, J = 8.0, 1.0 Hz, P5), 7.56 – 7.50 (m, 4H, P2+P3), 7.52 (tt, J = 8.0, 1.8 Hz, 4H, P4)

^{13}C NMR (100 MHz in $CDCl_3$, δ): 159.28, 155.61, 139.88, 133.93, 126.86, 124.42, 121.69, 120.89, 109.03.

ESM-Pos Ms (m/z): $C_{32}H_{21}N_6$ for [MH^+], calculated 489.1822, found 489.1816.

Synthesis of 5,5′-bis(4-(9H-carbazol-9-yl)phenyl)-2,2′-bipyrimidine (M2).

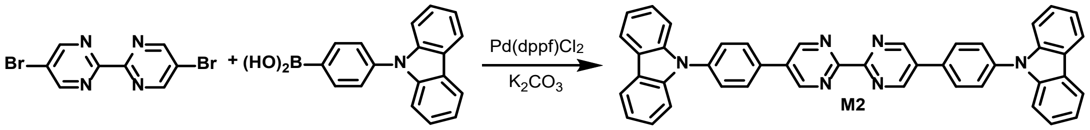

To a 100 mL flask charged with 85 mg (0.27 mmol) of 5,5’-dibromo-2,2’-bipyrimidine and 162 mg (0.56 mmol) of 9H-Carbazole-9-(4-phenyl) boronic acid pinacol ester, 12 mL of degassed THF and a solution of 112 mg of K_2CO_3 dissolved in 3 mL of H_2O were added under Argon. Then, 9.9 mg (0.014 mmol) of [1,1′-Bis(diphenylphosphino)ferrocene]dichloropalladium(II) was added, the temperature was increased to 80˚C and the mixture was stirred overnight. The reaction mixture was then cooled and filtered. The solution was extracted with chloroform, washed with water and brine, dried with Na_2SO_4, and the solvent was removed under vacuum. The crude product was purified by column chromatography (dichloromethane) to yield a yellow powder (135 mg, 78% yield). Light yellow crystals suitable for X-ray diffraction were grown from a slow diffusion in chloroform/hexane mixed solution.

^{1}H NMR (400 MHz in $CDCl_3$, δ): 9.40 (s, 4H, P1), 8.20 (ddd, J = 7.7, 1.2, 0.7 Hz, 4H, P7), 8.0 (d, J = 7.2 Hz, 4H, P2), 7.85 (d, J = 8.4 Hz, 4H, P3), 7.55 – 7.46 (m, 8H, P4+P5), 7.38 – 7.34 (tt, J = 8.3, 1.2 Hz, 4H, P6).

^{13}C NMR (100 MHz in $CDCl_3$, δ): 155.05, 139.52, 127.75, 126.97, 125.17, 122.68, 119.48, 119.41, 108.67.

ESM-Pos Ms (m/z): $C_{44}H_{29}N_6$ for [MH^+], calculated 641.2448, found 641.2441.

Synthesis of 4,4'-([2,2'-bipyrimidine]-5,5'-diyl)bis(N,N-diphenylaniline) (M3)

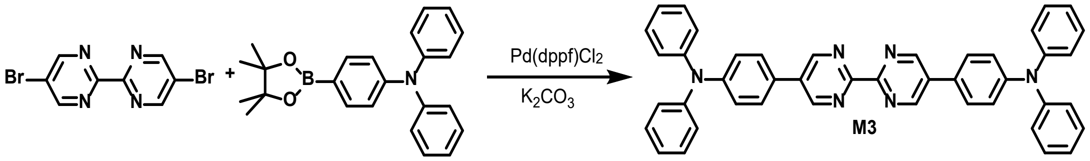

The synthesis of **M3** is the same as for **M2** except that 4-(diphenylamino)phenyl boronic acid was used instead of 9H-Carbazole-9-(4-phenyl) boronic acid pinacol ester to yield a yellow powder (146 mg, 84% yield). Yellow crystals suitable for X-ray diffraction were grown from a slow diffusion in chloroform/hexane mixed solution.

^{1}H NMR (400 MHz in CD_2Cl_2, δ): 9.16 (s, 4H, P1), 7.61 (d, J=7.6 Hz, 4H, P2) 7.33 (t, J = 12 Hz, 8H, P4), 7.21 – 7.09 (m, 16H, P3+P5+P6).

^{13}C NMR (100 MHz in CD_2Cl_2, δ): 155.67, 149.78, 147.91, 130.19, 128.40, 127.60, 125.82, 124.49, 123.69.

ESM-Pos Ms (m/z): $C_{44}H_{33}N_6$ for [MH^+], calculated 645.2761, found 645.2763.

Synthesis of 4,4'-([2,2'-bipyrimidine]-5,5'-diyl)bis(N,N-bis(4-methoxyphenyl)aniline) (M4)

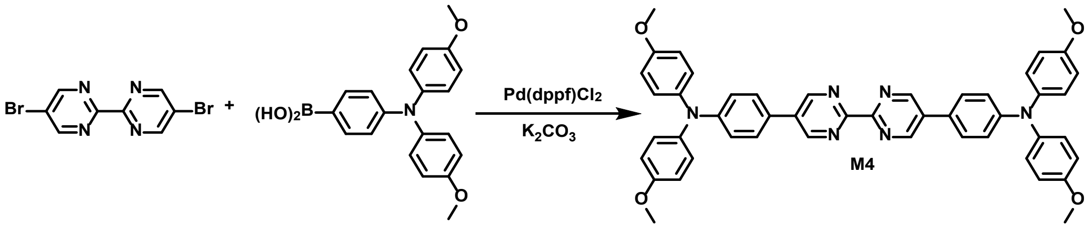

The synthesis of **M4** is the same as for **M2** except that 4-(bis(4-methoxyphenyl)amino)phenyl boronic acid was used instead of 9H-Carbazole-9-(4-phenyl) boronic acid pinacol ester and degassed DMF/water (4 : 1) mixture as the solvent to yield an orange powder (531 mg, yield: 89%). Yellow crystals suitable for X-ray diffraction were grown from a slow diffusion in dichloromethane/hexane mixed solution.

^{1}H NMR (400 MHz in $CDCl_3$, δ): 9.17 (s, 4H, P1), 7.49 (dt, J = 11.0, 3.5 Hz, 4H, P2), 7.12 (dt, J = 11.3, 2.9 Hz, 8H, P4), 7.03 (dt, J = 11.0, 3.0 Hz, 4H, P3), 6.87 (dt, J = 11.3, 2.9 Hz, 8H, P5), 3.81 (s, 12H, P6).

^{13}C NMR (100 MHz in $CDCl_3$, δ): 156.70, 155.10, 150.24, 140.19, 127.80, 127.40, 124.71, 120.23, 115.10, 55.73.

ESM-Pos Ms (m/z): $C_{48}H_{41}N_6O_4$ for [MH^+], calculated 765.3184, found 765.3183.

Synthesis of 4,4'-(4,4'-bis(trifluoromethyl)-[2,2'-bipyrimidine]-5,5'-diyl)bis(N,N-diphenylaniline) (M5)

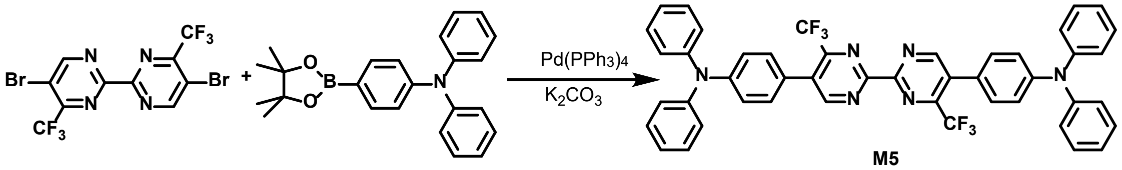

The synthesis of **M5** is the same as for **M3** except that **2b** was used instead of **1b** and catalyzed by tetrakis(triphenylphosphine)palladium(0) to yield a yellow powder (2 mg, 9.7% yield). It is not enough for recording the ^{13}C NMR spectrum. Because of lack of time, more **M5** could not be prepared.

^{1}H NMR (400 MHz in CD_2Cl_2, δ): 9.16 (s, 2H, P1), 7.35 – 7.28 (m, 12H, P2+P4), 7.19 – 7.12 (m, 16H, P4+P5+P6).

ESM-Pos Ms (m/z): $C_{46}H_{31}F_6N_6$ for [MH^+], calculated 781.2509, found 781.2496.

Synthesis of 5,5'-bis(5-hexylthiophen-2-yl)-2,2'-bipyrimidine (M6)

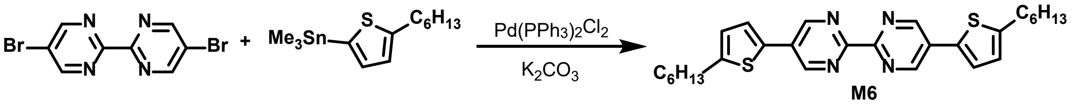

(5-hexylthiophen-2-yl)trimethylstannane used in the synthesis was synthesized according to the reported procedures[142].To a 100 mL flask charged with 300 mg (0.95 mmol) of **1b** and 377 mg (1.14 mmol) of (5-hexylthiophen-2-yl)trimethylstannane, 20 mL of dry THF was added under Argon. Then, 67 mg (0.095 mmol) of bis(triphenylphosphine)palladium(II) dichloride was added, the temperature was increased to 80°C and the mixture was stirred for 2 days. The reaction mixture was then cooled and filtered. The solution was extracted with chloroform, washed with water and brine, dried with Na_2SO_4, and the solvent was removed under vacuum. The crude product was purified by column chromatography using dichloromethane as eluent to yield a pale-yellow solid (289 mg, 62%).

^{1}H NMR (400 MHz in $CDCl_3$, δ): 9.12 (s, 4H), 7.37 (d, J = 3.6 Hz, 2H), 6.86 (dt, J = 3.6, 1.0 Hz, 2H), 2.87 (t, J = 7.5 Hz, 4H), 1.73 (sept, J = 7.4 Hz, 4H), 1.46 – 1.27 (m, 13H), 0.96 – 0.82 (m, 6H).

^{13}C NMR (100 MHz in $CDCl_3$, δ): 159.70, 153.70, 149.59, 133.21, 128.69, 125.93, 125.84, 77.34, 77.03, 76.71, 31.58, 31.53, 30.37, 28.75, 22.56, 14.08.

ESM-Pos Ms (m/z): $C_{28}H_{35}N_4S_2$ for [MH^+], calculated 491.2298, found 491.2297.

Synthesis of 4-(4,4'-bis(trifluoromethyl)-[2,2'-bipyrimidin]-5-yl)-N,N-bis(4-methoxyphenyl)aniline (M7)

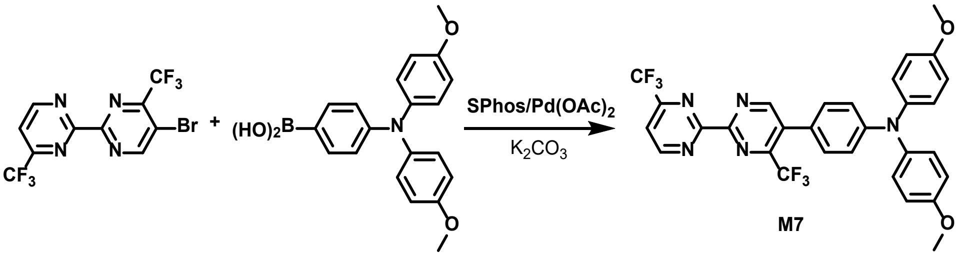

M7

The synthesis of **M7** is the same as for **M4** except that **2c** was used instead of **1b** and SPhos/Pd(OAc)$_2$ as catalyst to yield a red solid (45 mg, yield: 47%). Orange crystals suitable for X-ray diffraction were grown from a slow diffusion in chloroform/hexane mixed solution.

^{1}H NMR (400 MHz in $CDCl_3$, δ): 9.31 (s, 1H, P1), 9.15 (s, 1H, P3), 7.80 (d, J = 4.88 Hz, 1H, P2), 7.20 (d, J = 8.08 Hz, 2H, P4), 7.15 (d, J = 8.20 Hz, 4H, P6), 6.98 (d, J = 8.36 Hz, 2H, P5), 6.89 (dt, J = 6.64, 2.24 Hz, 4H, P7), 3.82 (s, 6H, P8).

^{13}C NMR (100 MHz in $CDCl_3$, δ): 162.15, 161.28, 160.59, 159.28, 156.65, 152.56, 145.62, 140.80, 139.81, 135.04, 129.71, 128.17, 127.54, 126.77, 118.94, 118.47, 117.30, 115.37, 114.95, 106.89, 103.84, 55.55.

ESM-Pos Ms (m/z): $C_{30}H_{22}F_6N_5O_2$ for [MH^+], calculated 598.1672, found 598.1651.

2.2.3 General method for photophysical measurements

All the samples in solutions were prepared in spectral grade solvents and with recrystallized compounds. They were tested in 1cm-quartz cuvettes. To prepare diluted solution (10^{-5}-10^{-6} M), mother solutions with concentration of 1×10^{-3} M of each compound were made before diluting to the desired concentration. For the measurement of each compound, we firstly studied a 1×10^{-6} M solution and its absorption spectrum was recorded. Since here the working concentration of solution is not determined, to minimize reabsorption effect and to avoid aggregates of molecules, we want the absorbance below 0.1, and normally it is for our compounds. Then the molecule was excited at the wavelength corresponding to the absorption maximum to record the emission spectrum. In reverse, with knowing the emission maximum, we recorded the excitation spectrum by analyzing at the maximum of emission to make sure that the excitation wavelength used for emission measurements was optimum. For samples in solid-state, they were deposited on glass substrate and measured with a special holder. The PLQY, absorptance and external quantum yield of films were measured with integration sphere in Université Clermont Auvergne as a cooperation.

2.2.3.1 Determination of working concentration

For each compound, the emission measurements of solutions with different concentrations were carried out in order to determine the proper working concentration. The latter should belong to the linear domain of the plot of the intensity of emission versus the concentration. This is in particular to avoid the presence of aggregate. Generally, for the compounds of the present study, the working concentration should be below 1×10^{-5} M.

2.2.3.2 Photoluminescence quantum yield measurement related to standards

Measurements of PLQY were carried out both with an integration sphere and references to make sure that reliable values were taken. Two references were chosen, which are quinine sulfite and norharmane[143]. The PLQY of quinine sulfite in 0.5 M sulfuric acid aqueous solution is 0.546 when excited at 366 nm[144]. The PLQY of norharmane in 0.5 M sulfuric acid aqueous solution is 0.60when excited at 360 nm[145]. To perform the PLQY measurements with standards, we followed the procedures below:

(1) Record the UV-vis absorbance spectrum of the solvent background for the chosen sample. Make sure the absorbance value is below 0.1. Note down the absorbance at the excitation wavelength to be used.

(2) Record the fluorescence spectrum of the same solution. Calculate and note down the integrated fluorescence intensity (that is, the area of the fluorescence spectrum).

(3) Repeat steps 1 and 2 for five solutions with different concentrations of the chosen sample.

(4) Plot a graph of integrated fluorescence intensity v.s. absorbance. The result should be a straight line with gradient value, and intercept = 0 (see **Figure 2-6**).

(5) Repeat steps 1 to 4 for the standards and all the samples. And for each standard and sample, three independent measurements, which means three values of gradient were obtained.

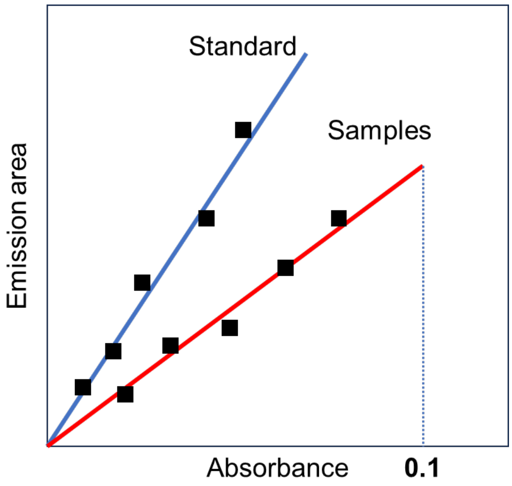

Figure 2-6 Indication of PLQY measurements.

The value of the quantum yield can be calculated by the following equation:

$$\Phi_x = \Phi_{ST}\left(\frac{Grad_x}{Grad_{ST}}\right)\left(\frac{\eta_X^2}{\eta_{ST}^2}\right)$$

Where the ST and X represent standard and test sample respectively, Φ is the photoluminescence quantum yield, $Grad$ is the value of the slope from the fitting line and η is the refractive index of the solvent.

First, the two standard compounds are cross-calibrated using this equation. This is achieved by calculating the quantum yield of each standard sample relative to the other to check if the measurements are well done. For each test sample, two Φ values will be obtained, one relative to standard quinine sulfite, the other to standard norharmane. The simple average of these two values represents the quantum yield of the test sample. The error in the reported value must be considered based upon the observed errors in the gradients; a value of ±10% is normal. For each sample and standard, three independent measurements were carried out which means three slope values for each sample and three for each standard. In this case, we can calculate 9 different values of PLQY related to each standard and 18 values in total. The average value has been taken as the PLQY for the tested compound.

2.2.3.3 Low temperature PL, delayed emission and excited-state lifetime

Firstly, assure the absorbance of testing sample is below 0.1. The fluorescence-decaying measurements were carried out with a method of Time-Correlated Single Photon Counting (TCSPC), using a 364.1 nm pulse with a period of 50 ns, generated by EPL-365 picosecond pulsed diodes. The instrument respond (IR) was measured with a Ludox solution. The decaying curve of sample was process by a reconvolution fitting to acquire the lifetimes.

The low temperature measurements were performed in a special quartz tube immersed into liquid nitrogen. The sample should be completely frozen before the measurement. For delayed emission and phosphorescence lifetime, they were measured with a microsecond flashlamp or pulse, using the multichannel scaling (MCS) method.

To obtain delayed emission spectra, the gated time was set to record the emission spectrum of a certain part during each period of pulse. The decay curves which are shown in the text are presented in ***Appendix IV***.

2.2.4 Fabrication of thin films

The fabrication of thin films involves three solution-processable methods: drop-casting, spin-coating and slot-die process using a coating bench. The slot-die films were made in Université Clermont Auvergne. Some of the samples went through the thermal annealing process. Films were deposited on a hot plate with 120 °C surface temperature for 3 hours. After that, they were allowed to slowly cool down to ambient temperature for 12 hours.

2.2.4.1 General method for drop-casted films

This method is used for the quick checks of neat films. Solutions of pure luminophores in THF or DCM with certain concentrations were prepared and filtered through 0.45 μm syringe filters previously. The glass substrates were cleaned in ethanol with ultrasonic bath, then rinsed with acetone. Then 100 μL of prepared solution was carefully dropped on the glass substrates and covered the whole surface. They were left in the fume hood overnight for completely evaporating solvent.

2.2.4.2 General method for spin-coated films

The method is used for making neat and dopped films in PMMA and CBP, for the good homogeneity and transparency. Solutions of pure luminophores or fluorophores/matrix in THF or DCM with 10 g/L concentrations were prepared and filtered through 0.45 μm syringe filters previously. The glass substrates were cleaned in ethanol with ultrasonic bath, then rinsed with acetone. Then 100 μL of prepared solution was carefully dropped on the glass substrates and covered the whole surface. They were spin coated at 2000 rpm for 60 seconds.

2.2.4.3 General method for slot-die films

A 0.5 g/mL THF solution of PMMA was prepared and stirred overnight to obtain a viscous gel. For 10 wt% films, 30 mg of luminophores was dissolved in 0.5 mL THF and mixed with 0.5 g of PMMA gel, and stirred for 30 minutes for evenly mixing them. The acquired sol-gel was dropped on a plastic substrate deposited on a hot coating bench (50 °C) and pressed by a bar-coater knife with a fixed thickness of 200 μm. Then the films were peeled out of the substrates after drying. Those films fabricated through this method have consistent thickness, good homogeneity and transparency. They were used for PLQY and photostability tests.

2.2.5 Fabrication of the hybrid LEDs

Firstly, a 10wt% PMMA solution in toluene and a 10 g/L THF solution of **M4** were made. Then a solution containing 10wt% M4 and 90wt% PMMA was made by mixing the previous two solution. The blue LEDs were purchased on Amazon and fabricated by Lumetheus. The dimensions of the LEDs are 3.5 x 0.5 x 0.5 cm with an emission wavelength of 465 nm and a power of 90 mW.

A dip-coater (Kibron Langmuir-Boldgett Trough G2) was used in the process. The LED was held by a holder which can move uniformly to completely immerse into the polymeric solution and stay for 5 minutes. Then it was withdrawn from the solution with a adjustable speed (100-200 mm/min). The LED was left vertically and dried in the fume hood for 1 hour.

The electroluminescence spectra of the hybrid LEDs were measured by Photo Research PR-655 Scanning Spectroradiometer. The LED is powered by Keithley 2430 power source.

2.3 Discussion on synthesis

As we showed in this chapter, a series of D-A molecules comprising BPM as acceptor has been synthesized and characterized by various means such as NMR, Mass spectrometry and single-crystal XRD.

New compounds **2a**, **2b** and **2c** were isolated and fully characterized. In their ^{13}C NMR spectra (***Appendix II***, **Figure S2-1** and **S2-3**), we have observed C-F coupling due to CF_3 group, which has the same effect as C-H coupling. This C-F coupling leads to the occurrence of multiplets in their ^{13}C NMR spectra, since only C-H decoupling technique was adopted without C-F decoupling. This is solid evidence of the introduction of the CF_3 groups. These spectra have been carefully analyzed and assigned.

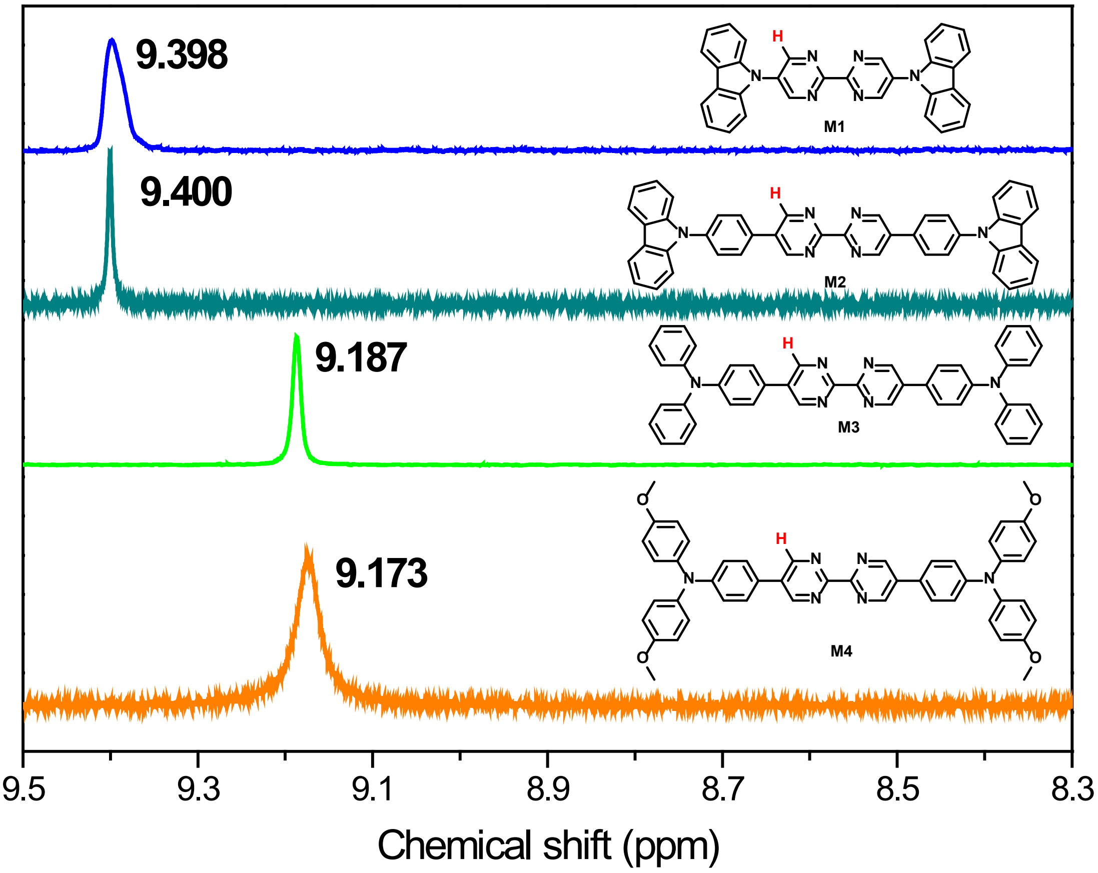

Figure 2-7 Chemical shifts of the pyrimidine protons in ^1H NMR spectra of **M1-M4** in chloroform-*d1*.

As the target of the synthesis, we were able to construct a new family of D-A-D molecules with different donor units (**M1-M4**) using 5,5'-dibromo-2,2'-bipyrimidine (**1b**) as the main starting material. Comparing their ^1H spectra in chloroform-d_1 (**Figure**

2-7), the high-field shift of their protons of the pyrimidine rings depending on the donor units was observed. They are 9.398, 9.400, 9.187 and 9.173 ppm respectively for **M1-M4**. The stronger electron-donating ability it has, the more prominent the shielding effect is, which leads to a high-field-shift of the resonance absorption peaks and the decrease of the chemical shifts. This indicates the order of the electron-donating power of the donor units in each compound is **M4** > **M3** > **M1** ≈ **M2**. In fact, the insertion of phenyls in **M2** slightly reduces the influence of carbazole comparing to **M1,** possibly due to the longer distance the phenyl rings induced.

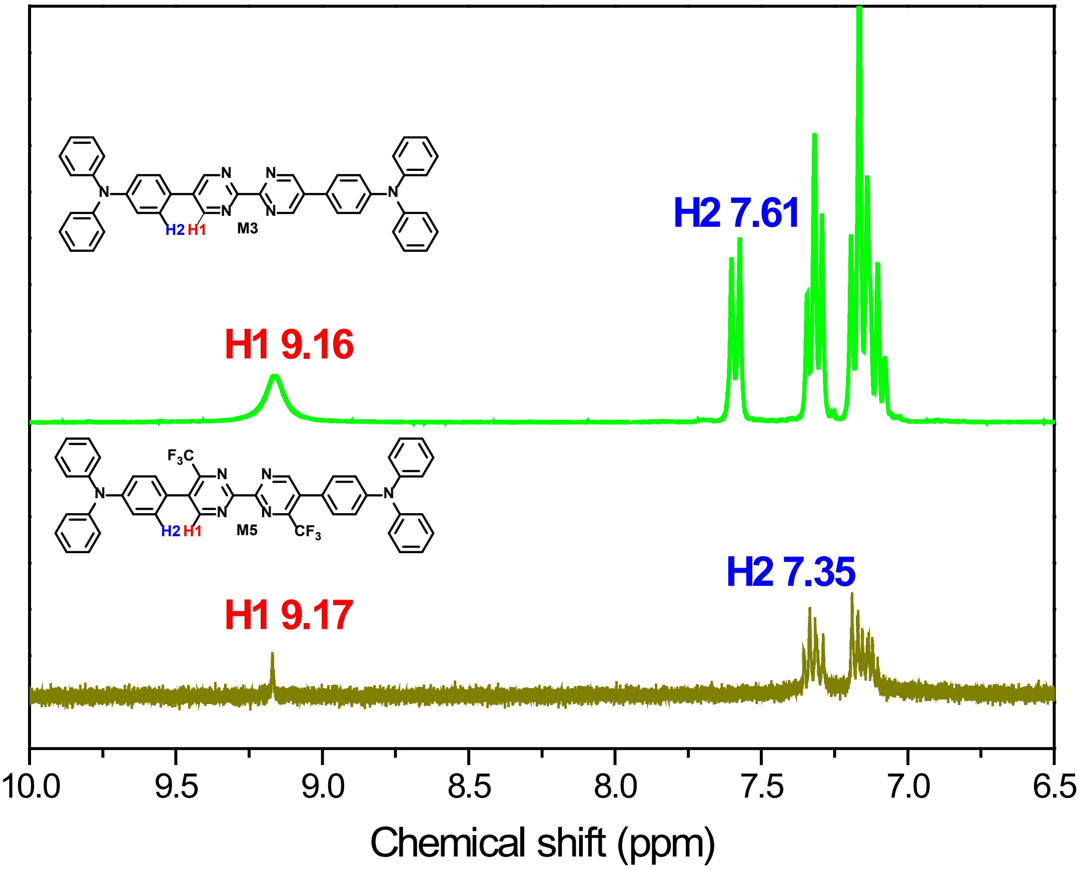

Figure 2-8 ^{1}H NMR spectra of **M3** and **M5** in dichloromethane-*d2*.

By attaching extra electron-withdrawing trifluoromethyl groups, we are able to compare the effect of acceptors with different electron affinities (**M3** and **M5**). In their NMR spectra (**Figure 2-8**). The protons H1 on the pyrimidine unit of **M5** have a down-field shift due to the electron-withdrawing inductive effect of the CF_3 groups. Meanwhile the steric effect of CF_3 enlarge the torsion angles between phenyl rings and

BPM core. Protons H2 in **M5** may locate in the shielded region (above and below the conjugated plane) of the pyrimidine rings, which results in an enhanced shielding effect and thus a significantly lower chemical shift than that of **M3**. Same phenomenon is found in the ^{1}H NMR spectrum of the CF_3-substituted **M7** with the chemical shift of corresponding proton of 7.20 ppm (***Appendix II,*** **Figure S2-11**), owing to the twisted conformation between the phenyl and pyrimidine with a big torsion angle of 69. 1° (see **Table 2-1**).

Revealed by the X-ray diffraction analysis of their single crystals, for **M1-M4**, the two pyrimidine rings appear almost coplanar with small inter-rings torsion angles (**Table 2-1**), as we expected from the design strategy. And for **M2-M4**, the torsion angles between phenyl and BPM cores are moderate (31-34°), indicating their rather planar geometries. **M1** and **M7** show twisted overall conformation. Their single crystal X-ray structures are shown in **Figure 2-9**. The detailed single-crystal X-ray diffraction data are presented in ***Appendix III***.

Table 2-1 Torsion angles between two pyrimidine rings in single crystals of **M1-M4**.

Molecule	**M1**	**M2**	**M3**	**M4**	**M7**
θ^a	9.7°	0.2°	0.2°	5.7°	20.0°
α^b	59.2°	34.4°	34.2°	31.6°	69.1°

[a] Torsion angles between two pyrimidine rings. [b] Torsion angles between pyrimidine and the other side neighboring groups.

The difficulties about the synthesis concentrate on the bromination of **1a** and **2a** due to a low reactivity. In **1a**, due to electron-withdrawing nature of the two nitrogen atoms in the pyrimidine rings, the 2,4,6 positions are deactivated towards electrophilic substitutions, while the position 5 is not as electron-deficient as other positions[122]. It is possible to perform electrophilic substitutions like bromination without activating groups but under harsh conditions. However, for **2a**, the strong electron-withdrawing CF_3 at the 4 and 4' positions destroyed the last hope. Even under extreme conditions (high temperature, high pressure, long reaction time), it was still very hard to undergo the bromination. Therefore, the mono-bromo product **2c** was obtained as the main product in a very low yield and the yield of the dibromo product **2b** is even lower. For this reason, the synthetic method **3** (in **Scheme 2-1**) was performed to obtain di-halogenated BPM derivatives in better yields according to literature[140].

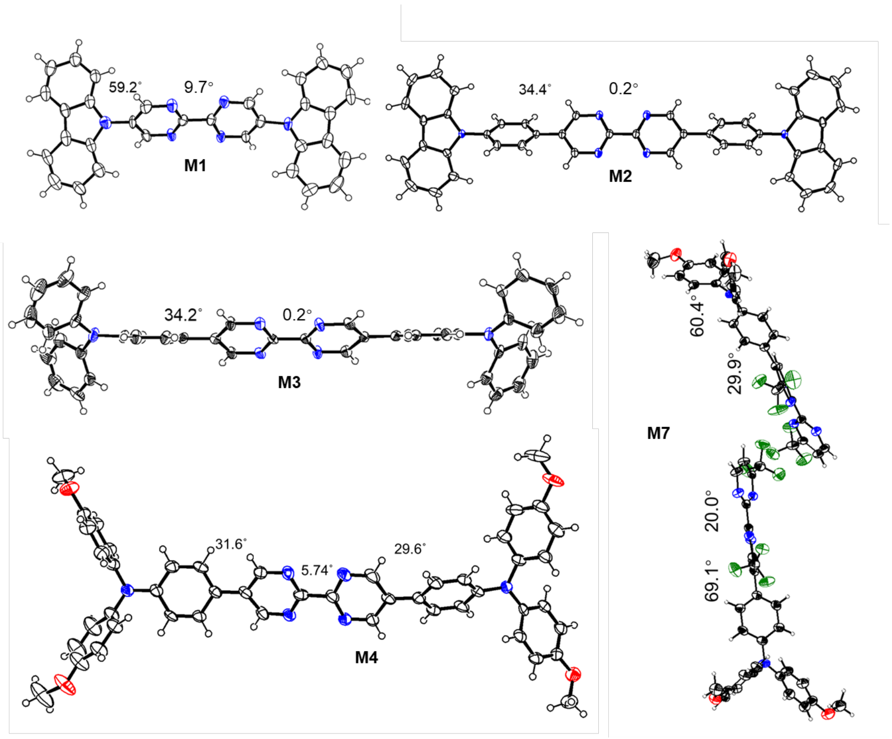

Figure 2-9 Single cystal X-ray structures of **M1-4** and **M7**, black for carbon, blue for nitrogen, red for oxgen and olive for fluorine.

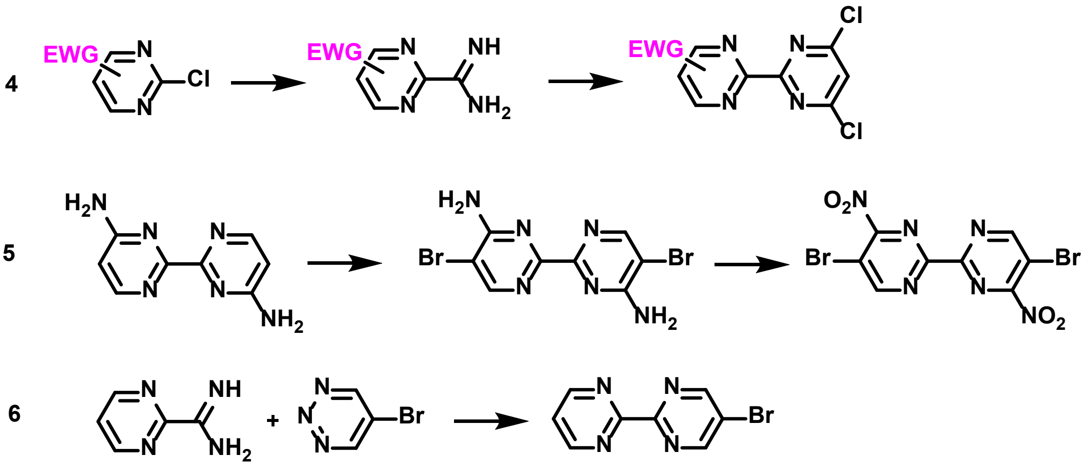

Scheme 2-2 Perspectives on the synthesis of halogenated BPM.

Starting from a substituted chloropyrimidine, it may give an efficient way to obtain di-halogenated BPM derivatives with various electron-withdrawing substitutions (see **Scheme 2-2, 4**). Besides this, the introduction of activation groups like -NH_2 and -OH could boost the reactivity for electrophilic substitution (see **Scheme 2-2, 5**). Then, $-NH_2$ could be oxidized into $-NO_2$ to obtain the electron-withdrawing groups. We also found another interesting method applied in the pharmacy domain to synthesize brominated BPM in a very high yield[146] (see **Scheme 2-2, 6**), which worths a try in the future. The other point that needs to be illustrated is that the reactivity of each position of the pyrimidine halides follows the general order position 4(6) > 2 ≥ 5[147]. For this reason, the highly efficient catalyst system for the Suzuki coupling is necessary. Especially for trifluoromethyl-substituted BPM, the hindrance of trifluoromethyl groups blocks the bromine substitution and limits the reactivity of bromine. Since the synthesis of **M5** with Pd $(PPh_3)_4$ showed a very low yield, the catalyst system SPhos/palladium diacetate was selected for its high reactivity in order to improve the yield of **M7**.

There are also some syntheses which were not successfully performed. For examples, we have tried to synthesize the larger molecules **M8**, **M9** and **M10** with longer conjugation (**Figure 2-10).** However, their solubility was too low to carry out column chromatography for the purifications due to the large and rigid benzothiophene and pyrene groups. No pure products were obtained; thus, we could not investigate their photophysical properties. Therefore, we synthesized **M6** containing long alkyl chains to increase the solubility.

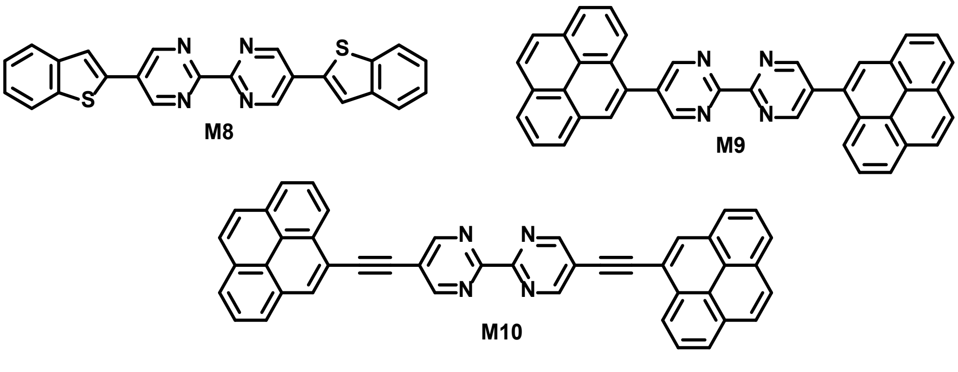

Figure 2-10 Products **M8-M10** which were not successfully purified.

2.4 Summary

In this chapter, firstly we illustrated the general design for the desired D-A molecules and attached importance on the choices of D and A moieties respectively, as well as the way to connect them (with or without π-linkers). By describing the merits and shortages of different groups, the aromatic amines, particularly triphenylamine and carbazole derivatives, are selected as D units, as they are well-known for electron-rich and they show strong absorption in near-UV. Triphenylamine can provide the potential to introduce AIE property in D-A compound. BPM derivatives are finally selected as A units, for their high electron affinity, strong absorption, good thermal and photostability and novelty in the construction of D-A system.

Then the experimental methods and details, including synthesis, film fabrications and photophysical measurements, are described. The discussion of synthesis is highlighted. For the synthesis of BPM building blocks, two different pathways are proposed. Compound **1a** is obtained as a main starting material. **2a** and **2b** are also used for the construct D-A system. Seven D-A and D-A-D compounds are successfully synthesized and characterized. **M1-M4** and **M6** share the same acceptor core which is BPM. But they contain various donor moieties, which are carbazole, phenyl carbazole, triphenylamine, dimethoxy triphenylamine and hexyl thiophene. **M3** and **M5** share the same donor part, while the acceptor core of **M5** is substituted with CF_3. By analyzing their NMR spectra, the inductive and steric effect of different substitutions are revealed. The stronger electron-donating abilities of triphenylamine derivatives than carbazole lead to high-filed shifts of the BPM protons, while the electron-withdrawing strength of CF_3 causes a low-filed shift. The steric effect of CF_3 increases the shielding effect on the protons of the phenyl bridge in **M5** and **M7**, and makes their chemical shift high-field shift. The single crystal structures of **M1-M4** and **M7** are acquired from X-ray diffraction. For **M1-M4**, the two pyrimidine rings are nearly coplanar with small torsion angles (0-10°). The multiple characterizations have already revealed some of the effected from the different structures, and can be further proved by the photophysical studies in the next chapters.

Chapter III Photophysical properties in solution

After successfully isolating the target donor-acceptor (D-A) compounds, in this chapter, we will focus on the studies of their photophysical properties in diluted solution, including absorption spectra, photoluminescence (PL) spectra and decay curves at both room and low temperature, in order to determine the photophysical characters of the isolated molecules. From the comparison between different compounds, we could reveal the effects of different substitutions and conformations of the molecules, to have a better understanding on the property-structure relationship. Then solvent effect was studied to investigate the internal charge-transfer process (ICT). In the end, by the estimations of different energy levels, their electronic structures are revealed.

3.1 Photophysical properties at room temperature in solution

Firstly, we will focus on the absorption and PL spectra of these compounds at room temperature to have a picture of their photophysical parameters: determination of working concentration (linear domain), absorption and emission wavelength (λ_{abs} and λ_{em}), molar absorption coefficient, photoluminescence quantum yield (PLQY), fluorescence lifetime (FLT), and CIE coordinates. The measurements of linear domain and PLQYs relative to standards are presented in ***Appendix IV***. For the convenience of comparison, **M1-M6** were diluted in chloroform, since it is a common good solvent for all compounds. Figures for **M7** was shown in toluene solution, since it is nearly non-emissive in chloroform. The parameters applied for recording those spectra are listed in figures and corresponding legends.

3.1.1 Absorption and PL properties of M1 in solution

M1 showed a broad sky-blue fluorescence with the intensity maximum at 487 nm, and an absorption in near-UV with a peak value at 385 nm. As we described in **Chapter II**, two different methods were adopted for measuring PLQY, with an integration sphere, and with standards. The photophysical parameters are summarized in **Table 3-1**.

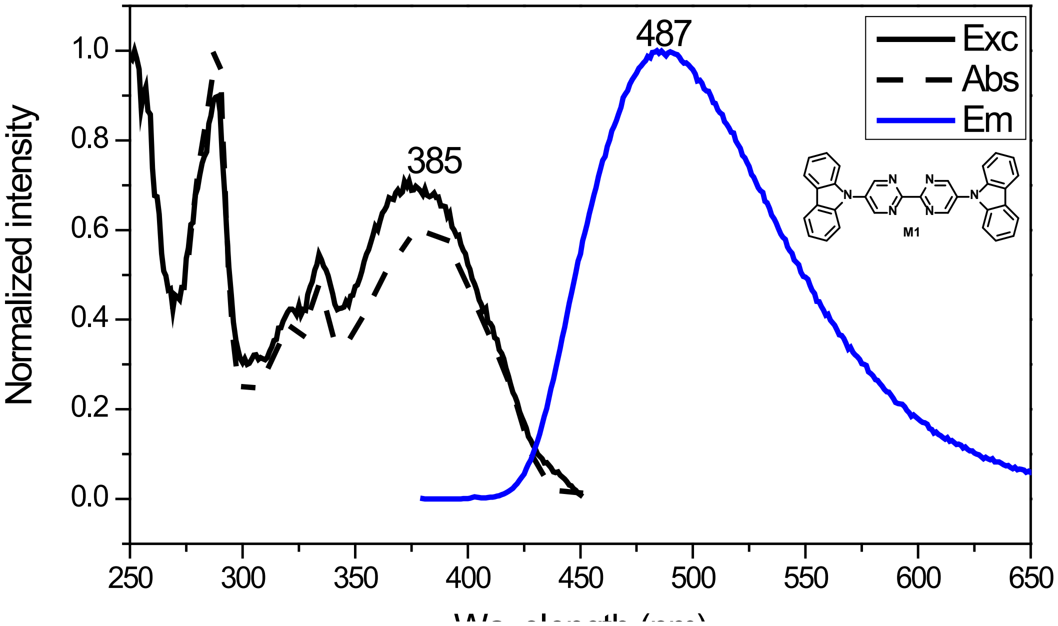

Figure 3-1 Normalized absorption, excitation and emission sepctra of **M1** solution (1×10^{-6} M in chlorofrom, room temperature, 2/2 nm slits).

Table 3-1 Photophysical properties of **M1** at room temperature[a].

λ_{abs}	ε^{b}	λ_{em}	$\Phi_{I}{}^{c}$	$\Phi_{s}{}^{d}$	τ_{fluo} (ns, %)
385	0.15	487	0.18	0.13	0.11 (77.42) 3.24 (22.58)

[a] 1×10^{-6} M solution in chloroform. [b] Molar absorption coefficient, 10^{4} L·mol^{-1}·cm^{-1}. [c] PLQY measured with an integration sphere, with an estimated relaitve error ±10%. [d] PLQY measured with standards, with an estimated error ±10%.

The process of determining the linear domain for **M1** has been shown in **Figure S4-1**. The emission spectra of solutions with different concentrations were recorded. The intensity maximum has been plotted with the concentration. Those points from 1×10^{-6} M to 1×10^{-5} M can be fitted with good linearity (>0.99), indicating in this range the emission properties are detected from isolated molecules. Hence, the linear domain is defined as the concentration below 1×10^{-5} M, where the following measurements will be done.

The slope values were obtained following the method in **Chapter II**, and were listed in the ***Appendix IV***, **Table S4-1** and **S4-2**. There are nine calculated values for each quantum yield standards. The average values and error square (R^2) are presented. The average values of PLQY are very close for two standards, and the error are small, indicating reliable results.

3.2.2 Absorption and PL properties of M2 in solution

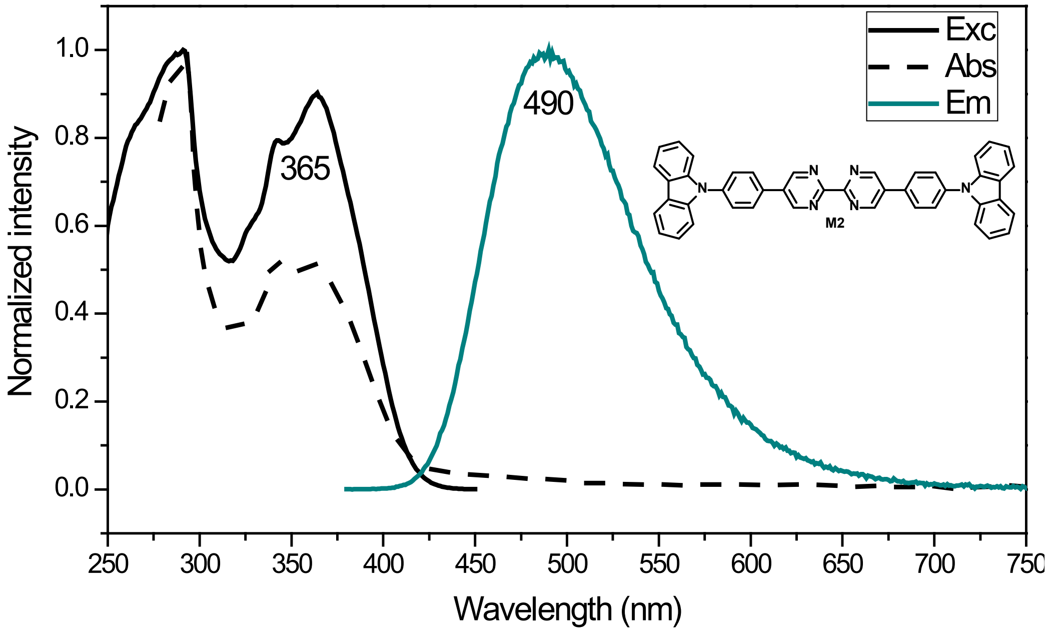

Figure 3-2 Normalized absorption, excitation and emission sepctra of **M2** solution, (1×10^{-6} M in chlorofrom, room temperature, 1/1 nm slits).

As shown in **Figure 3-2**, **M2** showed a sky-blue fluorescence with high PLQY (0.72 with two methods) in chloroform solution. It absorbs in near-UV region. The calculations of PLQY relative to references are shown in **Table S4-3** and **S4-4**. The working concentration for **M2** is below 1×10^{-5} M (see **Figure S4-2**). The photophysical parameters are listed in **Table 3-2**.

Table 3-2 Photophysical properties of **M2** at room temperature[a].

λ_{abs}	ε[b]	λ_{em}	Φ_I[c]	Φ_s[d]	τ_{fluo} (ns, %)
365	4.20	490	0.72	0.72	0.97 (7.70) 3.74 (92.30)

[a] 1×10^{-6} M solution in chloroform. [b] Molar absorption coefficient, 10^4 L·mol^{-1}·cm^{-1}. [c] PLQY measured with an integration sphere, with an estimated relaitve error ±10%. [d] PLQY measured with standards, with an estimated error ±10%.

3.2.3 Absorption and PL properties of M3 in solution

M3 showed a green fluorescence with high PLQY (72%), shown in **Figure 3-3**. The photophysical parameters are summarized in **Table 3-3**. The calculations of PLQY are shown in **Table S4-5** and **S4-6**. The determination of linear domain for **M2** is shown in **Figure S4-3**. The working concentration should be below 1×10^{-5} M.

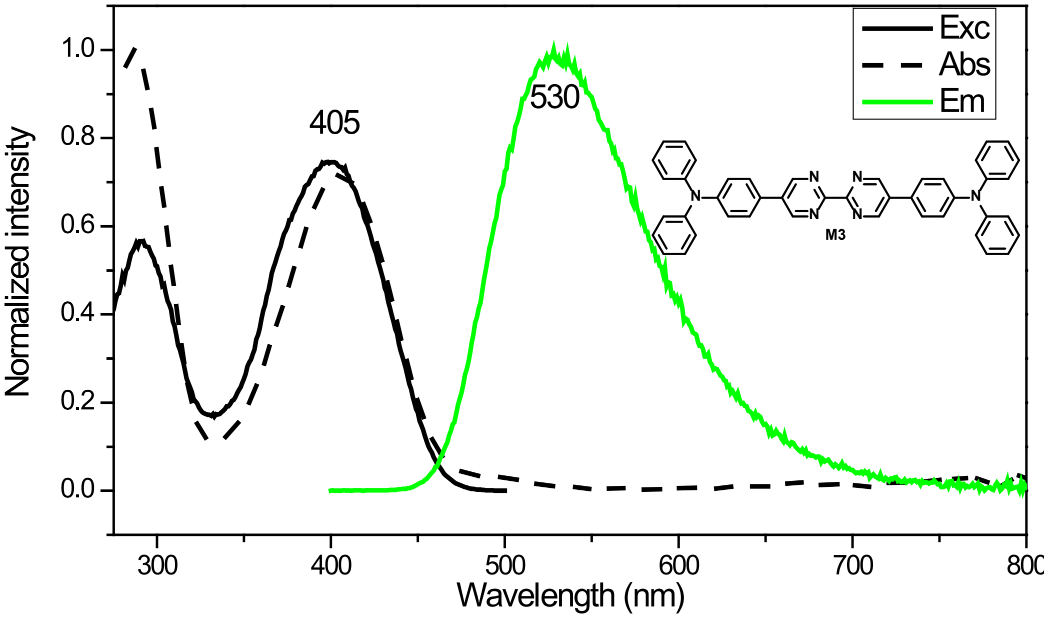

Figure 3-3 Normalized absorption, excitation and emission sepctra of **M3** solution (1×10^{-6} M in chlorofrom, room temperature, 1/1 nm slits).

Table 3-3 Photophysical properties of **M3** at room temperature [a].

λ_{abs}	ε^{b}	λ_{em}	Φ_{I}^{c}	Φ_{s}^{d}	τ_{fluo} (ns, %)
405	3.22	530	0.64	0.77	2.84 (100)

[a] 1×10^{-6} M solution in chloroform. [b] Molar absorption coefficient, 10^{4} L·mol^{-1}·cm^{-1}. [c] PLQY measured with an integration sphere, with an estimated error ±10%. [d] PLQY measured with standards, with an estimated error ±10%.

3.2.4 Absorption and PL properties of M4 in solution

M4 showed an orange-red emission with an intensity maximum at 604 nm in chloroform solution. The PLQY was only measured with an integration sphere. The determination of linear domain for **M4** is shown in **Figure S4-4**. The working concentration should be below 1×10^{-5} M.

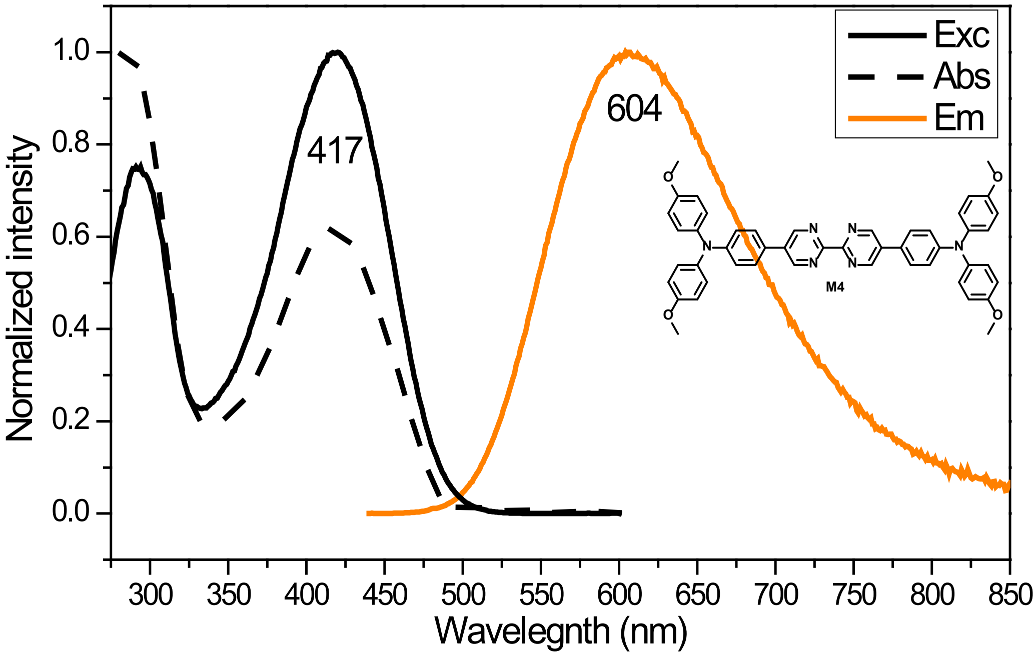

Figure 3-4 Normalized absorption, excitation and emission sepctra of **M4** solution (1×10^{-6} M in chlorofrom, room temperature, 2/2 nm slits).

Table 3-4 Photophysical properties of **M4** at room temperature^{a}.

λ_{abs}	ε^{b}	λ_{em}	Φ_{I}	τ_{fluo} (ns, %)
417	4.50	604	0.16	1.13 (97.49) 2.79 (2.51)

^{a} 1×10^{-6} M solution in chloroform. ^{b} Molar absorption coefficient, 10^{4} L·mol^{-1}·cm^{-1}. ^{c} PLQY measured with an integration sphere, with an estimated relaitve error ±10%.

3.2.5 Absorption and PL properties of M5 in solution

M5 is also an orange-emitter in a chloroform solution with moderate PLQY (40%). The absorption, excitation and emission spectra are shown in **Figure 3-5**. Its photophysical parameters are listed in **Table 3-5**. Due the few quantities of the compound, we have not performed the tests on the solutions with different concentrations. However, 1×10^{-6} M should be in the range of linear domain since its similar size and structure to the other compounds. The measurements of the PLQY with a relative method are presented in **Table S4-7** and **S4-8**.

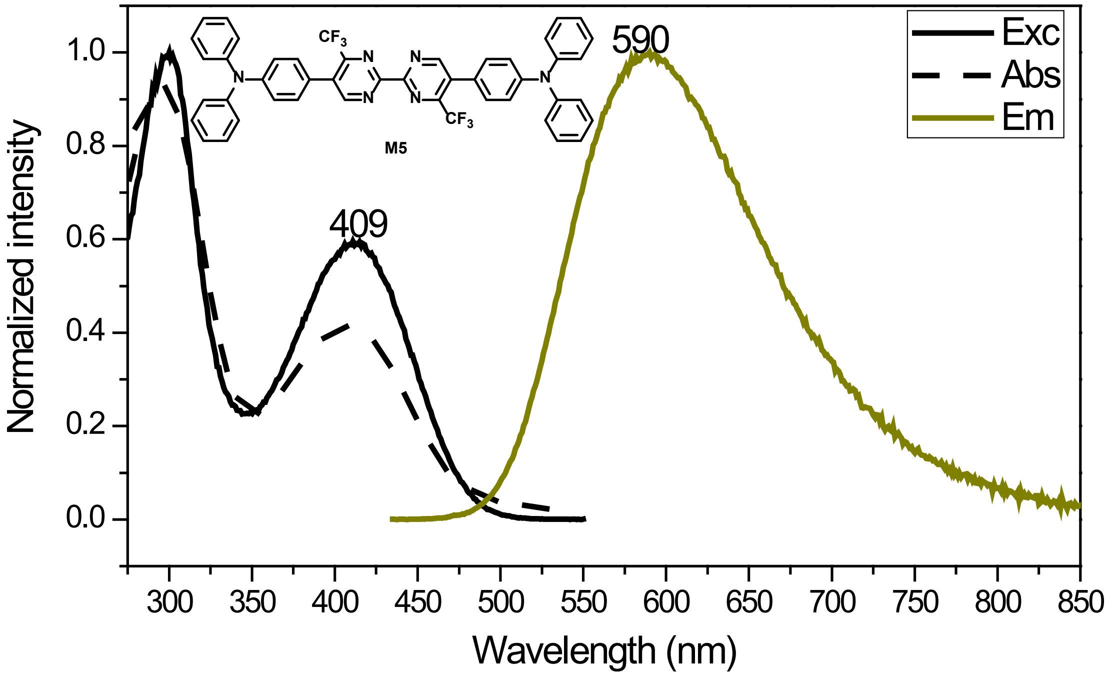

Figure 3-5 Normalized absorption, excitation and emission sepctra of **M5** solution (1×10^{-6} M in chlorofrom, room temperature, 1/1 nm slits).

Table 3-5 Photophysical properties of **M5** at room temperature^{a}.

λ_{abs}	ε^{b}	λ_{em}	Φ_{I}^{c}	Φ_{s}^{d}	τ_{fluo} (ns, %)
409	3.22	590	0.40	0.35	4.38 (97.78) 7.47 (2.22)

^{a} 1×10^{-6} M solution in chloroform. ^{b} Molar absorption coefficient, 10^{4} L·mol^{-1}·cm^{-1}. ^{c} PLQY measured with an integration sphere, with an estimated relaitve error ±10%. ^{d} PLQY measured with standards, with an estimated error ±10%.

3.2.6 Absorption and PL properties of M6 diluted solution

M6 is a deep-blue emitting compound in chloroform solution. The determination of linear domain for **M6** is shown in **Figure S4-5**. The working concentration should be below 1×10^{-5} M.

Table 3-6 Photophysical properties of **M6** at room temperature^{a}.

λ_{abs} (nm)	ε^{b}	λ_{em} (nm)	Φ_{s}^{c}	τ_{fluo} (ns, %)
370	3.22	438	0.24	0.03 (62.6) 0.44 (37.4)

^{a} 1×10^{-6} M solution in chloroform. ^{b} Molar absorption coefficient, 10^{4} L·mol^{-1}·cm^{-1}. ^{c} PLQY measured with standards, with an estimated relaitve error ±10%.

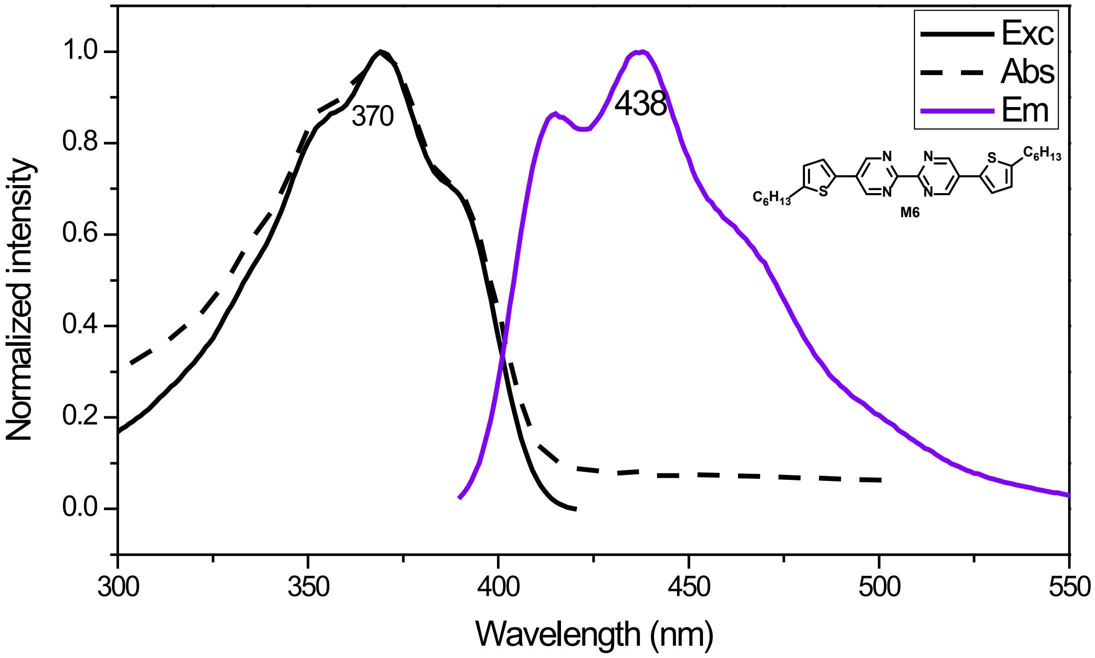

Figure 3-6 Normalized absorption, excitation and emission sepctra of **M6** solution (1×10^{-6} M in chlorofrom, room temperature, 1/1 nm slits).

The PLQY of **M6** was only measured with standards, which is found as 24%. The calculation processes are shown in **Table S4-9** and **S4-10**.

3.2.7 Absorption and PL properties of M7 diluted solution

M7 is almost non-emissive in $CHCl_3$ solution, hence the absorption, excitation and emission spectra were recorded in 10^{-6} M toluene solution. For the small quantity obtained, we have not performed the tests on the solutions with different concentrations. The UV-vis absorption and PL spectra are shown in **Figure 3-7**. The PLQY of M7 is measured with an integration sphere, which is found as 3%. The photophysical properties are summarized in **Table 3-7**.

Table 3-7 Photophysical properties of **M7** at room temperature[a].

λ_{abs} (nm)	ε[b]	λ_{em} (nm)	Φ_I[c]	τ_{fluo} (ns, %)
401	2.8	590	0.03	1.82 (100)

[a] 1×10^{-6} M solution in chloroform. [b] Molar absorption coefficient, 10^4 L·mol^{-1}·cm^{-1}. [c] PLQY measured with integration sphere, with an estimated relaitve error ±10%.

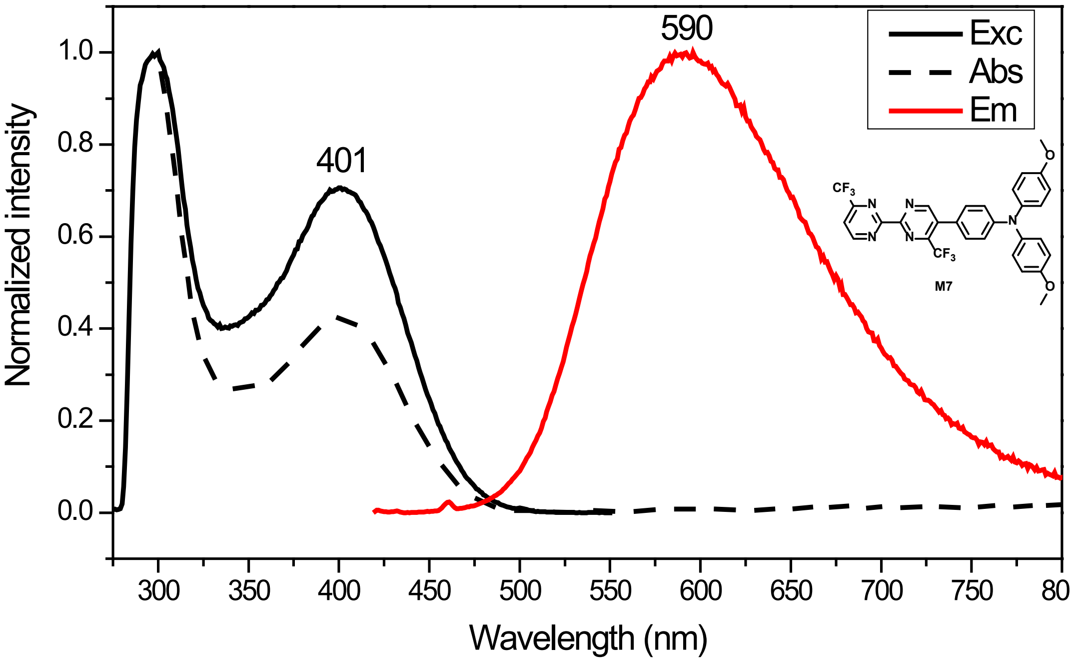

Figure 3-7 Normalized absorption, excitation and emission sepctra of **M7** solution (1×10^{-6} M in toluene, room temperature, 2/2 nm slits).

3.2.8 Comparative study

We have recorded absorption, excitation, and emission spectra in 1×10^{-6} M diluted solution of the newly-synthesized compounds (See **Figure 3-9** and **3-10)**. Among them, **M1, M2** and **M6** show blue emission, **M3** is red-emitting, **M4** and **M5** are orange-red-emitting in chloroform solutions (**Figure 3-11**). All the compounds exhibit broad emission bands in PL spectra. However, except **M6**, they all exhibit dual absorption band: the one occurring in the higher-energy region is attributed to a localized π-π* transition, while that at lower energies varies from the near-UV to the blue region. It is attributed to an ICT[75,148], because of the presence of the binding between donor and acceptor groups.

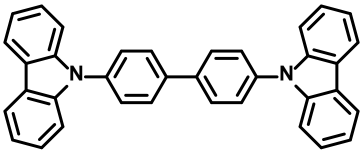

Figure 3-8 Structure of CBP.

In order to conduct the comparative study, a widely applied compounds 4,4′-

Bis(N-carbazolyl)-1,1′-biphenyl (CBP) was introduced[149,150]. The structure of CBP is shown in Figure 3-8. The photophysical parameters are summarized in **Table 3-8.**

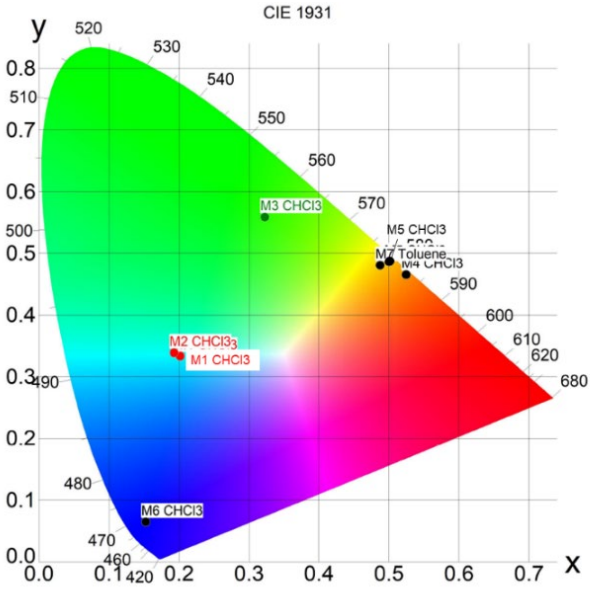

Figure 3-9 Chromaticity diagram of M1-6 (chloroform) and M7 (toluene).

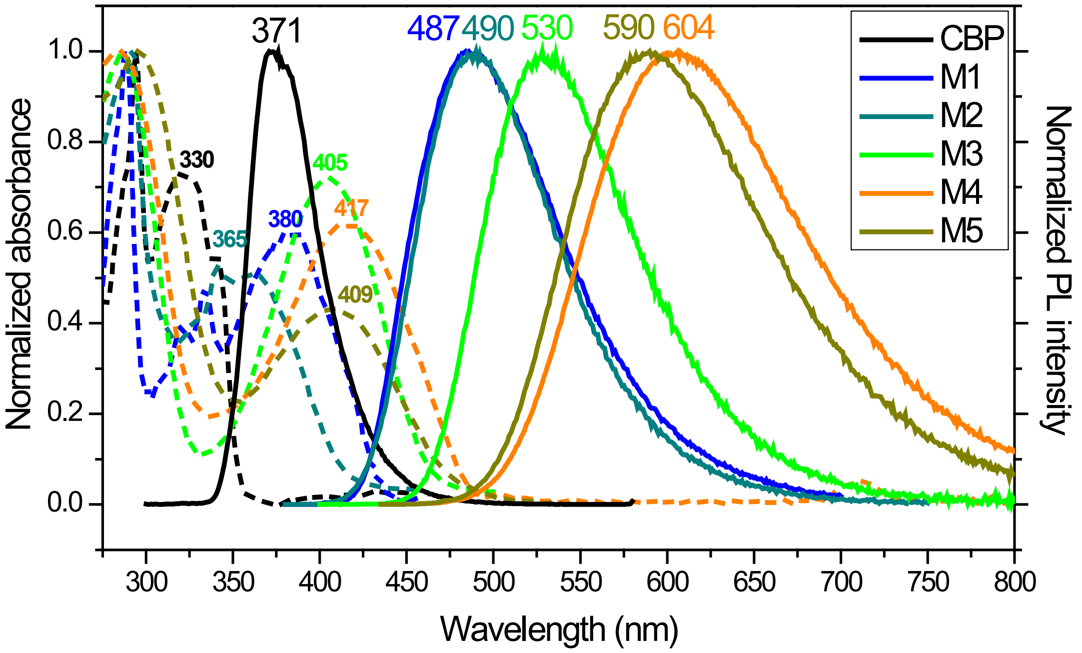

Figure 3-10 Absorption (dash lines) and emission sepctra of CBP and **M1-M5** in chloroform solutions (1×10^{-6} M).

CBP has a similar structure than **M1** except the diphenyl core, but showed a completely different absorption and PL spectra (**Figure 3-9**). In the UV-vis absorption spectra of CBP, from high to low energies, there are two main peaks, a sharp peak at

293 nm attributed to absorption of the diphenyl group[150], and a broad one between 300-350 nm with the typical character of the π-π* transition in carbazole derivatives[151,152]. For **M1**, except the sharp absorption band at 287 nm due to BPM, and a broad band between 300-350 due to the carbazole groups, there is another broad band at 380 nm with relatively high absorbance attributed to a charge-transfer (CT) state, as an outcome of the cooperation between the electron-rich carbazole and electron-deficient BPM moieties. This implies that the donor-acceptor strategy we have adopted is an effective way to red-shift the absorption. For the same reason, **M1** possesses an emission band at 490 nm which red-shifts more than 100 nm with respect to that of CBP, which is at 371 nm.

Table 3-8 Photophysical parameters of **M1-7** and CBP at room temperature[a].

Molecule	λ_{abs} (nm)	ε [b]	λ_{em} (nm)	Φ_I [c]	Φ_s [d]	τ_{fluo} (ns, %)	CIE coord.
CBP	330	3.95	371	- [f]	0.82	- [f]	- [f]
M1	385	0.15	487	0.18	0.13	0.11 (77.42) 3.24 (22.58)	(0.20, 0.33)
M2	365	4.20	490	0.72	0.72	0.97 (7.70) 3.74 (92.30)	(0.19, 0.34)
M3	405	3.22	530	0.64	0.72	2.84 (100)	(0.32, 0.56)
M4	417	4.50	604	0.16	- [f]	1.13 (97.49) 2.79 (2.51)	(0.52, 0.47)
M5	409	3.22	590	0.40	0.35	4.38 (97.78) 7.47 (2.22)	(0.50, 0.49)
M6	370	3.22	438	- [f]	0.24	0.03 (62.6) 0.44 (37.4)	(0.15, 0.06)
M7 [e]	401	2.8	590	0.03	- [f]	1.82 (100)	(0.49, 0.48)

[a] 1×10^{-6} M solution in chloroform. [b] Molar absorption coefficient, 10^4 L·mol^{-1}·cm^{-1}. [c] PLQY measured with an integration sphere, with an estimated error ±10%. [d] PLQY measured with standards, with an estimated error ±10%. [e] **M7** was measured in 1×10^{-6} M toluene solution. [f] Not measured.

Comparing **M1** and **M2**, the effect of phenyl groups working as π-spacers in **M2** is found not as expected to improve the conjugation. The phenyl group results in a blue-shifted absorption due to its high resonance energy[153]: it confines the π-electrons and increases the energy barrier for their participations in delocalized orbital. However, **M2** shows a much higher PLQY and molar absorption coefficient than **M1**, probably due to a more twisted conformation in **M1** which can cause less overlapped HOMO and LUMO.

From **M2** to **M3**, the electron-donating groups are changed from carbazole to diphenylamine to obtain a compound in which BPM is linked to a triarylamine. Triarylamines are known to be better electron donors that carbazole derivatives[154]. As the result, **M3** performs a red shift in both absorption (405 nm) and emission (503 nm) bands (**Figure 3-10**). By grafting additional electron-donating methoxy groups into diphenylamine, the improved D-A strength in **M4** further pushed the absorption (417 nm) and emission (604 nm) to the red (**Figure 3-10**).

The design of **M5** was built on another strategy to push the emission to the red. The insertion of additional electron-withdrawing substituents on the BPM core was expected to make it more electron-deficient. Thus, when going from **M3** to **M5**, a dramatic bathochromic shift of the emission from 530 to 590 nm occurred, reflecting the enhanced acceptor strength of the BPM moiety in **M5**. However, **M5** shows a relatively lower PLQY about 40%. This can be explained by the different molecular conformation. Although, we have not successfully grown single crystals of **M5** suitable for XRD, the very twisted conformation between the phenyl ring and CF_3 substituted BPM (torsion angle > 60°) has been observed in **M7** (**Figure 2-9**). On one hand, the steric hindrance of CF_3 groups breaks the planarity between phenyl and pyrimidines rings, reduces the orbital overlap between D-A moieties and probably results in a lower emission efficiency; on the other hand, electron-withdrawing ability of CF_3 also can enhance the D-A strength and push the absorption/emission to the red.

Unlike the other compounds, in the UV-Vis absorption spectrum (**Figure 3-10**) of **M6**, the typical absorption peak of BPM derivatives around 290 nm disappears. The absorption band is structured, and occurs between 300-400 nm, similarly to conjugated thiophene-pyridine co-oligomers[155], implying an enhanced conjugation due to possible coplanar conformation. As reported, thiophene substituted *via* the 2-position usually creates planarity with neighboring units[156,157]. The improved conjugation including thiophenes and pyrimidines results in a new excited state of the whole molecule, leading to an effective bathochromic shift in absorption, comparing to the π-π* absorption bands of other molecules. This is a useful aspect for the future design of D-A compounds to use thiophene as a π-bridge instead of phenyl in order to improve the conjugation. **M6** exhibits a deep blue emission at 438 nm and the smallest Stokes' shift among these compounds.

The last comparison will be made between **M4** and **M7** in toluene solutions. Generally, D-π-A-π-D molecules should show a more effective ICT than D-π-A molecules if they possess the same donors and acceptors[158]. However, **M7** performs a significant bathochromic shift of the emission to 590 nm while the maximum of emission is only at 516 nm for **M4** (**Figure 3-15**), implying the productive improvement of the electron-deficiency owing to the CF_3-substituted BPM acceptor. **M7** showed a low PLQY, possibly due to the similar reason for **M5**. The bulky CF_3 substitutions break the coplanarity between phenyl and pyrimidine, but its powerful inductive effect enhances the D-A strength.

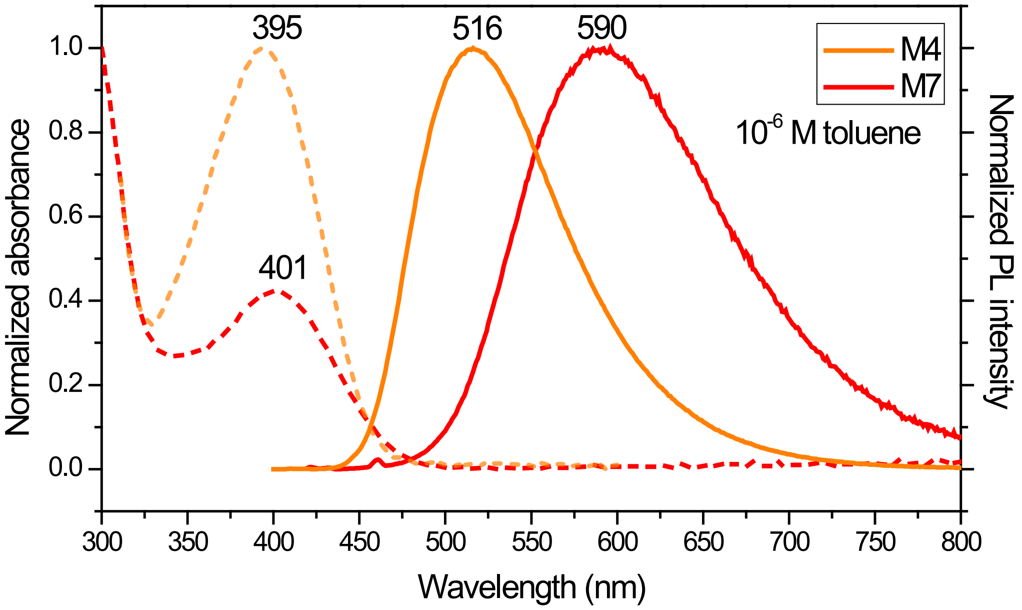

Figure 3-11 Absorption (dash lines) and PL spectra of **M4** and **M7**.

In summary, as expected by the molecular design, **M1**-**M7** have shown a tunable emission color according to the types and combinations of different donor and acceptor moieties. Especially, in order to acquire red emitters, grafting additional electron-donating and electron-withdrawing groups on the donors and BPM acceptor, respectively, further enhanced the D-A strength and shift the emission color to the red.

3.3 Solvent effects

In D-A molecules, the process of ICT is significantly influenced by the environment, and in particular the solvent system in solution. Herein, we have studied the absorption and PL properties of **M1**-**M7** in different solvents. The compounds perform solvent-dependent absorption and emission. In more polar solvents, they exhibit red-shifts in emission with a drop of the PLQY, which is called positive solvatochromism[81,159]. When a molecule is excited by a source of light, the excited state of the molecule can interact with the surrounding solvent molecules to a varying extent depending on the polarity of the solvent. This process is called solvent relaxation[160] (see **Figure 3-12**), which leads to the stabilization in a non-radiative pathway of the excited-state energy of the fluorophores. Due to the ICT effect, these emissive compounds usually have more polar excited states. Therefore, in a more polar environment, the excited states are more stable, leading to a bathochromic shift in emission[160].

For example, in **Figure 3-13**, emission spectra of **M2** in chloroform, THF and DMF are shown. Their dielectric constants (ε) are 4.8, 7.6 and 36.7 respectively, indicating the polarity of these solvents. The emission maxima are located at 490, 500 and 549 nm in these three solvents, respectively, showing a bathochromic shift regarding the increasing of the polarity. In **M1, M2** and **M6** solutions, the solvent effects were observed, but not as significant as in **M3**, **M4, M5** and **M7,** due to their weaker push-pull strength. Also, the relatively lower solubility of **M1** and **M2** limits the choice of the solvents. Besides of those, each of **M3**, **M4** and **M7** exhibits their unique behaviors upon changing the solvent. Thus, in this section, we will focus more on the solvent effects on **M3**, **M4** and **M7**.

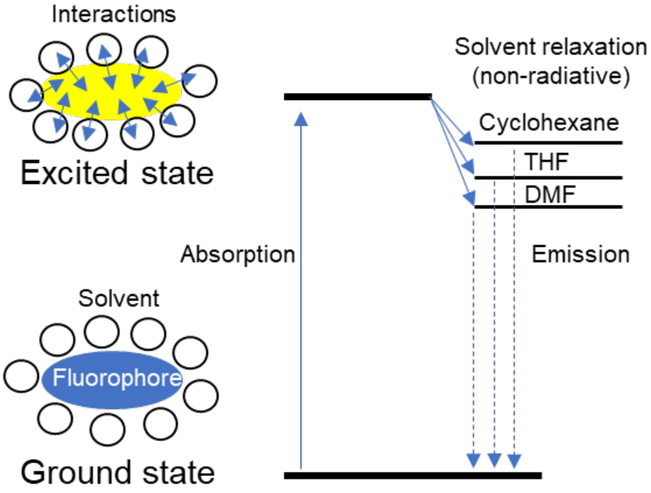

Figure 3-12 Indication of the solvent relaxation process.

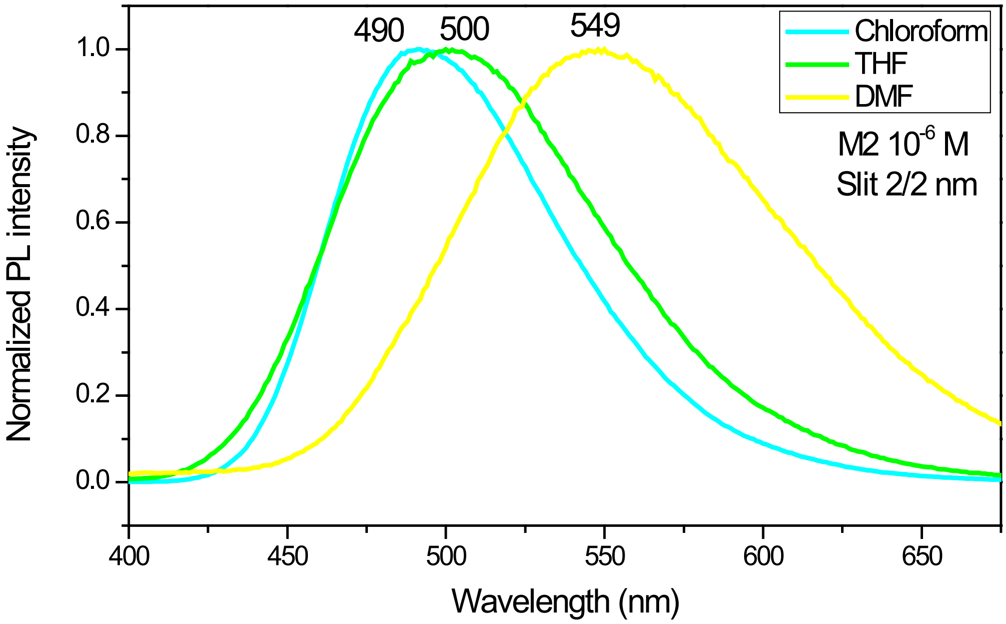

Figure 3-13 Emission sepctra of **M2** in chloroform, THF and DMF solutions.

3.3.1 Solvent effect on M4

As it is shown in **Figures 3-14**, the emission maximum shifts from 458 nm to almost 700 nm while the polarity increases. The dielectric constant (ε) is often used to represent the solvent polarity (see **Table 3-14**). Similar to reported references[161], these scatters tends to reach a plateau when ε is above 25 (see **Figure 3-15**). In cyclohexane, the emission spectrum shows the defined structure of vibrational sublevels. However, the vibrational details are lost when the polarity increases, and the emission band turns to be broader. In chloroform, **M4** shows a more red-shifted emission than that in bromobenzene and THF, which are more polar solvents. The same phenomenon was found in dichloromethane and is possibly explained by the existence of an Ar-H…Cl interaction as shown by the X-ray crystal structure (**Figure 3-15**).

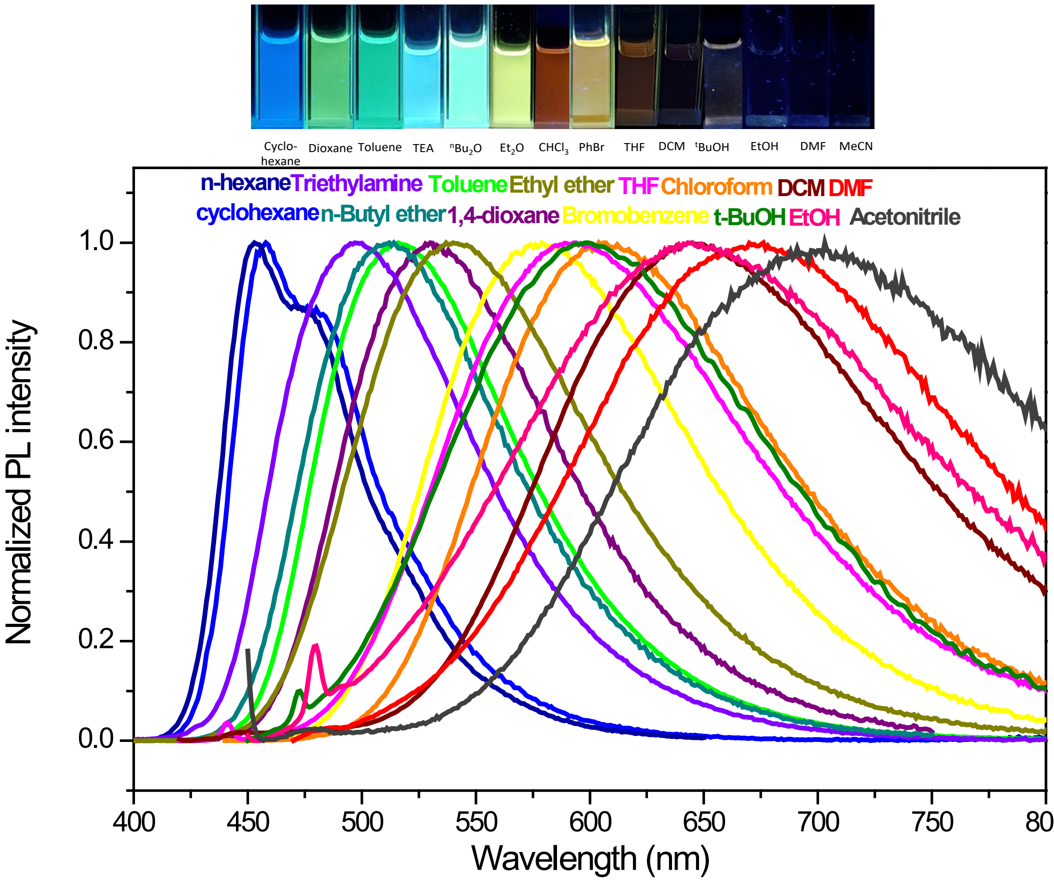

Figure 3-14 Emission sepctra of **M4** solutions in different solvents, 1×10^{-6} M.

In order to understand the role ICT plays in this phenomenon, the fluorescence decays have been recorded in each solvent and the corresponding fluorescence lifetimes (τ) were determined. They are summarized in **Table 3-9**. For most of the solutions, the decay curves can be well fitted with mono- or biexponential, but the latter gives smaller errors. The observation of biexponential decay reveals that an apparent one-band emission could be an overlay of locally excited state (LE) and CT fluorescence, the wide emission band could be caused by multispecies[158,162,163]. The coexistence of two excited states reflects a thermodynamic equilibrium between them. To achieve this equilibrium, the rate of the transition between LE and CT states must be much faster than the radiative decay of them[164]. In this case, LE and CT states should address at close energy levels, and generate a broad and approximate mono-band. In non-polar solvents, LE state is the favored one, revealing that the longer lifetime with highest percentage is attributed to LE state. In solvents with higher polarities, the situation is the opposite: CT excited states with shorter lifetimes dominate. The general tendency is a shortening of the lifetime appears with the increasing polarity of the solvent (**Figure 3-17**).

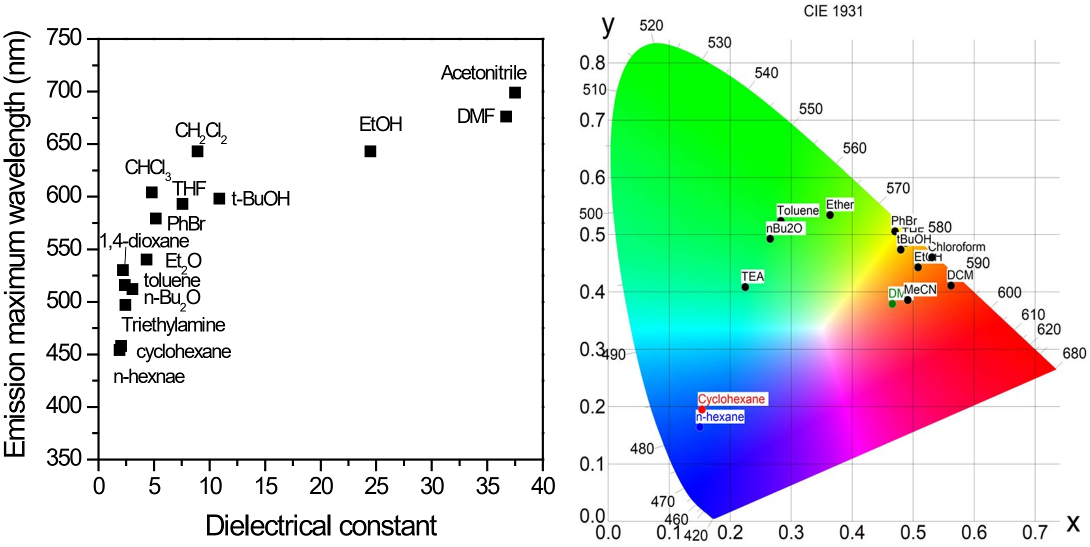

Figure 3-15 Fluorescence maximum wavelength as a function of solvent dielectric constants and chromacity diagram of **M4** solutions in different solvents, 1×10^{-6} M.

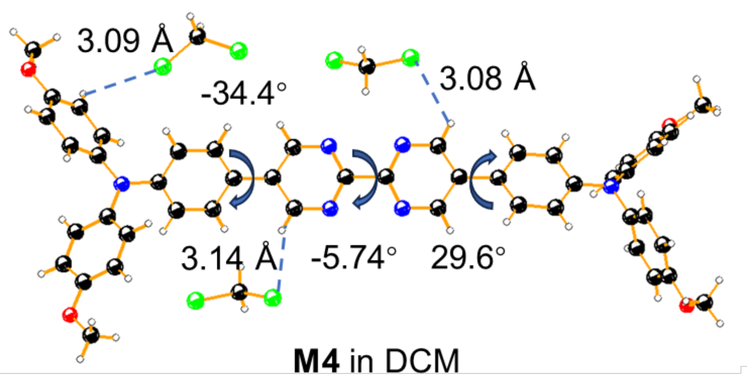

Figure 3-16 Single-crystal structures of **M4** in DCM, black for carbon, blue for nitrogen, red for oxygen, green for chlorine and grey for hydrogen.

Table 3-9 Photophysical properties of **M4** in different solutions (10^{-6} M).

Solvent	λ_{abs} (nm)	λ_{em} (nm)	P [a]	ε [b]	Φ [c]	τ (ns)	CIE coord.
n-Hexane	383	454	0.1	1.9	0.88	0.81 (13.4%) 1.54 (86.6%)	(0.15,0.16)
Cyclohexane	384	458	0.2	2.04	0.73	0.74 (5.07%) 1.66 (94.93%)	(0.15,0.20)
1,4-Dioxane	387	530	4.8	2.21	0.98	3.37 (100%)	(0.28,0.52)
Toluene	395	516	2.4	2.38	0.91	1.36 (7.72%) 2.69 (92.28%)	(0.33,0.55)
Triethylamine	391	497	1.8	2.42	0.99	0.93 (16.42%) 2.17 (83.58%)	(0.22,0.41)
Di-n-butyl ether	389	512	-[e]	3.08	0.99	1.36 (7.72%) 2.77 (92.28%)	(0.27,0.49)
Diethyl ether	387	540	2.8	4.34	0.94	0.34 (0.82%) 3.34 (99.18)	(0.47,0.51)
Chloroform	413	604	4.1	4.81	0.19[d]	1.13 (97.49%) 2.79 (2.51%)	(0.53,0.46)
Bromobenzene	405	579		5.17	0.37	2.43 (100%)	(0.36,0.53)
THF	391	593	4.0	7.58	0.10	0.58 (97.84%) 3.39 (2.16%)	(0.49,0.49)
DCM	407	643	3.1	8.93	0.03	0.26 (96.14%) 3.04 (3.86%)	(0.56,0.41)
Tert-butanol	416	598	-[e]	10.9	0.074	0.26 (94.36%) 2.16 (5.64%)	(0.48,0.47)
Ethanol	423	643	5.2	24.5	-[f]	-[f]	(0.47,0.38)
DMF	392	676	6.4	36.7	-[f]	0.23 (100%)	(0.51,0.44)
Acetonitrile	393	699	5.8	37.5	-[f]	-[f]	(0.49,0.39)

[a] Polarity index. [b] Dielectric constant. [c] Estimated by the absorbance and emission area using chloroform solution as a standard with an error ±10%. [d] Measured with integration sphere. [e] not found. [f] Too low to be measured.

The PLQY values are relatively lower in polar solvents, as the consequence of the stronger solvent relaxation. As we explained, solvent relaxation is a non-radiative transition. The enhanced non-radiative transition in polar environment will damage the emission efficiency. However, in solvents with medium polarities like chloroform, dichloromethane and THF, where the CT state is the leading species, the solvent relaxation is not so intense but the PLQYs have already significantly decreased. This points out that the main reason for the damaged quantum yield in medium-polar solvents is that the CT state has a fast rate of non-radiative decay. In the meantime, **M4** is very emissive in non-polar solvent. This distinguishing difference in quantum yield reflects a bright LE state and a less-emissive CT excited state.

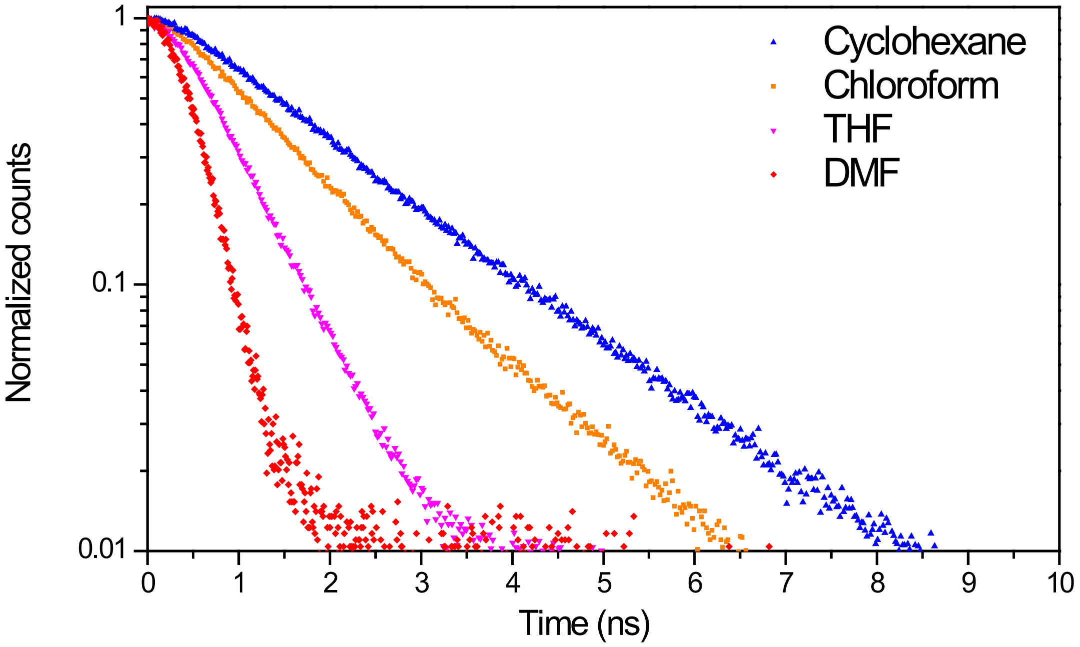

Figure 3-17 Fluorescence decay of **M4** in different solvents.

To better understand the solvent polarity effect, the Lippert-Mataga relation was applied including 15 solvents. This relation has been widely used to correlate the energy difference between absorption and emission ($\nu_a - \nu_f$), known as the Stokes' shift, with the solvent polarity represented by the term *f(ε,n)*, which is function of the dielectric constant (ε) and the refractive index (n). The formula is described as

$$\nu_a - \nu_f = \frac{2}{hc}\left(\frac{\varepsilon - 1}{2\varepsilon + 1} - \frac{n^2 - 1}{2n^2 + 1}\right)\frac{(\mu_E - \mu_G)^2}{a^3} + \text{constant}$$

where ν_a and ν_f are the wavenumbers (cm^{-1}) of the absorption and emission, respectively, h is the Planck's constant, c is the speed of light, a is the radius of the cavity in which the fluorophore resides, μ_E and μ_G are the dipole moment of excited and ground states, respectively, and the term

$$f(\varepsilon, n) = \frac{\varepsilon - 1}{2\varepsilon + 1} - \frac{n^2 - 1}{2n^2 + 1}$$

is the resultant effect of both the mobility of electrons in the solvent and the dipole moment of the solvent. From the slope of the fitting line, μ_E can be calculated while knowing μ_G and a.

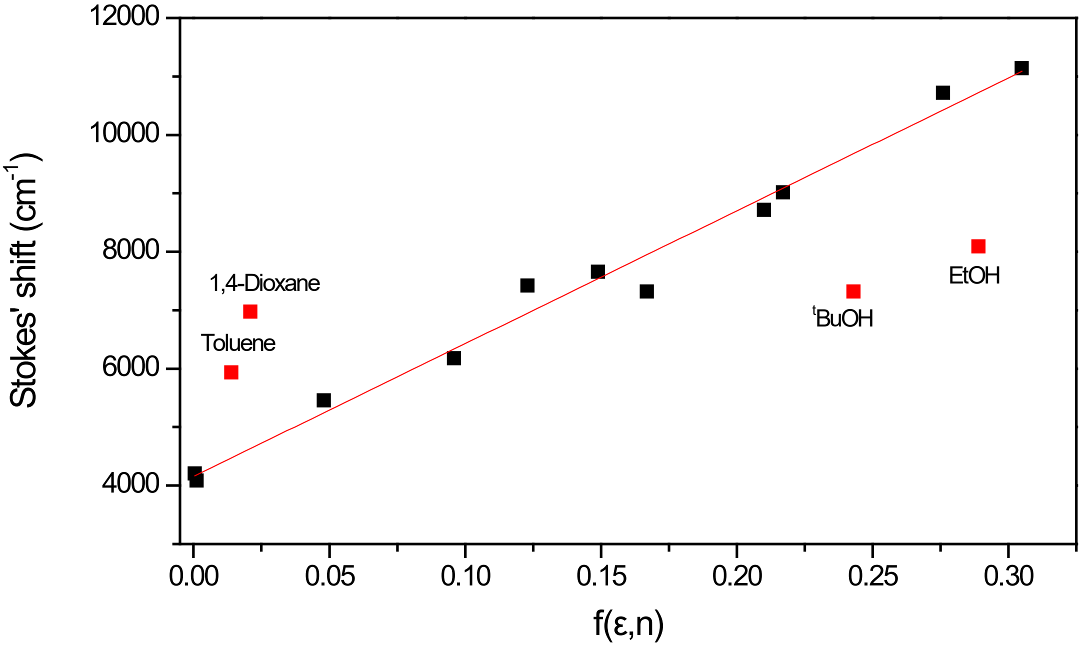

Figure 3-18 Lippert-magata plot for **M4** in different solvents.

Lippert-Mataga plot for **M4** in 15 different solvents is shown in **Figure 3-18**. All the solvent parameters, absorption and emission energies are listed in **Table 3-10**. Most of the points perform a good linear correlation (R = 0.992) with a slope of 22723 cm^{-1}, while the scatters for toluene, 1,4-dioxane and two protic solvents tert-butanol and ethanol are omitted. In toluene solution, the higher Stokes' shift is possibly caused by the presence of π-π stacking[161]. As for 1,4-dioxane, because of its quadrupole moment[165], it shows a better solvating capability than that revealed by its dielectric constant, leading to a high Stokes' shift. Protic solvents somehow can stabilize the ground state more than the excited state, leading to a lower ν_a, a relatively higher ν_f and a small Stokes' shift than these neighboring aprotic solvents. This is probably owing to formation O-H…O hydrogen bonding between methoxy groups of **M4** and solvents in ground state. However, once the molecule is excited, the hydrogen bonding will be weakened owing to the ICT, since the lone pair in the methoxy O could participate in the ICT process.

Table 3-10 Summary of solvent parameters and photophysical properties of **M4**.

Solvent	ν_a (cm^{-1})	ν_f(cm^{-1})	$\nu_a - \nu_f$(cm^{-1})	ε [a]	n [b]	$f(\varepsilon,n)$
Cyclohexane	26041.67	21834.06	4207.606	2.04	1.427	0.0005
n-Hexane	26109.66	22026.43	4083.229	1.90	1.375	0.0012
Toluene	25316.46	19379.84	5936.611	2.38	1.494	0.014
1,4-Dioxane	25839.79	18867.92	6971.869	2.21	1.422	0.021
Triethylamine	25575.45	20120.72	5454.723	2.42	1.401	0.048
Di-n-butyl ether	25706.94	19531.25	6175.691	3.08	1.399	0.096
Bromobenzene	24691.36	17271.16	7420.201	5.17	1.558	0.123
Chloroform	24213.08	16556.29	7656.784	4.81	1.443	0.149
Diethyl ether	25839.79	18518.52	7321.275	4.34	1.452	0.167
THF	25575.45	16863.41	8712.041	7.58	1.407	0.21
DCM	24570.02	15552.1	9017.925	8.93	1.424	0.217
Tert-butanol	24038.46	16722.41	7316.054	10.9	1.388	0.243
DMF	25510.2	14792.9	10717.3	36.7	1.427	0.276
Ethanol	23640.66	15552.1	8088.562	24.5	1.362	0.289
Acetonitrile	25445.29	14306.15	11139.14	37.5	1.344	0.305

[a] Dielectric constant. [b] refractive index.

3.3.2 Solvent effect on M3

A similar solvatochromic test was conducted on **M3**. The results are summarized in **Table 3-11**. As **M4**, **M3** also performs a positive solvatochromic effect. In **Figure 3-19**, one can see a structured emission band in cyclohexane, and a gradual red-shift with loss of the vibrational levels while increasing the polarity of the solvent. The longer λ_{em} obtained in chloroform than that in THF is probably due to the Ar-H…Cl interaction, which can be found in the crystal structure (shown in **Figure 3-20**).

Different from **M4**, **M3** shows a moderate quantum yield in non-polar solvent, indicating a not so bright LE with a shorter lifetime (< 1 ns). The PLQY keeps increasing with the polarity of the solvent. In the meantime, the contribution of longer lifetime rises, owing to the domination of the CT excited state. This trend demonstrates a brighter CT state than LE in **M3**, which is in the opposite way than found for **M4**, even though the only difference in the structure is the introduction of the methoxy groups. In highly polar solvents, the emission efficiency of **M3** drops because of the important non-radiative solvent relaxations. Specifically, as a protic solvent, ethanol quenches the emission of **M3** way more significantly, leading to a short lifetime of the CT excited state. A possible explanation could be the existence of some reactions/interactions between the protic environment and the CT excited state of **M3**.

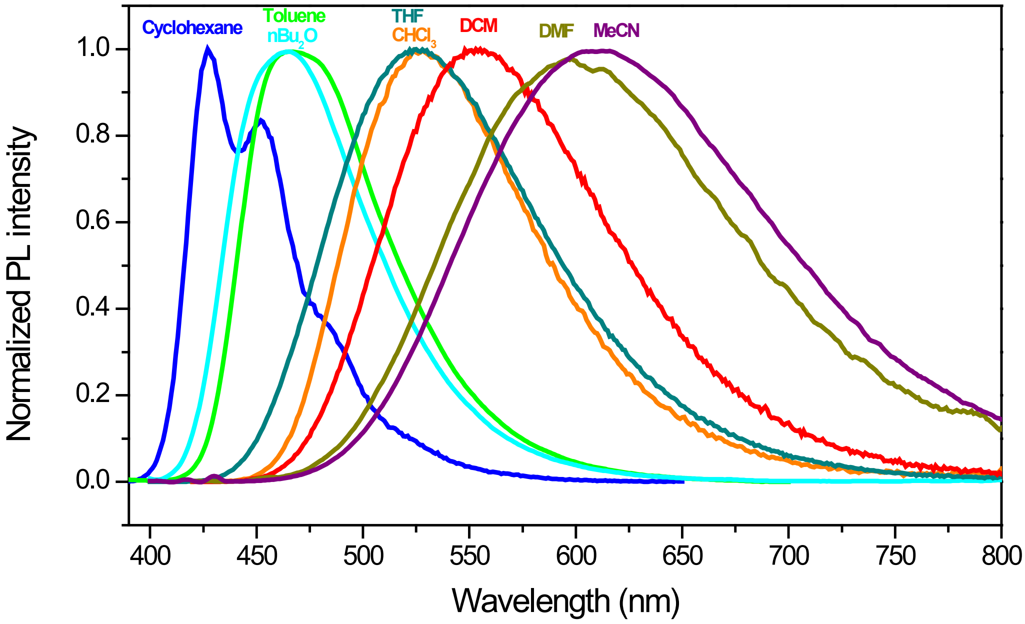

Figure 3-19 Emission sepctra of **M3** solutions in different solvents, 10^{-6} M.

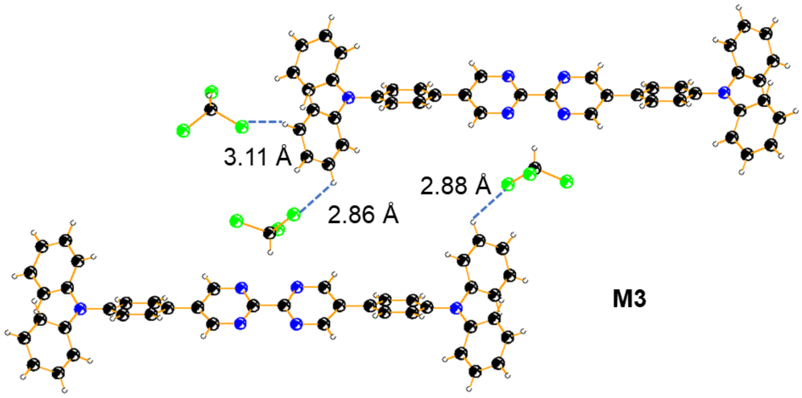

Figure 3-20 Ar-H…Cl interaction between **M3** and $CHCl_3$.

Table 3-11 Summary of solvent parameters and photophysical properties of **M3**.

Solvent	ε [a]	$f(\varepsilon,n)$	λ_{abs} (nm)	λ_{em} (nm)	$\nu_a - \nu_f$ (cm^{-1})	Φ [b]	τ (ns)
Cyclohexane	2.04	0.0005	375	427	3247.46292	0.20	0.46 (89.34%) 0.94 (10.64%)
n-Hexane	1.90	0.0012	376	431	3393.888532	0.23	0.39 (59.17%) 1.09 (40.83%)
Toluene	2.38	0.014	385	467	4560.749743	0.35	0.95 (36.01%) 1.58 (63.99%)
Di-n-butyl ether	3.08	0.096	377	464	4973.474801	0.40	0.93 (42.87%) 1.69 (57.13%)
Chloroform	4.81	0.149	405	530	5823.433496	0.62 [c]	2.87 (100%)
THF	7.58	0.210	378	526	7443.619611	0.50	0.81 (4.53%) 3.05 (95.47%)
DCM	8.93	0.217	395	554	7265.91418	0.47	3.61 (100%)
DMF	36.7	0.276	383	598	9387.252548	0.15	1.33 (100%)
Ethanol	24.5	0.289	423	612	7300.792657	0.01	0.24 (100%)
Acetonitrile	37.5	0.305	382	611	9811.39836	0.18	- [d]

[a] Dielectric constant. [b]. Estimated by the absorbance and emission area using chloroform solution as a standard with an error ±0.02. [c] Measured with integration sphere. [d] not measured.

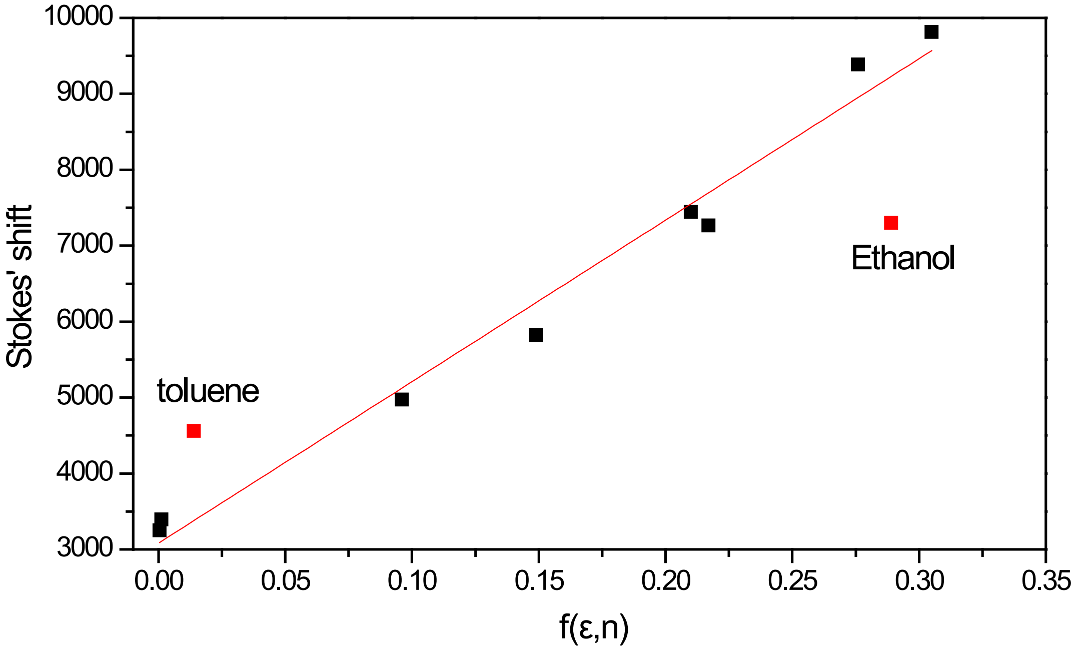

Figure 3-21 Lippert-magata plot for **M3** in different solvents.

A good linearity (R = 0.991) was obtained for the Lippert-Mataga plot (**Figure 3-21**). Similarly, the scatter of toluene is above the fitting line, while the one for ethanol is below. The slope value is 21268, smaller than that for **M4**. Unfortunately, values of a and μ_G could not be determined and the excited-state dipole moment could not be calculated. However, considering the structure of **M3** and **M4**, they should have similar a, and **M4** should have a bigger μ_G due to the presence of the polar methoxy groups, implying that μ_E of **M4** is bigger than **M3**. In another word, **M4** should have a larger excited-state dipole moment than **M3**.

3.3.3 Solvent effect on M7

We also conducted the solvatochromic experiments on **M7** (**Figure 3-22**). Starting from cyclohexane and toluene, a bathochromic shift from 529 to 590 nm was observed as usual. However, when the solvent was changed to chloroform, a dual-peak emission was found with extremely low emission intensity. Upon continuously increasing the polarity, the emission still appeared as a dual peak with a negligeable overall emission intensity. The shorter-wavelength band locates in the same position as the cyclohexane solution, where the LE preponderates. The longer-wavelength part is much more to the red with large Stoke's shifts (**Table 3-12**). This is the similar to the so-called twisted intramolecular charge transfer (TICT)[166]. In the initially formed LE state, a rotation around the single bond connecting the D-A moities can happen towards a perpendicular configuration to enter the TICT state[167]. During the process, an electron can eventually transfered from D to A, which causes a complete charge separation[168]. Due to this, the TICT states are highly polar and can be better stablilized in more polar solvents. This could explain the observation of the dual emission in $CHCl_3$ and THF instead of cyclohexane and toluene. On the other hand, as it leads to a orbitally decoupled π-system of the donor and acceptor units, the emission from TICT to ground state is overlap forbidden, conducting to an extremly low quantum yield[166].

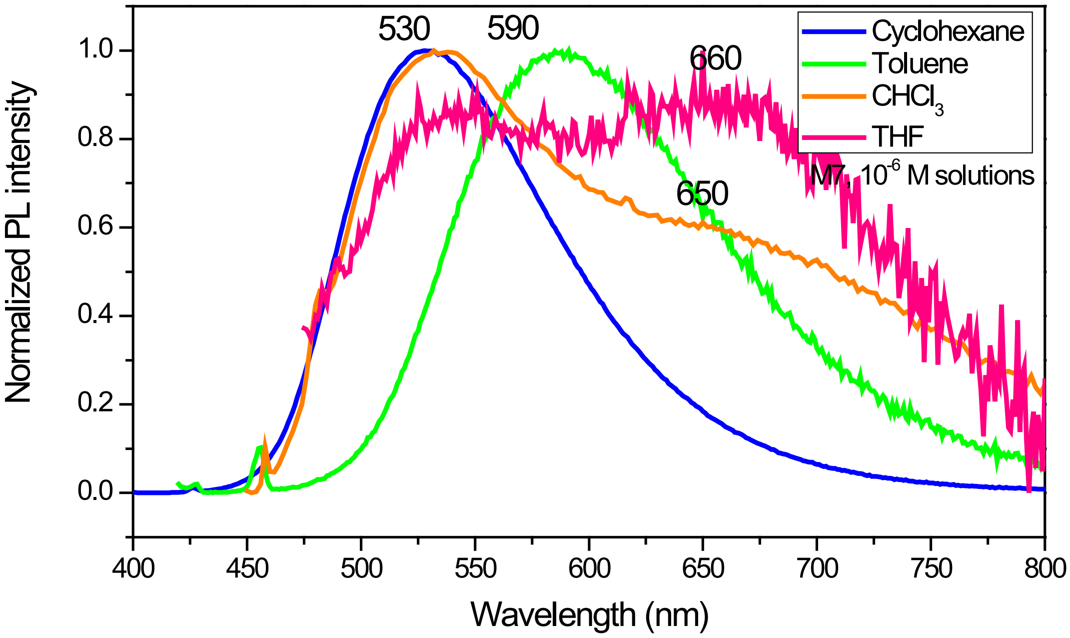

Figure 3-22 Emission sepctra of **M7** solutions in different solvents, 1×10^{-6} M.

To confirm our assumption, the emission spectra of **M7** in chloroform at 77K was recorded. It is shown in **Figure 3-23**. The molecular rotation is constrained at low tempearture, and locked in the conformation favoring to LE state. Therefore, the TICT emission band is diminished, leading to an emission band at 553 nm.

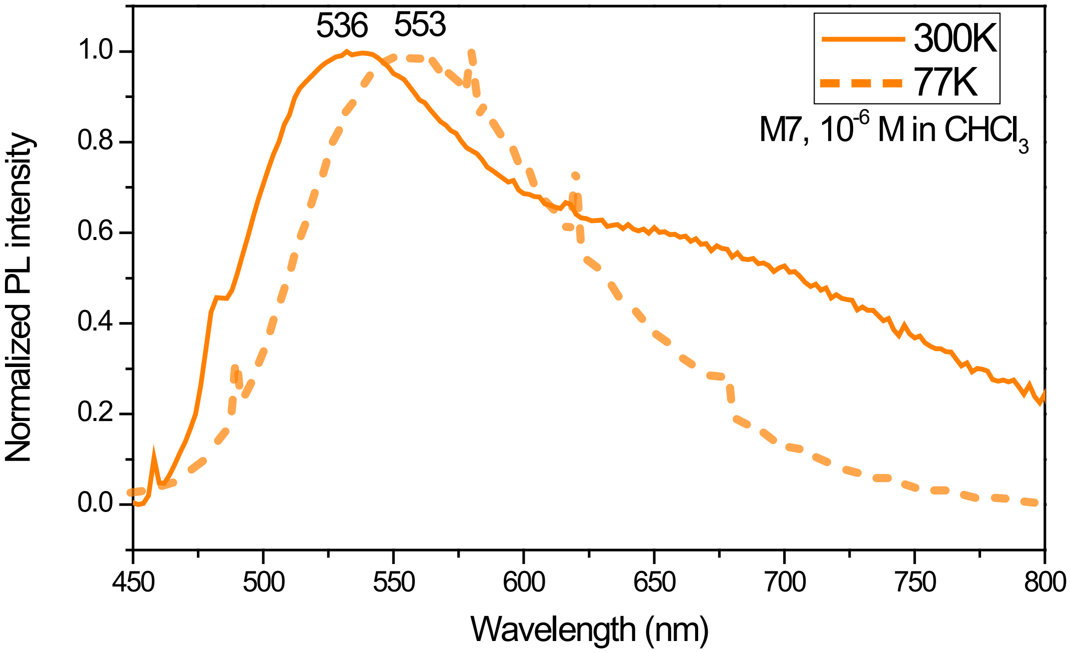

Figure 3-23 Emission sepctra of **M7** chloroform solution at 300K and 77 K.

Table 3-12 Summary of solvent parameters and photophysical properties of **M7**.

Solvent	ε [a]	λ_{abs}	λ_{em}	Φ [b]	$\nu_a - \nu_f$ (cm^{-1})	τ (ns)
Cyclohexane	2.04	395	529	0.55	6412.864	1.64 (9.87%) 5.00 (90.13%)
Toluene	2.38	401	590	0.03	7988.503	1.82 (100%)
Chloroform	4.81	420	536	- [c]	5152.807	0.30 (6.73%) 4.49 (93.27%)
			650		8424.908	0.12 (71.65 %) 4.18 (28.35%)
THF	7.58	390	542 660	- [c]	6059.619 9584.431	- [c]

[a] Dielectric constant. [b]. Estimated by the absorbance and emission area with an error ±0.02. [c] Too low to be measured.

Measurements of the lifetimes were carried out and are summarized in **Table 3-12**. In non-polar cyclohexane where LE state is populated, the longer lifetime around 5 ns is the major one, demonstrating that the LE state has a longer lifetime. In toluene, the CT state is the leading excited species, with a shorter lifetime and a lower PLQY of 3%. In chloroform solution, **M7** exhibits a dual-peak emission. At the 536-nm peak, the preponderating species is the LE state with 4.49-ns lifetime and 93% contribution. At the 650-nm peak, the LE state possesses less than 30% of the contribution. The favored specie has a lifetime of 0.12 ns, which is much shorter than that of the CT state in toluene and should belong to the TICT state.

Then, the excitation spectra analyzing at 554 and 650 nm were recorded (**Figure 3-24**). They showed different excitation maxima at 397 and 410 nm, respectively. Comparison with the absorption spectra of **M7** in different solvents, some interesting facts can be pointed out: the excitation spectrum recorded at 563-nm λ_{em} is appearing at the same position of the absorption band in cyclohexane, where the LE state is leading. The excitation spectrum in chloroform recorded at 650-nm λ_{em} is red-shifted due to the TICT.

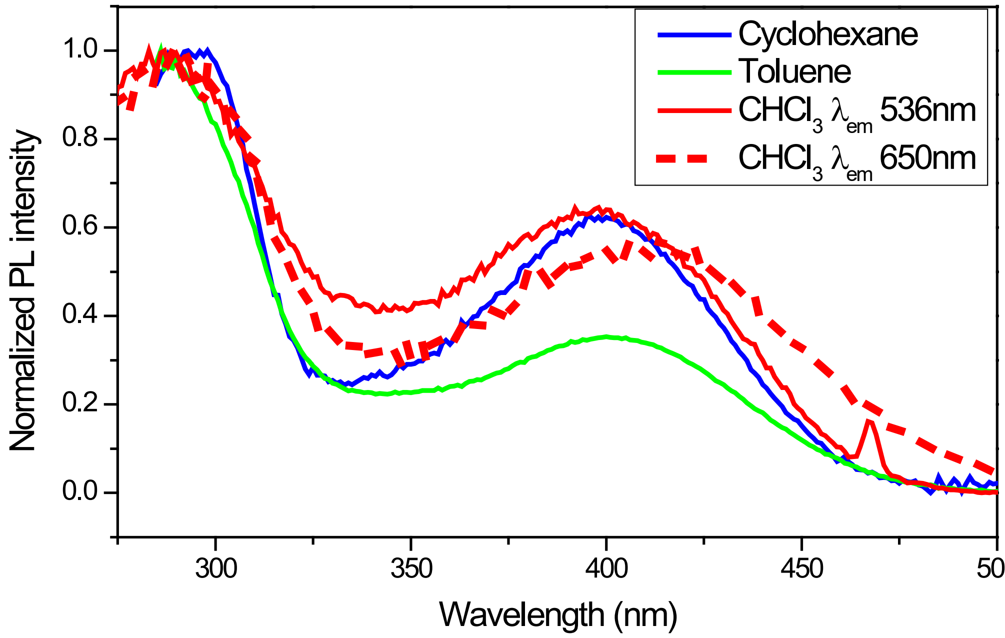

Figure 3-24 Excitation spectra of **M7** in cyclohexane, toluene and chloroform (with λ_{em} of 536 and 650 nm repectively).

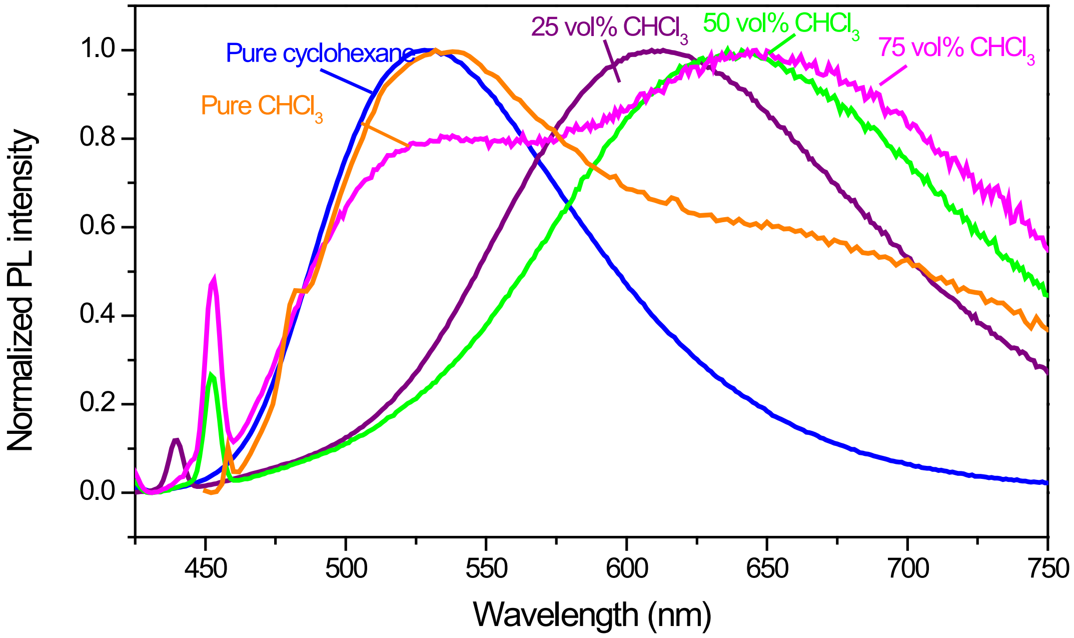

Figure 3-25 Emission spectra of **M7** in cyclohexane/chloroform mixture.

To investigate in detail the transition between the LE/ICT and TICT states, a binary solvent system made of cyclohexane and chloroform has been investigated (**Figure 3-25**). **M7** emits at 529 nm in pure cyclohexane with a PLQY of 55%. The fluorescence intensity and efficiency kept being quenched with the rise of the chloroform fraction

(**Figure 3-26**). While the volume fraction of chloroform increased to 25% and 50%, the emission red-shifted to 611 and 636 nm respectively, owing to an increase in the occurrence of the CT state caused by the increase in polarity. As we can see from the lifetime of 25% chloroform solution, the shorter lifetime (0.79 ns) representing ICT states is the majority among the two values, which is in the similar situation to the toluene solution (**Table 3-12**).

Table 3-13 Photophysical properties of **M7** in cyclohexane/chloroform soltuions.

Solvent	λ_{em} (nm)	Φ [a]	τ (ns, %)
Cyclohexane (CH)	529	0.55	1.64 (9.87) 5.00 (90.13)
25% $CHCl_3$/CH	611	0.12	0.79 (94.44) 3.41 (5.56)
50% $CHCl_3$/CH	636	- [c]	0.30 (60.20) 3.08 (39.80)
75% $CHCl_3$/CH	540	- [c]	- [b]
	646		- [b]
$CHCl_3$	542	- [c]	0.30 (6.73%) 4.49 (93.27%)
	660	- [c]	0.12 (71.65 %) 4.18 (28.35%)

[a] Estimated by the absorbance and emission area with error ±0.02. [b] not measured. [c] Too low to be measured.

In 50% chloroform, the shorter lifetime decreased to 0.30 ns, same as the one observed in pure chloroform solution of **M7**, indicating the entering to the TICT state. When the chloroform fraction reaches 75% and 100%, the dual-emission appears again with two peak values of 540 and 646 nm. To be noted, it is the low overall emission intensity which gives the delusion that the 540-nm band appears more important and shows the dual-emission feature in the normalized emission spectrum with an "increasing" trend for higher-energy band. In fact, the fluorescence intensity is too low to demonstrate a clear tendency for that.

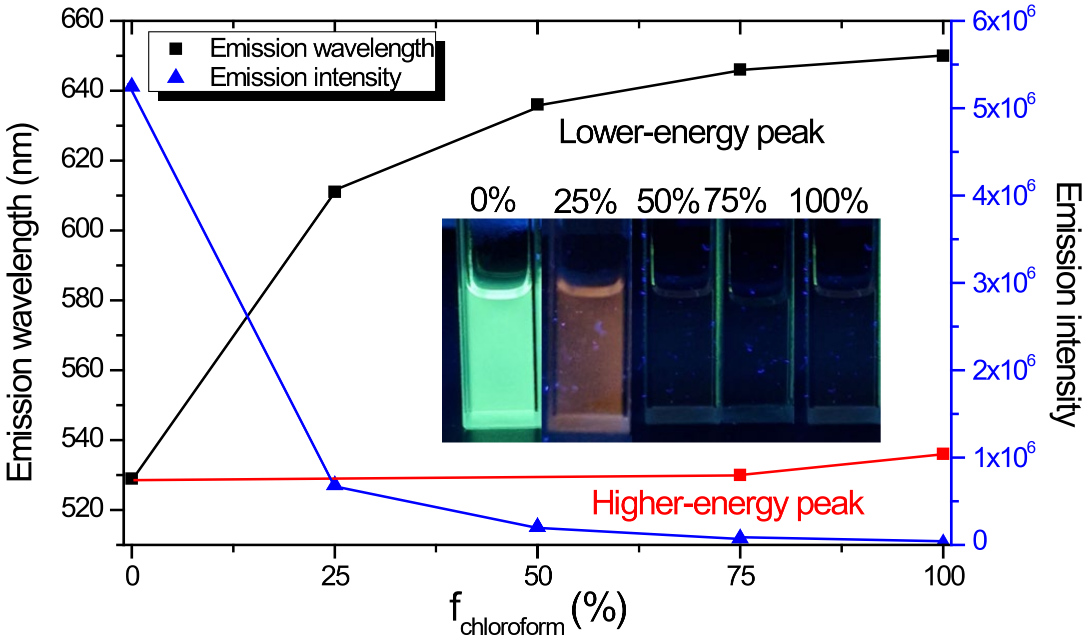

Figure 3-26. Evolution of emission wavelength (black) and intensity (blue) of **M7** in cyclohexane/chloroform mixture.

3.4 Phosphorescence and electronic configuration

In the previous part, we focused on the fluorescence of the compounds, which is the radiative relaxation of the excited molecules from a singlet excited state (S1) to the ground state (S0). As discussed in **Chapter I**, there is a competing process of the non-radiative transition from S1 to a triplet state T1, as known as intersystem crossing (ISC). From T1, it is possible for the excited molecule to return to S0 through a radiative pathway, which is called phosphorescence. In a singlet state, all electron spins are paired, thus the spin of the excited electron is still paired with the ground state electron. In a triplet state the excited electron is no longer paired with the ground state electron; they will have the same spin direction (shown in **Figure 3-27**). Although the process of ISC and phosphorescence are “forbidden”, there is still the probability for them to happen due to the spin-orbit coupling when the two excited states S1 and T1 are close enough, because little or no energy is needed in the transition. Therefore, measuring the spectral profile of both the fluorescence and phosphorescence transitions of a molecule reveals important information on its electronic structure and for the potential applications. However, it is challenging to measure phosphorescence at room temperature, as T1 is depopulated by non-radiative relaxation. By cooling down the sample, the non-radiative relaxation rate is decreased, then the phosphorescence can be observed and the triplet states can be located. Moreover, with knowing the absorption onset wavelength, the optical bandgap can be estimated to reveal the whole picture of the electronic structures of the compounds.

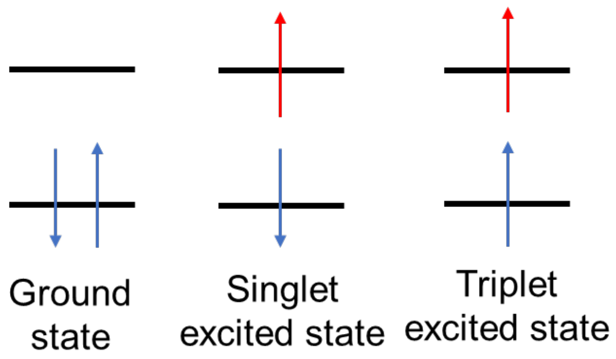

Figure 3-27 Indication of singlet and triplet excited states.

3.4.1 Low temperature PL and phosphorescence

The low temperature (77K) emission decay (**Figure 3-28)**, emission, and delayed emission spectra (From **Figure 3-29** to **3-35**) of **M1-M7** are shown below, the results are summarized in **Table 3-14**. From the emission decays at 77K with a 1-Hz flash lamp pulse, the phosphorescence lifetimes were determined. As shown in **Figure 3-28**, the initial spike of each decay is caused by fluorescence and the following slope is attributed to phosphorescence. The nitrogen atoms in the bipyrimidine core can favor the spin-orbit coupling and improve the efficiency of ISC[169,170]. Integrating after the initial spike, the contribution of phosphorescence in emission intensity can be calculated. **M1** exhibits the most contribution of phosphorescence, while **M4** performs the least. There is no observation of the triplet-state decay for **M6**. Their emission decays at 300 K were also measured in 1-second scale with the 1-Hz pulse. However, the fluorescence lifetimes at room temperature are even shorter than the pulse width, only the profiles of pulse decaying can be seen. Herein, the instrumental response (IR) is shown to distinguish the phosphorescence decay.

Table 3-14 Photophysical properties of **M1-M7** at 77K.

Molecule	λ_{fluo} (nm)	λ_{phos} (nm)	E_s (eV) [a]	E_t (eV) [b]	ΔE_{st} (eV)	τ_{phos} (ms)	I_{phos}/I_{PL}
M1	440	508	2.82	2.44	0.38	73.98 [c]	0.66 [c]
M2	425	531	2.92	2.34	0.58	158.8 [c]	0.49 [c]
M3	455	557	2.73	2.23	0.50	102.4 [d]	0.35 [d]
M4	464	545	2.67	2.27	0.40	85.91 [e]	0.21 [e]
M5	444	470	2.79	2.64	0.15	113.3 [e]	0.20 [e]
M6	417	600	2.97	2.07	0.91	n.d.	n.d.
M7	483	510	2.57	2.43	0.14	280.8 [e]	0.26 [e]

[a] $E_s = 1240/\lambda_{fluo}$. [b] $E_t = 1240/\lambda_{phos}$. [c] $\lambda_{em} = 550$ nm. [d] $\lambda_{em} = 600$ nm. [e] $\lambda_{em} = 630$ nm.

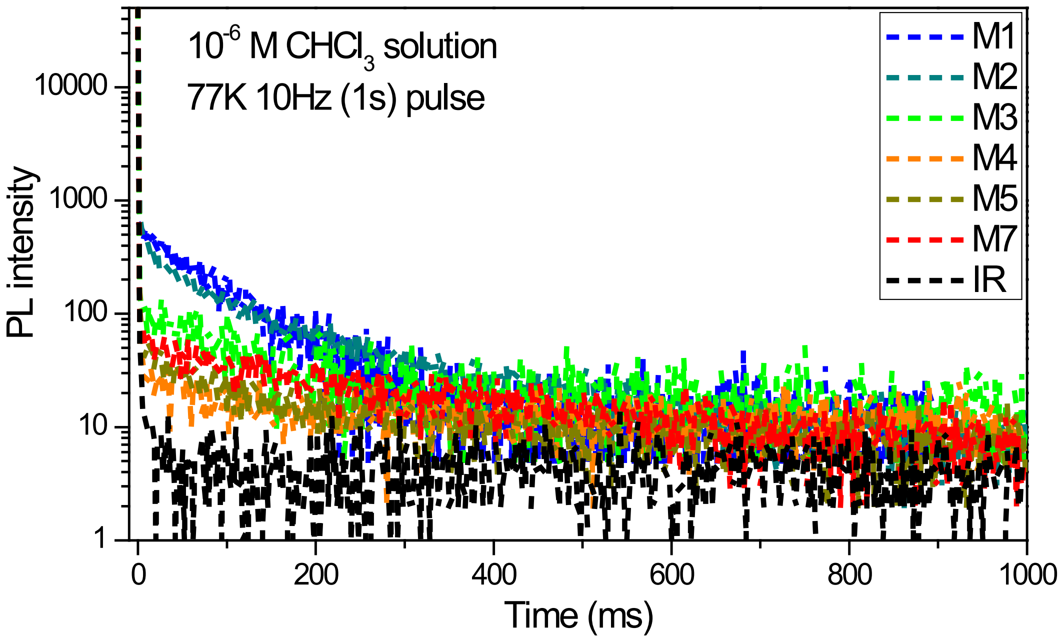

Figure 3-28 Emission decay of **M1-M7** with a 1-Hz (1-s period) flashlamp at 77K.

For **M1-M4** and **M6**, since the vibrational structures are clear, the corresponding wavelengths of highest-energy vibrational levels are taken as the 0-phonon component to estimate the position of the energy levels. For **M5** and **M7**, the emission spectra are not structured, the energy levels are calculated according to the blue-side onset wavelengths obtained by the tangent method[83]. The taken values of wavelength λ_{fluo} and λ_{phos} are used for the calculations of the energy levels of singlet (E_s) and triplet (E_t) states. To be noted, these estimations are approximations, but for comparing these compounds, the approximations are similar. As shown in **Table 3-21**, the singlet-triplet energy difference (ΔE_{st}) for **M4**, **M5** and **M7** are below 0.37, indicating that the singlet and triplet energy levels are very close.

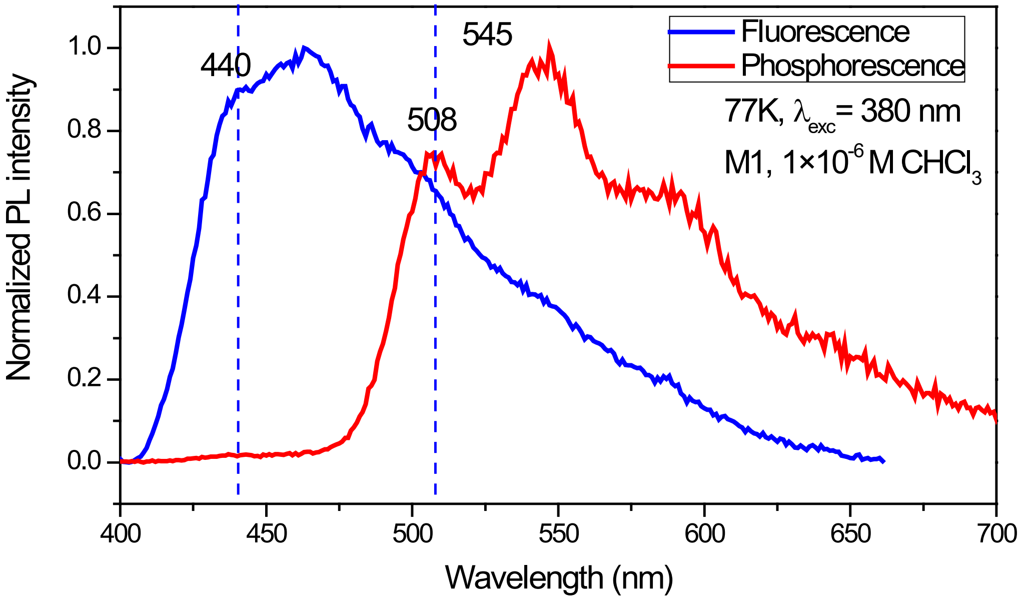

Figure 3-29 Fluorescence and phosphoresecne spectra of **M1** at 77K, slit 1/1 nm, phosphoresecne spectrum is measured with a 20-Hz pulse and a gating time of 5-50 ms.

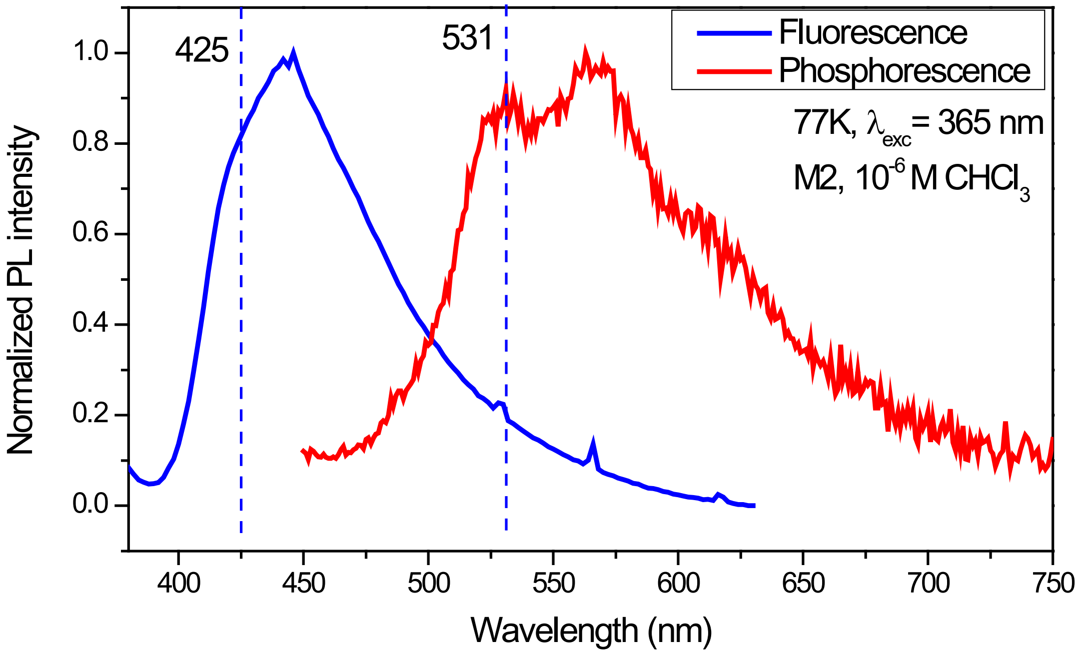

Figure 3-30 Fluorescence and phosphoresecne spectra of **M2** at 77K, slit 1/1 nm, phosphoresecne spectrum is measured with a 40-Hz pulse and a gating time of 5-25 ms.

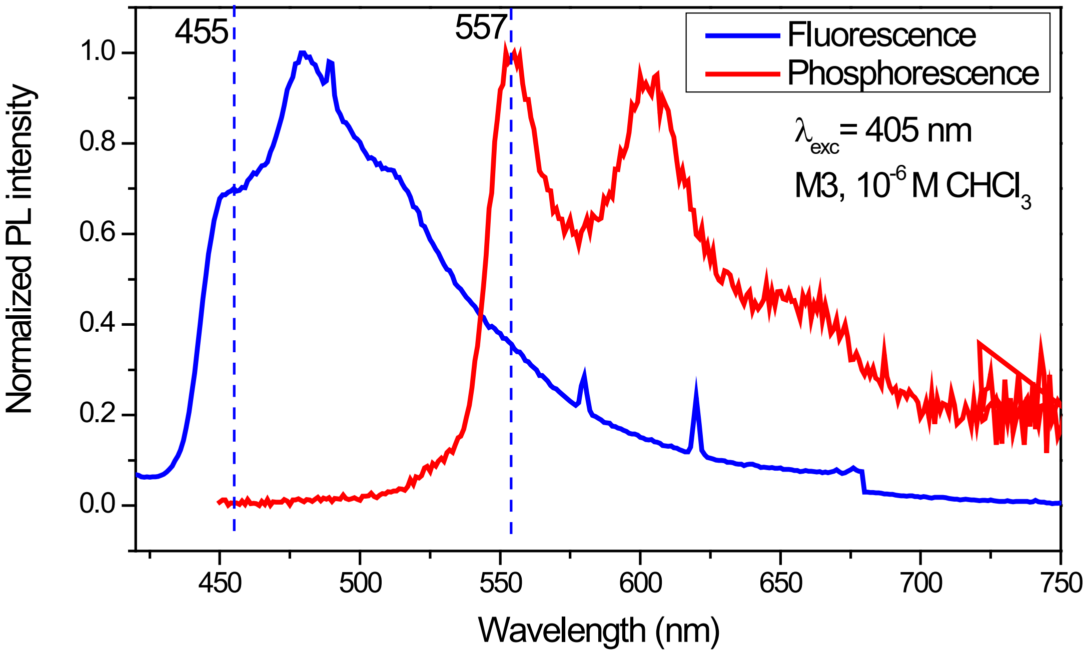

Figure 3-31 Fluorescence and phosphoresecne spectra of **M3** at 77K, slit 1/1 nm, phosphoresecne spectrum is measured with a 20-Hz pulse and a gating time of 10-50 ms.

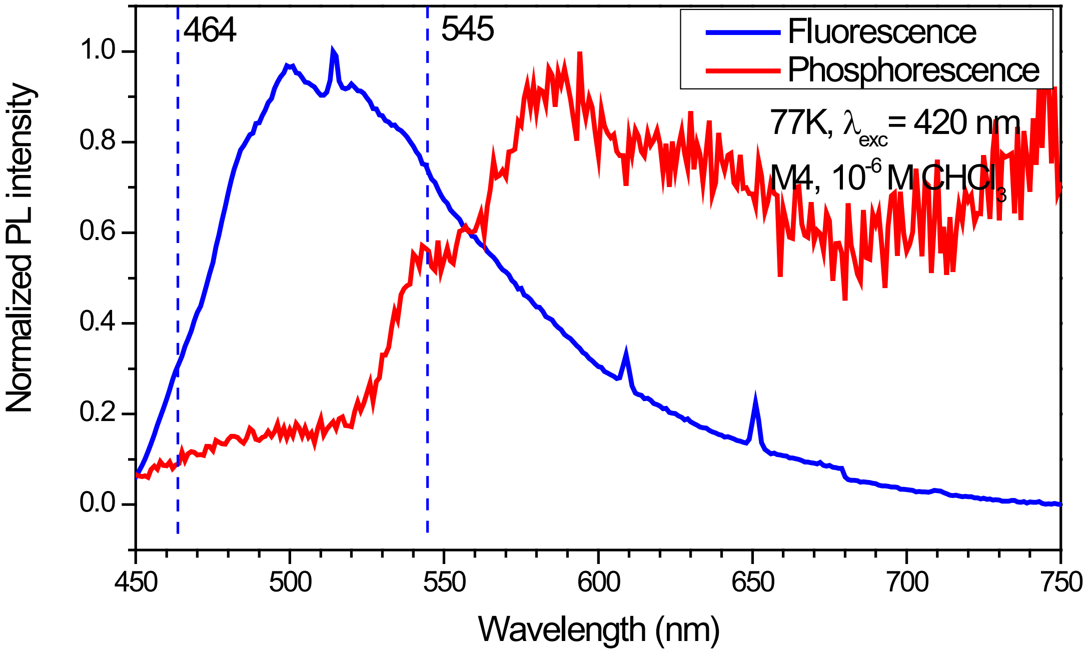

Figure 3-32 Fluorescence and phosphoresecne spectra of **M4** at 77K, slit 1/1 nm, phosphoresecne spectrum is measured with a 20-Hz pulse and a gating time of 10-50 ms.

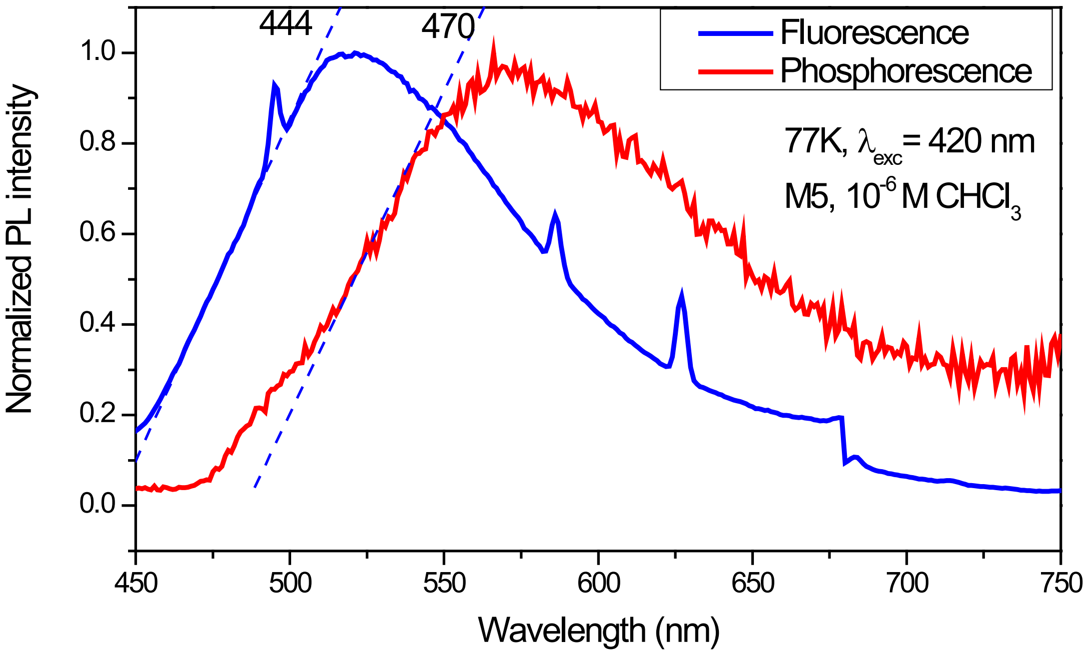

Figure 3-33 Fluorescence and phosphoresecne spectra of **M5** at 77K, slit 1/1 nm, phosphoresecne spectrum is measured with 20-Hz pulse and a gating time of 10-50 ms.

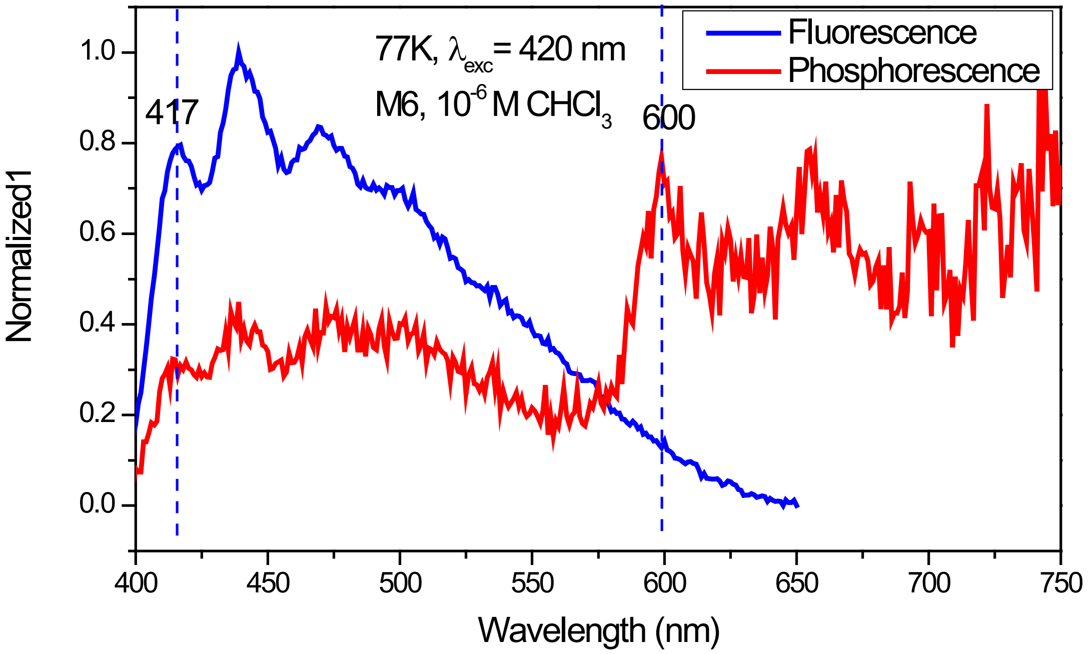

Figure 3-34 Fluorescence and phosphoresecne spectra of **M6** at 77K, slit 1/1 nm, phosphoresecne spectrum is measured with a 100-Hz pulse and a gating time 1-10 ms.

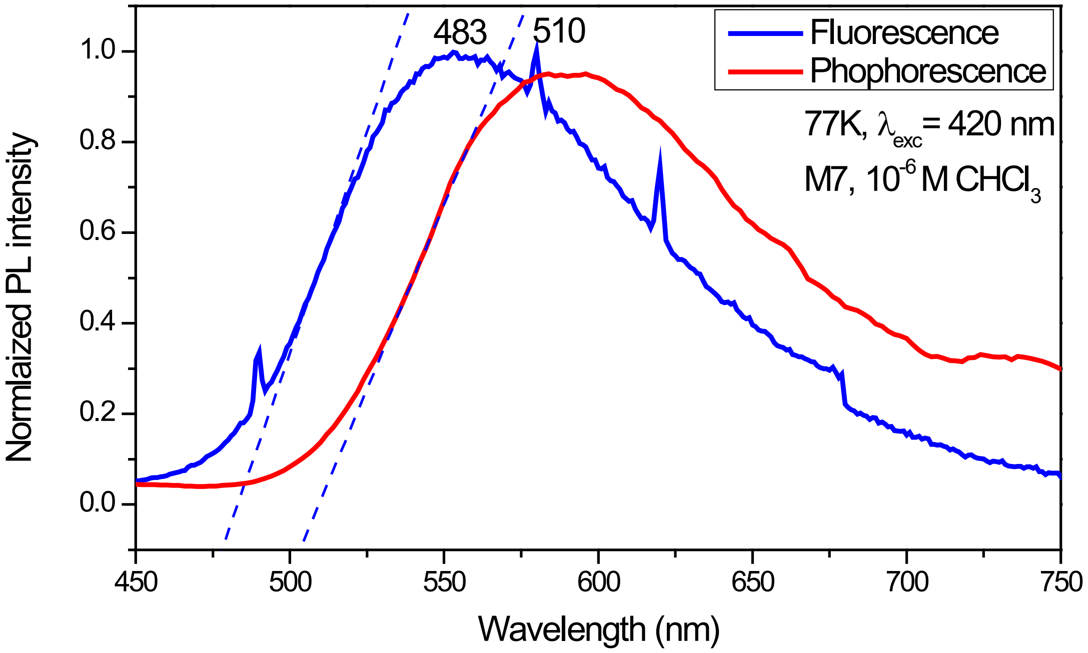

Figure 3-35 Fluorescence and phosphoresecne spectra of **M7** at 77K, slit 1/1 nm, phosphoresecne spectrum is measured with a 20-Hz pulse and a gating time 10-50 ms.

Notably, in the delayed spectrum of **M4** and **M6**, the fluorescence is not completely filtered. Because of the low phosphorescence intensity of **M6**, a faster pulse (100 Hz) and an early gating period (1-10 ms) have to be used to improve the emission intensity of the emitting triplet state. Therefore, the fluorescence partially remains.

3.4.2 Electronic configurations

The electronic diagrams of each compound that can be deduced from the measurements described above are shown in **Figure 3-36**. The energy levels are listed in **Table 3-15**. Those demonstrated the relative positions of the different energy levels of our compounds. We can see that insertion of a phenyl bridge reduces the energy level of the ground state of **M2**, but enlarges the band gap, showing the impact of the high resonance energy of the benzene rings. The enhancement of the D-A strength from **M2-M5** by adjusting **D/A** units is significantly narrowing bandgap. Changing the donor units from carbazole to diphenylamine, the ground state of **M3** shows an increased energy level, while the single state shows a decreased energy level, resulting in a narrowed bandgap. The methoxy groups in **M4** exhibits a same effect on the energy levels and bandgap. Comparing **M5** to **M3**, the CF_3 groups escalate the energies of both ground and singlet states, although the bandgap is reduced. This is the overall impact of the steric hindrance and electron-withdrawing properties of the CF_3 substitutions. As for the most planar **M6**, it shows an important ΔE_{st} of more than 0.9, while twisted compounds such as **M7** has a small energy difference between singlet and triplet excited states, indicating the conformations of compounds can deeply influenece their eletronic structures.

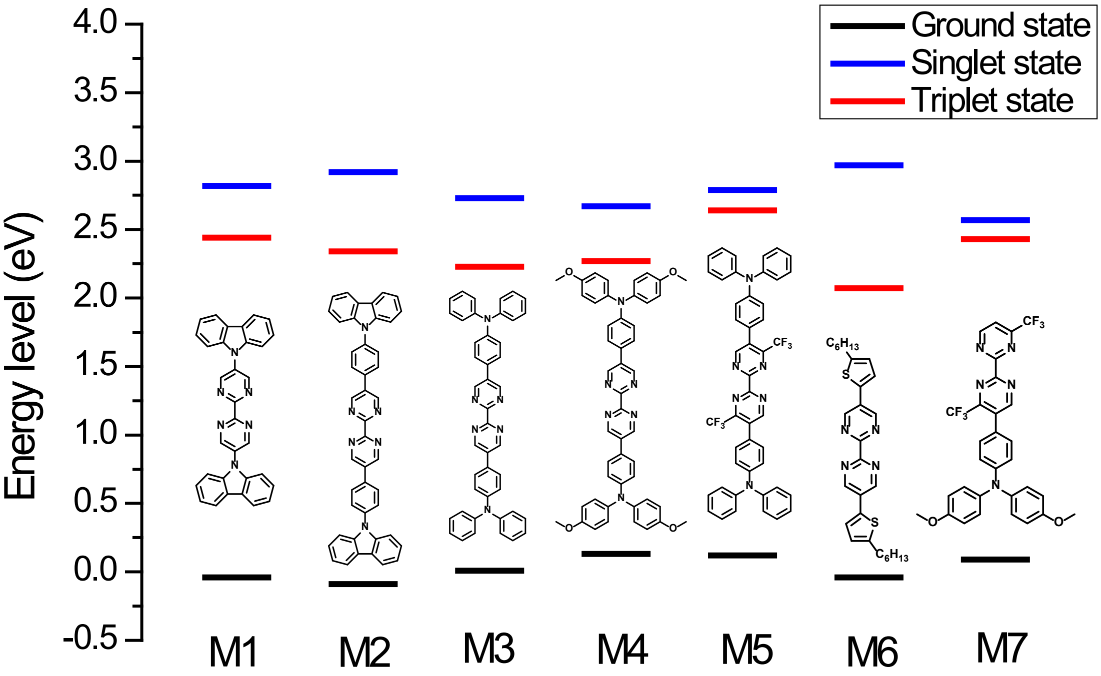

Figure 3-36 Electronic configurations diagram of **M1-M7**.

Table 3-15 Energy levels of **M1-M7**.

Molecule	λ_{abs} (nm) [a]	Optical bandgap (eV) [b]	E_g (eV)	E_s (eV)	E_t (eV)	ΔE_{st} (eV)
M1	434	2.86	-0.04	2.82	2.44	0.38
M2	412	3.01	-0.09	2.92	2.34	0.58
M3	456	2.72	0.01	2.73	2.23	0.50
M4	489	2.54	0.13	2.67	2.27	0.19
M5	482	2.57	0.12	2.79	2.64	0.15
M6	412	3.01	-0.04	2.97	2.07	0.91
M7	499	2.48	0.09	2.57	2.43	0.14

[a] Onset wavelength of absorption spectra. [b] Optical bandgap = $1240/\lambda_{abs}$.

3.5 Summary

In this chapter, diluted solutions of the newly synthesized D-A molecules comprising BPM were investigated as far as photophysical properties are concerned, in order to establish their photoluminescent behavior at the molecular level. Thanks to different D/A units and combinations, they exhibit tunable emission colors which cover nearly the whole visible spectrum from deep-blue to orange-red, implying an effective design strategy.

Solutions except that of **M1** can absorb light with high absorption coefficient (in the magnitude of 10^4 L·mol^{-1}·cm^{-1}) in the near-UV or/and blue regions. Also, some compounds have been found to be highly efficient emitters. Especially, **M2** and **M3** show more than 60% PLQY in chloroform, and **M4** exhibits more than 90% PLQY in toluene, triethylamine and ether.

Moreover, we systematically investigated the effects of solvents on absorption, emission and fluorescence lifetimes. These D-A molecules possessing internal charge transfer generally show a positive solvatochromism. By inspecting their locally and charge-transfer excited states, especially **M3**, **M4** and **M7**, the process of internal charge transfer has been carefully studied. **M3** shows a bright CT state, while **M4** has a very emissive LE state but less emissive CT state. The methoxy substitutions can change the ICT process profoundly. **M7** behaves a dual-peak emission in polar solvents, which is the consequence of the TICT. The solvent polarity is a facile mean to tune the emission properties of the fluorophores.

In the end, by monitoring emission decays, the low temperature fluorescence and phosphorescence spectra, the singlet and triplet excited states of each compound could be located. Combining with optical band obtaining from absorption spectrum, the ground states were also localized. These energy levels clearly reveal the structure-property relationships of our new molecules.

The high molar absorption coefficient, high emission efficiency and tunable emission color make these molecules of interest and open the way to apply them in the design of photoluminescent materials in solid state with excellent performances. The next chapter will thus describe the photophysical investigations on luminescent solid materials made from these compounds.

Chapter IV Solid state photophysical studies and white-emitting materials: towards applications

In the previous chapters, we have introduced the design and synthesis of emissive donor-acceptor (D-A) compounds, and the photophysical properties of isolated molecules in diluted solutions. However, the final goal of this thesis is to investigate the possibility to apply these organic compounds for the design of luminophores in hybrid colored and white light-emitting diodes (WLEDs) to have some clue about the possibility to find alternatives to the current inorganic phosphors. Therefore, it is of importance to investigate the PL performance of the compounds when deposited as solids. In this chapter, we will thus focus on their photophysical performance in the solid state, including powder and films, to testify whether they are promising options for the desired application.

4.1 Aggregation-induced emission (AIE)

As we mentioned in **Chapter I**, AIE is a well-adopted method to avoid the aggregation-caused quenching (ACQ) and can lead to an enhancement of the emission in the solid-state[113]. This phenomenon is caused by the restriction of intramolecular rotation (RIR) due to a special design of the molecular structure[171]. Triphenylamine is often used to construct AIE luminophores containing D-A pairs thanks to its propeller-like structure and electron-donating ability[95,96]. As its molecular structure reveals, the non-planar geometry can be illustrated by the torsion angles of -56°, 119° and 143° between each two of three phenyl rings[172]. Hence, it would be interesting to investigate if it can lead to AIE in **M3**, **M4** and **M7** that contain such group as donors.

To perform the tests, we dissolved these compounds in THF with a concentration of 1×10^{-3} M, then gradually diluting it to 100 times with a varying THF/water ratio. Since water is a bad solvent for these compounds, aggregation is expected to take place in the highly aqueous system. These investigations are reported in the next paragraphs.

4.1.1 AIE study on M3

Firstly, the AIE effect on **M3** has been examined. As shown in **Figure 4-1**, the emission maximum of **M3** in THF appears at 526 nm. While the water fraction (f_w) increases, the emission firstly red-shifts then blue-shifts. Upon addition of 10 vol% of water, the emission band is quenched significantly and red-shifts to 587 nm due to the high polarity of water. The solvent relaxation can lead to a bathochromic shift and a high rate of non-radiative decay (see **Chapter III**). The emission keeps monotonously quenching until the water fraction reaches 0.70. The emission band occurs at 565 nm and the intensity rises slightly with f_w increasing until 0.99. Since the water is a nonsolvent for **M3**, the molecules form aggregates in this highly aqueous system. Therefore, when f_w = 0.99, the **M3** molecules locate in a less polar environment than water inside of the aggregates[173], where they are surrounded by other **M3** molecules instead of water. According to the solvatochromic principle, the less polar environment should result in a hypochromic shift.

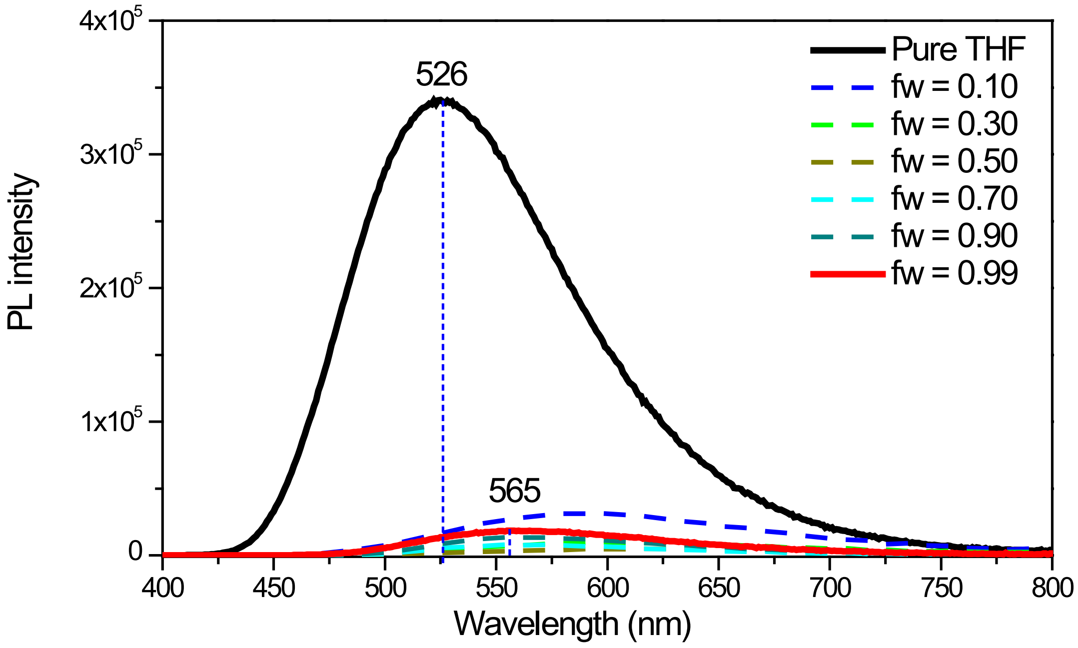

Figure 4-1 Emission sepctra of **M3** in THF/water mixture (1×10^{-5} M, λ_{exc} = 380 nm, 1/1 nm slits).

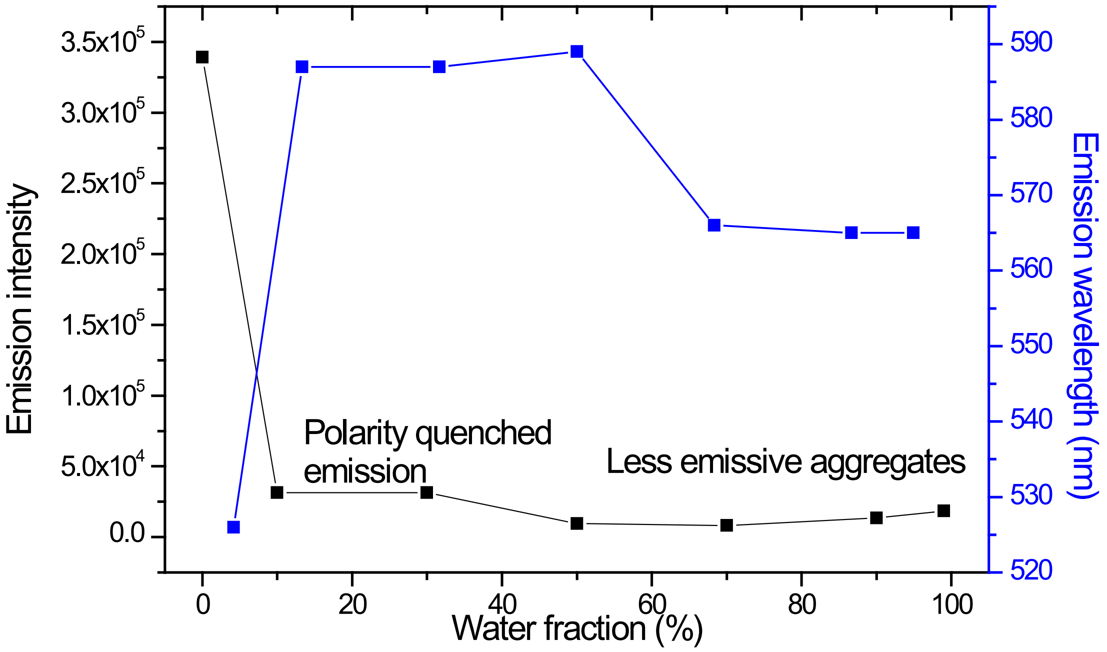

Figure 4-2 Emission wavelength (blue) and intensity of the maximum of **M3** in THF/water mixtrue with different f_w.

The lifetimes are listed in **Table 4-1**. As we have described about the solvent effect on **M3** in **§ 3.3.2**, the longer lifetime stands for the bright charge-transfer (CT) excited state, and the shorter one is attributed to the less emissive locally excited (LE) state. In a less polar environment, the less emissive LE state is more favored. The lifetime of the aggregates in a 99% water system is presented in **Table 4-1**. Comparing to the lifetime in a pure THF solution, the contribution of the LE state grows from 4.53% to 30.08%, while that of the CT state decreases from 85.47% to 40.52%. This also points out the less polar environment inside the aggregates. The 5.25 ns lifetime with 26.43% contribution is tentatively attributed to the aggregates, in other words, excimers, since they usually show longer lifetimes than monomers[174-176]. In π-conjugated materials, overlap between π-orbitals of neighboring molecules results in delocalization of the excitons, creating the excimers and leading to reduction in the energy barrier for charge transport[177]. On the other hand, this interaction creates a new non-radiative decay which could compete with the emissive pathway, resulting in the quenching of luminescence[92]. Therefore, excimers usually red-shift the emission and decrease the rate of radiative decay, thus the emission efficiency. The enlarged proportions of less emissive LE state and excimers damage the photoluminescence quantum yield (PLQY) in the 99% water mixture, giving a value of 0.14, not as good as that of 0.50 for a pure THF solution of **M3**.

Table 4-1 Photophysical properties of **M3** in THF/water mixture.

f_w (%)	λ_{abs} (nm)	λ_{em} (nm)	I_{em}	Φ [a]	τ [b] (ns, %)
0	378	526	339174	0.50	0.81 (4.53) 3.05 (85.47)
10	-[c]	587	31509	-[c]	-[c]
30	-[c]	587	9435	-[c]	-[c]
50	-[c]	589	4674	-[c]	-[c]
70	-[c]	566	8145	-[c]	-[c]
90	-[c]	565	13417	-[c]	-[c]
99	396	565	18523	0.14	0.45 (33.08) 1.64 (40.52) 5.25 (26.40)

[a] Photoluminescence quantum yield, with an estimated error ±10%. [b] Fluorescence lifetime. [c] not measured.

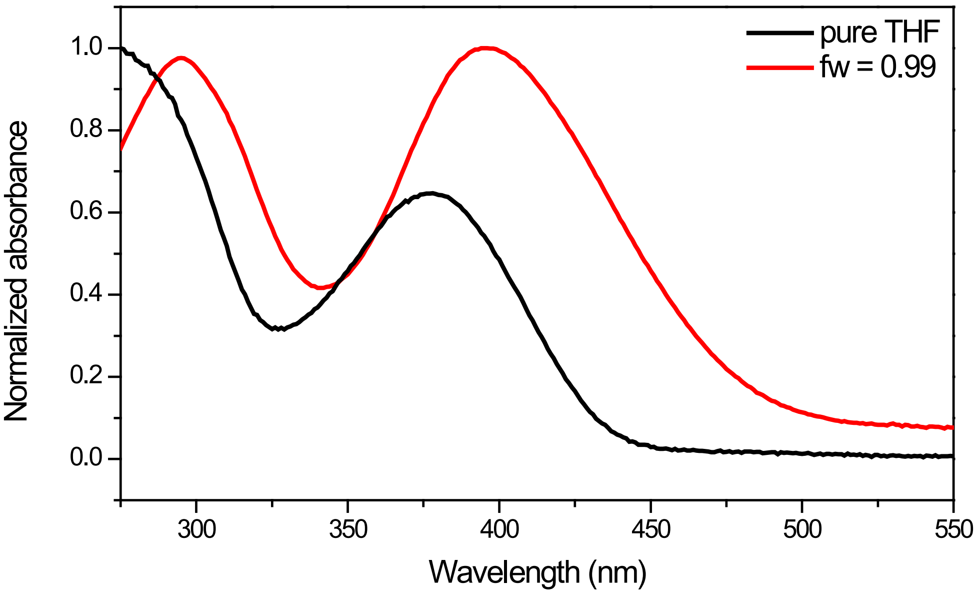

Figure 4-3 Normalized absorption sepctra of **M3** in THF/water mixture with a concentration of 1×10^{-5} M.

From the absorption spectrum of the mixture containing 99% of water (**Figure 4-3**), a red-shift and a broader absorption with a full width at half maximum (FWHM) of 5331 cm^{-1} is observed with respect to pure THF with an improved contribution of the lower-energy absorption with a FWHM of 4455 cm^{-1}, showing that aggregate might occur in the mixture containing 99% of water.

4.1.2 AIE study on M4

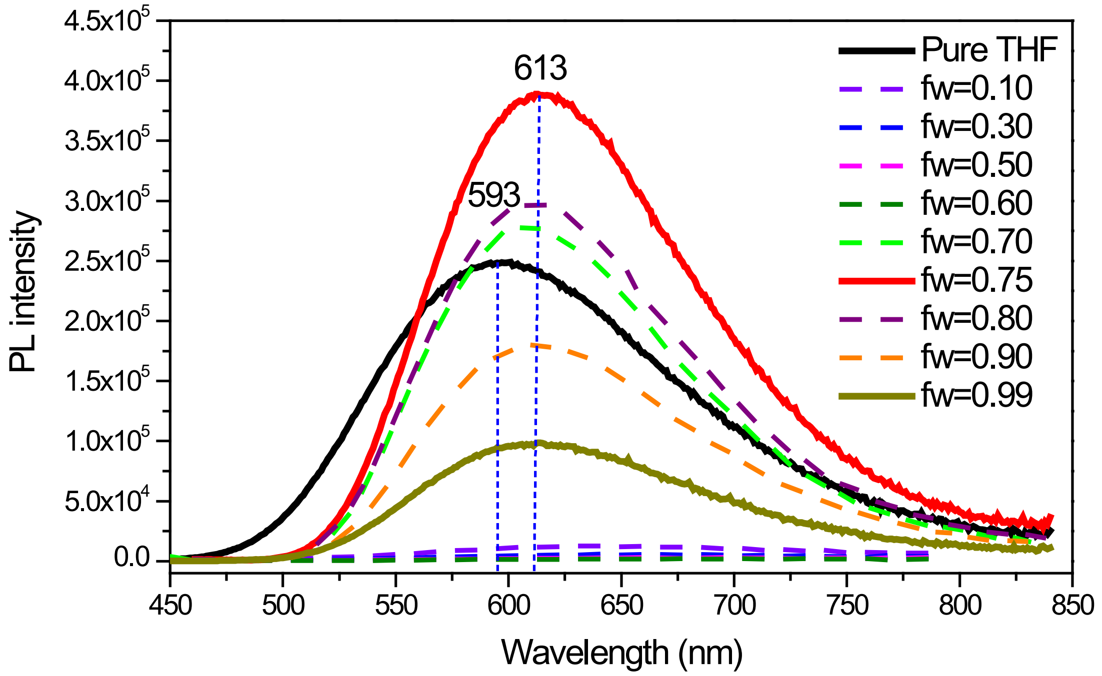

Figure 4-4 Emission sepctra of **M4** in THF/water mixture (1×10^{-5} M, 2/2 nm slits).

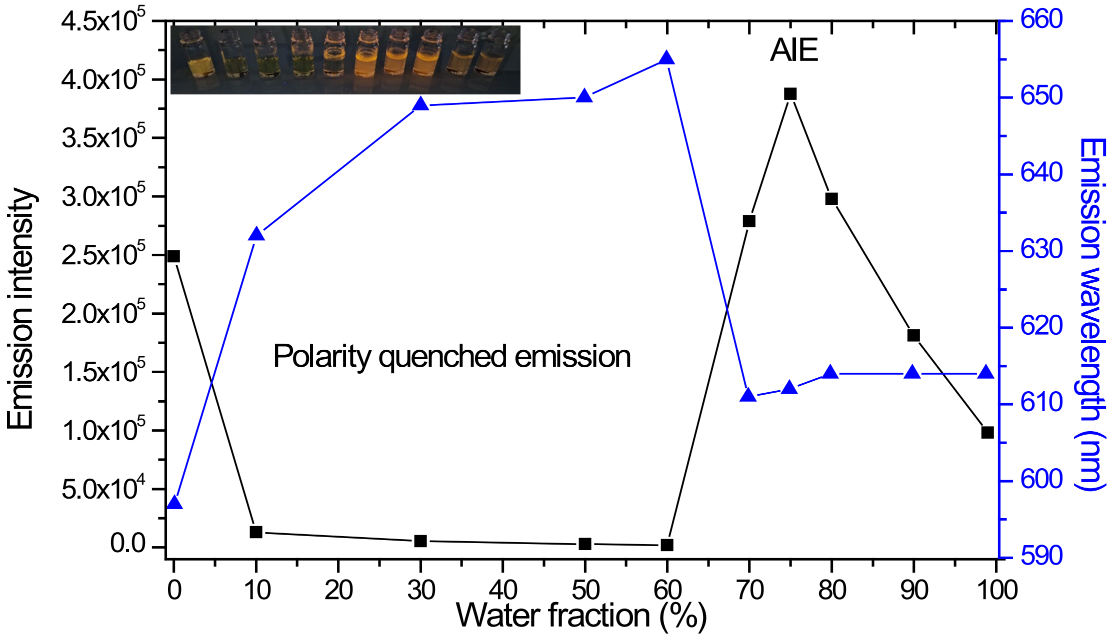

Figure 4-5 Emission wavelength (blue) and intensity of the maximum of **M4** in THF/water mixtrue with different f_w.

As shown in **Figures 4-4** and **4-5**, there is a tendency of first red-shift then blue-shift for the emission wavelength of **M4** in a THF/water mixture with increasing f_w, as observed for **M3**. At the beginning, the increasing f_w in the water/THF mixed solution of **M4** results in a quenching of the PL emission with an obvious red shift of more than 60 nm, owing to the high polarity of water. At the point where the water fraction reaches 70%, the formation of aggregates causes an enhanced emission with a maximum at 610 nm, due to the less polar surrounding inside the aggregates. The emission intensity reaches the maximum for 75% of water. Continuing increasing the water fraction, the emission intensity starts to drop again. The emission (λ_{em}) and excitation (λ_{exc}) wavelength with maximum intensities are summarized in **Table 4-2**.

Table 4-2 Photophysical properties of **M4** in THF/water mixture.

f_w (%)	λ_{exc}(nm)	λ_{em} (nm)	I_{em}	Φ [a]	τ [b] (ns, %)
0	391	593	202894	0.10	0.58 (97.84) 3.39 (2.16)
10	397	632	11142	- [c]	- [c]
30	405	649	5191	- [c]	- [c]
50	410	650	3282	- [c]	- [c]
60	420	655	1957	- [c]	- [c]
70	450	612	166695	- [c]	- [c]
75	454	613	321895	0.30	0.68 (18.09) 2.36 (81.03) 6.63 (0.88)
80	454	613	269650	- [c]	- [c]
90	423	614	173850	- [c]	- [c]
99	423	614	68715	0.05	0.63 (65.09) 1.89 (32.73) 5.45 (2.18)

[a] Photoluminescence quantum yield, with an estimated error ±10%. [b] Fluorescence lifetime. [c]too low to be measured.

To further understand why there is a second quenching of the emission when the water fraction exceeds 80%, the emission spectra over time were recorded for the samples containing 75% and 99% of water, respectively (**Figure 4-6**). With elapse of time, a blue-shift and enhanced emission was found in the 75% water system within the first 10 minutes, a situation that lasted for 10 more minutes. However, in the sample with 99% of water, the position of the emission band does not change. This difference indicates that in the 75% water system, the aggregation is slower, which allow the molecules to steadily assemble in an ordered way to generate crystalline aggregates; while in the 99% water system, M4 may quickly agglomerate in a random way to form less emissive amorphous aggregates[178,179]. After about 1 hour, **M4** started to phase out as an orange-emissive crystal-like precipitate when f_w = 0.75. However, no obvious precipitation was observed when f_w = 0.99, even after several days.

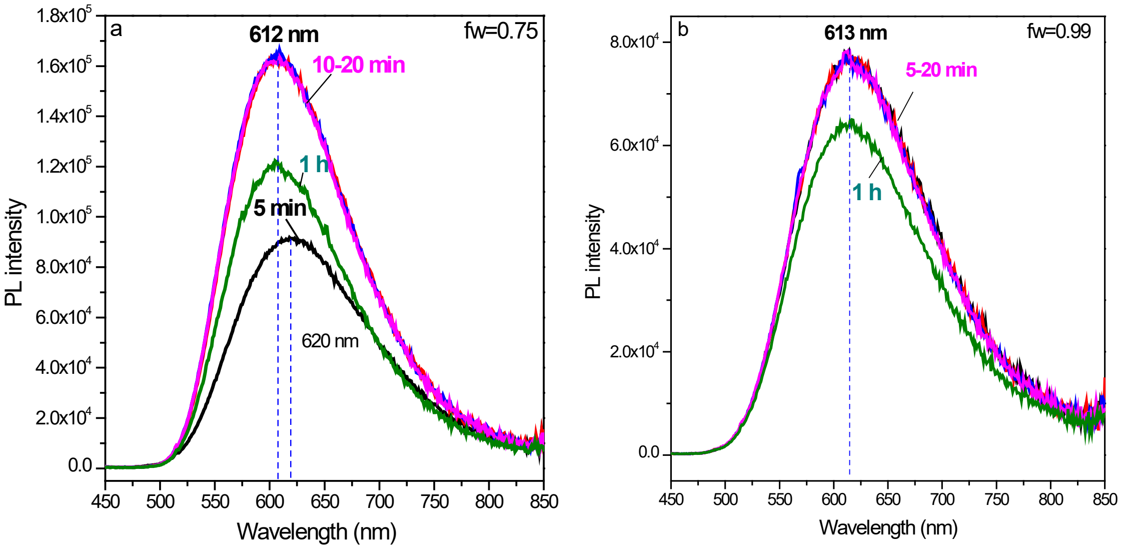

Figure 4-6 Emission spectra of **M4** in THF/water mixtrue with different f_w over time (1×10^{-5} M, 2/2 nm slits).

Dynamic light scattering (DLS) measurements lead to a consistent conclusion about aggregates formation. As shown in **Figure 4-7**, the average particle size in a 75% water system is growing from 771 nm to 893 nm in the initial 10 minutes, while that for the 99% water system remains almost the same (881 nm). The hundreds of nanometer-sized particles proves that the microparticles of **M4** are created in a highly aqueous system. The DLS results not only show the particle sizes of the two samples, but also reveal the growing aggregates in the 75% water system.

The absorption spectra of **M4** in pure THF, 75% and 99% water systems are shown in **Figure 4-8**. The two highly aqueous systems both show red-shifts of the absorption band due to aggregation. A more diffused absorption band appears when f_w = 0.75, which is probably due to the continuous growth of aggregates.

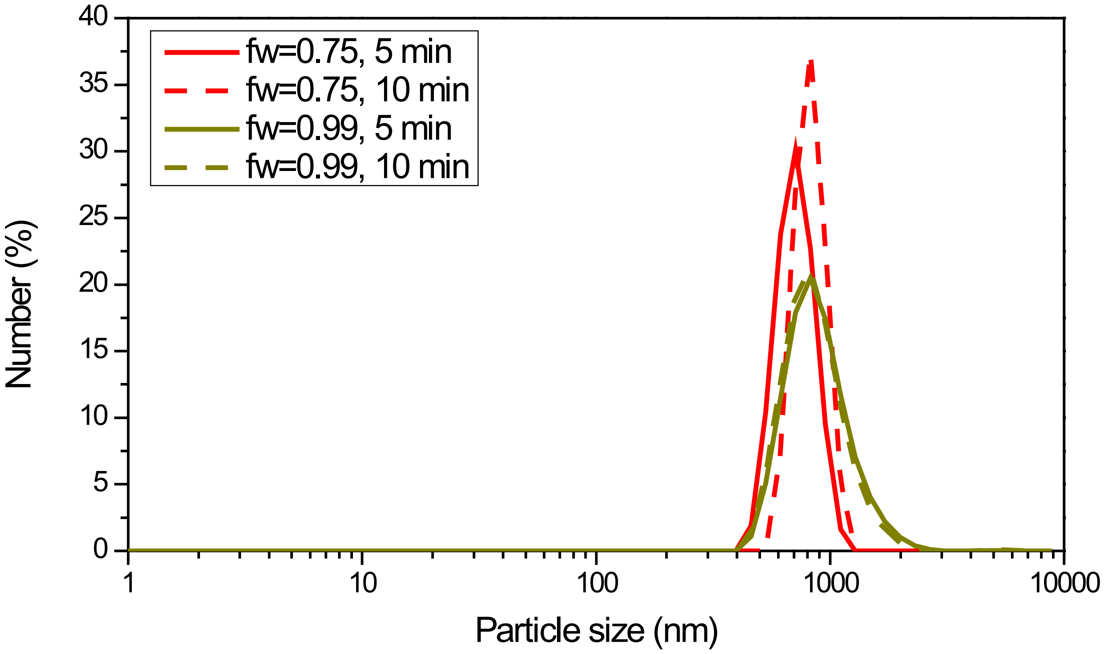

Figure 4-7 Distrubution of particle size of **M4** in THF/water mixtrue with different f_w.

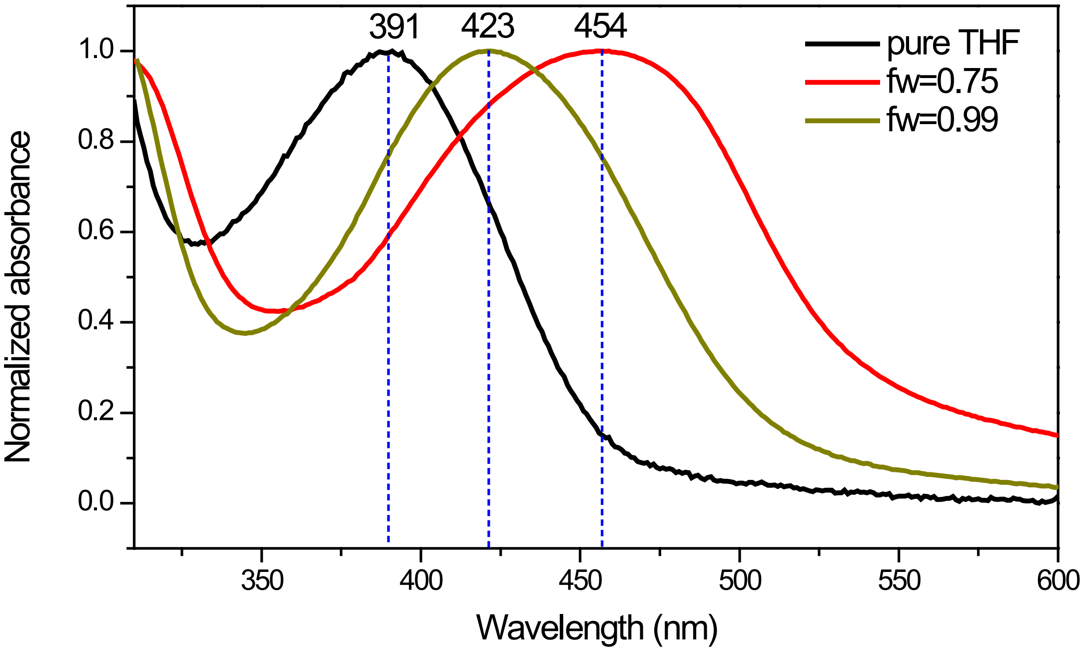

Figure 4-8 Normalized absorption sepctra of **M4** in THF/water mixture with a concentration of 1×10^{-5} M.

At that point, a legitimate question could be asked: why could **M4** form aggregates that are more emissive than isolated molecules in diluted solution, as indicated by the values of the quantum yield reported in **Table 4-2**? In order to answer this question, the lifetimes of the 75% and 99% water systems have been determined and are also listed in **Table 4-2**. As we discussed in the part dedicated to the solvent effect (§ **3.3.1**), concerning **M4**, the longer lifetime is that of the highly-emissive LE state, while the shorter one is that of the less emissive CT state. In the 75% water mixture, the relatively longer lifetime of 2.36 ns dominates with a contribution of 81.03%, indicating that the LE state benefits from aggregation. The longest lifetime of 6.63 ns is provisionally attributed to the aggregates/excimers, but with a tiny proportion (0.88%), indicating that relatively few π-π interactions occur inside the aggregates. The brighter LE states and smaller contribution of excimers than found in **M3** generate a more emissive aggregation state for **M4** in a 75% water system. Meanwhile, in the 99% water system, the shorter lifetime is predominant, showing that the less emissive CT state is the major one. The contribution of the excimer state rises to 2.18%. This explains the fact that the PLQY is obviously lower when $f_w = 0.99$ than that when $f_w = 0.75$.

4.1.3 AIE study on M7

The emission spectra of **M7** in a THF/water mixture with different f_w are shown in **Figure 4-9**. **M7** exhibits a dual emission in THF with an extremely low intensity. When 10% of water is added, the emission intensity is almost annihilated. The emission keeps quenched until f_w reaches 0.70, then the emission intensity recovers the same level of that in pure THF, but the emission band occurs at 620 nm with a loss of the dual-peak shape. Continuing increasing the portion of water up to 90% results in an enhancement of the emission. When $f_w = 99\%$, the emission intensity is 10-fold that of the pure THF solution, although being low with a PLQY of 1.1%.

To explain the change in emission described above, DLS measurements were first carried out. The average size of the particles was determined to be 91.3 nm with a narrow distribution, as shown in **Figure 4-10 a**, which proves the generation of nanoparticles (< 100 nm). Analyzing the correlation curves of the DLS results (**Figure 4-10 b)**, a stiff mono-exponential curves with a sharp slope is found, implying a highly monodisperse aggregation[180]. The curve is smooth at the end without any tails, due to the good stability of the particles without sedimentations. The significant red-shift in the absorption of the 99% water system is also a good indication of aggregation.

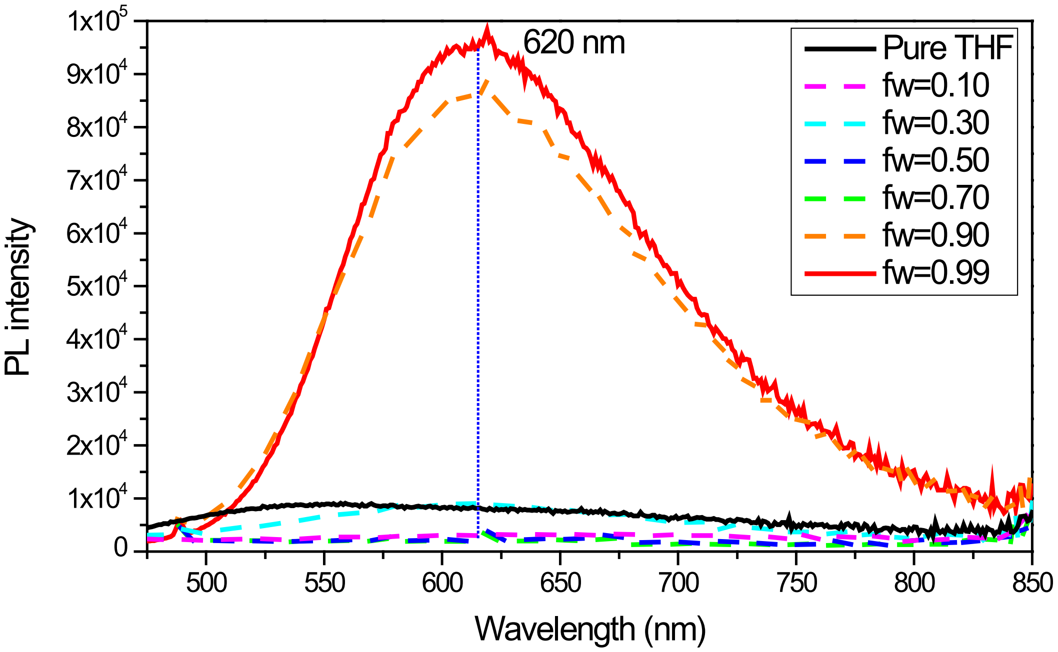

Figure 4-9 Emission sepctra of **M7** in THF/water mixture (1×10^{-5} M, λ_{exc} = 400 nm, 3/3 nm slits).

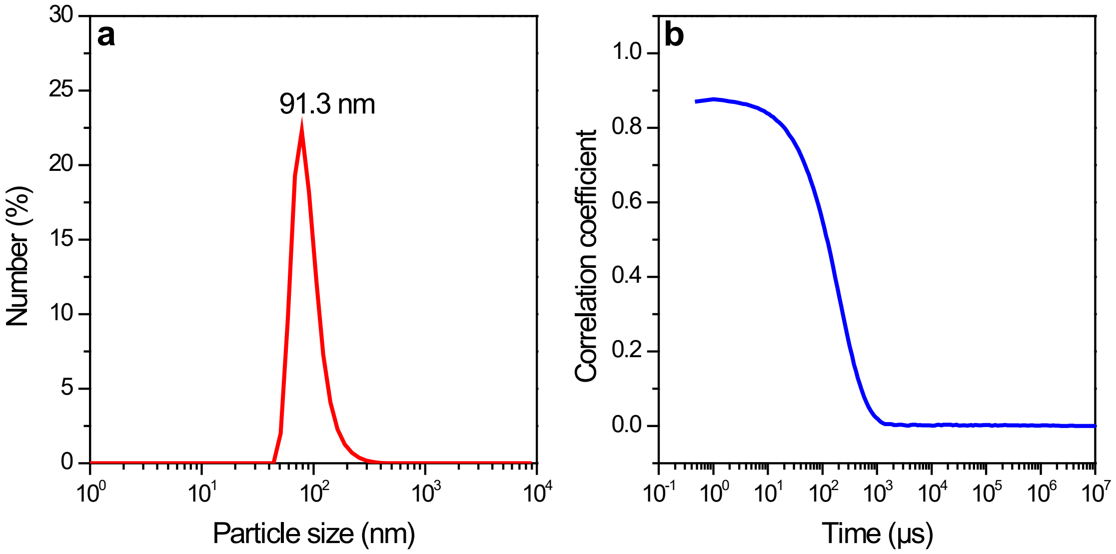

Figure 4-10 DLS spectrum and correlation curves of **M7** in 99% water mixture.

In the aggregation state of **M7**, the molecular motions are expected to be constrained by multiple intermolecular rigidifications due to the insertion of both methoxy and trifluoromethyl groups. As shown in the single crystal structure of **M7** (**Figure 4-12**), it is shown that there are many hydrogen bonds, such as OC-H…F (2.48

Å), Ar-H…O (2.93 Å) and Ar-H…F (2.73 Å), which generate a tight molecular packing[181]. The constrained molecules cannot generate the rotamers as in diluted THF, so the dual-emission is diminished, replaced by a broad emission band. The parallel phenyl planes have a long centroid distance of 5.38 Å, implying that there are no π-π interactions because of the non-cofacial π-planes. The emitting state of the excimer thus may decay radiatively faster, which could be the reason for the improved quantum yield (1.1%).

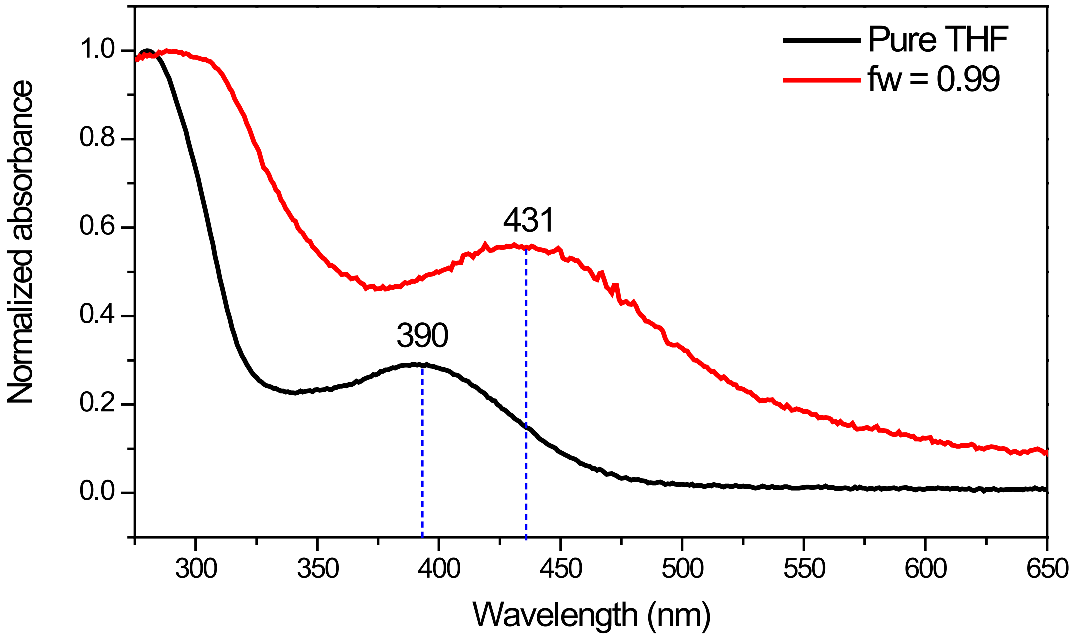

Figure 4-11 Normalized absorption sepctra of **M7** in THF/water mixture with a concentration of 1×10^{-5} M.

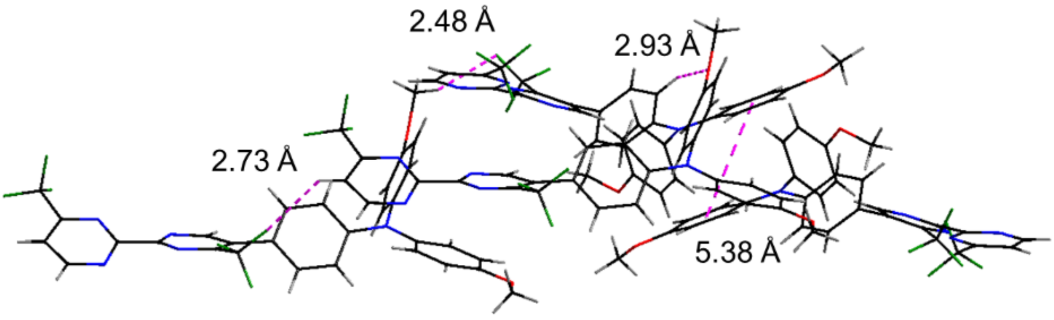

Figure 4-12 Molecular packing of **M7** in a single cystal, black for carbon, blue for nitrogen, red for oxygen, olive for fluorine, and grey for hydrogen.

Table 4-3 Photophysical properties of **M7** in THF/water mixture.

f_w (%)	λ_{abs} (nm)	λ_{em} (nm)	Φ (%) [a]	τ [b] (ns, %)
0	390	542, 660	- [d]	- [d]
70	- [c]	620	- [c]	- [c]
90	- [c]	620	- [c]	- [c]
99	431	620	1.1	0.47 (78.53) 1.57 (19.92) 5.30 (1.55)
Cyclohexane (CH)	400	529	55.0	1.64 (9.87) 5.00 (90.13)
25% $CHCl_3$/CH	- [c]	611	12.0	0.79 (94.44) 3.41 (5.56)

[a] Photoluminescence quantum yield, with an estimated error ±10%. [b] Fluorescence lifetime. [c] not measured. [d] too low to be measured.

Measurements of the lifetimes were also performed to understand more deeply the excited states in the aggregates. As shown in **Table 4-3**, the shortest lifetime of the aggregates in the 99% water system is 0.47 ns. Concerning its emission wavelength and PLQY and comparing them to the 25% CHCl3/CH system, it is reasonable to attribute the 0.47-ns species to the ICT state rather than the TICT states, as we have discussed in **§3.3.3**. It is the most important emitting state (contributes the 78.53% of the emission at 611 nm) and improves the PLQY relating to the pure THF solution. However, it is difficult to assign the other two lifetimes to whether LE or excimer states.

There was no observable precipitation after 2 days in the 99% water mixture and the emission remained constant. The aggregates identified above may thus have a good stability, which is probably due to the special structure of the molecule: the hydrophilic methoxy groups are positioned on one side of the molecule, while the hydrophobic trifluoromethyl groups point to the other side. These aggregates could have an inside part rich of π-electrons, while the outer part is polar thanks to the presence of the methoxy groups. The latter play a central role in the stabilization of the aggregates in water, and the aggregates could thus be viewed as micelles.

4.2 Solid-state photophysical studies

Now that some understandings on the behavior of these fluorophores in aggregates have been done from the previous discussion, we will focus in this section on their photophysical properties in the solid state, including powders and films.

4.2.1 PL properties of the powders

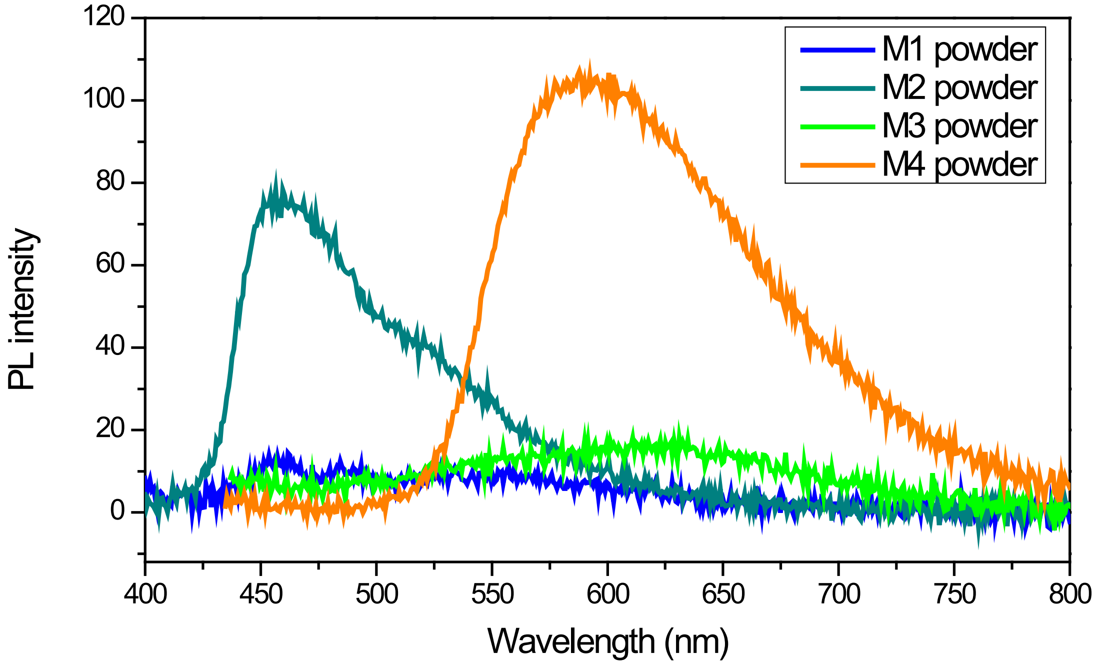

Figure 4-13 Emission spectra of the powders of **M1-M4**.

Table 4-4 Summary of the photophysical properties of powders of **M1-M4**.

Molecule	λ_{pow} (nm)	Φ_{pow} ^{a} (%)
M1	460, 550	6.7
M2	460, 525	10.7
M3	520, 605	4.4
M4	595	27.2

^{a} Photoluminescence quantum yield, with an estimated error ±10%.

The emission spectra of the powders of **M1-M4** were recorded and are shown in **Figure 4-13**. They all show a broad emission with shoulders. More concentrated distribution of fluorophores in powders can lead to stronger intermolecular interactions and, then, more probability to form excimers. Notably, the powders of **M2** and **M4** show distinctively higher PLQY, possibly due to the packing of these two compounds. In fact, these two powders are made of single crystals, as they were obtained after recrystallization, while samples of **M1** and **M3** are microcrystalline powders. As revealed by the X-ray crystal structures, **M1** and **M3** are not entirely planar, the twisted molecular conformation affords a loose molecular arrangement leading to an amorphous solid state. Some groups like phenyl and carbazole may still have the freedom to rotate or vibrate to some extent, then the emission may be partially quenched. In crystals, there are many weak non-covalent bonds between neighboring molecules that can help to further rigidify a molecular conformation and arrange the molecules in an ordered way. The ordered arrangements of the molecules could block molecular motion and prevent non-radiative decay, resulting in an improved PL performance[173]. Meanwhile, the moderately twisted conformations can avoid the formation of π stacks and consequent quenching by aggregation. This can be related to a phenomenon called the crystallization-induced emission enhancement (CIEE), reported in a few cases[112,179,182]. CIEE molecules with an ordered molecular packing and enhanced emissive performance are expected to possibly be used in optoelectronic devices[183,184]. More studies on the photophysical properties of the single crystals of our compounds should be done in the future and could not be performed in this work due to lack of time. For instance, **M4** have different molecular conformations and packings in the crystals obtained from THF and DCM solutions. Studying on their PL performances could reveal the direct structure-property relationship[185,186].

4.2.2 Photophysical properties of the doped films

Firstly, the absorption and emission spectra and the CIE coordinates as well as the lifetimes of each film with 10wt% of luminophores doped into PMMA made from 10 g/L of DCM solutions by spin-coating are presented in **Figure 4-14** and commented below. To be noted, there are usually spikes in the emission spectra of these films, but they do not correspond to any transitions. PLQY values obtained with an integration sphere for the films made by the slot-die-coating method with a fixed thickness of 200 μm, as well as the absorptance and the external quantum yield (Φ_{ex}). As defined in **§1.3.3**, PLQY is the ratio of the number of photons emitted by the fluorophores to that absorbed. Absorptance is the ratio of the number of the photons absorbed by fluorophores to that of the photons from external source. Φ_{ex} is the ratio of the number of photons emitted by the fluorophores to that from the external source, equal to the value of PLQY times A, representing the conversion efficiency from the external light source to the emitted light. The absorption and emission properties of those films are summarized in **Table 4-4**. The lifetimes are listed in **Table 4-5**.

4.2.2.1 Absorption and emission properties

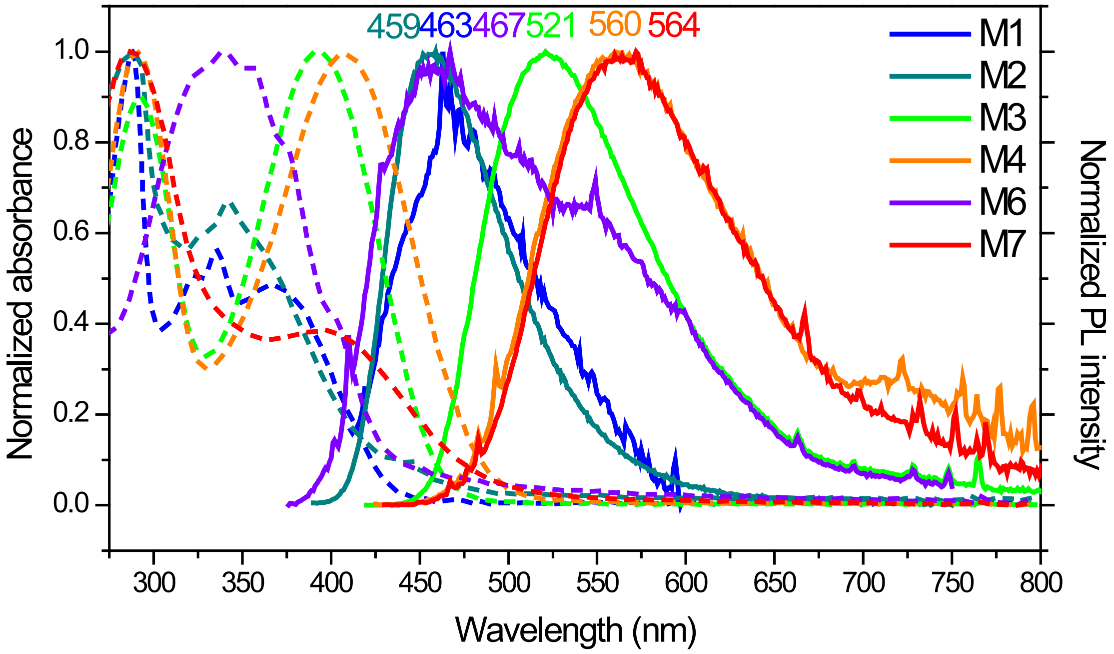

Figure 4-14 Normalized absorption (doted lines) and emission spectra of the 10wt% films of **M1-M4**, **M6** and **M7** doped in PMMA, slit 1/1 nm.

The emission spectra are not perfectly following Gaussian distributions. They all have tails in the long-wavelength area, which is likely owing to the formation of excimers, as we observed in AIE tests (**§ 4.1**). Excimers usually show red-shifting and structureless emission band with a lower intensity than the corresponding single molecule[187]. All the samples except **M6** display a blue-shift compared to the chloroform solutions, since the environment is less polar in PMMA films[97,174].

Table 4-4 Summary of absorption and emission properties of **M1-M7** films (10 wt% in PMMA).

Film[a]	λ_{abs} (nm)	λ_{film} (nm)	Φ_{film} [a] (%)	A [c] (%)	Φ_{ex} [c]	CIE coordinates
M1	368	463	- [b]	- [b]	- [b]	(0.227, 0.253)
M2	343	459	35.7	84.6	27.1	(0.158, 0.158)
M3	393	521	45.4	86.8	39.4	(0.313, 0.537)
M4	407	560	82.2	88.2	72.5	(0.427, 0.525)
M6	339	467	- [b]	- [b]	- [b]	(0.251, 0.281)
M7	397	564	- [b]	- [b]	- [b]	(0.430, 0.509)

[a] Photoluminescence quantum yield, with λ_{exc} of 305 nm for **M2** and **M3**, 310 nm for **M4**, an estimated relative error ±10%. [b] Not measured. [c] Measured at the same λ_{exc}.

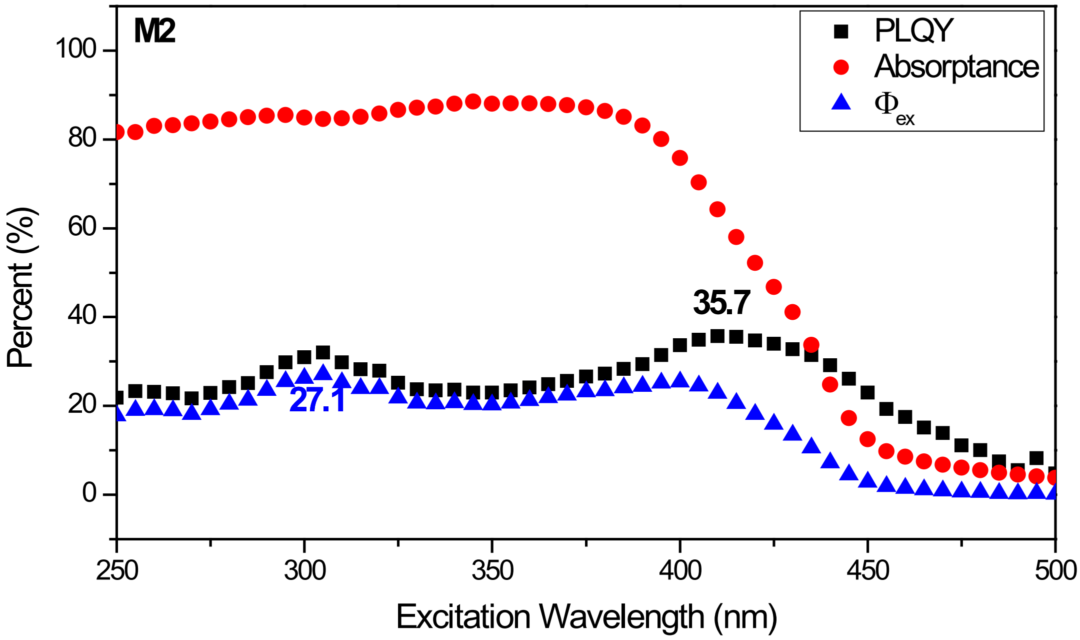

Figure 4-15 Absorptance, PLQY and Φ_{ex} of **M2** depending on the λ_{exc}.

As shown in **Figure 4-14**, all the samples show absorption from near-UV to blue region ranging from 300-450 nm, which is desired for the target application as down-converters of near-UV light. As shown in **Figures 4-15** to **4-17**, **M2**, **M3** and **M4** can absorb more than 80% of photons from an external near-UV source ranging from 300-400 nm. The efficient absorption provides the chance to fully convert the near-UV source into visible light, when applied in the hybrid LEDs. To the best of our knowledge, there are no reports about this parameter for organic down-converters.

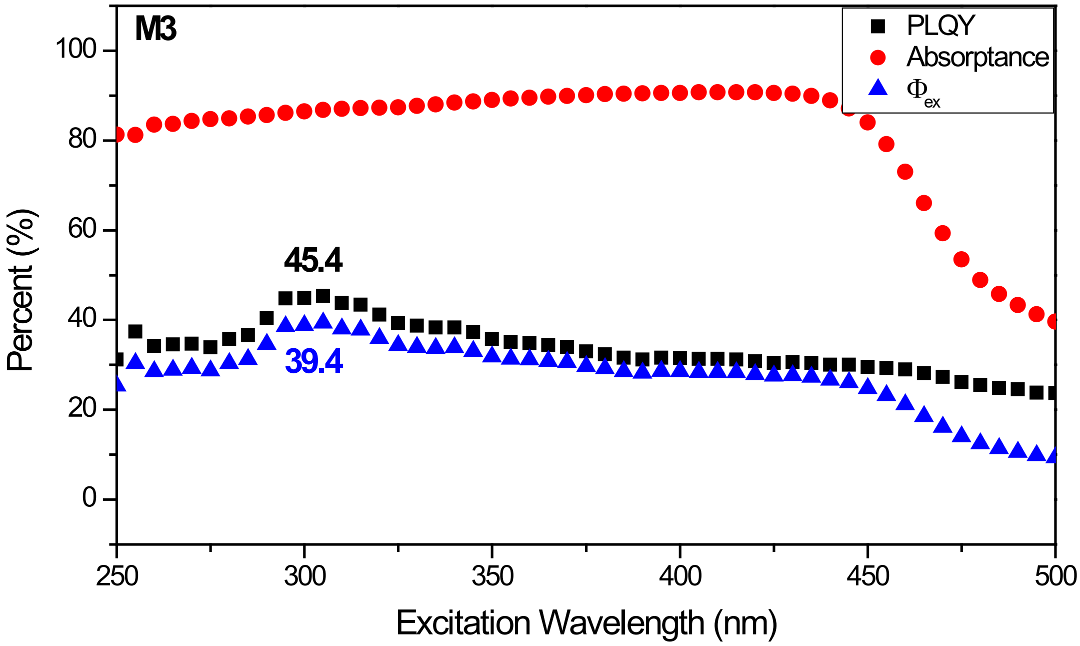

Figure 4-16 Absorptance, PLQY and Φ_{ex} of **M3** depending on the λ_{exc}.

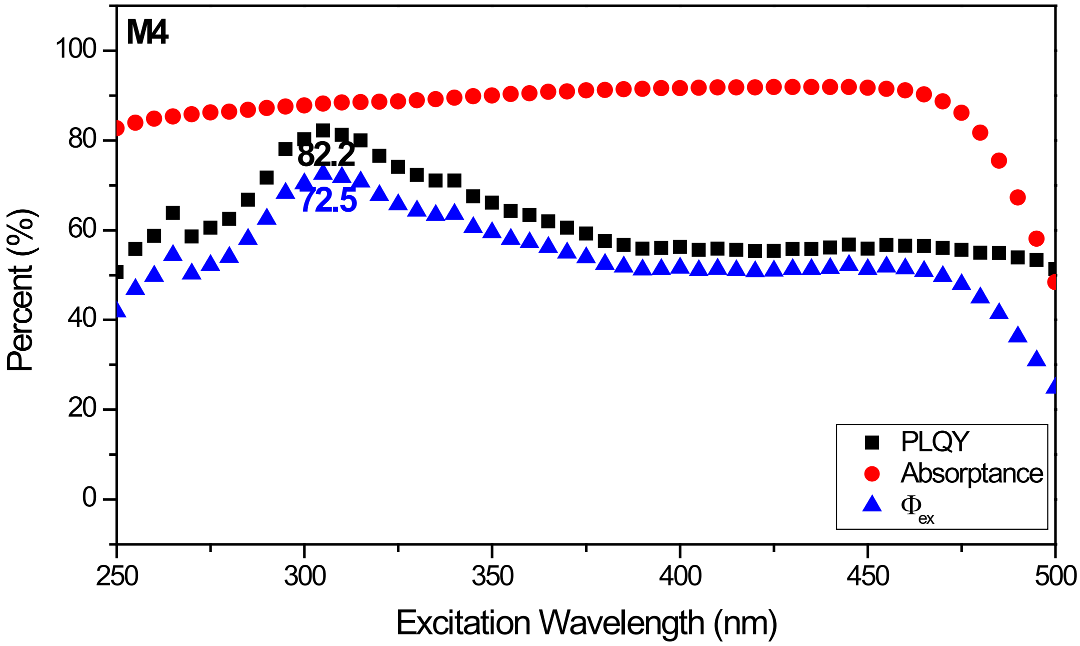

Figure 4-17 Absorptance, PLQY and Φ_{ex} of **M4** depending on the λ_{exc}.

Among these samples, the films of **M1**, **M2** and **M6** are blue-emitting, with maxima located at (0.23, 0.25), (0.16, 0.16) and (0.25, 0.28) in the CIE diagram, respectively. The film of **M2** shows the highest PLQY of 35.7% when excited at 410 nm, but the highest Φ_{ex} appears as 27.1% when it is excited at 305 nm. Unfortunately, we did not analyze the quantum yield of **M1** and **M6** film for the limited experimental condition. M6 is the only one sample showing red-shifted emission comparing to its chloroform solution. As reported, the thiophene/pyrimidine oligomers are expected to have a planar conformation[188], and thiophene usually positions nearly coplanarly with the neighboring aromatic units[189]. Effectively, the absorption spectrum of **M6** shows an additional shoulder in a lower-energy area compared to **M1** and **M2**, which could be a piece of evidence. Herein, **M6** may have a more planar conformation that could cause the presence of stronger π-π stacking and explain its red-shifted emission with the shoulder in the solid-state.

M3 emits in the green region when doped at 10 wt% in PMMA, with a maximum of intensity at 521 nm, the PLQY was measured to be 45.4%. The sample of **M3** shows the highest PLQY and Φ_{ex} at the same excitation wavelength (λ_{exc}) of 305 nm, which are 45.4% and 39.4% respectively. The 10 wt% film of **M4** is yellow-emissive with a maximum of intensity at around 560 nm. **M4** performs the highest PLQY among all the samples when excited at 310 nm, which is 82.2%, with an absorptance of 88.2% and a Φ_{ex} of 72.5%. In other words, 88.2% of the photons from the UV-source are absorbed, and 82.2% of the absorbed photons are converted to emitted photons of **M4**, in total, 72.5% of the photons from the UV-source were converted. These values demonstrate that the film with 10 wt% of **M4** doped in PMMA is the most efficient one to down-convert UV light. Also, it can convert blue light with a considerably good ratio into yellow, which is around 50%, a little less than the reported value of 60%[71]. This points out that we can also use only **M4** as down-convertor to embed with blue inorganic LED to fabricate hybrid WLED. A huge improvement of the emission efficiency is obtained when going from **M3** to **M4.** The only difference in the chemical structure is the presence of two methoxy groups per triarylamine moiety in **M4**. As expected, they enhance the electron-donating ability of the donor units, thus the D-A interaction, leading to a red-shift in both absorption and emission for the film of **M4**. Also, the methoxy groups change the rate of the radiative decay. As illustrated in the discussion about the solvent effect (**§ 3.2.2**), **M3** shows a less emissive LE state than the CT state, while **M4** behaves in the opposite way. In PMMA films, the environment is less polar than in chloroform. The leading excited states for both molecules are the LE states, thus the film of **M4** is highly emissive and shows almost twice the PLQY of **M3**. For the same reason, the emission maximum of **M7** is observed at 564 nm, with a faint red-shift compared to the cyclohexane solution (see **§ 3.2.3)**. The environment for **M7** in PMMA film is more polar than the cyclohexane solution. Literature reports that the effective local dielectric constant for PMMA thin films is in the range of 5.9–8.3[190]. However, the bulky PMMA may block the molecular rotation in excited state and lock the conformation favorable to LE state.

4.2.2.2 Fluorescence lifetimes

In order to have a deeper insight about the emitting species, the fluorescence lifetimes have been measured at the maximum of emission (τ_s) and at the tails (τ_l), and the lifetimes of isolated molecules in diluted solutions (τ_{sol}) are given for comparison (see **Table 4-5**).

Typically, three lifetimes can be extracted from the measurements in 10wt% doped films, corresponding to LE, CT, and excimer states. Indeed, a third species appears in the lifetimes of each solid-state samples, with respect to those of single molecules measured in solution. It is rational to attribute the new lifetimes to the presence of excimers. The values of the lifetime for each excited state are expected to stay the same in τ_s and τ_l but with different contributions. In fact, only for **M4**, these values can be considered the same. Therefore, we will focus on the analysis of the data of **M4** in details afterwards. The general trend is that the average lifetime is getting longer in the longer-wavelength components (**Table 4-5**).

Giving **M4** as an example, the fluorescence decay curves in a 10^{-6} M solution (isolated molecules) and in a 10 wt% doped film in PMMA are shown in **Figure 4-18**. A slower decay can be observed in the film with respect to that in chloroform. For the longer-wavelength tail (λ_{em} = 700 nm), the decay is even slower than that obtained at

560 nm. In chloroform, the lifetime of 1.13 ns corresponds to the CT state, the other one of 2.79 ns stands for the LE state, the leading excited state is the CT state with a contribution of 97.49%. Similarly, for the film of **M4**, at the wavelength of the emission maximum (λ_{film}), the shortest-lifetime (0.56 ns) species should represent the CT state, the 2.42-ns belongs to the LE state and the longest one of 7.22 ns is tentatively attributed to the excimer state. Regarding the contribution of the lifetimes, in the PMMA film, the LE state is the leading species. This proves that the molecular motion is locked in PMMA film: the intermolecular rotation is blocked from the conformation of CT state when it is excited. The contribution of the excimer is as low as 4.07%, indicating that a content of 10wt% of the fluorophores could avoid massive quenching caused by aggregation. In the longer-wavelength shoulder, the short-lifetime (0.56 ns) species disappears, and the contribution of the excimer state increases to 8.13%, pointing out that the tail is a mutual consequence of the CT and excimer states, where the proportion of excimers is increased. The longer wavelength of emission together with the more important contribution of the new excited state point to the formation of excimers.

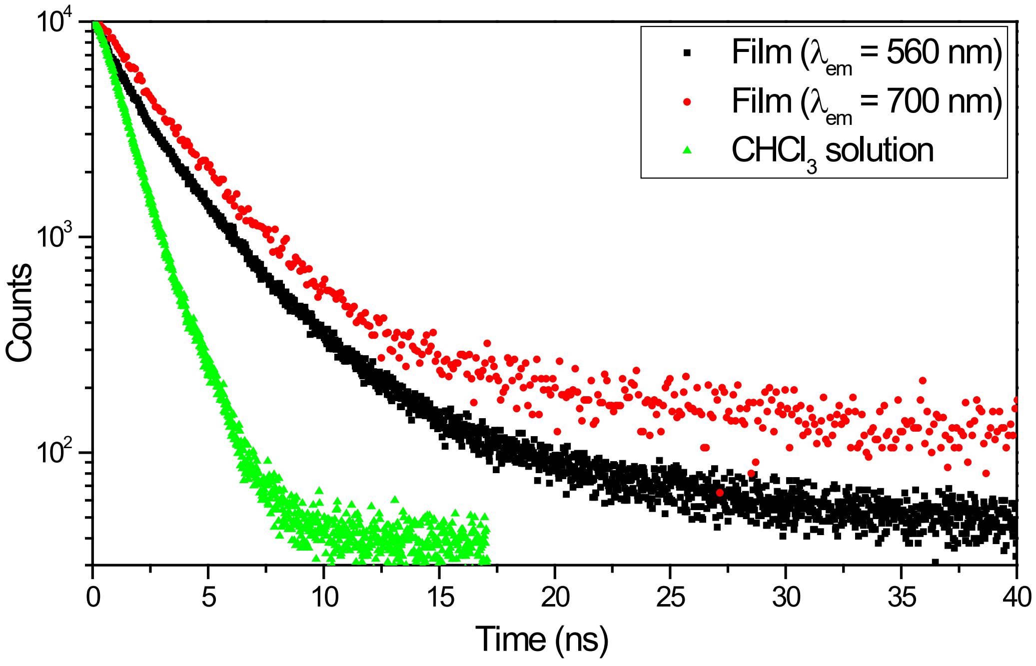

Figure 4-18 Fluorescence deacy curves of **M4** in 10^{-6} M solution and in 10 wt% doped film in PMMA with λ_{em} = 560 and 700 nm, repectively.

Table 4-5 Summary of fluorescence lifetimes of **M1-M7** films [a].

Molecule	τ_{sol} [h] (ns, %)	τ_s [c] (ns, %)	Average τ_s (ns)	τ_l (ns, %)	Average τ_l (ns)
M1	0.11 (77.42) 3.24 (22.58)	0.34 (61.46) 1.37 (30.77) 3.91 (7.77)	0.93	0.53 (49.52) 1.97 (38.09) 5.06 (12.39) [d]	1.64
M2	0.97 (7.70) 3.74 (92.30)	0.36 (63.68) 1.78 (31.93) 5.34 (4.39)	1.03	- [b]	- [b]
M3	2.84 (100)	0.61 (47.48) 2.38 (48.83) 7.52 (3.69)	1.73	2.41 (86.18) 6.37 (13.82) [e]	2.96
M4	1.13 (97.49) 2.79 (2.51)	0.56 (42.23) 2.42 (53.70) 7.22 (4.07)	1.83	2.42 (91.87) 7.36 (8.13) [f]	2.82
M6	0.03 (62.6) 0.44 (37.4)	0.10 (85.33) 0.57 (13.87) 2.14 (0.80)	0.18	0.64 (58.03) 6.17 (41.97) [g]	2.96
M7	1.64 (9.87) 5.00 (90.13) [h]	0.66 (13.75) 2.19 (52.36) 4.86 (20.23)	2.22	1.29 (34.89) 2.90 (56.81) 13.31 (8.30) [f]	3.20

[a] 10 wt% films doped in PMMA, made from 10 g/L of DCM solutions by spin-coating. [b] Not measured. [c] Measured at $\lambda_{film.}$ [d] Measured at 515 nm. [e] Measured at 610 nm. [f] Measured at 700 nm. [g] Measured at 600 nm. [h] lifetimes in 1×10^{-6} M chloroform solutions, except for **M7** which was measured in cyclohexane.

4.2.3 Tuning the PL properties of the films

In this section, we will focus on the possibility to tune the PL properties of **M4** in films, especially the emission color and PLQY, since the previous studies have shown it to be the most efficient fluorophore.

4.2.3.1 Tuned by different coating methods

Firstly, the way to fabricate the films importantly influences the emission color. If the emission spectra of drop-casted, spin-coated and slot-die-coated films (both contain 10wt% of **M4** doped in PMMA) are put together (in **Figure 4-19**), we can see a narrower and more symmetric emission band without the tail for the slot-die-coated film compared to the films obtained from the two other methods. This implies a better dispersion of the fluorophore that yields a more homogenous blend in the slot-die-coated film, and avoid or minimize the formation of excimers. Another reason for the narrow and symmetric band observed in the case of the slot-die-coated film could be the different thermal history, as the films were prepared on a hot plate at 60 °C. The extra thermal energy may help the molecules to disperse more evenly, resulting in the elimination of any emission shoulder due to the presence of intermolecular interactions. Meanwhile, the drop-casting and spin-coating processes were performed at room temperature. As it was illustrated previously, 10 wt% is not enough to generate massive excimers, thus emission is mostly due to single molecules. The drop-casting film shows the most red-shifted emission.

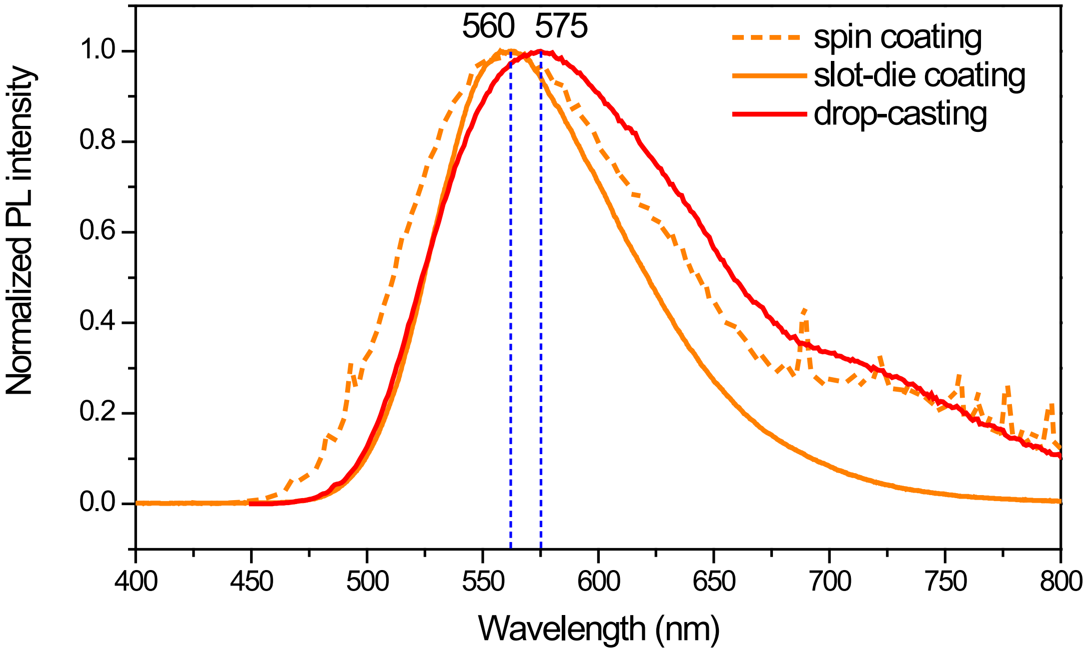

Figure 4-19 Emission spectra of drop-casted, spin-coated, and slot-die-coated films of **M4** (10 wt% in PMMA, $\lambda_{exc} = 400$ nm) from 10 g/L DCM solutions.

4.2.3.2 Tuned by different doping rates/quantities

Inspired by the different emission of pure powders and PMMA-doped deposits, the influence of the doping rate of **M4** in the PMMA matrix on the photophysical properties of the the resulting films has been evaluated. Therefore, 200-µm-thick films with 10, 25, 50, 75wt% of **M4** doped in PMMA were prepared with the slot-die coating method. Their absorptance and quantum yield were measured with an integrating sphere with different excitation wavelengths. The correlations between Φ_{ex} and excited wavelengths are shown in **Figure 4-20**. For all the samples, the highest Φ_{ex} is obtained upon excitation at wavelengths in the range 300-330 nm. Therefore, the emission spectra of all the films were recorded with a λ_{exc} of 310 nm. They are shown in **Figure 4-21**. The photophysical properties of the films are listed in **Table 4-6**.

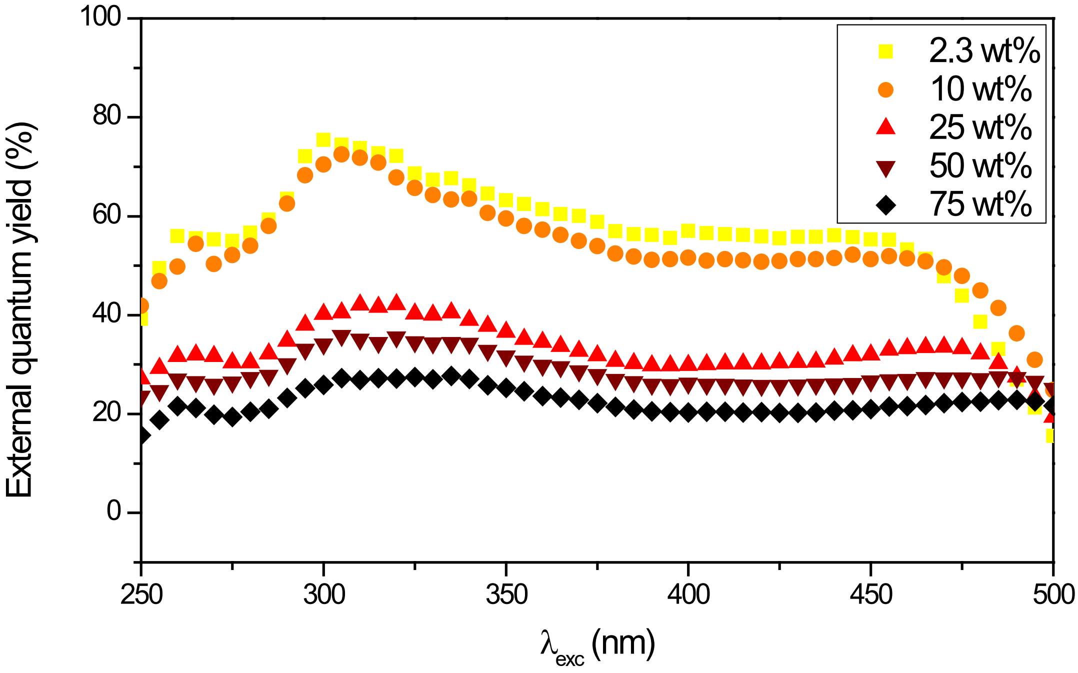

Figure 4-20 Correlations external quantum yield and excitation wavelength of slot-die-coating films of **M4** (2.3, 10, 25, 50, 75 wt% doped in PMMA and neat film).

The emission spectra show a bathochromic shift with the increase in the content of the fluorophore. The maximum fluorescence wavelengths vary from 533 nm to 578 nm only by changing the doping rate. The CIE coordinates are adjusted from (0.39, 0.58) to (0.50, 0.48). However, both the internal and external quantum yields drop when the content of **M4** increases, as formation of excimers is more probable. This phenomenon is identical with the previous description about the effect of the excimers.

From 2.3 to 10 wt%, the emission shifts from 533 nm to 560 nm with a tiny loss of PLQY and a similar external quantum yield. This is due to a low content of excimers in both doping rates. It is also due to the improved absorption when the deposit contains a biggest quantity of fluorophore. The quantum yield decreases dramatically when the portion of **M4** exceeds 25%, while the absorption remains similar until the portion of **M4** is over 75%.

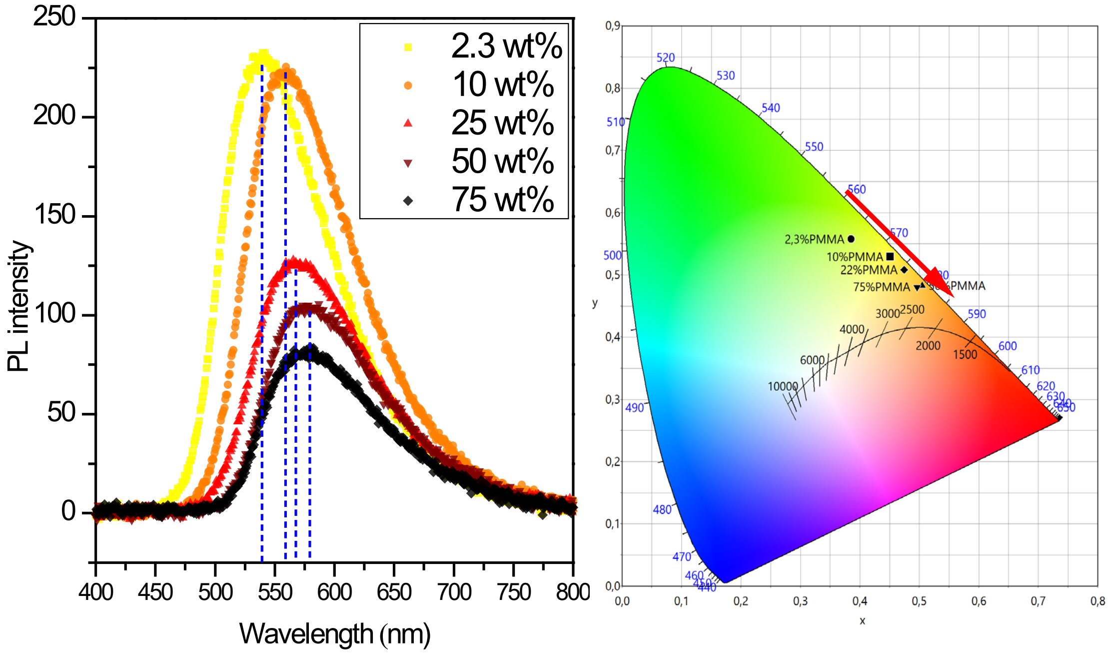

Figure 4-21 Emission spectra of slot-die-coating films of **M4** (2.3, 10, 25, 50, 75 wt% doped in PMMA and neat film, λ_{exc} = 315 nm), recorded by integrating sphere.

Table 4-6 Summary of the photophysical properties of **M4** films with different doping rate.

Portion of **M4** (wt %)	λ_{em}(nm)	Φ [a] (%)	A (%) [b]	Φ_{ex} (%) [c]	CIE coord.
2.3	533	89.0	82.9	73.8	(0.386, 0.578)
10	560	82.2	88.2	72.5	(0.451, 0.530)
25	571	48.4	87.0	42.1	(0.474, 0.508)
50	578	40.5	86.9	35.1	(0.505, 0.483)
75	578	37.7	71.3	26.9	(0.496, 0.481)

[a] Photoluminescence quantum yield, λ_{exc} = 315 nm, with an estimated error ±10%. [b] Absorptance, λ_{exc} = 315 nm, with an estimated error ±10%. [c] External quantum yield, λ_{exc} = 315 nm, with an estimated error ±10%.

Similarly, if more product is deposited, but the doping rate remains the same, the emission also shows a red shift with a loss in emission intensity due the existence of more aggregates/excimers. Three drop-casted films of pure **M4** were made from THF solutions with 100 µL of 2 g/L, 10 g/L and 20 g/L, corresponding to 2.6×10^{-3}, 1.3×10^{-2} and 2.6×10^{-2} mol/L, respectively. In other words, 0.2, 1 and 2 mg (0.26, 1.3 and 2.6 mmol) of fluorophore are deposited on the glass subtract of the same size. As shown in **Figure 4-22**, the emissions are found in the orange-red region. The emission of the sample made from 10 g/L solution can reach the CIE coordinates of (0.59, 0.40). The PLQY of the films deposited from 10 g/L solutions is measured to be 11.6%. The emission intensity undergoes a slight quenching when the concentration rising from 2 g/L to 10g/L, but decreases a lot when the film is deposited from 20 g/L solution.

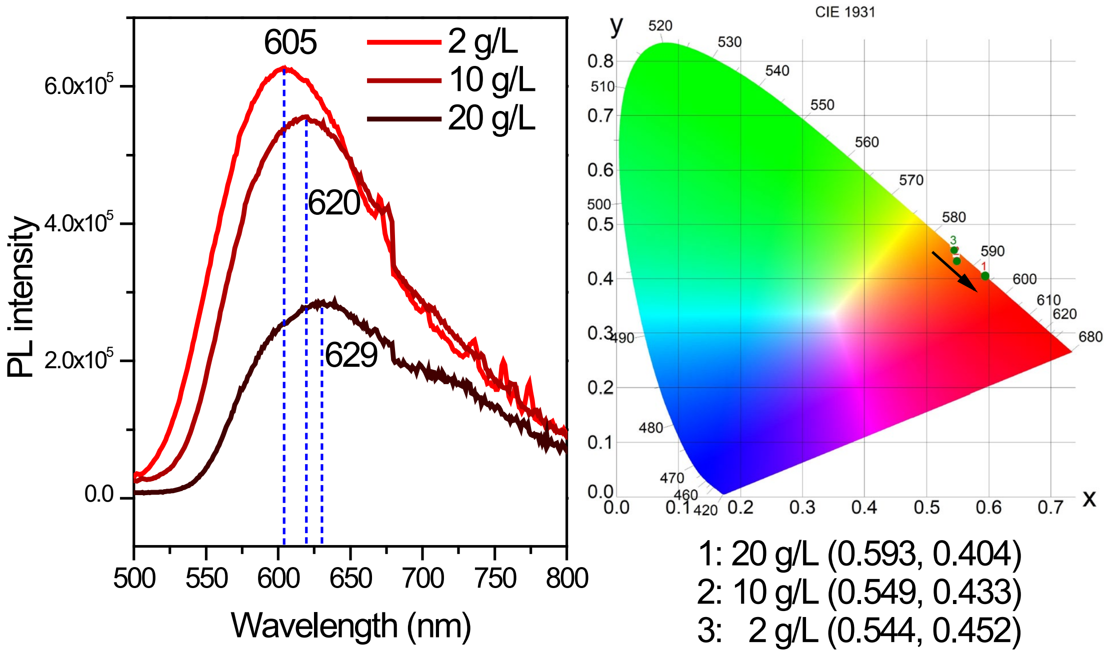

Figure 4-22 Emission spectra of drop-casting films of **M4** comprising 0.2, 1 and 2 mg of fluorophore, deposited from THF solutions, λ_{exc} = 400 nm, slit 1.5/1.5 nm.

4.2.3.2 Tuned by different solvents and annealing methods

The choice of the solvent also affects the PL performance of the corresponding films. As shown in **Figure 4-23**, the spin-coating neat film of **M4** made from THF shows a bathochromic shift and a reduced intensity of emission with respect to that made from DCM. To be noted, the emission intensities of the solid samples strongly rely on quality of the films and orientation of the samples towards the excitation light and detector. The PLQY would be more convincing here to conduct the comparison of their fluorescence efficiencies. However, they were not obtained limited by the experimental conditions. The film made from the DCM solution shows a lower-energy absorption band (**Figure 4-24**). To find an explanation, we look back to the different molecular conformations and packings occurring in crystals obtained from THF and DCM solutions. In DCM, **M4** has a more planar conformation with a small torsion angle between pyrimidines of 5.74°, while the corresponding angle amounts to 25.2° in the crystal obtained from THF. Thus, a better conjugation can be obtained when the deposit is from a DCM solution, leading to a red-shifted absorption.

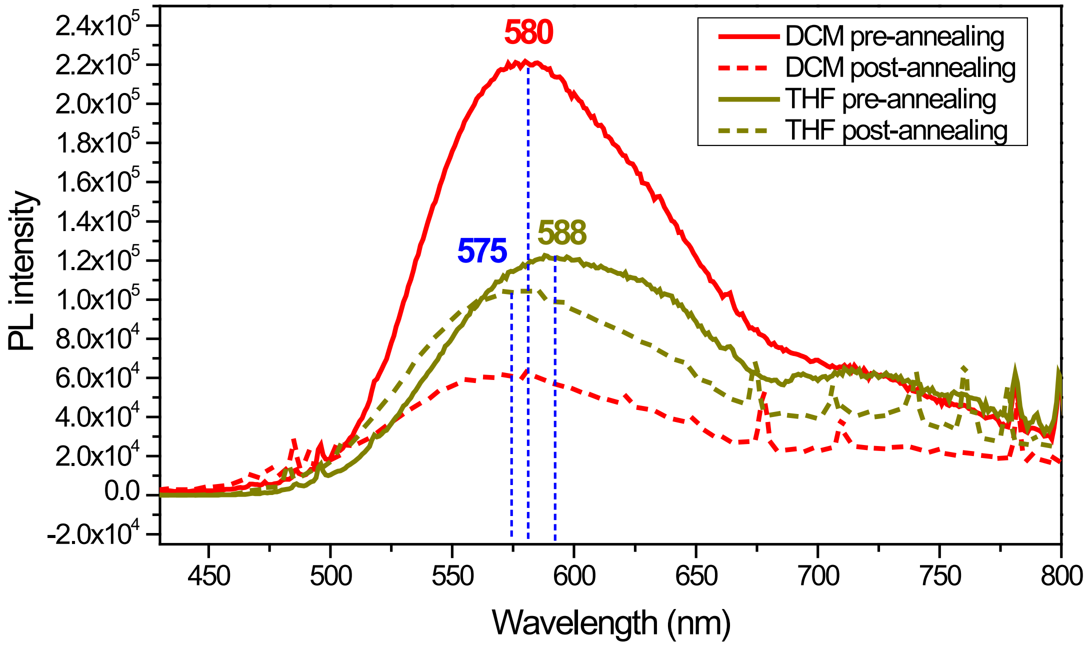

Figure 4-23 Emission spectra of spin-coating neat films of **M4** deposited from 20 g/L DCM and THF solutions, λ_{exc} = 400 nm, slit 1/1 nm.

The molecular packing obtained from DCM is also different from that in THF (see **Figure 4-25**). In DCM, the two corresponding pyrimidine rings from two molecules (pym1 and pym1′) are perfectly parallel with a dihedral angle of 0.0° and the perpendicular distance is 3.48 Å. These two molecules are rigidified by this π-π stacking and CH…π interactions (2.79 Å). However, from the top view, the third molecule shows a shift without any overlap of the aromatic rings, indicating a pattern of dimers. Nevertheless, in THF, there exist π-π stackings between pyrimidines (pym1 and pym1′, dihedral angle of 0.0°, 3.30 Å) on the one hand, and between pyrimidine and phenyl rings (pym2 and ph1′, dihedral angle of 5.86°), on the other hand, which lead to the formation of infinite stacks. Thus, stronger π-π interactions take place in the packing obtained from THF with respect to that obtained from DCM. For this reason, the emission band of the film obtained from THF exhibits a red-shifted emission with very important shoulders.

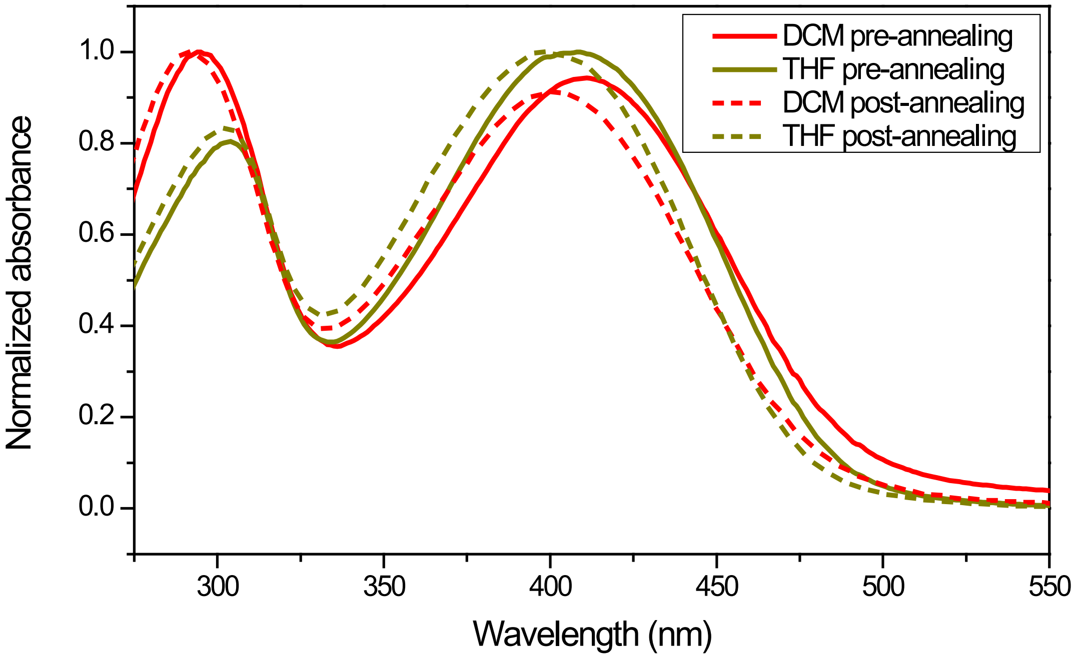

Figure 4-24 Absorption spectra of spin-coating neat films of **M4** deposited from 20 g/L DCM and THF solutions.

Thermal annealing causes a blue-shift of both the absorption and emission for both films. After heating on a hot plate at 120 °C for 3 hours and cooling to room temperature, the emission maximum shifts to 575 nm while the absorption maximum shifts to 409 nm. It is reasonable to believe that the heat gives the energy for molecular motion and changes the different conformation caused by diverse solvents.

In conclusion, in this part, we have discovered several ways to tune the emission properties of **M4** processed in films, including changing the coating method, adjusting doping rates, and playing with the solvent and the concentration. The emission color can be controlled to be in the range from greenish yellow to orange and red.

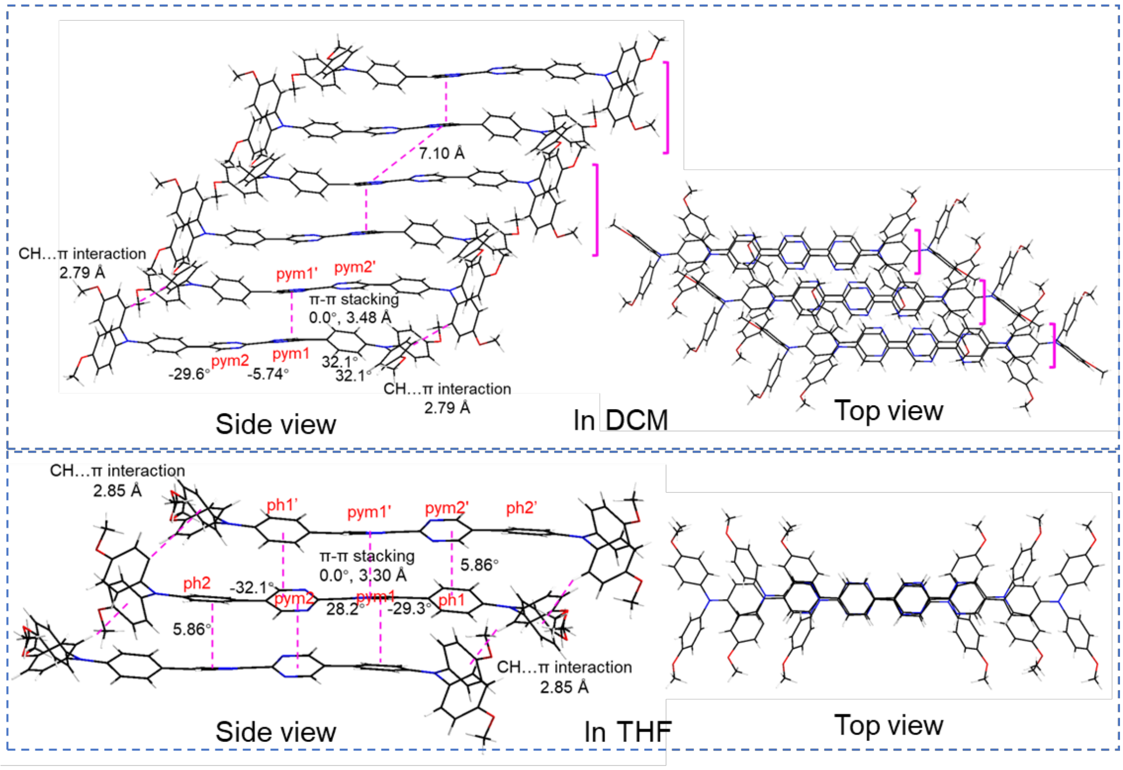

Figure 4-25 Single crystal structures of **M4** in DCM and THF, black for carbon, blue for nitrogen, red for oxygen and grey for hydrogen.

4.3 Photo-stability studies

In order to characterize the stability of the films under continuous UV light exposure, a 375 nm UV LED was covered by films containing the molecules and the corresponding emission spectra were recorded over time. Note that such photostability measurements are relatively rarely reported for samples containing organic emitters[191]. We chose the films made through the slot-die coating method with a fixed thickness of 200 µm, to truly compare the photostability among luminophores **M2**, **M3** and **M4**, as they have shown the best emission efficiencies. These tests were conducted in Université Clermont Auvergne.

By recording the emission spectra of 10 wt% films doped in PMMA comprising different luminophores under a constant UV emitter with an adjustable power (100-300 mW/cm^2) over time and a distance of 37 cm between the sample and the UV source, we analyzed the integration area of each measurement (I) and calculated the ratio relative to the initial area (I/I_0) over the time.

The emission spectra of **M2**-**M4** over the time are shown in **Figure 4-26**, **4-27** and **4-28**, respectively. The films of **M2** and **M3** show dual-peak like emission. With the elapse of the time, the higher-energy parts of the emission (corresponding to emission of the monomers) are quenched more dramatically than the lower energy parts (corresponding to emission of the excimers), indicating a better photostability for the excimers than for isolated molecules of **M2** and **M3**. The intermolecular rigidification may help to stabilize the fluorophores. For M4, it shows a reverse behavior, where the lower-energy part diminishes faster.

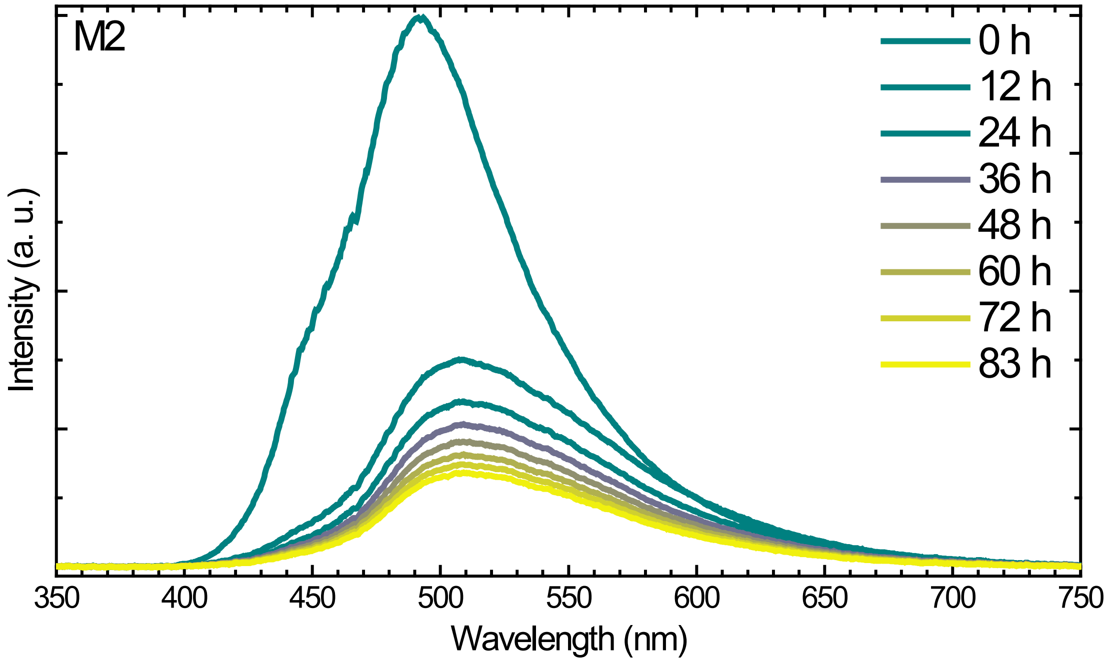

Figure 4-26 Evolution of the emission spectrum of a slot-die coated films of 10 wt% of **M2** in PMMA.

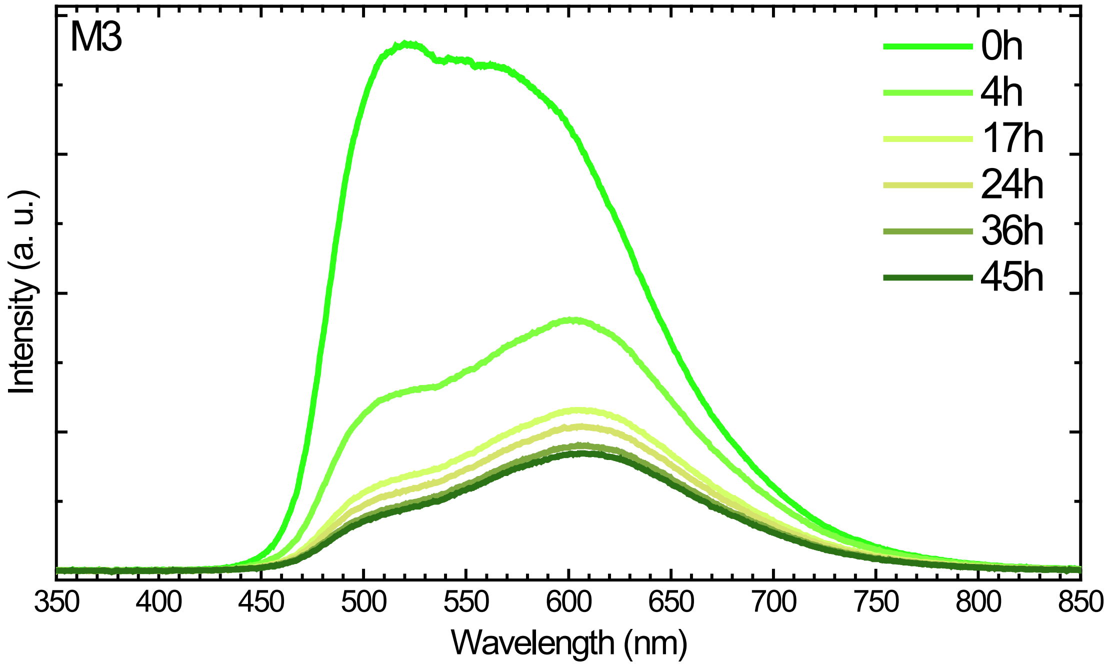

Figure 4-27 Evolution of the emission spectrum of a slot-die coated films of 10 wt% of **M3** doped in PMMA.

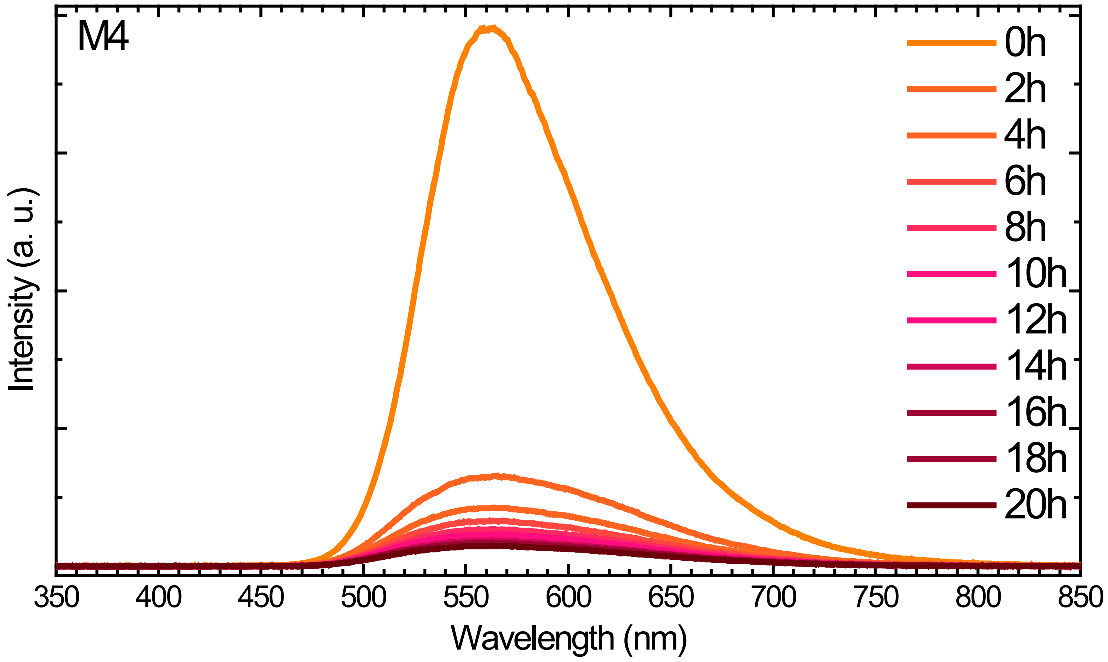

Figure 4-28 Evolution of the emission spectrum of a slot-die coated film, 10 wt% **M4** doped in PMMA.

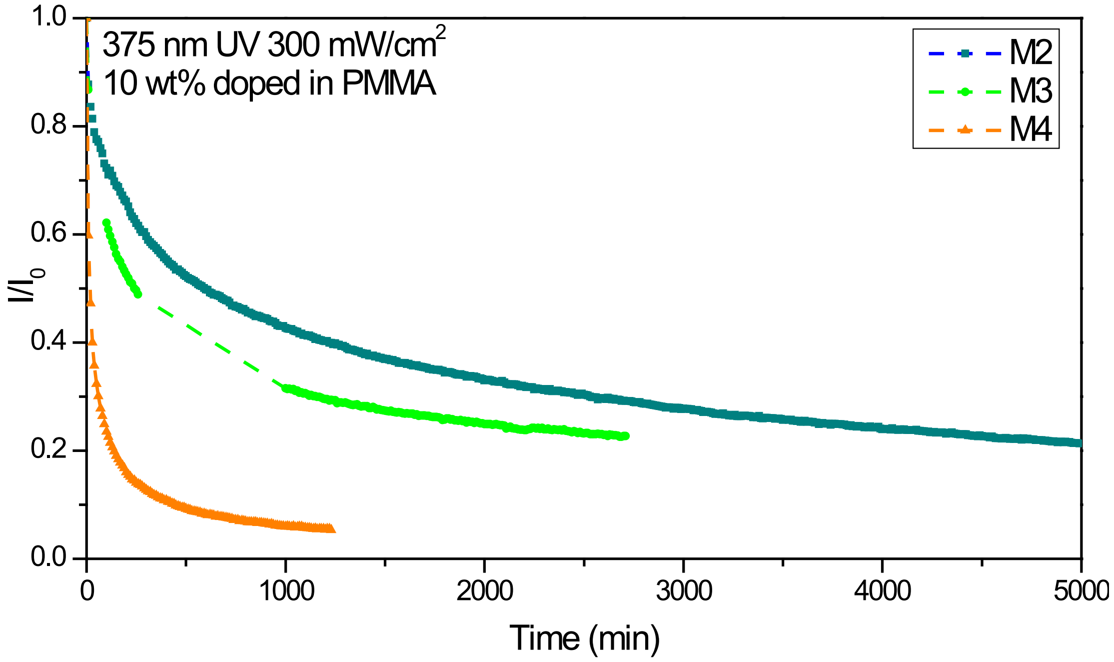

Figure 4-29 Degradation of slot-die coating thin films, 10 wt% **M2-M4** doped in PMMA, under the 375 nm UV source with the power of 300 mW/cm^2.

Based on the I/I_0 analysis, the degradation curves have been plotted to demonstrate the process of emission quenching induced by the UV source. As shown in **Figure 4-29**, the degradation curves go through two main stages: In the starting stage, the emission drops dramatically, following it reaches a plateau. The PL intensity follows an exponential decay. After 2 hours of irradiation with a power of 300 mW/cm^2, the films of **M2** and **M3** have lost about 30% and 40% of the initial emission intensity, respectively, while that of **M4** lost almost 80% of the initial emission intensity. **After** 83 hours (5000 minutes) of irradiation, the film of **M2** shows an intensity at 21% of the initial one. For **M3**, there is 22% of the initial PL intensity remaining after 45 hours (2900 minutes) of continuous exposure. **M4** only emits about 5% of the initial intensity after just 17 hours (1000 minutes). These data indicate that **M2** and **M3** show relatively better photostabilities than **M4** in films doped in PMMA at a rate of 10 wt%.

When the power of the UV source is reduced to the one third (100 mW/cm^2) of the full power, an improvement of the photostability of the film of **M4** is observed (**Figure 4-30**). Indeed, the emission decreased by 80% within 73 hours (4380 minutes) and kept decreasing with a very slow rate. After 167 hours (10000 minutes), there still remains 15% of the initial emission. This indicates a slower degradation of **M4** in less powerful conditions.

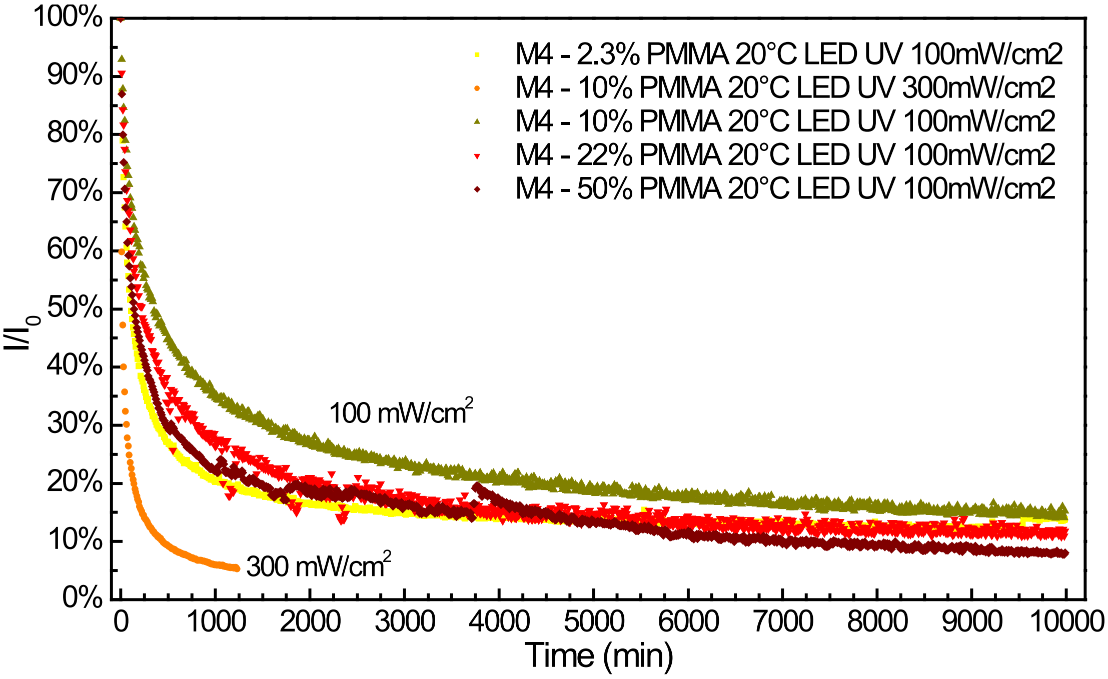

Figure 4-30 Degradation of slot-die coating thin films of **M4** doped in PMMA, with different doping rate, under the 375 nm UV source with the power of 100 or 300 mW/cm^2.

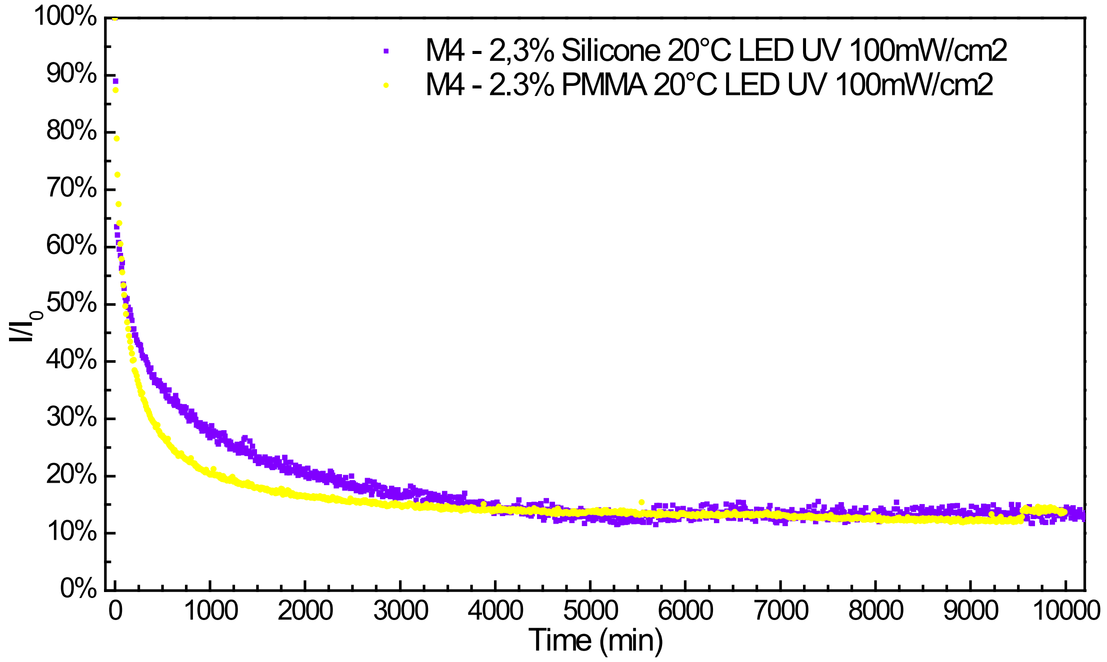

Figure 4-31 Degradation of slot-die coating thin films of 2.3 wt% **M4** doped in PMMA and silicone, under the 375 nm UV source with the power of 100 mW/cm^2.

The degradation rate is also influenced by the doping rate of the film. The deposit with 2.3% of **M4** decomposes faster than the one containing 10% of **M4**. The fewer quantity of fluorophore in the former is the reason. The sample with 10% of fluorophore exhibits the best photo-stability. When the proportion of **M4** exceeds 10%, the photostability starts to decrease again. As we know, the photodegradation of organic compounds in atmosphere is caused by the highly active singlet oxygen upon the absorption of light and consequent hydroxyl radicals[192-194]. The higher concentration of **M4** might increase its chance to contact with the radicals and decompose.

Finally, the PMMA matrix was changed to silicone. The degradation curves are shown in **Figure 4-31**. The initial fast drop of emission is slightly slowed down by the silicone matrix. The emission reaches the final plateau at more than 4000 mins in the silicone film, while the corresponding value is 2000 min in the PMMA film. However, the final plateau occurs at the same value of 13% for the I/I_0 ratio.

4.4 Hybrid white-light-emitting materials

As the final goal of this thesis, we are aiming at investigating the possibility of **M1**-**M7** to convert near-UV light into qualified white light. This was investigated in both solution and solid state. Even though the perfect white light locates at (0.33,0.33) in the CIE diagram, the white region still ranges a big area.

4.4.1 White-light-emitting solution

Considering the emission color and PLQY, the mixture of **M2** and **M4**, and that of **M6** and **M4** appear as the most promising combinations. The observations were first conducted in chloroform solutions with a total concentration of 1×10^{-6} M.

In the combination of **M2** and **M4**, we started with a 1:1 ratio between the two compounds. In this solution, an excess of blue component was found, even though the orange-red component increased when using longer excitation wavelength. For this reason, the portion of **M4** is required to be increased. The solutions **M2**: **M4** = 1: 9 was thus investigated (**Figure 4-32**). The CIE coordinates of the light emitted by this blend after excitation at 375 nm is (0.32, 0.38), which is close to pure white light. The relatively higher Y coordinate is more likely to be due to the green emission from 520 nm to 560 nm shown by both **M2** and **M4**. Therefore, the deep-blue emitting **M6** could reduce the excess of green component when blended with **M4**.

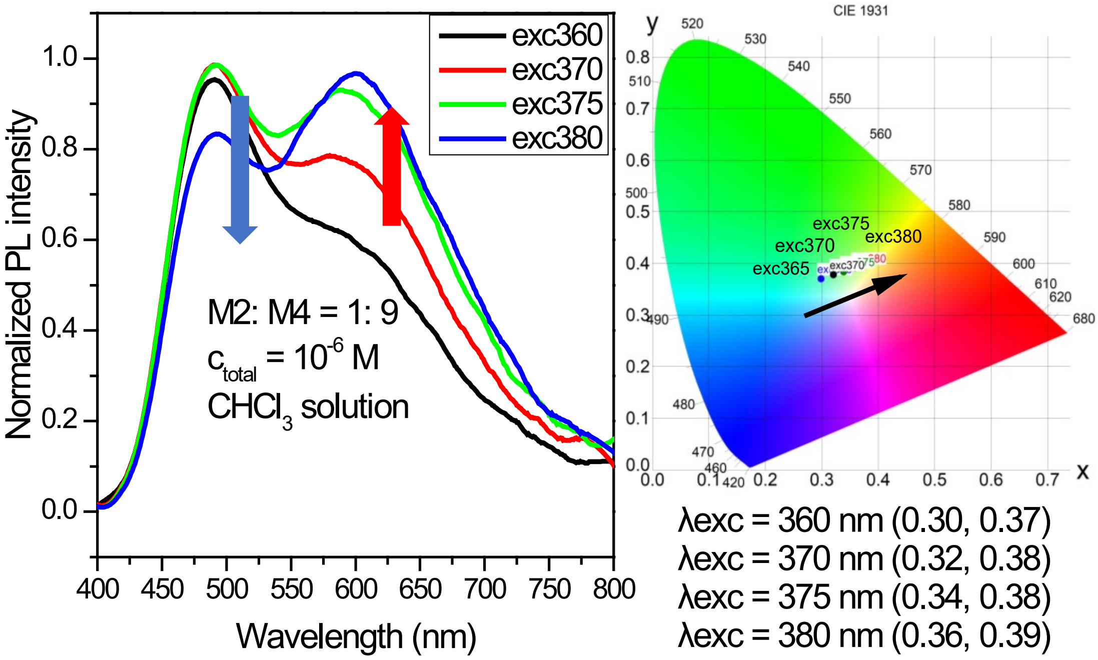

Figure 4-32 Emission spectra and CIE diagram of the mixed $CHCl_3$ solution (**M2**: **M4** = 1: 9, total concentration of 1×10^{-6} M, slit 1/1 nm).

As shown in **Figure 4-33**, the mixture of **M6** and **M4** shows a purple emission due to the lack of green emission. As we expected, the Y coordinate is lowered from 0.38 to 0.29 upon excitation at 375 nm, relatively to the blend of **M2** and **M4**. In this case, an addition of a small amount of green-emitting **M3** could be a good supply to push the emission towards the white center.

Thus, the emission spectrum of the ternary mixture comprising **M6**, **M3** and **M4** (2: 1: 20) in chloroform has been recorded, it is shown in **Figure 4-34**. A warm white light (0.37, 0.34) has been achieved by this formula, showing a good balance between the blue, green and red components. Unfortunately, because of lack of time, no more investigations of this mixture including PLQY was done.

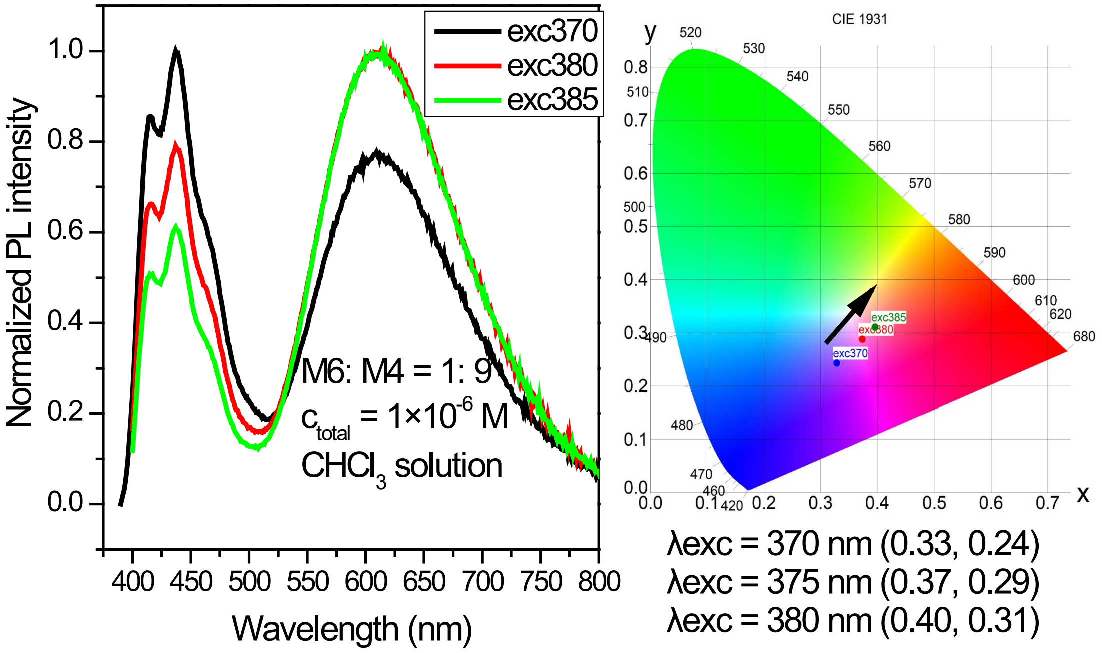

Figure 4-33 Emission spectra and CIE diagram of the mixed CHCl$_3$ solution (**M6**: **M4** = 1: 9, total concentration of 1×10^{-6} M, slit 2/2 nm).

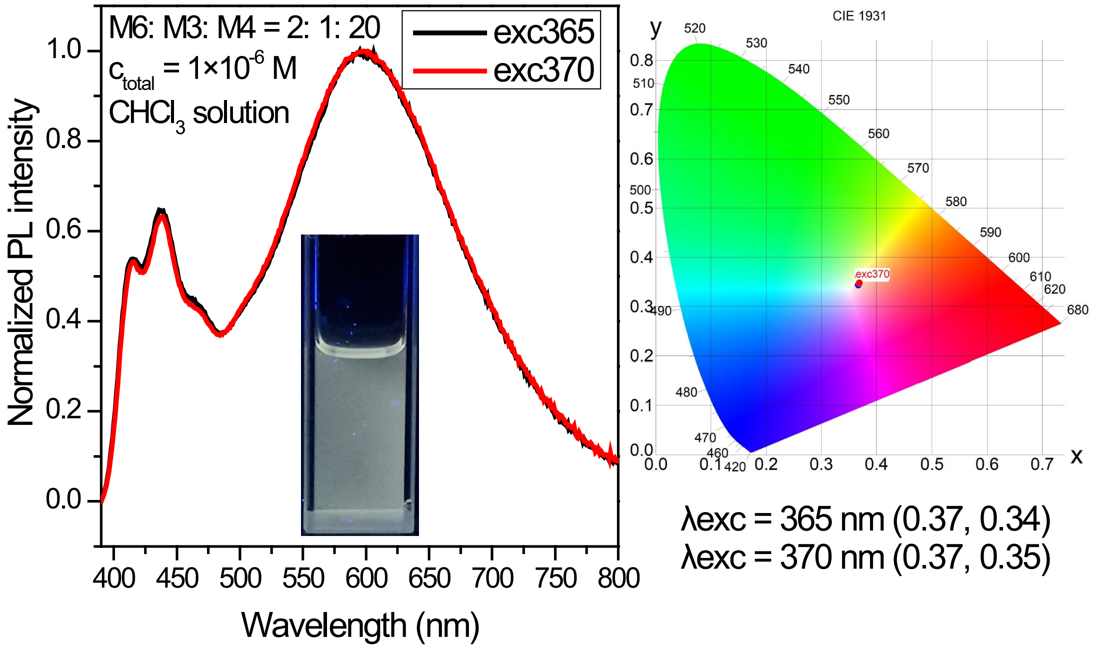

Figure 4-34 Emission spectra and CIE diagram of the mixed CHCl$_3$ solution (**M6**: **M3**: **M4** = 2: 1: 20, total concentration of 1×10^{-6} M, slit 2/2 nm).

4.4.2 White-light-emitting films

As reported in paragraph **4.2.4**, the emission properties of the fluorophores are quite different in films with respect to those in solution. **M4** is more emissive in the solid state than in solution. In solution, much more **M4** is needed in order to achieve white light; in the solid state, it is the opposite trend. In order to investigate the different combinations of fluorophores, we fabricated the non-doped films by spin-coating from the mixed DCM solutions with a concentration of 20 g/L.

As for the choice of the blue-emitter, there are three possible candidates, **M1**, **M2** and **M6**. Due to the poor solubility of **M2**, the desired concentration could not be obtained, which makes it not a good option. Therefore, the combinations of **M1/M4** and **M6/M4** were investigated.

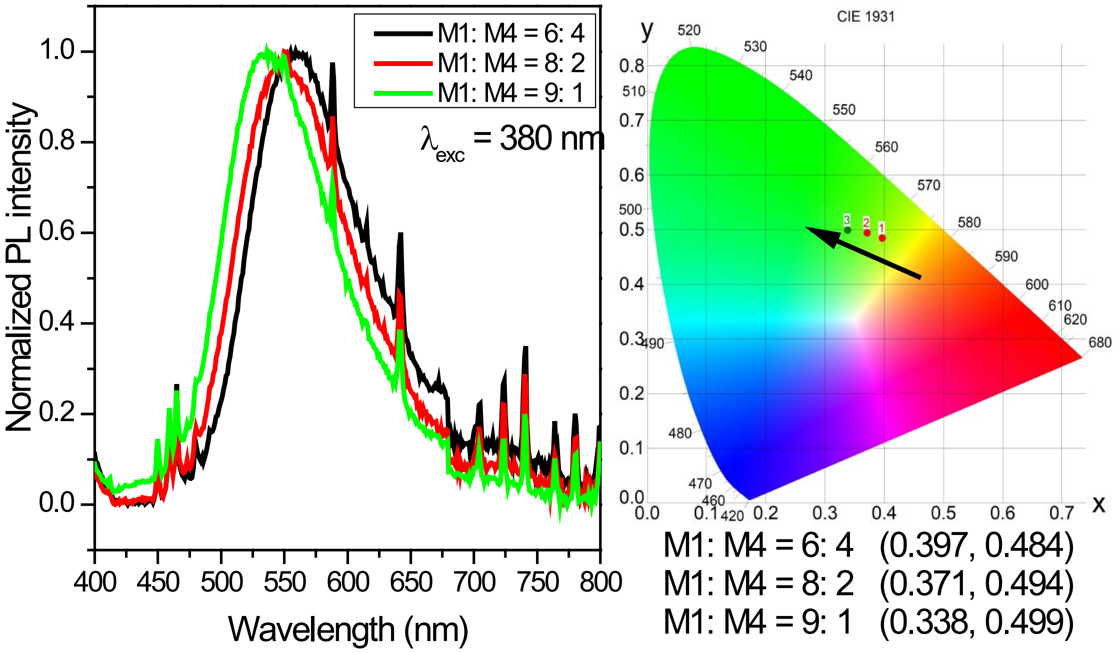

Figure 4-35 Emission spectra and CIE diagram of the mixed films (**M1**: **M4** = 6: 4, 8: 2 and 9: 1, slit 1/1 nm).

Hybrid films of **M1/M4** with different ratios of 6: 4, 8: 2 and 9: 1 were studied, while excited at 380 nm. Their emission spectra and the resulting chromaticity diagrams are shown in **Figure 4-35**. The 6:4 sample shows a yellowish light, due to the high proportion of **M4**. Continuing increasing the portion of **M1**, the emission blue shifts. However, it is difficult to get white light by adding more quantities of blue emitters. The evolving trace can be seen in the CIE diagram. Increasing the portion of **M1** will decrease the concentration of **M4**, leading to a shift of its emission and reduction of the emission in the range of 650-750 nm. Thus, the X coordinate is decreased but the Y coordinate is increased. Meanwhile, due to strong absorption of **M4**, reabsorption of the emission of **M1** can occur in the range of 400-450 nm where there is an overlap between the emission of **M1** and the absorption of **M4**. The same trend is observed in the blend of **M6/M4**.

4.4.3 Hybrid LEDs

As we have not obtained white-emitting films, the strategy we have taken is to cover a blue LED by yellow-emitting **M4**. In particular, as the 10wt% film of **M4** shows high conversion efficiency and the best photostability among the films with different doping rates, it is chosen for covering the blue LED.

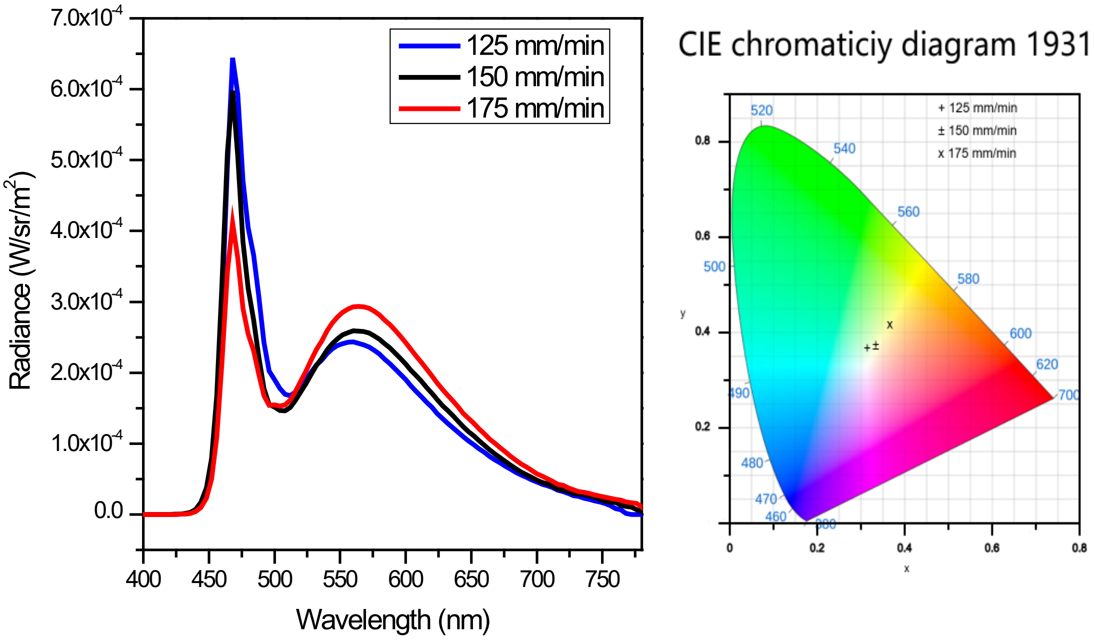

Figure 4-36 EL spectra and CIE diagram of hybrid LEDs.

The blue LED is coated by a dip-coater. We have optimized different withdrawal speeds, 125, 150 and 175 mm/min, to control the thickness of the coating layer and the emission color. Their (electroluminescence) EL spectra and CIE diagram are shown in **Figure 4-36**. With the withdrawal speed increasing, the blue component in the EL spectra decreases and the yellow component increases. The thickness of the coating layer increases with faster withdrawal speed where there is the more viscous drag from the polymeric solution attached on the LED[195]. When the withdrawal speed is set as 150 mm/min, the LED shows a white light with CIE coordinates of (0.334, 0.372) and CCT of 5460 K, which is close to the normal day light (5500K). The LED fabricated with withdrawal speed of 125 mm/min has a blueish emission while the one with 175 mm/min withdrawal speed has a yellowish white emission. The emission properties of these three LEDs are presented in **Table 4-7**. The thickness of the coating layer is measured with the films on glass substrate with exact same parameters. The photos of the bare blue LED and white-emitting covered LED with withdrawing speed of 150 mm/min (on and off) are shown in **Figure 4-38**.

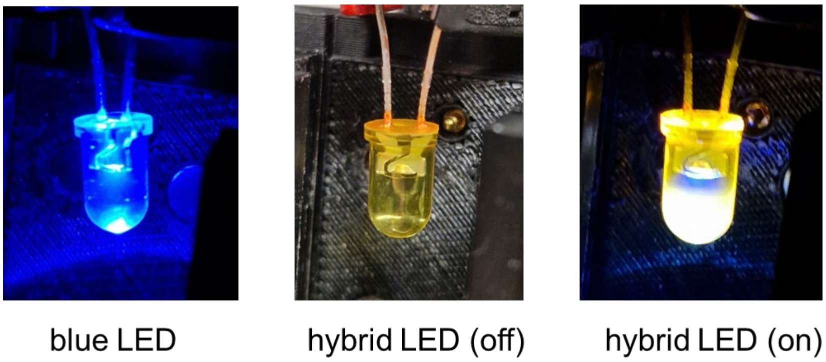

Figure 4-37 Photos of bare blue LED and hybrid LEDs.

Table 4-7 Emission properties of hybrid LEDs based on **M4**

Withdrawal speed (mm/min)	CCT (K)	CIE coord.	Thickness [a] (nm)
125	6236	(0.314, 0.367)	974
150	5461	(0.334, 0.372)	2225
175	4566	(0.367, 0.416)	2417

[a] Thickness of the double-face coated film on glass substrate, measured with profoliometer.

The lifespan of the device has also been investigated. The decay curve of the hybrid LED is presented in **Figure 4-38**. The LED stays on continuously the its EL spectra were recorded at each time. The relative emission intensity of the 560 nm band is calculated and plotted over time, showing an exponential-like decay. In 4 hours, the emission intensity at 560 nm decreases around 10%. After 237 hours, there is still 27% of the initial intensity.

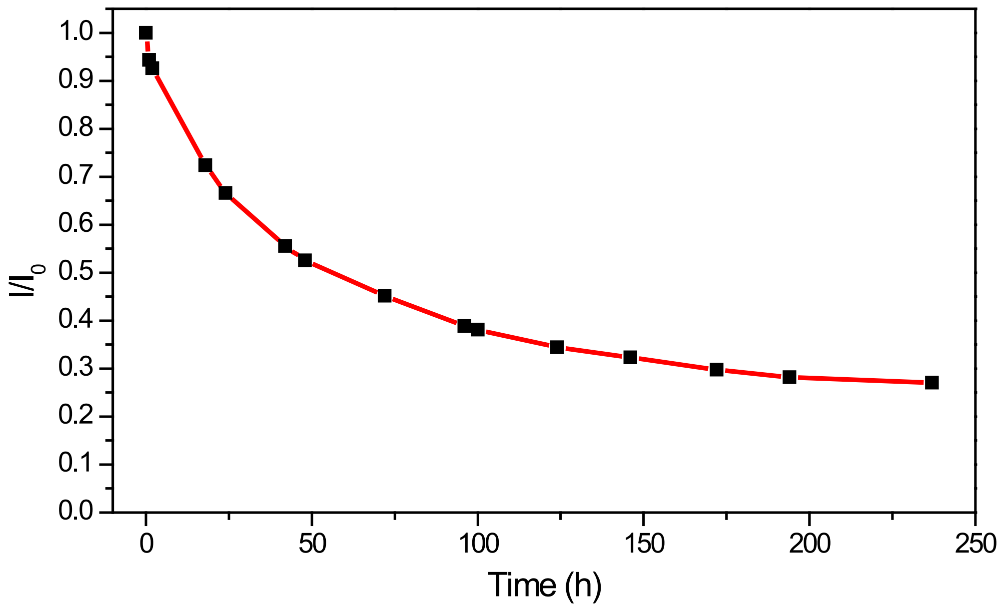

Figure 4-38 Decay curve of the hybrid LED.

4.5 Conclusion

In this chapter, we have investigated the photophysical properties of solid-state samples (aggregates in suspension, thin films and powders), which are very important towards real applications as fluorophores in hybrid WLEDs.

The AIE effects on **M3**, **M4** and **M7** have been examined in THF/water mixture. AIE was detected for all three molecules and is rather to be due to the non-coplanarity induced by the triarylamine groups. **M3** has a less-emissive aggregated state with a PLQY of 14% whereas it is 50 % in diluted THF solution. The aggregates of **M4** and **M7** show enhanced emission intensity and quantum yield with respect to the performance of the monomers in THF. Especially for **M4**, due to a proper molecular packing, the aggregates in a 75% water system exhibit a good quantum yield of 30%.

For all the compounds (except for **M5)**, the films doped at a rate of 10wt% in PMMA were fabricated and investigated. For **M1**, **M2** and **M6**, the films emit in the blue area. The film containing **M2** shows a PLQY of 35.7%. The film with **M3** is green emissive, while that of **M4** and **M7** are yellow emissive. The 10wt% doped film of **M4** was found to show a PLQY as high as 82.2%, and an external quantum yield of 72.5%, which is about 20% higher than the reported conversion efficiency of polyphenylene derivatives, which is 60% for converting the 450-nm blue light to green-yellow[71]. The doping rate of 10% does not favor the formation of massive aggregates in PMMA films.

The deposited quantities of fluorophores, doping rates, coating method and even the solvent used in the coating process can significantly impact the emission properties, owing to distinct consequent molecular arrangements. The film of **M4** deposited from THF shows a bathochromic shift compared to that from DCM. By optimizing the conditions of deposition, the emission of **M4** can be tuned to give a red-emissive material. The neat film made by drop-casting from THF with a concentration of 10 g/L shows a red emission at 620 nm with a PLQY of 11.6%.

Photostability tests were carried out on the 10wt% films of **M2**, **M3** and **M4** to estimate their lifetime under a continuous UV irradiation. Under a source of irradiation with a power of 300 mW/cm^2, **M2** and **M3** tend to a plateau at about 20% of the initial intensity, while the corresponding value is only 5% for the film containing 10wt% of **M4**. This value can be increased to 20% by setting the power of the irradiation source at 100 mW/cm^2, suggesting that **M4** is more suitable in a low-power scenario. The doping rates can also influence the photo-stability, and 10wt% films show the slowest degradation.

In the end, the possibility to design white-emitting samples both in solutions and films was investigated. In chloroform, the warm white light with CIE coordinates of (0.37, 0.34) could be obtained in a ternary mixture of **M3**, **M4** and **M6** with a ratio of 2: 1: 20. White-emitting films could not be obtained. White hybrid LED is made based on M4 and blue inorganic LED, showing a white light with CIE coordinates of (0.33, 0.37) and CCT of 5460 K.

Chapter V Conclusions and perspectives

5.1 Conclusions

Initially, we reviewed the luminescence and luminescent materials, especially on the history of light-emitting diodes (LEDs). The target application for the materials developed in this thesis is hybrid LEDs by embedding the inorganic near-UV or blue LEDs based on InGaN with the organic down-converters to generate ideal white light with good quality. The organic materials possess the advantage over the inorganic phosphors which are employed in the commercial system, not only because they are metal-free (especially of rare-earth elements), but also their excellent absorption and emission performances.

In this work, we have designed and synthesized a series of donor-acceptor (D-A) molecules comprising a novel building block, 2,2'-bipyrimidine (BPM) derivatives, as acceptor. The electron-donating moieties are chosen from triarylamines and thiophene derivatives. The syntheses of D-A molecules were carried out mainly through Suzuki coupling and Stille reaction. Seven final products were successfully purified and characterized.

The photophysical measurements in diluted solution were conducted to examine their photoluminescent (PL) performances. The working concentration were determined and set at most 1×10^{-5} M. In chloroform solutions, **M1**, **M2** and **M6** exhibits emission in blue region, **M3** emits in green, **M4**, **M5** and **M7** can emit in orange-red, depending on their distinctive D-A strengths and thus bandgaps. They all show broad emission band. Some of them shows efficient fluorescence: the photoluminescence quantum yields (PLQYs) of **M2** and **M3** are 72% and 64% respectively in chloroform solution, and **M4** exhibits more than 90% PLQY in toluene, triethylamine and ether solutions. Except **M6**, they all exhibit dual absorption band: the one occurring in the higher-energy region is attributed to a localized π-π* transition, while that at lower energies varies from the near-UV to the blue region, attributed to an internal charge-transfer (ICT).

The solvent effects on **M3**, **M4** and **M7** were investigated. **M3** shows a bright CT state, while **M4** has a very emissive LE state but less emissive CT state. The methoxy substitutions can change the ICT process profoundly. **M7** behaves a dual-peak emission in polar solvents, which is the consequence of the TICT. The solvent polarity is a facile mean to tune the emission properties of the fluorophores. By inspecting the phosphorescence and fluorescence at low temperature (77K), the energy levels of triplet and singlet excited states can be located. The electronic structures of each sample were revealed and discussed combining the crystal structures.

Then we turned to their solid-state PL properties since the final target of this thesis is to apply them as solid materials for hybrid LEDs. The AIE tests on **M3**, **M4** and **M7** were carried out. The aggregates of **M4** and **M7** exhibit enhanced emission and quantum yield than their THF solution. The aggregates of **M4** have an emission with the maximum intensity occurring at 613 nm with a PLQY of 30%, comparing to 593 nm and 5% of its THF solution. The powders of **M1**, **M2**, **M3** and **M4** were taken to the PL measurements. The powder of **M4** emits the maximum at 593 nm with a PLQY of 27.2%.

By investigating the absorption, emission and fluorescence lifetimes of their films doped in PMMA, the 10wt% is proved to be a good dopant rate to avoid the massive aggregations for these fluorophores. The 10wt% films of **M4** shows a strong emission with a PLQY of 82%, and can convert 72.5% of the photons emitted from the external 310-nm source. The color-tuneability of the solid samples of **M4** has been examined. By controlling the coating method, amounts of the fluorophore and the solvent system, we can achieve a red emission at 620 nm with a PLQY of 11.6%. The photostability tests were carried out under a continuous UV irradiation. Under a source of irradiation with a power of 300 mW/cm^2, **M2** and **M3** tend to a plateau at about 20% of the initial intensity, while the corresponding value is only 5% for a film containing 10wt% of **M4**.

This value can be increased to 20% by setting the power of the irradiation source at 100 mW/cm^2, suggesting **M4** is more suitable in a low-power scenario. 10wt% film shows the best results. In order to generate white, blenders of fluorophores with different emitting colors were studied. In chloroform solution, the warm white light with CIE coordinates of (0.37, 0.34) could be obtained in a ternary mixture of **M3**, **M4** and **M6** with a ratio of 2: 1: 20. In solid state, we have not obtained white-emitting materials. White hybrid LED is made based on M4 and blue inorganic LED, showing a white light with CIE coordinates of (0.33, 0.37) and CCT of 5460 K.

5.2 Perspectives

Despite those have been done in this thesis, there are still plenty of works and improvements concerning this topic can be further realized. With these works to be done, this project could be brought to the next stage.

5.2.1 Synthesis

Firstly, the synthesis of BPM derivatives, especially of those substituted by electron-withdrawing groups need to be improved. Some promising synthetic routes are proposed in **§ 2.3** in order to avoid the harsh reacting conditions and to augment the yield.

Then the efficient red emitters are also required to really fulfill the visible spectrum, as **M4**, **M5** and **M7** are emitting in orange-red region. Referring to some interesting designs in literature[189,196,197], here some new structures are introduced below in **Figure 5-1**. In **MA-MD**, the insertion of the thiophene as π-linker is proved to be an effective method for the design of deep-red or near infrared emitters, for its coplanar molecular conformation towards the nearby segments and expand the conjugation[189]. The 2-(2,2-diphenylvinyl)thiophene (DPVT) comprised **ME** and **MF** are also expected to emit in red. Due to the C-C double bond, the DPVT moieties show a nearly planar structure which expand from thiophene to one of the phenyl, with the other phenyl almost perpendicular towards the thiophene[196]. **ME** and **MF** are expected to have a well-conjugated system from the BPM core to the ending phenyls and a bathochromic shift in emission comparing to the current molecules. They should also exhibit good solid-state emission efficiencies, because the perpendicular phenyl rings can prevent the enormous π-π stackings which might quench the fluorescence. **MG** is also a promising red-emitter, with the additional electron-withdrawing cyano group which can deeply reduce the bandgap and red-shift the emission. The C-C double bond and C-N triple bond are also the enhancements of the molecular conjugation.

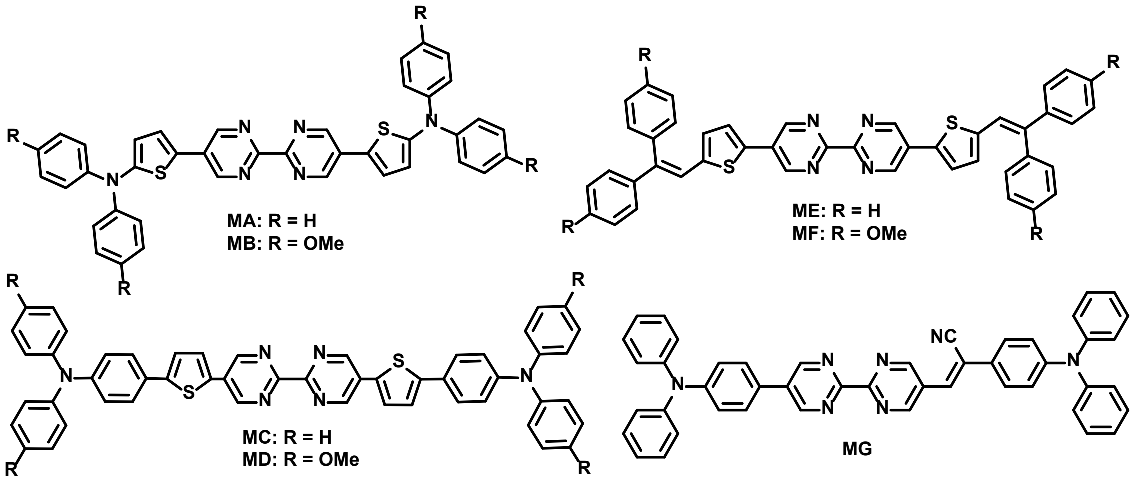

Figure 5-1 Proposed design for red-emitters.

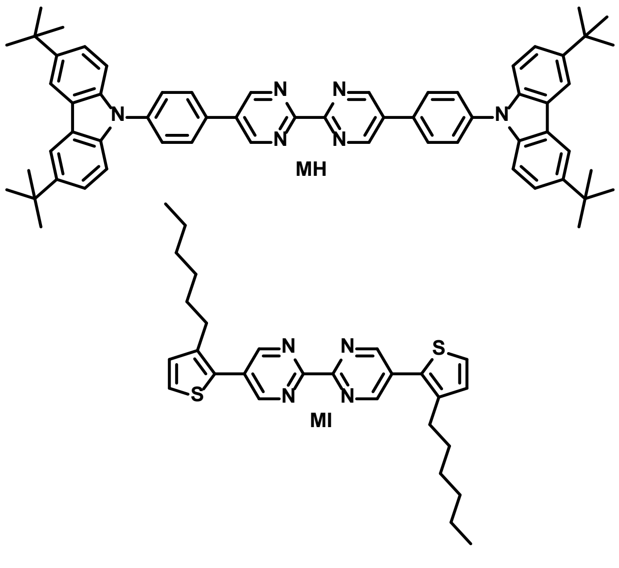

Figure 5-2 Modifications on blue-emitting molecules

Concerning the blue-emitting materials, **M2** has a good PLQY of 35.7% in 10wt%

PMMA film. The biggest problem for **M2** is its poor solubility, which brings difficulties to the solution-processable coating. **M6** emits in deep-blue area in solutions, but it shows a red-shift in emission of its solid state and gives undesired green component. In order to overcome these problems, some modifications on these two compounds are proposed (**Figure 5-2**). The design idea on **MH** is to increase the solubility by grafting the aliphatic chains on carbazole units. As for **MG**, by changing the position of the hexyl chains from 5-position of thiophene to 3-position, the steric hindrance of the chain may bring a slight twist within the thiophen and pyrimidine, and adjust the molecular packing to reduce the green component for avoiding the massive π-π interactions[198].

5.2.2 Solid-state photophysical measurements

First of all, the quality of the fluorescence spectra of the solid samples should be improved. One possible way is to improve the quality of the films. More works should be done to optimize the conditions for fabricating the films. The other strategy is to replace the glass subtract with quartz to eliminate the spikes occurring in the spectra.

The PLQYs and fluorescence lifetimes of all the solid samples should be measured ideally to fully investigate the emission efficiencies. Especially for the crystals of **M4**, they should different molecular conformations when growing from different solutions. It would be out of interests to inspect the distinctive photophysical properties originating from the diverse molecular conformations and establish solid property-structure relationships.

5.2.3 Photostability

Concerning the photodegradation tests, **M4** shows a fast degradation under the continuous UV irradiation. It would be meaningful to study its degradation process by using NMR or IR spectroscopy. Based on the results, the structure of the compound could be modified to improve its photostability. The other strategies, like changing matrix, introducing photostabilizers could be also considered.

5.2.4 White-emitting materials

We have obtained a white-emitting solution with a set of CIE coordinates of (0.37, 0.34), which is a ternary mixture comprising **M6**, **M3** and **M4** (2: 1: 20) in chloroform solution. It is a nice result and deserve more detailed studies on its absorption property, PLQY and energy transfer between different emitters.

For the solid sample, the white-emitting film is not successfully fabricated without any matrix. Herein, some ideas on how to make hybrid white light are proposed. First, a new blue emitter which shows a PLQY as high as **M4** in the solid state and with proper solubility is necessary, and it would be better if it emits with high emission intensity in deep blue, as we proposed in **§5.2.1**. The blue-emitting polymers are also considerable. It is also considerable to develop a new red-emitter which has an emission more shifted to the red, as they are shown in **§5.2.1**. The other strategy is to adopt two layers of films with different emission color to achieve white light. It is also possible to employ a blue LED as the light pump and covered with the films with different weight percentage of **M4** to generate the white light.

5.2.5 Thermal property

Thermal properties of our compounds should also be investigated such as differential scanning calorimetry (DSC) and thermal gravimetric analysis (TGA), from which we could obtain the glass-transition temperatures, melting temperatures, the weight-loss percentage and temperatures, etc. This information is meaningful for the future application in hybrid LEDs.

References

(1) Nair, G. B.; Dhoble, S. J.: 1 - Introduction to luminescence. In *The Fundamentals and Applications of Light-Emitting Diodes*; Nair, G. B., Dhoble, S. J., Eds.; Woodhead Publishing, 2021; pp 3-33.

(2) Stokes, G. G. On the change of refrangibility of light. *Philos. Trans. R. Soc. London* **1997**, *142*, 463-562.

(3) Williams, F. High-field electroluminescence. *J. Lumin.* **1981**, *23*, 1-16.

(4) Nakamura, S. InGaN/AlGaN blue-light-emitting diodes. *J. Vac. Sci. Technol. A* **1995**, *13*, 705-710.

(5) David, S. P.; Gaume, R.: Electroluminescent Thin Film Phosphors. In *Thin Film Structures in Energy Applications*; Babu Krishna Moorthy, S., Ed.; Springer International Publishing: Cham, 2015; pp 243-269.

(6) Blasse, G.; Grabmaier, B. C.: Energy Transfer. In *Luminescent Materials*; Blasse, G., Grabmaier, B. C., Eds.; Springer Berlin Heidelberg: Berlin, Heidelberg, 1994; pp 91-107.

(7) Mahalingam, V.; Thirumalai, J.; Krishnan, R.; Mantha, S. Up/down conversion luminescence and charge compensation investigation of Ca0.5Y1−x(WO4)2:xLn3+ (Ln=Pr, Sm, Eu, Tb, Dy, Yb/Er) phosphors. *Spectrochim. Acta, Part A Mol Biomol Spectrosc.* **2016**, *152*, 172-180.

(8) Ogi, T.; Kaihatsu, Y.; Iskandar, F.; Wang, W.-N.; Okuyama, K. Facile Synthesis of New Full-Color-Emitting BCNO Phosphors with High Quantum Efficiency. *Adv. Mater.* **2008**, *20*, 3235-3238.

(9) Ziessel, R.; Sabbatini, N.; Guardigli, M.; Bolletta, F.; Manet, I. Luminescence of Eu 3+ and Tb 3+ complexes of a novel branched macrocyclic ligand containing 2, 2'-bipyridine and 9-methyl-1, 10-phenanthroline subunits. *New J. Chem.* **1993**, *17*, 323-324.

(10) Nair, G. B.; Dhoble, S. J. White light emission through efficient energy transfer from Ce3+ to Dy3+ ions in Ca3Mg3(PO4)4 matrix aided by Li+ charge compensator. *J. Lumin.* **2017**, *192*, 1157-1166.

(11) Ye, S.; Xiao, F.; Pan, Y. X.; Ma, Y. Y.; Zhang, Q. Y. Phosphors in phosphor-converted white light-emitting diodes: Recent advances in materials, techniques and properties. *Materials Science and Engineering: R: Reports* **2010**, *71*, 1-34.

(12) Armelao, L.; Quici, S.; Barigelletti, F.; Accorsi, G.; Bottaro, G.; Cavazzini, M.; Tondello, E. Design of luminescent lanthanide complexes: From molecules to highly efficient photo-emitting materials. *Coord. Chem. Rev.* **2010**, *254*, 487-505.

(13) Montalti, M.; Credi, A.; Prodi, L.; Gandolfi, M. T.: *Handbook of photochemistry*; CRC press, 2006.

(14) Latva, M.; Takalo, H.; Mukkala, V.-M.; Matachescu, C.; Rodríguez-Ubis, J. C.; Kankare, J. Correlation between the lowest triplet state energy level of the ligand and lanthanide (III) luminescence quantum yield. *J. Lumin.* **1997**, *75*, 149-169.

(15) Juris, A.; Balzani, V.; Barigelletti, F.; Campagna, S.; Belser, P. l.; von Zelewsky, A. v. Ru (II) polypyridine complexes: photophysics, photochemistry, eletrochemistry, and chemiluminescence. *Coord. Chem. Rev.* **1988**, *84*, 85-277.

(16) Cabral Campello, M. P.; Palma, E.; Correia, I.; Paulo, P. M. R.; Matos, A.; Rino, J.; Coimbra, J.; Pessoa, J. C.; Gambino, D.; Paulo, A.; Marques, F. Lanthanide complexes with phenanthroline-based ligands: insights into cell death mechanisms obtained by microscopy techniques. *Dalton Transactions* **2019**, *48*, 4611-4624.

(17) Moore, E. G.; Xu, J.; Jocher, C. J.; Castro-Rodriguez, I.; Raymond, K. N. Highly luminescent lanthanide complexes of 1-hydroxy-2-pyridinones. *Inorganic chemistry* **2008**, *47*, 3105-3118.

(18) Milián-Medina, B.; Gierschner, J. “Though It Be but Little, It Is Fierce”: Excited State Engineering of Conjugated Organic Materials by Fluorination. *The Journal of Physical Chemistry Letters* **2017**, *8*, 91-101.

(19) Gierschner, J.; Shi, J.; Milián-Medina, B.; Roca-Sanjuán, D.; Varghese, S.; Park, S. Luminescence in Crystalline Organic Materials: From Molecules to Molecular Solids. *Advanced Optical Materials* **2021**, *9*, 2002251.

(20) Gierschner, J.; Mack, H.-G.; Lüer, L.; Oelkrug, D. Fluorescence and absorption spectra of oligophenylenevinylenes: Vibronic coupling, band shapes, and solvatochromism. *J. Chem. Phys.* **2002**, *116*, 8596-8609.

(21) Kasha, M. Characterization of electronic transitions in complex molecules. *Discuss. Faraday Soc.* **1950**, *9*, 14-19.

(22) Gierschner, J.; Park, S. Y. Luminescent distyrylbenzenes: tailoring molecular structure and crystalline morphology. *J. Mater. Chem. C* **2013**, *1*, 5818-5832.

(23) Oelkrug, D.; Tompert, A.; Egelhaaf, H.-J.; Hanack, M.; Steinhuber, E.; Hohloch, M.; Meier, H.; Stalmach, U. Towards highly luminescent phenylene vinylene films. *Synth. Met.* **1996**, *83*, 231-237.

(24) Gierschner, J.; Ehni, M.; Egelhaaf, H.-J.; Milián Medina, B.; Beljonne, D.; Benmansour, H.; Bazan, G. C. Solid-state optical properties of linear polyconjugated molecules: π-stack contra herringbone. *J. Chem. Phys.* **2005**, *123*.

(25) Smith, T.; Guild, J. The C.I.E. colorimetric standards and their use. *Trans. Opt. Soc.* **1931**, *33*, 73.

(26) Halim, N. S. A.; Wahid, M. H. A.; Hambali, N. A. M. A.; Rashid, S.; Shahimin, M. M. In *Tilte*2017; EDP Sciences.

(27) Lin, Q. Luminescent hybrid materials for LED lighting. Université Paris Saclay (COmUE), 2019.

(28) Round, H. J. A note on carborundum. *Electrical World* **1907**, *19*, 309.

(29) Holonyak, N., Jr.; Bevacqua, S. F. COHERENT (VISIBLE) LIGHT EMISSION FROM Ga(As1−xPx) JUNCTIONS. *Appl. Phys. Lett.* **2004**, *1*, 82-83.

(30) Nakamura, S.; Mukai, T.; Senoh, M. Candela-class high-brightness InGaN/AlGaN double-heterostructure blue-light-emitting diodes. *Appl. Phys. Lett.* **1994**, *64*, 1687-1689.

(31) Setsuhisa, T.; Shunsuke, F.; Satoru, Y.; Akihiko, S.; Shigeru, Y. YAG glass-

ceramic phosphor for white LED (II): luminescence characteristics. *Proc.SPIE* **2005**, *5941*, 594112.

(32) Oh, M.-S.; Kwon, M.-K.; Park, I.-K.; Baek, S.-H.; Park, S.-J.; Lee, S. H.; Jung, J. J. Improvement of green LED by growing p-GaN on In0.25GaN/GaN MQWs at low temperature. *J. Cryst. Growth* **2006**, *289*, 107-112.

(33) Iida, D.; Zhuang, Z.; Kirilenko, P.; Velazquez-Rizo, M.; Najmi, M. A.; Ohkawa, K. 633-nm InGaN-based red LEDs grown on thick underlying GaN layers with reduced in-plane residual stress. *Appl. Phys. Lett.* **2020**, *116*, 162101.

(34) Muramoto, Y.; Kimura, M.; Nouda, S. Development and future of ultraviolet light-emitting diodes: UV-LED will replace the UV lamp. *Semicond. Sci. Technol.* **2014**, *29*, 084004.

(35) Tang, C. W.; VanSlyke, S. A. Organic electroluminescent diodes. *Appl. Phys. Lett.* **1987**, *51*, 913-915.

(36) Chiang, C.-J.; Kimyonok, A.; Etherington, M. K.; Griffiths, G. C.; Jankus, V.; Turksoy, F.; Monkman, A. P. Ultrahigh Efficiency Fluorescent Single and Bi-Layer Organic Light Emitting Diodes: The Key Role of Triplet Fusion. *Adv. Funct. Mater.* **2013**, *23*, 739-746.

(37) Li, W.; Pan, Y.; Xiao, R.; Peng, Q.; Zhang, S.; Ma, D.; Li, F.; Shen, F.; Wang, Y.; Yang, B.; Ma, Y. Employing ∼100% Excitons in OLEDs by Utilizing a Fluorescent Molecule with Hybridized Local and Charge-Transfer Excited State. *Adv. Funct. Mater.* **2014**, *24*, 1609-1614.

(38) Uoyama, H.; Goushi, K.; Shizu, K.; Nomura, H.; Adachi, C. Highly efficient organic light-emitting diodes from delayed fluorescence. *Nature* **2012**, *492*, 234-238.

(39) Zou, S.-J.; Shen, Y.; Xie, F.-M.; Chen, J.-D.; Li, Y.-Q.; Tang, J.-X. Recent advances in organic light-emitting diodes: toward smart lighting and displays. *Mater. Chem. Front.* **2020**, *4*, 788-820.

(40) Kulkarni, A. P.; Tonzola, C. J.; Babel, A.; Jenekhe, S. A. Electron Transport Materials for Organic Light-Emitting Diodes. *Chem. Mater.* **2004**, *16*, 4556-4573.

(41) Kim, J.-M.; Kim, J.-J. Charge transport layers manage mobility and carrier density balance in light-emitting layers influencing the operational stability of organic light emitting diodes. *Org. Electron.* **2019**, *67*, 43-49.

(42) Pai, D. M.; Yanus, J. F.; Stolka, M. Trap-controlled hopping transport. *J. Phys. Chem.* **1984**, *88*, 4714-4717.

(43) Kido, J.; Ohtaki, C.; Hongawa, K.; Okuyama, K.; Katsutoshi Nagai, K. N. 1,2,4-Triazole Derivative as an Electron Transport Layer in Organic Electroluminescent Devices. *Jpn. J. Appl. Phys.* **1993**, *32*, L917.

(44) Fink, R.; Heischkel, Y.; Thelakkat, M.; Schmidt, H.-W.; Jonda, C.; Hüppauff, M. Synthesis and application of dimeric 1, 3, 5-triazine ethers as hole-blocking materials in electroluminescent devices. *Chem. Mater.* **1998**, *10*, 3620-3625.

(45) Shah, B. K.; Neckers, D. C.; Shi, J.; Forsythe, E. W.; Morton, D. Anthanthrene Derivatives as Blue Emitting Materials for Organic Light-Emitting Diode Applications. *Chem. Mater.* **2006**, *18*, 603-608.

(46) Zhang, H.; Liu, X.; Gong, Y.; Yu, T.; Zhao, Y. Synthesis and characterization of SFX-based coumarin derivatives for OLEDs. *Dyes Pigm.* **2021**, *185*, 108969.

(47) Sainova, D.; Miteva, T.; Nothofer, H. G.; Scherf, U.; Glowacki, I.; Ulanski, J.; Fujikawa, H.; Neher, D. Control of color and efficiency of light-emitting diodes based on polyfluorenes blended with hole-transporting molecules. *Appl. Phys. Lett.* **2000**, *76*, 1810-1812.

(48) Endo, A.; Ogasawara, M.; Takahashi, A.; Yokoyama, D.; Kato, Y.; Adachi, C. Thermally Activated Delayed Fluorescence from Sn4+–Porphyrin Complexes and Their Application to Organic Light Emitting Diodes — A Novel Mechanism for Electroluminescence. *Adv. Mater.* **2009**, *21*, 4802-4806.

(49) Endo, A.; Sato, K.; Yoshimura, K.; Kai, T.; Kawada, A.; Miyazaki, H.; Adachi, C. Efficient up-conversion of triplet excitons into a singlet state and its application for organic light emitting diodes. *Appl. Phys. Lett.* **2011**, *98*.

(50) Han, J.; Huang, Z.; Miao, J.; Qiu, Y.; Xie, Z.; Yang, C. Narrowband blue emission with insensitivity to the doping concentration from an oxygen-bridged triarylboron-based TADF emitter: nondoped OLEDs with a high external quantum efficiency up to 21.4%. *Chem. Sci.* **2022**, *13*, 3402-3408.

(51) Kondakov, D. Y.; Lenhart, W. C.; Nichols, W. F. Operational degradation of organic light-emitting diodes: Mechanism and identification of chemical products. *J. Appl. Phys.* **2007**, *101*, 024512.

(52) OLED TV estimated lifespan shorter then expected. *HDTV Info Europe. Hdtvinfo.eu* **2008-05-08**.

(53) Fallahi, A.; Taromi, F. A.; Mohebbi, A.; Yuen, J. D.; Shahinpoor, M. A novel ambipolar polymer: from organic thin-film transistors to enhanced air-stable blue light emitting diodes. *J. Mater. Chem. C* **2014**, *2*, 6491-6501.

(54) Shen, J. Y.; Lee, C. Y.; Huang, T.-H.; Lin, J. T.; Tao, Y.-T.; Chien, C.-H.; Tsai, C. High Tg blue emitting materials for electroluminescent devices. *J. Mater. Chem.* **2005**, *15*, 2455-2463.

(55) Yuan, M.; Quan, L. N.; Comin, R.; Walters, G.; Sabatini, R.; Voznyy, O.; Hoogland, S.; Zhao, Y.; Beauregard, E. M.; Kanjanaboos, P.; Lu, Z.; Kim, D. H.; Sargent, E. H. Perovskite energy funnels for efficient light-emitting diodes. *Nat. Nanotechnol* **2016**, *11*, 872-877.

(56) Xiao, Z.; Kerner, R. A.; Zhao, L.; Tran, N. L.; Lee, K. M.; Koh, T.-W.; Scholes, G. D.; Rand, B. P. Efficient perovskite light-emitting diodes featuring nanometre-sized crystallites. *Nat. Photonics* **2017**, *11*, 108-115.

(57) Lin, K.; Xing, J.; Quan, L. N.; de Arquer, F. P. G.; Gong, X.; Lu, J.; Xie, L.; Zhao, W.; Zhang, D.; Yan, C.; Li, W.; Liu, X.; Lu, Y.; Kirman, J.; Sargent, E. H.; Xiong, Q.; Wei, Z. Perovskite light-emitting diodes with external quantum efficiency exceeding 20 per cent. *Nature* **2018**, *562*, 245-248.

(58) Moreno, I.; Contreras, U. Color distribution from multicolor LED arrays. *Opt. Express* **2007**, *15*, 3607-3618.

(59) Cho, J.; Park, J. H.; Kim, J. K.; Schubert, E. F. White light-emitting diodes:

History, progress, and future. *Laser Photonics Rev.* **2017**, *11*, 1600147.

(60) Blasse, G.; Bril, A. Investigation of Some Ce3+-Activated Phosphors. *J. Chem. Phys.* **2004**, *47*, 5139-5145.

(61) Jacobs, R. R.; Krupke, W. F.; Weber, M. J. Measurement of excited-state-absorption loss for Ce3+ in Y3Al5O12 and implications for tunable 5d→4f rare-earth lasers. *Appl. Phys. Lett.* **2008**, *33*, 410-412.

(62) Gorrotxategi, P.; Consonni, M.; Gasse, A. Optical efficiency characterization of LED phosphors using a double integrating sphere system. *Journal of Solid State Lighting* **2015**, *2*, 1.

(63) Bachmann, V.; Ronda, C.; Meijerink, A. Temperature Quenching of Yellow Ce3+ Luminescence in YAG:Ce. *Chem. Mater.* **2009**, *21*, 2077-2084.

(64) Jang, H. S.; Im, W. B.; Lee, D. C.; Jeon, D. Y.; Kim, S. S. Enhancement of red spectral emission intensity of Y3Al5O12:Ce3+ phosphor via Pr co-doping and Tb substitution for the application to white LEDs. *J. Lumin.* **2007**, *126*, 371-377.

(65) Chawla, S.; Roy, T.; Majumder, K.; Yadav, A. Red enhanced YAG:Ce, Pr nanophosphor for white LEDs. *J. Exp. Nanosci.* **2014**, *9*, 776-784.

(66) Shi, H.; Zhu, C.; Huang, J.; Chen, J.; Chen, D.; Wang, W.; Wang, F.; Cao, Y.; Yuan, X. Luminescence properties of YAG:Ce, Gd phosphors synthesized under vacuum condition and their white LED performances. *Opt. Mater. Express* **2014**, *4*, 649-655.

(67) McLellan, B. C.; Corder, G. D.; Golev, A.; Ali, S. H. Sustainability of the Rare Earths Industry. *Procedia Environmental Sciences* **2014**, *20*, 280-287.

(68) Barbet, A.; Paul, A.; Gallinelli, T.; Balembois, F.; Blanchot, J.-P.; Forget, S.; Chénais, S.; Druon, F.; Georges, P. Light-emitting diode pumped luminescent concentrators: a new opportunity for low-cost solid-state lasers. *Optica* **2016**, *3*, 465-468.

(69) Huyal, I. O.; Koldemir, U.; Ozel, T.; Demir, H. V.; Tuncel, D. On the origin of high quality white light emission from a hybrid organic/inorganic light emitting diode using azide functionalized polyfluorene. *J. Mater. Chem.* **2008**, *18*, 3568-3574.

(70) Benson, K.; Ghimire, A.; Pattammattel, A.; Kumar, C. V. Protein Biophosphors: Biodegradable, Multifunctional, Protein-Based Hydrogel for White Emission, Sensing, and pH Detection. *Adv. Funct. Mater.* **2017**, *27*, 1702955.

(71) Hide, F.; Kozodoy, P.; DenBaars, S. P.; Heeger, A. J. White light from InGaN/conjugated polymer hybrid light-emitting diodes. *Appl. Phys. Lett.* **1997**, *70*, 2664-2666.

(72) Yu, T.; Liu, L.; Xie, Z.; Ma, Y. Progress in small-molecule luminescent materials for organic light-emitting diodes. *Sci. China Chem.* **2015**, *58*, 907-915.

(73) Havinga, E. E.; ten Hoeve, W.; Wynberg, H. A new class of small band gap organic polymer conductors. *Polym. Bull.* **1992**, *29*, 119-126.

(74) Rybakiewicz, R.; Ganczarczyk, R.; Wiosna-Salyga, G.; Bobowska, I.; Banasiewicz, M.; Charyton, M.; Skorka, L.; Zagorska, M.; Pron, A. Luminescent organic materials based on donor-acceptor-donor compounds containing carbazole

donors and acceptors of varying strength: Spectroscopy, redox properties and application in organic light emitting diodes. *Opt. Mater.* **2020**, *108*, 110428.

(75) Gibson, G. L.; McCormick, T. M.; Seferos, D. S. Atomistic Band Gap Engineering in Donor–Acceptor Polymers. *J. Am. Chem. Soc.* **2012**, *134*, 539-547.

(76) Jayakannan, M.; van Hal, P. A.; Janssen, R. A. J. Synthesis and structure-property relationship of new donor–acceptor-type conjugated monomers and polymers on the basis of thiophene and benzothiadiazole. *J. Polym. Sci., Part A: Polym. Chem.* **2001**, *40*, 251-261.

(77) Jenekhe, S. A.; Lu, L.; Alam, M. M. New Conjugated Polymers with Donor−Acceptor Architectures: Synthesis and Photophysics of Carbazole−Quinoline and Phenothiazine−Quinoline Copolymers and Oligomers Exhibiting Large Intramolecular Charge Transfer. *Macromolecules* **2001**, *34*, 7315-7324.

(78) Beaujuge, P. M.; Subbiah, J.; Choudhury, K. R.; Ellinger, S.; McCarley, T. D.; So, F.; Reynolds, J. R. Green Dioxythiophene-Benzothiadiazole Donor−Acceptor Copolymers for Photovoltaic Device Applications. *Chem. Mater.* **2010**, *22*, 2093-2106.

(79) Choi, M.-W.; Kim, G.; Seitkazina, A.; Kim, S.-Y.; Yoon, W. S.; Kwon, J. E.; Kim, S.; Park, S. Y. A novel fluorescent bis-lactam scaffold presenting high photostability and brightness. *Dyes Pigm.* **2022**, *207*, 110699.

(80) Horak, E.; Robić, M.; Šimanović, A.; Mandić, V.; Vianello, R.; Hranjec, M.; Steinberg, I. M. Tuneable solid-state emitters based on benzimidazole derivatives: Aggregation induced red emission and mechanochromism of D-π-a fluorophores. *Dyes Pigm.* **2019**, *162*, 688-696.

(81) Li, W.; Liu, D.; Shen, F.; Ma, D.; Wang, Z.; Feng, T.; Xu, Y.; Yang, B.; Ma, Y. A Twisting Donor-Acceptor Molecule with an Intercrossed Excited State for Highly Efficient, Deep-Blue Electroluminescence. *Adv. Funct. Mater.* **2012**, *22*, 2797-2803.

(82) Zhang, H.-Y.; Yang, H.-Y.; Zhang, M.; Lin, H.; Tao, S.-L.; Zheng, C.-J.; Zhang, X.-H. A novel orange-red thermally activated delayed fluorescence emitter with high molecular rigidity and planarity realizing 32.5% external quantum efficiency in organic light-emitting diodes. *Materials Horizons* **2022**, *9*, 2425-2432.

(83) Cai, Z.; Wu, X.; Liu, H.; Guo, J.; Yang, D.; Ma, D.; Zhao, Z.; Tang, B. Z. Realizing Record-High Electroluminescence Efficiency of 31.5 % for Red Thermally Activated Delayed Fluorescence Molecules. *Angew. Chem. Int. Ed.* **2021**, *60*, 23635-23640.

(84) Zade, S. S.; Bendikov, M. From Oligomers to Polymer: Convergence in the HOMO−LUMO Gaps of Conjugated Oligomers. *Org. Lett.* **2006**, *8*, 5243-5246.

(85) Facchetti, A. π-Conjugated Polymers for Organic Electronics and Photovoltaic Cell Applications. *Chem. Mater.* **2011**, *23*, 733-758.

(86) Ricks, A. B.; Solomon, G. C.; Colvin, M. T.; Scott, A. M.; Chen, K.; Ratner, M. A.; Wasielewski, M. R. Controlling Electron Transfer in Donor−Bridge−Acceptor Molecules Using Cross-Conjugated Bridges. *J. Am. Chem. Soc.* **2010**, *132*, 15427-15434.

(87) Tsuda, A.; Osuka, A. Fully Conjugated Porphyrin Tapes with Electronic

Absorption Bands That Reach into Infrared. *Science* **2001**, *293*, 79-82.

(88) Wakamiya, A.; Taniguchi, T.; Yamaguchi, S. Intramolecular B–N Coordination as a Scaffold for Electron-Transporting Materials: Synthesis and Properties of Boryl-Substituted Thienylthiazoles. *Angew. Chem. Int. Ed.* **2006**, *45*, 3170-3173.

(89) Zhu, C.; Guo, Z.-H.; Mu, A. U.; Liu, Y.; Wheeler, S. E.; Fang, L. Low Band Gap Coplanar Conjugated Molecules Featuring Dynamic Intramolecular Lewis Acid–Base Coordination. *J. Org. Chem.* **2016**, *81*, 4347-4352.

(90) Luo, J.; Xie, Z.; Lam, J. W. Y.; Cheng, L.; Chen, H.; Qiu, C.; Kwok, H. S.; Zhan, X.; Liu, Y.; Zhu, D.; Tang, B. Z. Aggregation-induced emission of 1-methyl-1,2,3,4,5-pentaphenylsilole. *Chem. Commun.* **2001**, 1740-1741.

(91) Tang, B. Z.; Zhan, X.; Yu, G.; Sze Lee, P. P.; Liu, Y.; Zhu, D. Efficient blue emission from siloles. *J. Mater. Chem.* **2001**, *11*, 2974-2978.

(92) Hong, Y.; Lam, J. W. Y.; Tang, B. Z. Aggregation-induced emission: phenomenon, mechanism and applications. *Chem. Commun.* **2009**, 4332-4353.

(93) Chen, H. Y.; Lam, W. Y.; Luo, J. D.; Ho, Y. L.; Tang, B. Z.; Zhu, D. B.; Wong, M.; Kwok, H. S. Highly efficient organic light-emitting diodes with a silole-based compound. *Appl. Phys. Lett.* **2002**, *81*, 574-576.

(94) Chen, J.; Xu, B.; Yang, K.; Cao, Y.; Sung, H. H. Y.; Williams, I. D.; Tang, B. Z. Photoluminescence Spectral Reliance on Aggregation Order of 1,1-Bis(2‘-thienyl)-2,3,4,5-tetraphenylsilole. *J. Phys. Chem. B* **2005**, *109*, 17086-17093.

(95) Ning, Z.; Chen, Z.; Zhang, Q.; Yan, Y.; Qian, S.; Cao, Y.; Tian, H. Aggregation-induced Emission (AIE)-active Starburst Triarylamine Fluorophores as Potential Non-doped Red Emitters for Organic Light-emitting Diodes and Cl2 Gas Chemodosimeter. *Adv. Funct. Mater.* **2007**, *17*, 3799-3807.

(96) Liu, Y.; Tao, X.; Wang, F.; Dang, X.; Zou, D.; Ren, Y.; Jiang, M. Aggregation-Induced Emissions of Fluorenonearylamine Derivatives: A New Kind of Materials for Nondoped Red Organic Light-Emitting Diodes. *J. Phys. Chem. C* **2008**, *112*, 3975-3981.

(97) Lv, C.; Liu, W.; Luo, Q.; Yi, H.; Yu, H.; Yang, Z.; Zou, B.; Zhang, Y. A highly emissive AIE-active luminophore exhibiting deep-red to near-infrared piezochromism and high-quality lasing. *Chem. Sci.* **2020**, *11*, 4007-4015.

(98) Sajjad, M. T.; Manousiadis, P. P.; Chun, H.; Vithanage, D. A.; Rajbhandari, S.; Kanibolotsky, A. L.; Faulkner, G.; O'Brien, D.; Skabara, P. J.; Samuel, I. D. W.; Turnbull, G. A. Novel Fast Color-Converter for Visible Light Communication Using a Blend of Conjugated Polymers. *ACS Photonics* **2015**, *2*, 194-199.

(99) Gu, E.; Zhang, H. X.; Sun, H. D.; Dawson, M. D.; Mackintosh, A. R.; Kuehne, A. J. C.; Pethrick, R. A.; Belton, C.; Bradley, D. D. C. Hybrid inorganic/organic microstructured light-emitting diodes produced using photocurable polymer blends. *Appl. Phys. Lett.* **2007**, *90*.

(100) Heliotis, G.; Stavrinou, P. N.; Bradley, D. D. C.; Gu, E.; Griffin, C.; Jeon, C. W.; Dawson, M. D. Spectral conversion of InGaN ultraviolet microarray light-emitting diodes using fluorene-based red-, green-, blue-, and white-light-emitting polymer

overlayer films. *Appl. Phys. Lett.* **2005**, *87*.

(101) Taylor-Shaw, E.; Angioni, E.; Findlay, N. J.; Breig, B.; Inigo, A. R.; Bruckbauer, J.; Wallis, D. J.; Skabara, P. J.; Martin, R. W. Cool to warm white light emission from hybrid inorganic/organic light-emitting diodes. *J. Mater. Chem. C* **2016**, *4*, 11499-11507.

(102) Findlay, N. J.; Bruckbauer, J.; Inigo, A. R.; Breig, B.; Arumugam, S.; Wallis, D. J.; Martin, R. W.; Skabara, P. J. An organic down-converting material for white-light emission from hybrid LEDs. *Adv. Mater.* **2014**, *26*, 7290-7294.

(103) Findlay, N. J.; Orofino-Peña, C.; Bruckbauer, J.; Elmasly, S. E. T.; Arumugam, S.; Inigo, A. R.; Kanibolotsky, A. L.; Martin, R. W.; Skabara, P. J. Linear oligofluorene-BODIPY structures for fluorescence applications. *J. Mater. Chem. C* **2013**, *1*, 2249.

(104) Di Martino, D.; Beverina, L.; Sassi, M.; Brovelli, S.; Tubino, R.; Meinardi, F. Straightforward fabrication of stable white LEDs by embedding of inorganic UV-LEDs into bulk polymerized polymethyl-methacrylate doped with organic dyes. *Scientific reports* **2014**, *4*, 4400.

(105) Zabrowski, D. L.; Moormann, A. E.; Beck, K. R. The oxidation of aromatic amines in the presence of “electron-rich” aromatic systems. *Tetrahedron Lett.* **1988**, *29*, 4501-4504.

(106) Liu, Z.; Ojima, H.; Hong, Z.; Kido, J.; Tian, W.; Wang, X.-F. Solution-Processed Organic Photovoltaics Based on Indoline Dye Molecules Developed in Dye-Sensitized Solar Cells. *Molecules* **2013**, *18*, 3107-3117.

(107) Mahmood, A. Triphenylamine based dyes for dye sensitized solar cells: A review. *Sol. Energy* **2016**, *123*, 127-144.

(108) Blanchard, P.; Malacrida, C.; Cabanetos, C.; Roncali, J.; Ludwigs, S. Triphenylamine and some of its derivatives as versatile building blocks for organic electronic applications. *Polym. Int.* **2019**, *68*, 589-606.

(109) Zhang, W.; Wu, Y.; Zhu, H.; Chai, Q.; Liu, J.; Li, H.; Song, X.; Zhu, W.-H. Rational Molecular Engineering of Indoline-Based D-A-π-A Organic Sensitizers for Long-Wavelength-Responsive Dye-Sensitized Solar Cells. *ACS Appl. Mater. Interfaces* **2015**, *7*, 26802-26810.

(110) Xiao, P.; Frigoli, M.; Dumur, F.; Graff, B.; Gigmes, D.; Fouassier, J. P.; Lalevée, J. Julolidine or Fluorenone Based Push–Pull Dyes for Polymerization upon Soft Polychromatic Visible Light or Green Light. *Macromolecules* **2014**, *47*, 106-112.

(111) Pinheiro, H. M.; Touraud, E.; Thomas, O. Aromatic amines from azo dye reduction: status review with emphasis on direct UV spectrophotometric detection in textile industry wastewaters. *Dyes Pigm.* **2004**, *61*, 121-139.

(112) Yuan, W. Z.; Gong, Y.; Chen, S.; Shen, X. Y.; Lam, J. W. Y.; Lu, P.; Lu, Y.; Wang, Z.; Hu, R.; Xie, N.; Kwok, H. S.; Zhang, Y.; Sun, J. Z.; Tang, B. Z. Efficient Solid Emitters with Aggregation-Induced Emission and Intramolecular Charge Transfer Characteristics: Molecular Design, Synthesis, Photophysical Behaviors, and OLED Application. *Chem. Mater.* **2012**, *24*, 1518-1528.

(113) Hong, Y.; Lam, J. W. Y.; Tang, B. Z. Aggregation-induced emission. *Chem. Soc. Rev.* **2011**, *40*, 5361-5388.

(114) Chen, S.; Liu, Y.; He, M.; Huang, J. Synthesis of a Benzothiadiazole-Based D−A Molecule with Aggregation-Induced Emission and Controlled Assembly Properties. *Processes* **2021**, *9*, 1094.

(115) Jiang, H.; Wu, Y.; Islam, A.; Wu, M.; Zhang, W.; Shen, C.; Zhang, H.; Li, E.; Tian, H.; Zhu, W.-H. Molecular Engineering of Quinoxaline-Based D–A−π–A Organic Sensitizers: Taking the Merits of a Large and Rigid Auxiliary Acceptor. *ACS Appl. Mater. Interfaces* **2018**, *10*, 13635-13644.

(116) Cheng, L.; Ju, Z.; Ji, X.; Ma, Y.; Fan, J.; Sun, P.; Wang, S.; Dong, L.; Sun, H.; Zhang, J. Fused phthalimide-based A–DA′D–A small molecule: New protocol for n-type organic semiconductors. *Synth. Met.* **2023**, *293*, 117278.

(117) Gabrian, L.; Giurgi, G.-I.; Stroia, I.; Bogdan, E.; Crişan, A. P.; Hădade, N. D.; Grosu, I.; Terec, A. Exploring the Optoelectronic Properties of D-A and A-D-A 2,2′-bi[3,2-b]thienothiophene Derivatives. *Molecules* **2022**, *27*, 8463.

(118) Tarafdar, G.; Johnson, J. C.; Larson, B. W.; Ramamurthy, P. C. BODIPY based A-D-A molecules: Effect of CF3 group substitution at meso phenyl group. *Dyes Pigm.* **2020**, *177*, 108289.

(119) Wang, Z.-Y.; Wang, J.-Y.; Pei, J. Embedding pyridine units in acceptors to construct donor-acceptor conjugated polymers. *Chin. Chem. Lett.* **2019**, *30*, 25-30.

(120) Ganesan, P.; Ranganathan, R.; Chi, Y.; Liu, X.-K.; Lee, C.-S.; Liu, S.-H.; Lee, G.-H.; Lin, T.-C.; Chen, Y.-T.; Chou, P.-T. Functional Pyrimidine-Based Thermally Activated Delay Fluorescence Emitters: Photophysics, Mechanochromism, and Fabrication of Organic Light-Emitting Diodes. *Chem. Eur. J.* **2017**, *23*, 2858-2866.

(121) Wiley, J. R.; Robinson, J. M.; Ehdaie, S.; Chen, E. C. M.; Chen, E. S. D.; Wentworth, W. E. The determination of absolute electron affinities of the purines and pyrimidines in DNA and RNA from reversible reduction potentials. *Biochem. Biophys. Res. Commun.* **1991**, *180*, 841-845.

(122) Jubeen, F.; Iqbal, S. Z.; Shafiq, N.; Khan, M.; Parveen, S.; Iqbal, M.; Nazir, A. Eco-friendly synthesis of pyrimidines and its derivatives: A review on broad spectrum bioactive moiety with huge therapeutic profile. *Synth. Commun.* **2018**, *48*, 601-625.

(123) Jakob, A.; Ecorchard, P.; Köhler, K.; Lang, H. 2,2′-Bipyrimidine transition metal complexes: Synthesis, reaction chemistry and solid state structures. *J. Organomet. Chem.* **2008**, *693*, 3479-3489.

(124) Zucchi, G. The Utility of 2,2′-Bipyrimidine in Lanthanide Chemistry: From Materials Synthesis to Structural and Physical Properties. *Int. J. Inorg. Chem.* **2011**, *2011*, 918435.

(125) Zucchi, G.; Le Goff, X. F. Magnetic properties of structurally characterized binuclear lanthanide complexes bridged by 2,2′-bipyrimidine. *Polyhedron* **2013**, *52*, 1262-1267.

(126) Griffin, J. D.; Pancoast, A. R.; Sigman, M. S. Interrogation of 2,2'-

Bipyrimidines as Low-Potential Two-Electron Electrolytes. *J. Am. Chem. Soc.* **2021**, *143*, 992-1004.

(127) Yang, Y.; Wu, F.; Lu, H.; Li, S.; Zhong, C.; Zhu, L. Bipyrimidine core structure-based hole transport materials for efficient perovskite solar cells. *Sustain. Energy Fuels* **2020**, *4*, 5271-5276.

(128) van Cleuvenbergen, S.; Kędziora, P.; Fillaut, J. L.; Verbiest, T.; Clays, K.; Akdas-Kilig, H.; Camerel, F. Chiral Side Groups Trigger Second Harmonic Generation Activity in 3D Octupolar Bipyrimidine-Based Organic Liquid Crystals. *Angew. Chem. Int. Ed.* **2017**, *56*, 9546-9550.

(129) Bora, U.; Abdallah, S.; Mhanna, R.; Nicolas, P.; Dok, A.; de Coene, Y.; Van Cleuvenbergen, S.; Jeannin, O.; Malval, J. P.; Clays, K.; Bellec, N.; Ocak, H.; Bilgin-Eran, B.; Camerel, F.; Akdas-Kilic, H. New Multifunctional Bipyrimidine-Based Chromophores for NLO-Active Thin-Film Preparation. *Chemistry* **2023**, e202302930.

(130) Park, H.-J.; Han, S. H.; Lee, J. Y. Molecular Design of Thermally Activated Delayed-Fluorescent Emitters Using 2,2′-Bipyrimidine as the Acceptor in Donor–Acceptor Structures. *Chem. Asian J.* **2017**, *12*, 2494-2500.

(131) Park, H.-J.; Han, S. H.; Lee, J. Y.; Han, H.; Kim, E.-G. Managing Orientation of Nitrogens in Bipyrimidine-Based Thermally Activated Delayed Fluorescent Emitters To Suppress Nonradiative Mechanisms. *Chem. Mater.* **2018**, *30*, 3215-3222.

(132) Bekiari, V.; Thiakou, K. A.; Raptopoulou, C. P.; Perlepes, S. P.; Lianos, P. Structure and photophysical behavior of 2,2′-bipyrimidine/lanthanide ion complexes in various environments. *J. Lumin.* **2008**, *128*, 481-488.

(133) Gompper, R.; Brandl, S.; Mair, H.-J. Use of conjugated compounds containing pyrimidine groups as electroluminescence materials. US5948551.

(134) Fernholt, L.; Rømming, C.; Samdal, S. On the Structure of 2, 2'-Bipyrimidine. Gas and Solid Phase Structure and Barrier to Internal Rotation. *Acta Chem. Scand.* **1981**, *35*, 707.

(135) Wu, Y.; Zhu, W. Organic sensitizers from D–π–A to D–A–π–A: effect of the internal electron-withdrawing units on molecular absorption, energy levels and photovoltaic performances. *Chem. Soc. Rev.* **2013**, *42*, 2039-2058.

(136) Albinsson, B.; Eng, M. P.; Pettersson, K.; Winters, M. U. Electron and energy transfer in donor-acceptor systems with conjugated molecular bridges. *Phys. Chem. Chem. Phys.* **2007**, *9*, 5847-5864.

(137) Lin, Q.; Huang, X.; Ramachandran, S.; Wang, X.; Boonsin, R.; Khendriche, Y.; Valleix, R.; Roblin, J.-P.; Boyer, D.; Chadeyron, G.; Zucchi, G. 2,2′-Bipyrimidine as a Building Block for the Design of Emissive Conjugated Polymers for Hybrid LED Lighting. *ACS Appl. Polym. Mater.* **2020**, *2*, 5581-5591.

(138) Romero, F. M.; Ziessel, R. A straightforward synthesis of 5-bromo and 5,5′-dibromo-2,2′-bipyridines. *Tetrahedron Lett.* **1995**, *36*, 6471-6474.

(139) Schwab, P. F. H.; Fleischer, F.; Michl, J. Preparation of 5-Brominated and 5,5‘-Dibrominated 2,2‘-Bipyridines and 2,2‘-Bipyrimidines. *J. Org. Chem.* **2002**, *67*, 443-449.

(140) Brunner, H. G. B., Kurt; Fory, Werner. 2-Phenyl-, 2-naphthyl-, and 2-heterocyclylpyrimidines as antidotes for protecting cultivated plants from phytotoxic damage caused by herbicides. EP96657.

(141) Li, Z.; Wu, Y.; Zhen, S.; Su, K.; Zhang, L.; Yang, F.; McDonough, M. A.; Schofield, C. J.; Zhang, X. In Situ Inhibitor Synthesis and Screening by Fluorescence Polarization: An Efficient Approach for Accelerating Drug Discovery. *Angew. Chem. Int. Ed.* **2022**, *61*, e202211510.

(142) Wanwong, S.; Poe, A.; Balaji, G.; Thayumanavan, S. The effect of heteroatom conformation on optoelectronic properties of cyclopentadithiophene derivatives. *Organic & Biomolecular Chemistry* **2014**, *12*, 2474-2478.

(143) Brouwer, A. M. Standards for photoluminescence quantum yield measurements in solution (IUPAC Technical Report). *Pure Appl. Chem.* **2011**, *83*, 2213-2228.

(144) Melhuish, W. H. Quantum efficiencies of fluorescence of organic substances: effect of solvent and concentration of the fluorescent solute1. *J. Phys. Chem.* **1961**, *65*, 229-235.

(145) Ghiggino, K.; Skilton, P.; Thistlethwaite, P. β-Carboline as a fluorescence standard. *Journal of photochemistry* **1985**, *31*, 113-121.

(146) Anderson, E. D.; Boger, D. L. Inverse Electron Demand Diels–Alder Reactions of 1,2,3-Triazines: Pronounced Substituent Effects on Reactivity and Cycloaddition Scope. *J. Am. Chem. Soc.* **2011**, *133*, 12285-12292.

(147) Peng, Z.-H.; Journet, M.; Humphrey, G. A Highly Regioselective Amination of 6-Aryl-2,4-dichloropyrimidine. *Org. Lett.* **2006**, *8*, 395-398.

(148) Ahn, M.; Kim, M. J.; Cho, D. W.; Wee, K. R. Electron Push-Pull Effects on Intramolecular Charge Transfer in Perylene-Based Donor-Acceptor Compounds. *J. Org. Chem.* **2021**, *86*, 403-413.

(149) Sun, K.; Sun, Y.; Liu, D.; Feng, Y.; Zhang, X.; Sun, Y.; Jiang, W. CBP derivatives dendronized self-host TADF dendrimer: Achieving efficient non-doped near-infrared organic light-emitting diodes. *Dyes Pigm.* **2017**, *147*, 436-443.

(150) Park, J. H.; Yun, C.; Koh, T.-W.; Do, Y.; Yoo, S.; Lee, M. H. Vinyl-type polynorbornene with 9,9′-(1,1′-biphenyl)-4,4′-diylbis-9H-carbazole side groups as a host material for highly efficient green phosphorescent organic light-emitting diodes. *J. Mater. Chem.* **2011**, *21*, 5422-5429.

(151) Walba, H.; Branch, G. E. The absorption spectra of some N-substituted p-aminotriphenylmethyl ions. *J. Am. Chem. Soc.* **1951**, *73*, 3341-3348.

(152) Johnson, G. E. Spectroscopic study of carbazole by photoselection. *J. Phys. Chem.* **1974**, *78*, 1512-1521.

(153) Bacon, G. E.; Curry, N. A.; Wilson, S. A.; Spence, R. A crystallographic study of solid benzene by neutron diffraction. *Proc. R. Soc. London, Ser. A* **1964**, *279*, 98-110.

(154) Seo, E. T.; Nelson, R. F.; Fritsch, J. M.; Marcoux, L. S.; Leedy, D. W.; Adams, R. N. Anodic Oxidation Pathways of Aromatic Amines. Electrochemical and Electron

Paramagnetic Resonance Studies. *J. Am. Chem. Soc.* **1966**, *88*, 3498-3503.

(155) Kumagai, A.; Fukumoto, H.; Yamamoto, T. Chemical and electrochemical oxidation of thiophene− pyridine and thiophene− pyrimidine co-oligomers in solutions. *The Journal of Physical Chemistry B* **2007**, *111*, 8020-8026.

(156) Geng, X.; Li, D.; Tang, K.; Wang, G.; Miao, Y.; Guo, K. π-Bridge dependent efficient aggregation-induced emission characteristic and significant mechanofluorochromic behavior. *Journal of Luminescence* **2022**, *248*, 118925.

(157) Coluccini, C.; Manfredi, N.; Calderon, E. H.; Salamone, M. M.; Ruffo, R.; Roberto, D.; Lobello, M. G.; De Angelis, F.; Abbotto, A. Photophysical and Electrochemical Properties of Thiophene-Based 2-Arylpyridines. *European Journal of Organic Chemistry* **2011**, *2011*, 5587-5598.

(158) Fakis, M.; Petropoulos, V.; Hrobarik, P.; Nociarova, J.; Osusky, P.; Maiuri, M.; Cerullo, G. Exploring Solvent and Substituent Effects on the Excited State Dynamics and Symmetry Breaking of Quadrupolar Triarylamine End-Capped Benzothiazole Chromophores by Femtosecond Spectroscopy. *The journal of physical chemistry. B* **2022**, *126*, 8532-8543.

(159) Gibson, G. L.; McCormick, T. M.; Seferos, D. S. Atomistic band gap engineering in donor-acceptor polymers. *Journal of the American Chemical Society* **2012**, *134*, 539-547.

(160) Lakowicz, J. R.: Mechanisms and Dynamics of Solvent Relaxation. In *Principles of Fluorescence Spectroscopy*; Lakowicz, J. R., Ed.; Springer US: Boston, MA, 1983; pp 217-255.

(161) Fung, S. Y.; Duhamel, J.; Chen, P. Solvent Effect on the Photophysical Properties of the Anticancer Agent Ellipticine. *J. Phys. Chem. A* **2006**, *110*, 11446-11454.

(162) Rettig, W.; Lippert, E. Twisting relaxation and dual fluorescence of p-N,N-dialkylaminobenzonitriles. *J. Mol. Struct.* **1980**, *61*, 17-22.

(163) Zachariasse, K. A.; Druzhinin, S. I.; Bosch, W.; Machinek, R. Intramolecular Charge Transfer with the Planarized 4-Aminobenzonitrile 1-tert-Butyl-6-cyano-1,2,3,4-tetrahydroquinoline (NTC6). *J. Am. Chem. Soc.* **2004**, *126*, 1705-1715.

(164) Ji, L.; Riese, S.; Schmiedel, A.; Holzapfel, M.; Fest, M.; Nitsch, J.; Curchod, B. F. E.; Friedrich, A.; Wu, L.; Al Mamari, H. H.; Hammer, S.; Pflaum, J.; Fox, M. A.; Tozer, D. J.; Finze, M.; Lambert, C.; Marder, T. B. Thermodynamic equilibrium between locally excited and charge-transfer states through thermally activated charge transfer in 1-(pyren-2'-yl)-o-carborane. *Chem Sci* **2022**, *13*, 5205-5219.

(165) Subuddhi, U.; Haldar, S.; Sankararaman, S.; Mishra, A. K. Photophysical behaviour of 1-(4-N,N-dimethylaminophenylethynyl)pyrene (DMAPEPy) in homogeneous media. *Photochem. Photobiol. Sci.* **2006**, *5*, 459-466.

(166) Grabowski, Z. R.; Rotkiewicz, K.; Rettig, W. Structural Changes Accompanying Intramolecular Electron Transfer: Focus on Twisted Intramolecular Charge-Transfer States and Structures. *Chem. Rev.* **2003**, *103*, 3899-4032.

(167) Scheller, Z. N.; Liese, D.; Siera, H.; Semleit, N.; Schmiedtchen, M.; Wölper,

C.; Haberhauer, G. The Origin of Dual-Emission in PLICT Compounds – an Empirical Approach. *Chem. Eur. J.*, *n/a*, e202304143.

(168) Wang, C.; Chi, W.; Qiao, Q.; Tan, D.; Xu, Z.; Liu, X. Twisted intramolecular charge transfer (TICT) and twists beyond TICT: from mechanisms to rational designs of bright and sensitive fluorophores. *Chem. Soc. Rev.* **2021**, *50*, 12656-12678.

(169) Louis, M.; Thomas, H.; Gmelch, M.; Haft, A.; Fries, F.; Reineke, S. Blue-Light-Absorbing Thin Films Showing Ultralong Room-Temperature Phosphorescence. *Adv. Mater.* **2019**, *31*, 1807887.

(170) Yang, J.; Zhen, X.; Wang, B.; Gao, X.; Ren, Z.; Wang, J.; Xie, Y.; Li, J.; Peng, Q.; Pu, K.; Li, Z. The influence of the molecular packing on the room temperature phosphorescence of purely organic luminogens. *Nat. Commun.* **2018**, *9*, 840.

(171) Taylor, P. N.; O'Connell, M. J.; McNeill, L. A.; Hall, M. J.; Aplin, R. T.; Anderson, H. L. Insulated Molecular Wires: Synthesis of Conjugated Polyrotaxanes by Suzuki Coupling in Water. *Angew. Chem. Int. Ed.* **2000**, *39*, 3456-3460.

(172) Martin, E.; Pulham, C. R.; Parsons, S. Experimental Crystal Structure Determination. *The Cambridge Crystallographic Data Centre* **2008**, CCDC 660790.

(173) Tong, J.; Wang, Y. J.; Wang, Z.; Sun, J. Z.; Tang, B. Z. Crystallization-Induced Emission Enhancement of a Simple Tolane-Based Mesogenic Luminogen. *J. Phys. Chem. C* **2015**, *119*, 21875-21881.

(174) Sebastian, E.; Sunny, J.; Hariharan, M. Excimer evolution hampers symmetry-broken charge-separated states. *Chemical Science* **2022**, *13*, 10824-10835.

(175) Sung, J.; Nowak-Król, A.; Schlosser, F.; Fimmel, B.; Kim, W.; Kim, D.; Würthner, F. Direct Observation of Excimer-Mediated Intramolecular Electron Transfer in a Cofacially-Stacked Perylene Bisimide Pair. *J. Am. Chem. Soc.* **2016**, *138*, 9029-9032.

(176) Margulies, E. A.; Shoer, L. E.; Eaton, S. W.; Wasielewski, M. R. Excimer formation in cofacial and slip-stacked perylene-3,4:9,10-bis(dicarboximide) dimers on a redox-inactive triptycene scaffold. *PCCP* **2014**, *16*, 23735-23742.

(177) Koren, A. B.; Curtis, M. D.; Francis, A. H.; Kampf, J. W. Intermolecular Interactions in π-Stacked Conjugated Molecules. Synthesis, Structure, and Spectral Characterization of Alkyl Bithiazole Oligomers. *J. Am. Chem. Soc.* **2003**, *125*, 5040-5050.

(178) Dong, Y.; Lam, J. W. Y.; Qin, A.; Li, Z.; Sun, J.; Sung, H. H. Y.; Williams, I. D.; Tang, B. Z. Switching the light emission of (4-biphenylyl)phenyldibenzofulvene by morphological modulation: crystallization-induced emission enhancement. *Chem. Commun.* **2007**, 40-42.

(179) Dong, Y.; Lam, J. W. Y.; Qin, A.; Sun, J.; Liu, J.; Li, Z.; Sun, J.; Sung, H. H. Y.; Williams, I. D.; Kwok, H. S.; Tang, B. Z. Aggregation-induced and crystallization-enhanced emissions of 1,2-diphenyl-3,4-bis(diphenylmethylene)-1-cyclobutene. *Chem. Commun.* **2007**, 3255-3257.

(180) Karmakar, S.: Particle Size Distribution and Zeta Potential Based on Dynamic Light Scattering: Techniques to Characterise Stability and Surface

distribution of Charged Colloids. 2019; pp 117-159.

(181) Cai, X.-M.; Lin, Y.; Tang, Z.; Zhang, X.; Mu, T.; Huang, S.; Zhao, Z.; Tang, B. Z. Filling the gap between molecular and aggregate states: how does molecular packing affect photophysical properties? *Chem. Eng. J.* **2023**, *451*, 138627.

(182) Zhao, N.; Yang, Z.; Lam, J. W. Y.; Sung, H. H. Y.; Xie, N.; Chen, S.; Su, H.; Gao, M.; Williams, I. D.; Wong, K. S.; Tang, B. Z. Benzothiazolium-functionalized tetraphenylethene: an AIE luminogen with tunable solid-state emission. *Chem. Commun.* **2012**, *48*, 8637-8639.

(183) Winzenberg, K. N.; Kemppinen, P.; Scholes, F. H.; Collis, G. E.; Shu, Y.; Birendra Singh, T.; Bilic, A.; Forsyth, C. M.; Watkins, S. E. Indan-1,3-dione electron-acceptor small molecules for solution-processable solar cells: a structure–property correlation. *Chem. Commun.* **2013**, *49*, 6307-6309.

(184) He, D.; Zhao, F.; Jiang, L.; Wang, C. A–D–A small molecule acceptors with ladder-type arenes for organic solar cells. *J. Mater. Chem. A* **2018**, *6*, 8839-8854.

(185) Hotta, S.; Yamao, T. The thiophene/phenylene co-oligomers: exotic molecular semiconductors integrating high-performance electronic and optical functionalities. *J. Mater. Chem.* **2011**, *21*, 1295-1304.

(186) Ma, S.; Du, S.; Pan, G.; Dai, S.; Xu, B.; Tian, W. Organic molecular aggregates: From aggregation structure to emission property. *Aggregate* **2021**, *2*, e96.

(187) Schillmöller, T.; Herbst-Irmer, R.; Stalke, D. Insights into Excimer Formation Factors from Detailed Structural and Photophysical Studies in the Solid-State. *Adv. Opt. Mater.* **2021**, *9*, 2001814.

(188) Kumagai, A.; Fukumoto, H.; Yamamoto, T. Chemical and Electrochemical Oxidation of Thiophene−Pyridine and Thiophene−Pyrimidine Co-Oligomers in Solutions. *The Journal of Physical Chemistry B* **2007**, *111*, 8020-8026.

(189) Qian, G.; Dai, B.; Luo, M.; Yu, D.; Zhan, J.; Zhang, Z.; Ma, D.; Wang, Z. Y. Band Gap Tunable, Donor−Acceptor−Donor Charge-Transfer Heteroquinoid-Based Chromophores: Near Infrared Photoluminescence and Electroluminescence. *Chem. Mater.* **2008**, *20*, 6208-6216.

(190) Yadigarli, A.; Song, Q.; Druzhinin, S. I.; Schönherr, H. Probing of local polarity in poly(methyl methacrylate) with the charge transfer transition in Nile red. *Beilstein Journal of Organic Chemistry* **2019**, *15*, 2552-2562.

(191) He, Y.; Wang, Y.; Guo, Y.; Ma, L. Fine adjustment of emission wavelength, light-conversion quality, photostability of blue-violet light conversion agents based on FRET effect. *Dyes Pigm.* **2023**, *217*, 111429.

(192) Li, K.; Zhang, P.; Ge, L.; Ren, H.; Yu, C.; Chen, X.; Zhao, Y. Concentration-dependent photodegradation kinetics and hydroxyl-radical oxidation of phenicol antibiotics. *Chemosphere* **2014**, *111*, 278-282.

(193) Scurlock, R. D.; Wang, B.; Ogilby, P. R.; Sheats, J. R.; Clough, R. L. Singlet Oxygen as a Reactive Intermediate in the Photodegradation of an Electroluminescent Polymer. *J. Am. Chem. Soc.* **1995**, *117*, 10194-10202.

(194) Dam, N.; Scurlock, R. D.; Wang, B.; Ma, L.; Sundahl, M.; Ogilby, P. R.

Singlet Oxygen as a Reactive Intermediate in the Photodegradation of Phenylenevinylene Oligomers. *Chem. Mater.* **1999**, *11*, 1302-1305.

(195) Yimsiri, P.; Mackley, M. R. Spin and dip coating of light-emitting polymer solutions: Matching experiment with modelling. *Chem. Eng. Sci.* **2006**, *61*, 3496-3505.

(196) Ma, S.; Zhou, K.; Hu, M.; Li, Q.; Liu, Y.; Zhang, H.; Jing, J.; Dong, H.; Xu, B.; Hu, W.; Tian, W. Integrating Efficient Optical Gain in High-Mobility Organic Semiconductors for Multifunctional Optoelectronic Applications. *Adv. Funct. Mater.* **2018**, *28*, 1802454.

(197) Luo, Q.; Li, L.; Ma, H.; Lv, C.; Jiang, X.; Gu, X.; An, Z.; Zou, B.; Zhang, C.; Zhang, Y. Deep-red fluorescence from isolated dimers: a highly bright excimer and imaging in vivo. *Chem. Sci.* **2020**, *11*, 6020-6025.

(198) Chen, C.-A.; Wang, S.-C.; Tung, S.-H.; Su, W.-F. Oligo(ethylene glycol) side chain effect on the physical properties and molecular arrangement of oligothiophene–isoindigo based conjugated polymers. *Soft Matter* **2019**, *15*, 9468-9473.

Appendix I List of molecules and abbreviations

Table S1-1 Table of molecules.

Code Name	**Structure**
M1	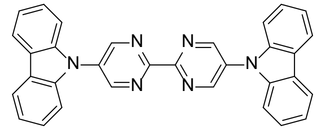
M2	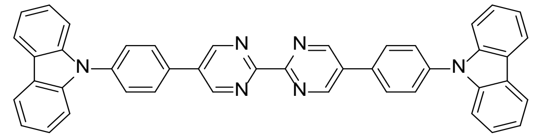
M3	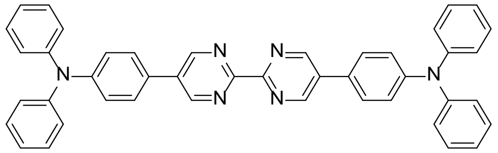
M4	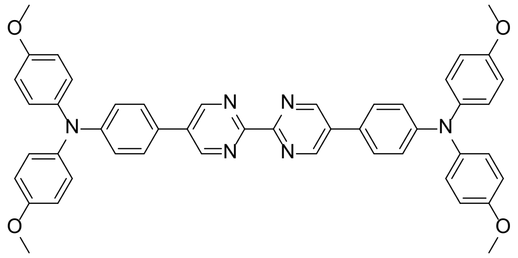
M5	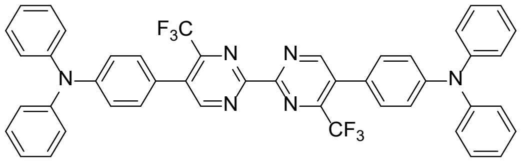
M6	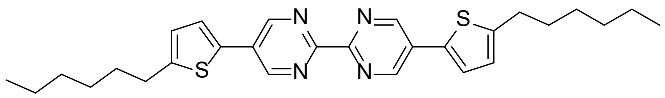
M7	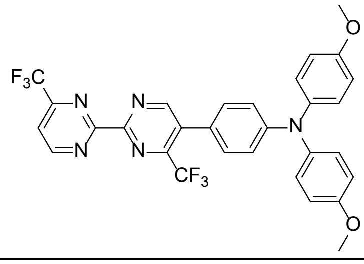
CBP	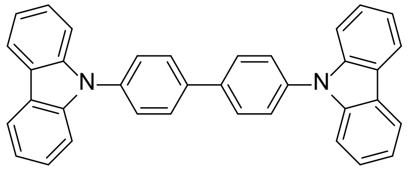

Table S1-2 List of abbreviatons

Abbreviation	Full term
LED	Light-emitting diode
WLED	White-light-emitting diode
EL	Electroluminescence
LCD	Liquid crystal display
PL	Photoluminescence
CT	Charge transfer
pc-WLED	Phosphor-converted white light-emitting diodes
HOMO	Highest Occupied Molecular Orbital
LUMO	Lowest Unoccupied Molecular Orbital
CCT	Calculated color temperature
CRI	Color rendering index
CIE	Commission Internationale de L'éclairage
OLED	Organic light-emitting diode
HTM	Hole transport material
ETM	Electron transport materials
PLED	Polymer light-emitting diode
EQE	External quantum efficiency
TADF	Thermal activated delayed fluorescence
PLQY	Photoluminescence quantum yield
YAG	Yttrium aluminum garnet
IP	Inorganic phosphors
D-A	Donor-acceptor
ICT	Internal charge transfer
AIE	Aggregation-induced emission
ACQ	Aggregation caused quenching
RIR	Restriction of intramolecular rotations
NLO	Non-linear optical
BPM	2,2'-bipyrimidine
HRMS	High resolution mass spectrometry
XRD	X-ray diffraction
TCSPC	Time-Correlated Single Photon Counting
IR	Instrument respond
MCS	Multichannel scaling
FlT	Fluorescence lifetime
LE	Locally excited
ISC	Intersystem crossing
FWHM	Full width at half maximum
DLS	Dynamic light scattering
CIEE	Crystallization-induced emission enhancement

Appendix II NMR and HR-MS spectra

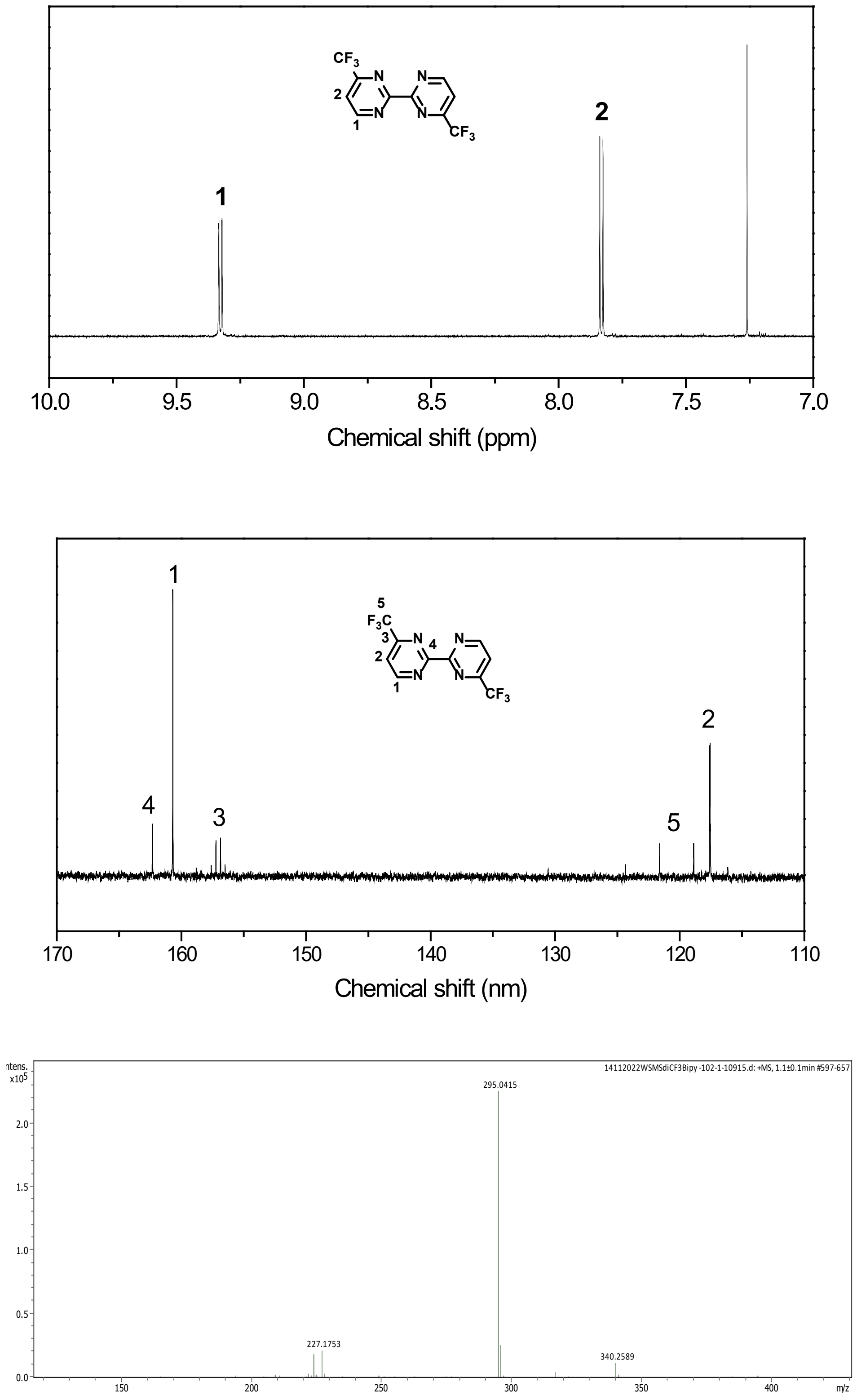

Figure S2-1 ^{1}H, ^{13}C NMR and ESM-Pos MS spectrum of **2a**.

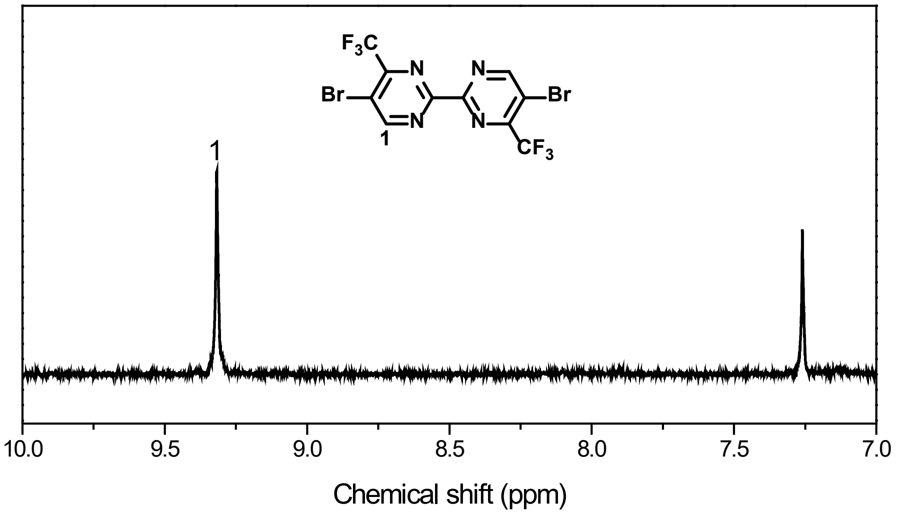

Figure S2-2 ^{1}H NMR spectrum of **2b**.

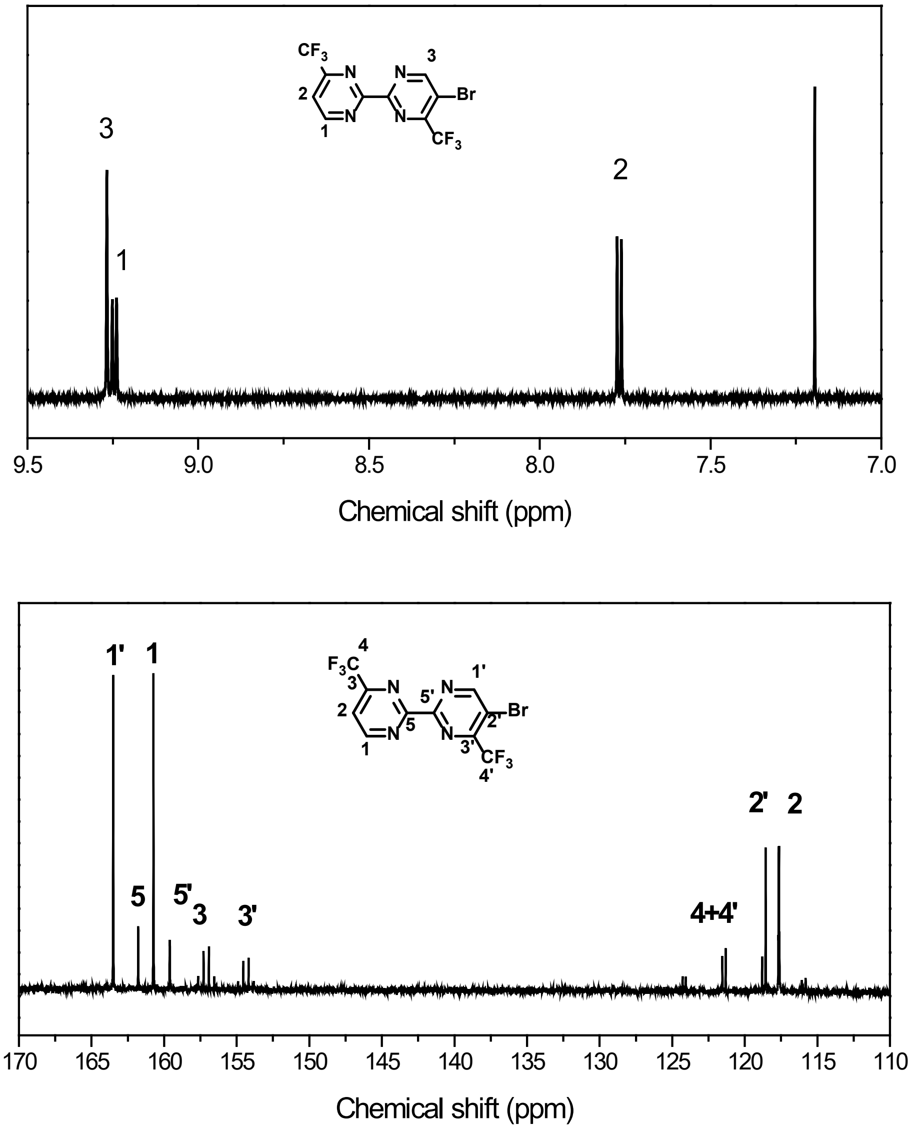

Figure S2-3. ^{1}H and ^{13}C NMR spectra of **2c**.

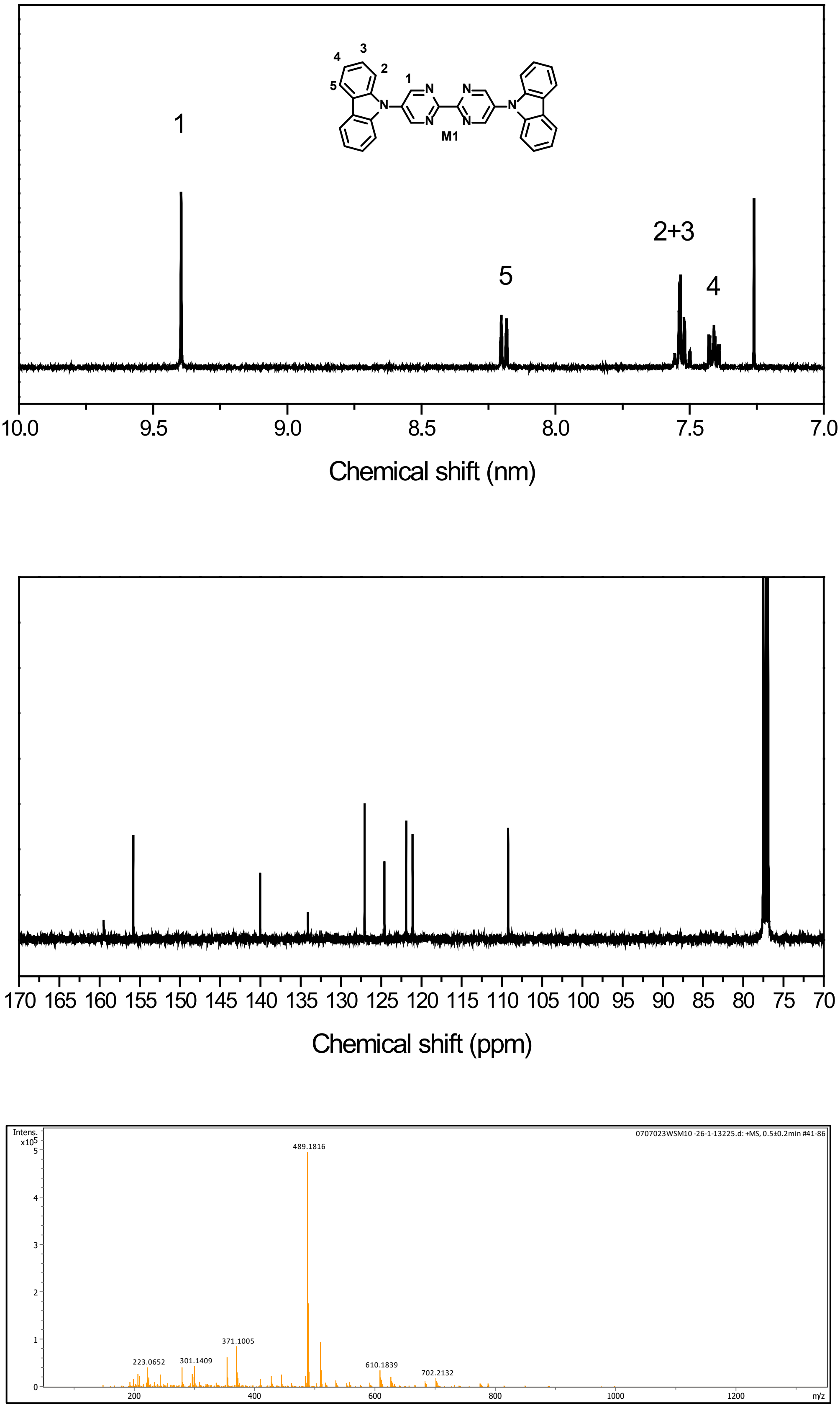

Figure S2-4 ^{1}H, ^{13}C NMR and ESM-Pos MS spectra of **M1**.

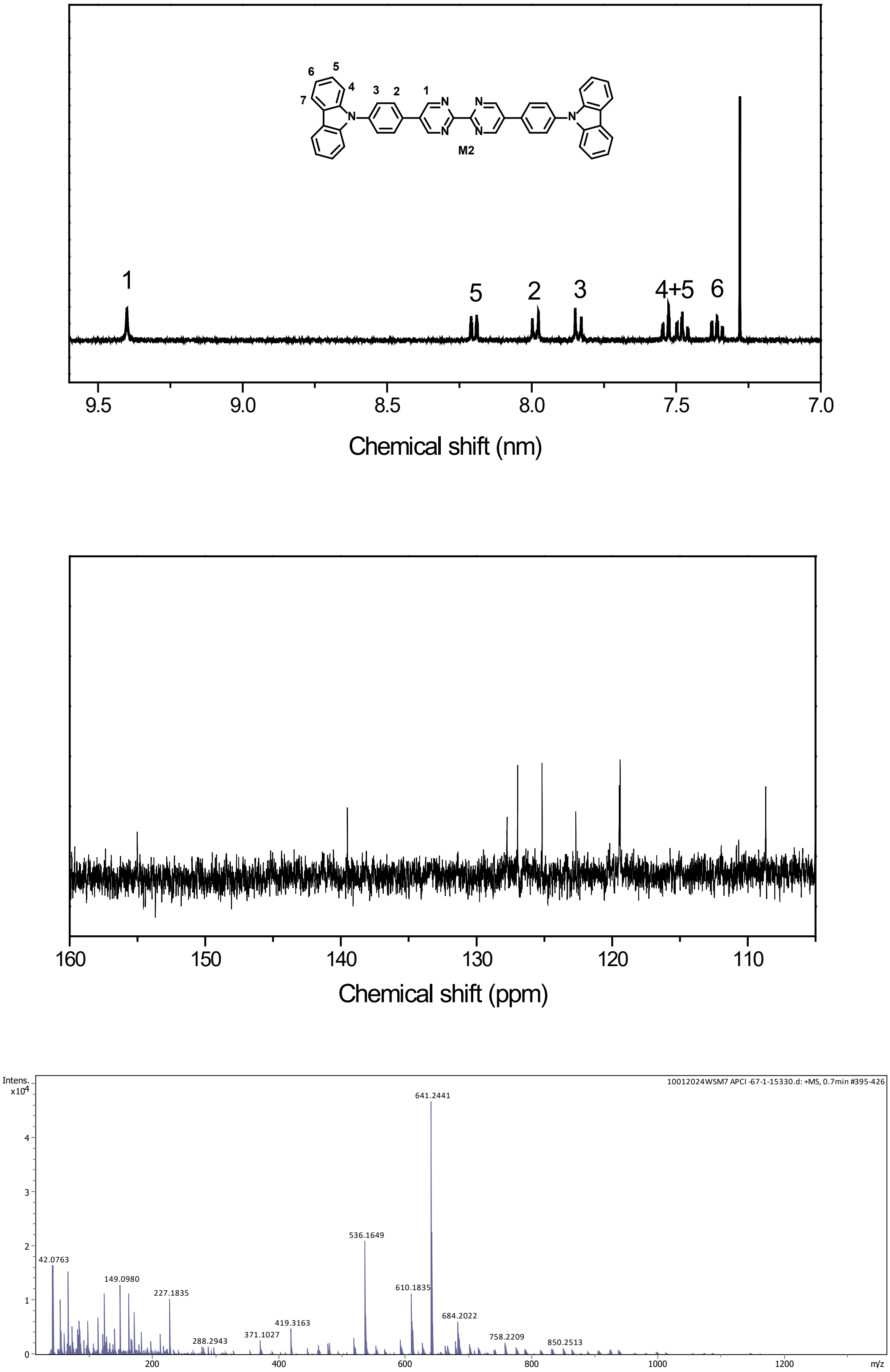

Figure S2-5 ^{1}H, ^{13}C NMR and ESM-Pos MS spectra of **M2**.

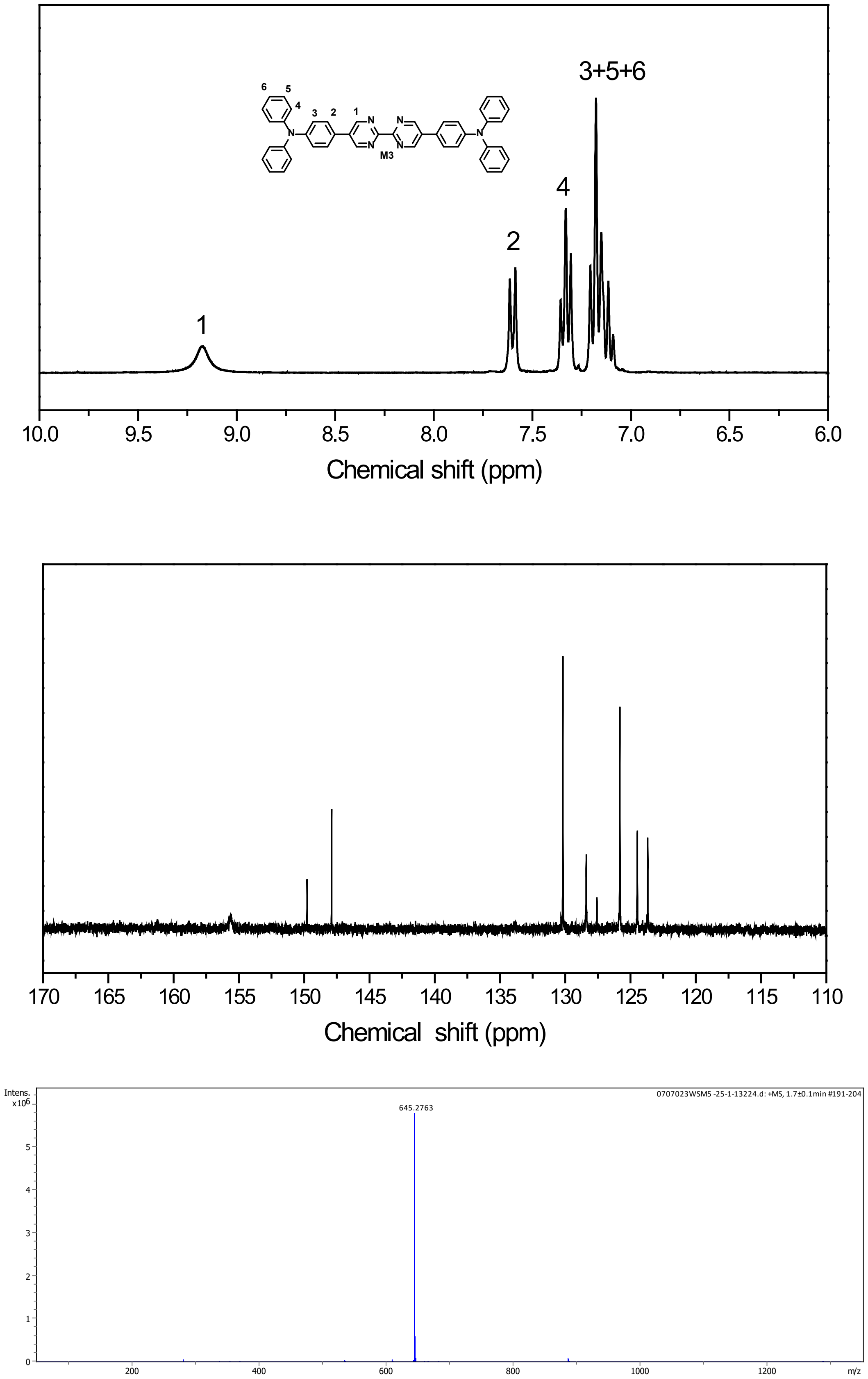

Figure S2-6 ^{1}H, ^{13}C NMR and ESM-Pos MS spectra of **M3**.

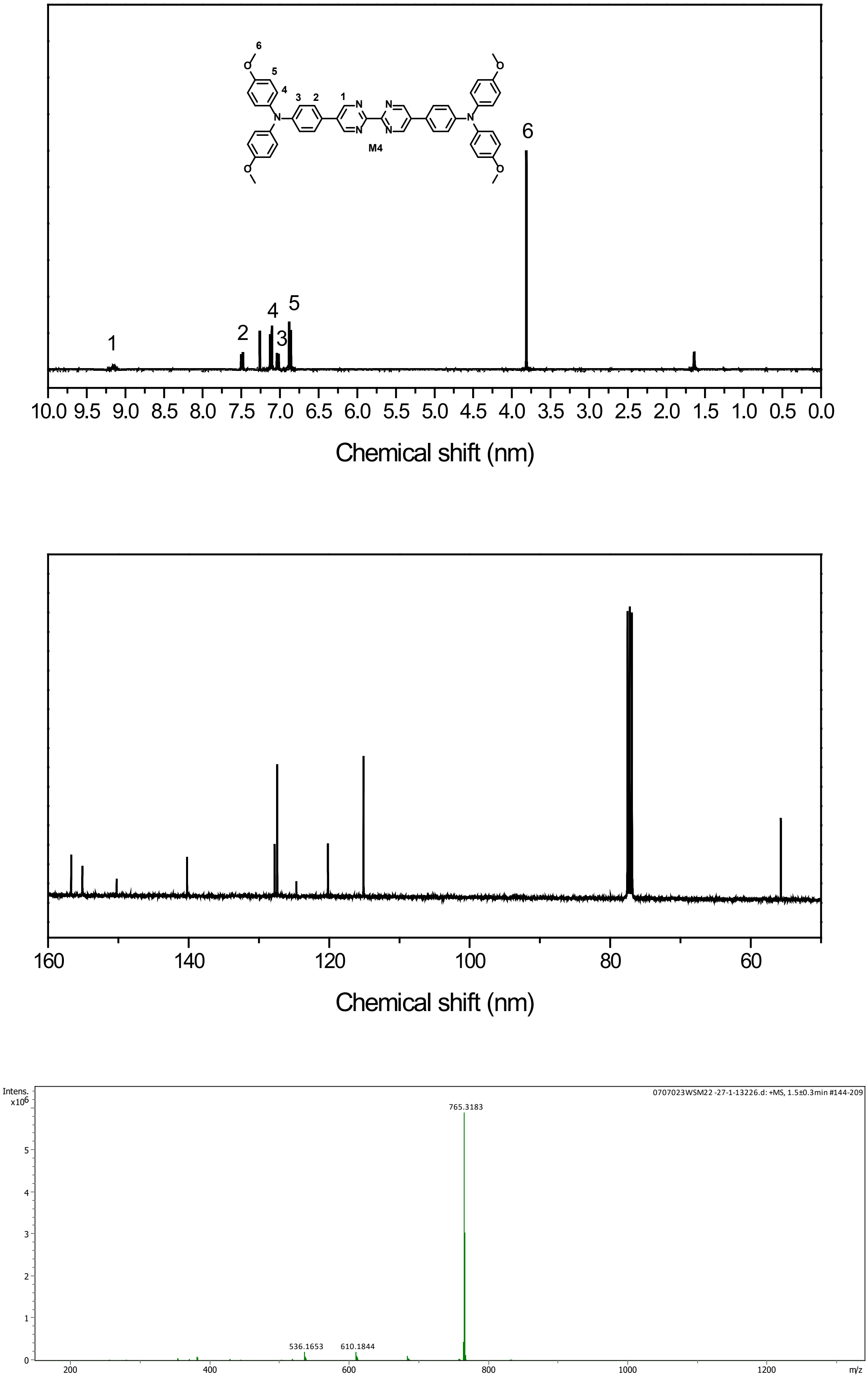

Figure S2-7 ^{1}H, ^{13}C NMR and ESM-Pos MS spectra of **M4.**

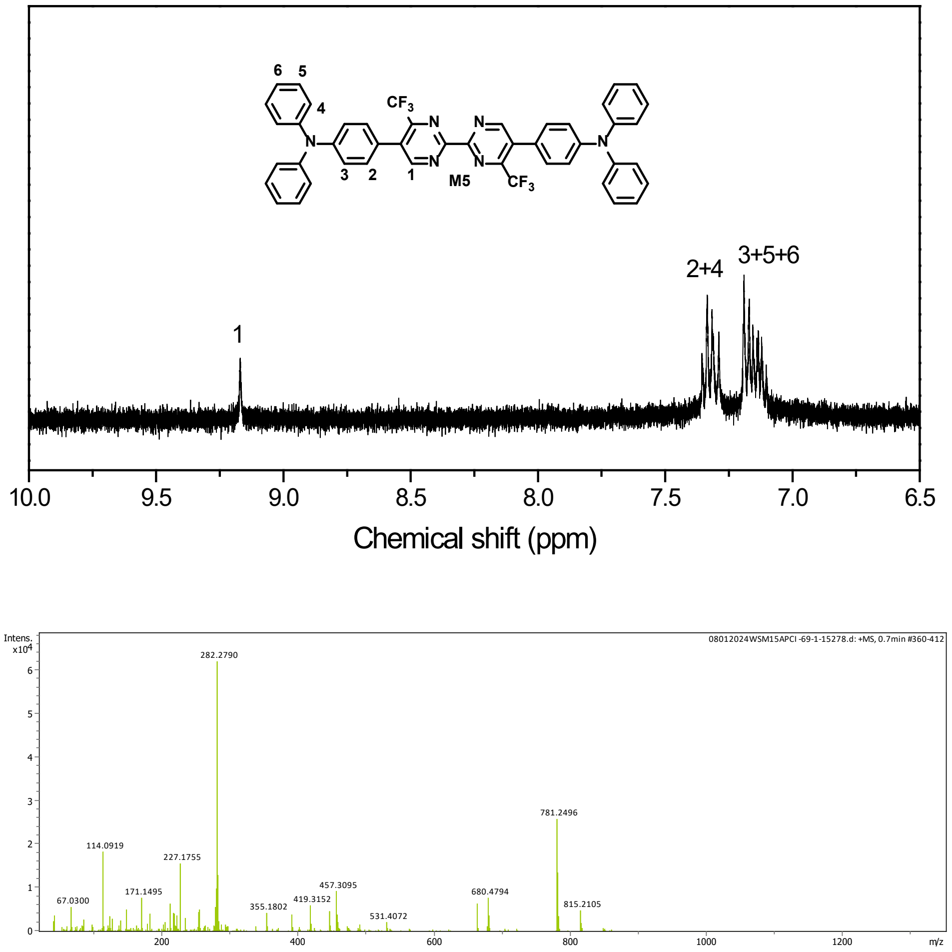

Figure S2-8. ^{1}H NMR and ESM-Pos MS spectra of **M5.**

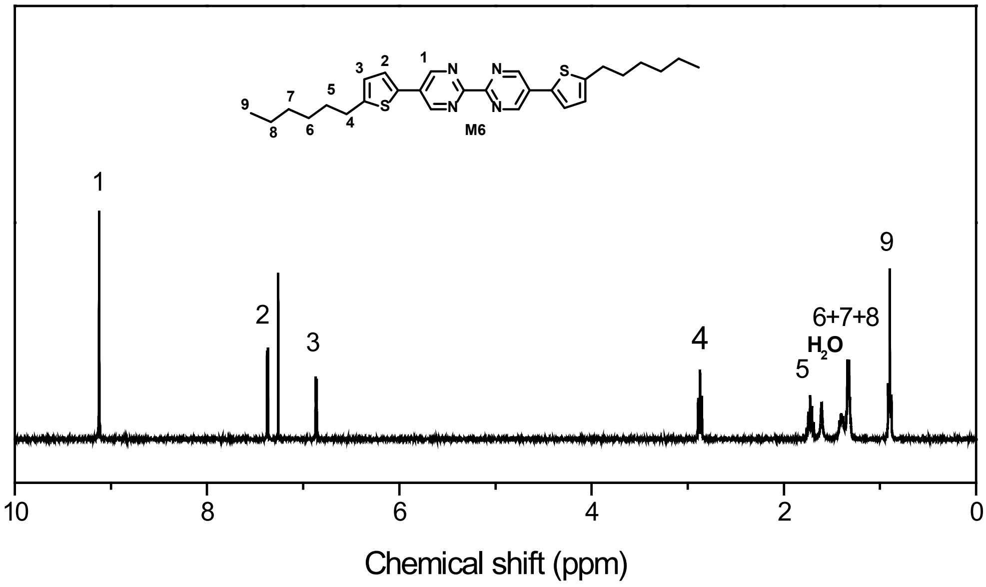

Figure S2-9. ^{1}H NMR spectra of **M6.**

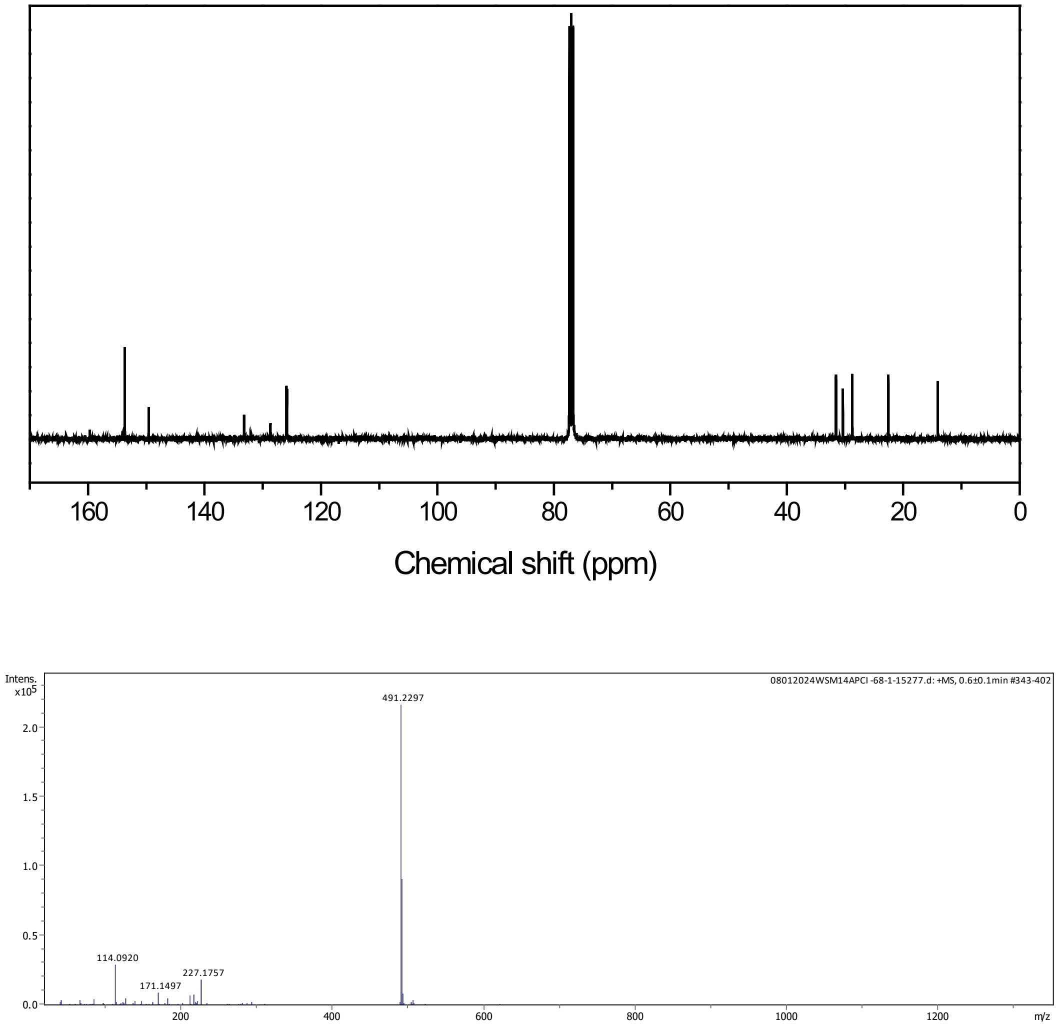

Figure S2-10. ^{13}C NMR and ESM-Pos MS spectra of **M6.**

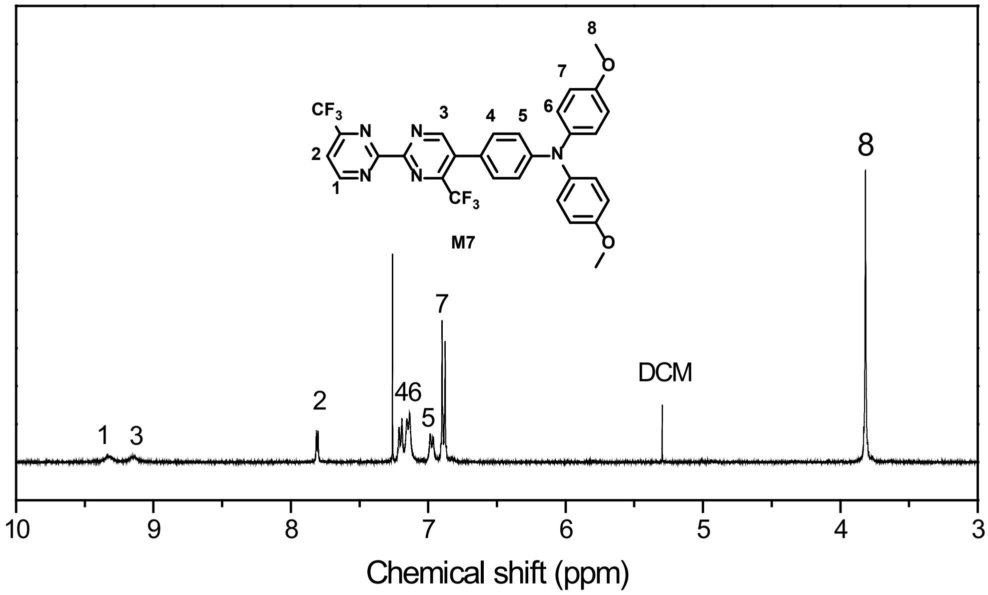

Figure S2-11. ^{1}H NMR spectra of **M7.**

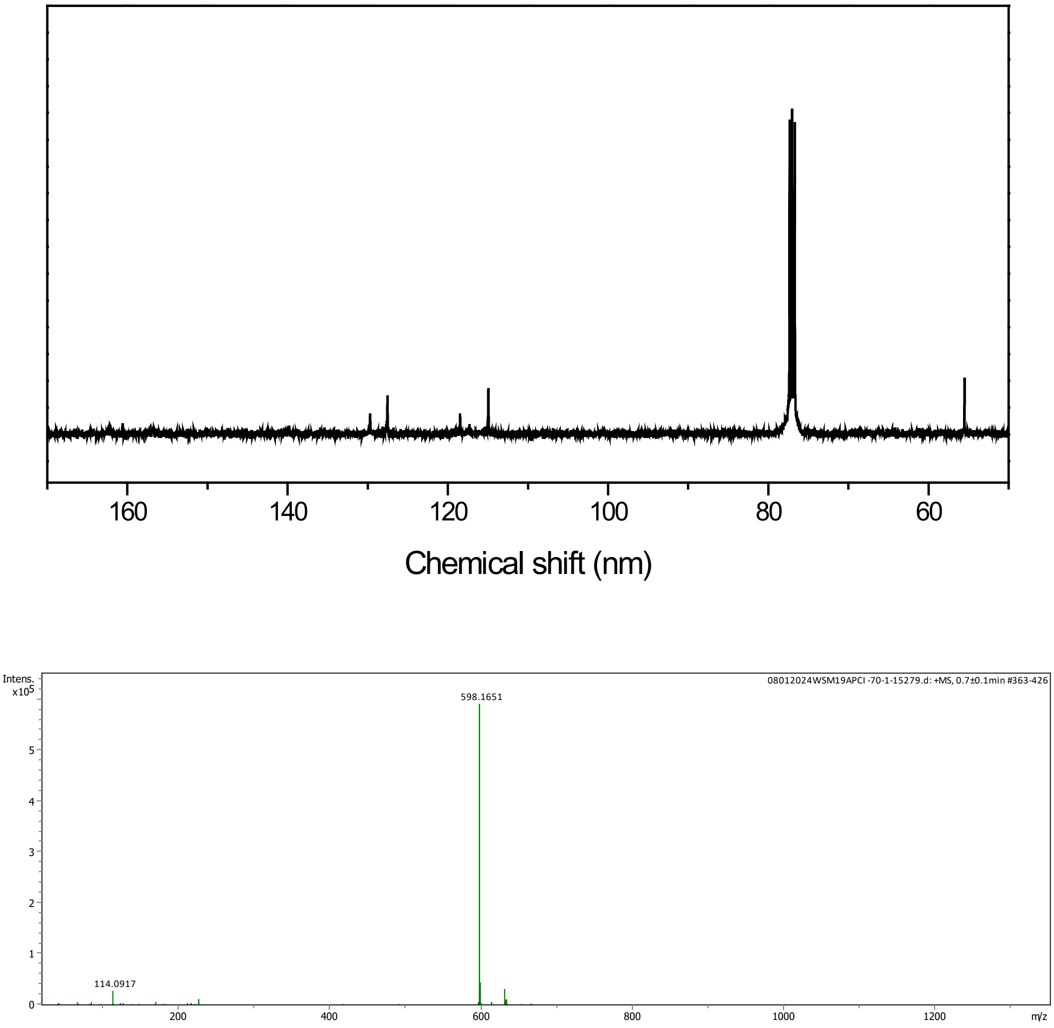

Figure S2-12. ^{13}C NMR and ESM-Pos MS spectra of **M7.**

Appendix III Single-crystal X-ray diffraction data

Table S3-1 Crystal data and structure refinement for **M1**.

Identification code	WSM10_CHCL3 hex
Empirical formula	$C_{33}H_{21}Cl_3N_6$
Formula weight	607.91
Temperature/K	150
Crystal system	orthorhombic
Space group	$P2_12_12_1$
a/Å	6.1878(2)
b/Å	15.7946(7)
c/Å	30.0898(12)
α /°	90
β /°	90
γ /°	90
Volume/Å^3	2940.8(2)
Z	4
ρ_{calc}g/cm^3	1.373
μ /mm^{-1}	0.346
F(000)	1248.0
Crystal size/mm^3	0.5 × 0.2 × 0.05
Radiation	Mo Kα (λ = 0.71073)
2Θ range for data collection/°	4.81 to 51.362
Index ranges	$-7 \leqslant h \leqslant 7, -19 \leqslant k \leqslant 17, -27 \leqslant l \leqslant 36$
Reflections collected	13688
Independent reflections	5614 [R_{int} = 0.0659, R_{sigma} = 0.1007]
Data/restraints/parameters	5614/96/417
Goodness-of-fit on F^2	1.028
Final R indexes [I>=2σ (I)]	R_1 = 0.0899, wR_2 = 0.2577
Final R indexes [all data]	R_1 = 0.1400, wR_2 = 0.2827
Largest diff. peak/hole / e Å^{-3}	0.43/-0.60

Table S3-2 Fractional Atomic Coordinates ($\times 10^4$) and Equivalent Isotropic Displacement Parameters (Å$^2\times 10^3$) for **M1**. U_{eq} is defined as 1/3 of of the trace of the orthogonalised UIJ tensor.

Atom	**x**	**y**	**z**	**U(eq)**
Cl01	6234.5(11)	4732.6(9)	5500.1(6)	46.0(3)
Cl02	-2974.1(11)	1847.8(9)	7913.4(6)	47.0(3)
Cl03	10393.1(11)	-1446.0(9)	11176.2(6)	45.4(3)
Cl04	4250.3(11)	5766.6(8)	6067.3(7)	47.0(3)
Cl05	-979.0(11)	1042.9(8)	7137.4(7)	49.4(3)
Cl06	12406.4(11)	-2325.2(8)	10464.9(7)	50.0(3)
Cl07	5498.1(11)	4339.2(9)	6941.1(6)	53.7(4)
Cl08	-2364.1(11)	2576.2(9)	6467.9(6)	52.8(4)
Cl09	11067.4(12)	-825.5(10)	9726.1(6)	56.3(4)
Cl0A	6389.3(14)	7065.8(8)	7228.9(6)	55.0(4)
Cl0B	7668.8(16)	8575.9(11)	6328.1(8)	75.8(5)
Cl0C	4892.5(16)	8537.5(11)	6579.5(11)	94.5(6)
N00F	3284(3)	3037(2)	6707.7(16)	26.2(8)
N00G	1295(3)	2316(2)	7191.3(16)	27.7(8)
N00H	-78(3)	3779(2)	6650.5(16)	26.8(8)
N00I	13321(3)	366(2)	9985.2(16)	28.1(8)
N00J	1920(3)	4470(2)	6127.7(16)	28.1(8)
N00K	-2896(3)	8269(2)	4601.8(17)	28.8(8)
N00L	15298(3)	1094(2)	9492.0(17)	30.8(8)
N00M	6222(3)	-1514(2)	8478(2)	39.2(9)
N00N	10292(3)	4843(2)	8117(2)	41.7(10)
C00O	1227(4)	3804(2)	6511.7(17)	21.0(8)
C00P	13246(4)	1843(2)	9311.3(18)	22.8(9)
C00Q	-844(4)	5998(2)	5573.9(19)	23.4(9)
C00R	1989(4)	3003(3)	6828.2(18)	22.9(9)
C00S	-129(4)	5225(2)	5912.4(18)	22.5(8)
C00T	-2090(4)	6233(3)	5881.5(19)	24.1(9)
C00U	-2757(4)	6966(3)	5563.5(18)	25.5(9)
C00W	3352(4)	1574(2)	7368.1(18)	22.9(9)
C00X	12490(4)	2622(3)	9005(2)	25.7(9)
C00Y	14616(4)	397(2)	9858.0(18)	23.5(9)
C00Z	-2226(4)	7504(3)	4927(2)	26.0(9)
C010	3950(4)	2317(3)	6985.8(19)	27.0(9)
C011	14608(4)	1796(3)	9234(2)	27.9(9)
C012	-737(4)	4487(3)	6346.5(19)	27.2(9)
C013	4108(4)	772(2)	7665(2)	25.5(9)
C014	-319(4)	6541(2)	4933.9(19)	25.8(9)

C015	12996(4)	3197(3)	8369.1(19)	28.2(9)
C016	1231(4)	5173(3)	5839.2(19)	27.3(9)
C017	-995(4)	7269(2)	4613(2)	27.4(9)
C018	5325(4)	579(3)	7320(2)	26.5(9)
C019	5505(4)	-736(3)	8213(2)	32.2(10)
C01A	12658(4)	1084(3)	9712.0(19)	27.0(9)
C01B	6022(4)	-162(3)	7588(2)	31.1(10)
C01C	1998(4)	1614(3)	7445(2)	29.6(10)
C01D	3614(4)	195(3)	8293(2)	29.4(10)
C01E	-4256(4)	8303(3)	4683(2)	32.6(10)
C01F	10535(4)	3538(3)	9026(2)	32.2(10)
C01G	11248(4)	2810(3)	9328(2)	30.8(10)
C01H	-2172(4)	9015(3)	4260(2)	30.9(10)
C01I	4305(4)	-545(3)	8567(2)	34.1(10)
C01J	-1709(4)	2007(3)	7204(2)	28.0(9)
C01K	-4935(4)	7621(3)	4693(2)	31.6(10)
C01L	11044(4)	4106(3)	8398(2)	33.5(10)
C01M	12025(4)	5863(3)	7810(2)	33.2(10)
C01N	12280(4)	3915(3)	8078(2)	32.9(10)
C01O	5543(4)	-2258(3)	8899(2)	34.6(11)
C01P	10904(4)	5614(3)	7683(2)	34.8(10)
C01Q	11678(4)	-1333(3)	10479.3(19)	30.6(10)
C01R	8352(4)	4166(3)	8117(2)	34.8(11)
C01S	4927(4)	4741(3)	6165.2(19)	30.2(10)
C01T	8911(4)	4807(3)	8222(2)	34.4(10)
C01U	4443(4)	-2464(3)	8725(2)	37.7(11)
C01V	-1116(4)	9183(3)	4495(2)	36.8(11)
C01W	8162(4)	-865(3)	8538(2)	36.2(11)
C01X	12605(5)	6606(3)	7397(2)	39.8(11)
C01Y	-6280(5)	7653(3)	4785(2)	42.2(12)
C01Z	7603(4)	-1505(3)	8430(2)	37.5(11)
C020	-2520(5)	9595(3)	3675(2)	39.8(12)
C021	7010(5)	4148(3)	8210(2)	46.5(13)
C022	-403(5)	9903(3)	4162(2)	43.4(12)
C023	10349(5)	6127(3)	7138(2)	41.5(12)
C024	-1814(5)	10338(3)	3340(2)	50.4(14)
C025	9514(5)	-887(4)	8486(2)	48.9(13)
C026	12089(5)	7118(3)	6843(3)	49.1(13)
C027	-4995(5)	9022(3)	4767(3)	47.6(13)
C028	3800(5)	-3196(3)	9132(3)	51.6(14)
C029	6762(5)	5388(4)	8541(2)	51.5(15)

C02A	-754(5)	10475(3)	3585(3)	50.9(14)
C02B	6217(5)	4762(4)	8410(2)	50.2(14)
C02C	5989(6)	-2799(3)	9477(2)	50.1(14)
C02D	-6999(5)	8381(4)	4856(3)	52.2(14)
C02E	8104(4)	5420(3)	8446(2)	41.4(12)
C02F	10948(5)	6874(3)	6722(2)	50.5(14)
C02G	5303(7)	-3516(4)	9865(2)	68(2)
C02H	10273(5)	-1565(4)	8360(3)	60.6(16)
C02I	8408(5)	-2164(3)	8263(3)	56.4(15)
C02J	6274(5)	8179(3)	6914(3)	55.2(15)
C02K	4225(7)	-3713(4)	9695(3)	65.8(18)
C02L	-6346(5)	9072(4)	4831(3)	60.9(16)
C02M	9721(6)	-2187(4)	8241(3)	77(2)

Table S3-3 Crystal data and structure refinement for **M2**.

Identification code	**M2**
Empirical formula	$C_{46}H_{30}Cl_6N_6$
Formula weight	879.46
Temperature/K	150
Crystal system	orthorhombic
Space group	Pbca
a/Å	9.0296(3)
b/Å	25.6470(11)
c/Å	18.0230(7)
α /°	90
β /°	90
γ /°	90
Volume/Å^3	4173.8(3)
Z	4
ρ_{calc}g/cm^3	1.400
μ /mm^{-1}	0.454
F(000)	1800.0
Crystal size/mm^3	0.291 × 0.128 × 0.127
Radiation	Mo Kα (λ = 0.71073)
2Θ range for data collection/°	4.52 to 61.186
Index ranges	$-8 \leqslant h \leqslant 12$, $-36 \leqslant k \leqslant 34$, $-25 \leqslant l \leqslant 24$
Reflections collected	31988
Independent reflections	5911 [R_{int} = 0.0285, R_{sigma} = 0.0296]
Data/restraints/parameters	5911/0/262
Goodness-of-fit on F^2	1.061
Final R indexes [I>=2σ (I)]	R_1 = 0.0523, wR_2 = 0.1410
Final R indexes [all data]	R_1 = 0.0827, wR_2 = 0.1563
Largest diff. peak/hole / e Å^{-3}	0.92/-0.69

Table S3-4 Fractional Atomic Coordinates (×10^4) and Equivalent Isotropic Displacement Parameters ($Å^2$×10^3) for **M2**. U_{eq} is defined as 1/3 of of the trace of the orthogonalised UIJ tensor.

Atom	**x**	**y**	**z**	**$U_{(eq)}$**
Cl01	9609.7(8)	5103.9(3)	6532.8(5)	62.9(2)
Cl02	7194.6(8)	5676.3(3)	7179.2(4)	60.8(2)
Cl03	8898.8(8)	6128.3(2)	5989.0(5)	65.2(2)
N004	63.2(16)	7993.6(5)	6148.8(9)	22.9(3)
N005	3184.0(16)	5277.7(5)	4864.9(9)	23.6(3)
N006	5348.3(17)	5614.7(6)	5440.9(10)	28.7(4)
C007	-1406.0(19)	8002.2(6)	6381.6(10)	21.6(4)
C008	2356.3(19)	6622.4(6)	5586.8(10)	20.8(3)
C009	521.7(19)	7276.3(6)	5299.7(10)	22.1(4)
C00A	3146.2(19)	6134.3(6)	5400.4(10)	21.4(3)
C00B	856.1(19)	7534.3(6)	5949.8(10)	21.6(3)
C00C	4592.2(19)	5247.1(6)	5084.5(10)	22.0(4)
C00D	1276.9(19)	6821.0(6)	5115.0(10)	22.2(4)
C00E	2480(2)	5719.3(6)	5030.9(10)	23.7(4)
C00F	-1761(2)	8517.0(7)	6600.9(10)	24.5(4)
C00G	-441(2)	8823.5(7)	6518.5(10)	25.6(4)
C00H	666(2)	8488.7(6)	6243.2(10)	23.8(4)
C00I	2683(2)	6887.2(7)	6239.8(11)	27.4(4)
C00J	1943(2)	7344.2(7)	6422.9(11)	27.2(4)
C00K	-2409(2)	7594.5(7)	6425.0(11)	27.5(4)
C00L	4613(2)	6054.9(7)	5587.2(12)	28.9(4)
C00M	2099(2)	8655.8(8)	6091.6(12)	31.8(4)
C00N	-3818(2)	7711.0(9)	6679.5(11)	33.9(5)
C00O	-3197(2)	8620.0(8)	6854.5(11)	33.1(5)
C00P	-71(3)	9342.2(7)	6665.0(12)	36.1(5)
C00Q	-4208(2)	8217.6(9)	6887.7(11)	37.4(5)
C00R	8186(2)	5552.8(7)	6363.0(12)	31.8(4)
C00S	2417(3)	9173.8(8)	6240.2(13)	41.0(5)
C00T	1352(3)	9510.6(8)	6529.9(13)	41.9(6)

Table S3-5 Crystal data and structure refinement for **M3**.

Identification code	**M3**
Empirical formula	$C_{46.67}H_{34.67}Cl_8N_6$
Formula weight	963.07
Temperature/K	150
Crystal system	triclinic
Space group	P-1
a/Å	10.4446(7)
b/Å	16.6702(11)
c/Å	21.2623(13)
α /°	70.555(5)
β /°	78.180(5)
γ /°	83.684(5)
Volume/Å^3	3413.4(4)
Z	3
ρ_{calc}g/cm^3	1.406
μ /mm^{-1}	0.536
F(000)	1478.0
Crystal size/mm^3	? × ? × ?
Radiation	Mo Kα (λ = 0.71073)
2Θ range for data collection/°	4.81 to 52
Index ranges	$-12 \leqslant h \leqslant 12, -20 \leqslant k \leqslant 20, -26 \leqslant l \leqslant 25$
Reflections collected	43550
Independent reflections	43550 [R_{int} = 0.0343, R_{sigma} = 0.0523]
Data/restraints/parameters	43550/0/820
Goodness-of-fit on F^2	1.111
Final R indexes [I>=2σ (I)]	R_1 = 0.0643, wR_2 = 0.2018
Final R indexes [all data]	R_1 = 0.1284, wR_2 = 0.2528
Largest diff. peak/hole / e Å^{-3}	1.70/-0.64

Table S3-6 Fractional Atomic Coordinates ($\times 10^4$) and Equivalent Isotropic Displacement Parameters ($Å^2 \times 10^3$) for **M3**. U_{eq} is defined as 1/3 of of the trace of the orthogonalised UIJ tensor.

Atom	x	y	z	$U_{(eq)}$
Cl01	6234.5(11)	4732.6(9)	5500.1(6)	46.0(3)
Cl02	-2974.1(11)	1847.8(9)	7913.4(6)	47.0(3)
Cl03	10393.1(11)	-1446.0(9)	11176.2(6)	45.4(3)
Cl04	4250.3(11)	5766.6(8)	6067.3(7)	47.0(3)
Cl05	-979.0(11)	1042.9(8)	7137.4(7)	49.4(3)
Cl06	12406.4(11)	-2325.2(8)	10464.9(7)	50.0(3)
Cl07	5498.1(11)	4339.2(9)	6941.1(6)	53.7(4)
Cl08	-2364.1(11)	2576.2(9)	6467.9(6)	52.8(4)
Cl09	11067.4(12)	-825.5(10)	9726.1(6)	56.3(4)
Cl0A	6389.3(14)	7065.8(8)	7228.9(6)	55.0(4)
Cl0B	7668.8(16)	8575.9(11)	6328.1(8)	75.8(5)
Cl0C	4892.5(16)	8537.5(11)	6579.5(11)	94.5(6)
N00F	3284(3)	3037(2)	6707.7(16)	26.2(8)
N00G	1295(3)	2316(2)	7191.3(16)	27.7(8)
N00H	-78(3)	3779(2)	6650.5(16)	26.8(8)
N00I	13321(3)	366(2)	9985.2(16)	28.1(8)
N00J	1920(3)	4470(2)	6127.7(16)	28.1(8)
N00K	-2896(3)	8269(2)	4601.8(17)	28.8(8)
N00L	15298(3)	1094(2)	9492.0(17)	30.8(8)
N00M	6222(3)	-1514(2)	8478(2)	39.2(9)
N00N	10292(3)	4843(2)	8117(2)	41.7(10)
C00O	1227(4)	3804(2)	6511.7(17)	21.0(8)
C00P	13246(4)	1843(2)	9311.3(18)	22.8(9)
C00Q	-844(4)	5998(2)	5573.9(19)	23.4(9)
C00R	1989(4)	3003(3)	6828.2(18)	22.9(9)
C00S	-129(4)	5225(2)	5912.4(18)	22.5(8)
C00T	-2090(4)	6233(3)	5881.5(19)	24.1(9)
C00U	-2757(4)	6966(3)	5563.5(18)	25.5(9)
C00W	3352(4)	1574(2)	7368.1(18)	22.9(9)
C00X	12490(4)	2622(3)	9005(2)	25.7(9)
C00Y	14616(4)	397(2)	9858.0(18)	23.5(9)
C00Z	-2226(4)	7504(3)	4927(2)	26.0(9)
C010	3950(4)	2317(3)	6985.8(19)	27.0(9)
C011	14608(4)	1796(3)	9234(2)	27.9(9)
C012	-737(4)	4487(3)	6346.5(19)	27.2(9)
C013	4108(4)	772(2)	7665(2)	25.5(9)
C014	-319(4)	6541(2)	4933.9(19)	25.8(9)

C015	12996(4)	3197(3)	8369.1(19)	28.2(9)
C016	1231(4)	5173(3)	5839.2(19)	27.3(9)
C017	-995(4)	7269(2)	4613(2)	27.4(9)
C018	5325(4)	579(3)	7320(2)	26.5(9)
C019	5505(4)	-736(3)	8213(2)	32.2(10)
C01A	12658(4)	1084(3)	9712.0(19)	27.0(9)
C01B	6022(4)	-162(3)	7588(2)	31.1(10)
C01C	1998(4)	1614(3)	7445(2)	29.6(10)
C01D	3614(4)	195(3)	8293(2)	29.4(10)
C01E	-4256(4)	8303(3)	4683(2)	32.6(10)
C01F	10535(4)	3538(3)	9026(2)	32.2(10)
C01G	11248(4)	2810(3)	9328(2)	30.8(10)
C01H	-2172(4)	9015(3)	4260(2)	30.9(10)
C01I	4305(4)	-545(3)	8567(2)	34.1(10)
C01J	-1709(4)	2007(3)	7204(2)	28.0(9)
C01K	-4935(4)	7621(3)	4693(2)	31.6(10)
C01L	11044(4)	4106(3)	8398(2)	33.5(10)
C01M	12025(4)	5863(3)	7810(2)	33.2(10)
C01N	12280(4)	3915(3)	8078(2)	32.9(10)
C01O	5543(4)	-2258(3)	8899(2)	34.6(11)
C01P	10904(4)	5614(3)	7683(2)	34.8(10)
C01Q	11678(4)	-1333(3)	10479.3(19)	30.6(10)
C01R	8352(4)	4166(3)	8117(2)	34.8(11)
C01S	4927(4)	4741(3)	6165.2(19)	30.2(10)
C01T	8911(4)	4807(3)	8222(2)	34.4(10)
C01U	4443(4)	-2464(3)	8725(2)	37.7(11)
C01V	-1116(4)	9183(3)	4495(2)	36.8(11)
C01W	8162(4)	-865(3)	8538(2)	36.2(11)
C01X	12605(5)	6606(3)	7397(2)	39.8(11)
C01Y	-6280(5)	7653(3)	4785(2)	42.2(12)
C01Z	7603(4)	-1505(3)	8430(2)	37.5(11)
C020	-2520(5)	9595(3)	3675(2)	39.8(12)
C021	7010(5)	4148(3)	8210(2)	46.5(13)
C022	-403(5)	9903(3)	4162(2)	43.4(12)
C023	10349(5)	6127(3)	7138(2)	41.5(12)
C024	-1814(5)	10338(3)	3340(2)	50.4(14)
C025	9514(5)	-887(4)	8486(2)	48.9(13)
C026	12089(5)	7118(3)	6843(3)	49.1(13)
C027	-4995(5)	9022(3)	4767(3)	47.6(13)
C028	3800(5)	-3196(3)	9132(3)	51.6(14)
C029	6762(5)	5388(4)	8541(2)	51.5(15)

C02A	-754(5)	10475(3)	3585(3)	50.9(14)
C02B	6217(5)	4762(4)	8410(2)	50.2(14)
C02C	5989(6)	-2799(3)	9477(2)	50.1(14)
C02D	-6999(5)	8381(4)	4856(3)	52.2(14)
C02E	8104(4)	5420(3)	8446(2)	41.4(12)
C02F	10948(5)	6874(3)	6722(2)	50.5(14)
C02G	5303(7)	-3516(4)	9865(2)	68(2)
C02H	10273(5)	-1565(4)	8360(3)	60.6(16)
C02I	8408(5)	-2164(3)	8263(3)	56.4(15)
C02J	6274(5)	8179(3)	6914(3)	55.2(15)
C02K	4225(7)	-3713(4)	9695(3)	65.8(18)
C02L	-6346(5)	9072(4)	4831(3)	60.9(16)
C02M	9721(6)	-2187(4)	8241(3)	77(2)

Table S3-7 Crystal data and structure refinement for **M4**(CH_2Cl_2/n-hexane).

Identification code	**M4**(CH_2Cl_2/n-hexane)
Empirical formula	$C_{50}H_{44}Cl_4N_6O_4$
Formula weight	934.71
Temperature/K	150
Crystal system	triclinic
Space group	P-1
a/Å	9.5485(15)
b/Å	11.3700(15)
c/Å	22.340(4)
α /°	87.516(12)
β /°	80.680(13)
γ /°	74.961(11)
Volume/Å^3	2311.4(6)
Z	2
ρ_{calc}g/cm^3	1.343
μ /mm^{-1}	0.308
F(000)	972.0
Crystal size/mm^3	? × ? × ?
Radiation	Mo Kα (λ = 0.71073)
2Θ range for data collection/°	4.472 to 50.054
Index ranges	$-11 \leqslant h \leqslant 11, -13 \leqslant k \leqslant 13, -26 \leqslant l \leqslant 26$
Reflections collected	17502
Independent reflections	7927 [R_{int} = 0.1077, R_{sigma} = 0.1971]
Data/restraints/parameters	7927/60/581
Goodness-of-fit on F^2	0.916
Final R indexes [I>=2σ (I)]	R_1 = 0.0763, wR_2 = 0.1814
Final R indexes [all data]	R_1 = 0.1903, wR_2 = 0.2200
Largest diff. peak/hole / e Å^{-3}	0.52/-0.31

Table S3-8 Fractional Atomic Coordinates (×10^4) and Equivalent Isotropic Displacement Parameters (Å^2×10^3) for **M4**(CH_2Cl_2/n-hexane). U_{eq} is defined as 1/3 of of the trace of the orthogonalised UIJ tensor.

Atom	x	y	z	U(eq)
Cl1	9122.3(18)	7270.1(13)	6467.8(8)	61.5(5)
Cl	11483.1(19)	8253.5(13)	5835.6(9)	72.1(6)
O005	1729(4)	-1934(3)	8141.2(18)	49.9(11)
O006	13290(5)	14214(3)	2275(2)	55.8(12)
N007	13108(5)	9409(4)	2007(2)	39.7(12)
N008	7311(5)	4419(4)	5105(2)	41.3(12)
O009	-1357(5)	6389(3)	9621.6(19)	72.6(14)
N00A	7862(5)	7360(4)	4649(2)	43.7(13)
N00B	9315(5)	5379(4)	4357(2)	40.8(12)
N00C	6061(5)	6401(4)	5461(2)	49.1(14)
N00D	1939(5)	2917(4)	7917(2)	46.7(13)
C00E	12385(6)	8848(4)	2474(2)	36.0(14)
C00F	9978(6)	7132(5)	3873(2)	38.1(14)
C00G	1880(5)	1689(4)	7973(2)	35.6(14)
C00H	12250(6)	7660(4)	2404(2)	35.7(14)
C00I	2135(6)	4397(4)	7112(3)	40.4(15)
C00J	10875(6)	7676(4)	3413(2)	35.1(14)
C00K	5292(6)	4651(4)	5915(2)	36.3(14)
C00L	11522(6)	7110(4)	2852(2)	38.6(14)
C00M	7117(6)	5611(5)	5114(2)	42.1(15)
O00N	13441(5)	8000(5)	-363(2)	90.1(14)
C00O	13187(6)	10644(5)	2084(3)	41.0(15)
C00P	1869(6)	-148(4)	8573(3)	42.7(15)
C00R	2713(6)	3320(5)	7397(3)	40.6(15)
C00S	1773(6)	-753(4)	8056(3)	37.3(14)
C00T	4360(6)	4165(4)	6381(2)	35.5(14)
C00U	1740(6)	-140(4)	7511(3)	39.8(15)
C00V	1773(5)	1068(4)	7472(3)	38.2(14)
C00W	13300(7)	13026(4)	2224(3)	44.4(16)
C00X	11801(6)	9391(5)	3030(3)	40.1(15)
C00Y	4116(6)	2649(4)	7161(3)	44.1(16)
C00Z	13219(6)	9035(5)	1392(3)	46.7(13)
C010	14271(6)	10876(5)	2349(3)	46.9(16)
C011	11060(6)	8829(4)	3487(3)	39.3(14)
C012	1913(6)	1070(5)	8519(3)	42.3(15)
C013	4909(6)	3057(4)	6662(3)	42.0(15)

C014	-293(6)	3783(4)	8636(2)	42.4(15)
C015	8750(6)	7819(5)	4246(3)	42.9(15)
C016	14338(6)	12055(5)	2434(3)	51.1(17)
C017	10180(6)	5884(5)	3971(2)	41.8(15)
C018	8171(6)	6151(5)	4679(3)	40.2(15)
C019	12147(6)	11623(5)	1881(3)	45.3(15)
C01A	1132(6)	3772(4)	8383(3)	45.3(16)
C01B	6388(6)	3970(5)	5499(2)	41.6(15)
C01C	5179(6)	5910(5)	5852(3)	50.1(16)
C01D	-453(7)	5523(5)	9222(3)	52.0(17)
C01E	1762(7)	4636(5)	8561(3)	54.7(18)
C01F	-1078(6)	4643(5)	9055(3)	52.2(17)
C01G	12204(6)	12794(5)	1961(3)	43.7(15)
C01H	11996(6)	9006(5)	1151(3)	48.4(13)
C01I	12127(7)	8654(5)	566(3)	54.6(14)
C01J	2919(6)	4816(4)	6619(3)	42.3(15)
C01K	10072(7)	7544(5)	5760(3)	60.5(19)
C01L	1621(7)	-2552(5)	7620(3)	60.3(19)
C01M	958(8)	5516(5)	8980(3)	63(2)
C01N	13460(8)	8332(6)	203(3)	71.1(14)
C01O	14502(8)	14442(5)	2485(3)	76(2)
C01Q	14549(7)	8710(6)	1033(3)	71.6(15)
C01R	-788(9)	7345(5)	9773(3)	88(3)
C01S	14681(8)	8367(7)	452(3)	83.1(17)
C01T	14797(9)	7816(8)	-776(3)	122(3)
Cl2	4297(2)	9667.6(18)	6179.4(9)	84.7(6)
Cl3	6879(2)	10241.1(14)	5474.2(9)	78.3(6)
C1	5917(8)	9209(7)	5700(4)	96(2)

Table S3-9 Crystal data and structure refinement for **M4**(THF).

Identification code	**M4**(THF)
Empirical formula	$C_{50.5}H_{45}Cl_5N_6O_4$
Formula weight	977.17
Temperature/K	150
Crystal system	triclinic
Space group	P-1
a/Å	10.547(2)
b/Å	11.286(2)
c/Å	22.899(4)
α /°	101.150(14)
β /°	94.464(15)
γ /°	99.329(17)
Volume/Å^3	2622.3(9)
Z	2
ρ_{calc}g/cm^3	1.238
μ /mm^{-1}	0.324
F(000)	1014.0
Crystal size/mm^3	? × ? × ?
Radiation	Mo Kα (λ = 0.71073)
2Θ range for data collection/°	4.524 to 50.052
Index ranges	$-12 \leqslant h \leqslant 12, -13 \leqslant k \leqslant 13, -27 \leqslant l \leqslant 27$
Reflections collected	24202
Independent reflections	9245 [R_{int} = 0.2339, R_{sigma} = 0.3781]
Data/restraints/parameters	9245/390/527
Goodness-of-fit on F^2	1.015
Final R indexes [I>=2σ (I)]	R_1 = 0.1309, wR_2 = 0.3571
Final R indexes [all data]	R_1 = 0.2767, wR_2 = 0.4156
Largest diff. peak/hole / e Å^{-3}	0.47/-0.48

Table S3-10 Fractional Atomic Coordinates ($\times 10^4$) and Equivalent Isotropic Displacement Parameters ($Å^2 \times 10^3$) for **M4**(THF). U_{eq} is defined as 1/3 of of the trace of the orthogonalised UIJ tensor.

Atom	x	y	z	U(eq)
O001	9584(5)	4957(5)	635.4(19)	47.9(13)
O002	-4083(5)	5667(5)	9509(2)	47.6(13)
O003	7668(6)	-2885(5)	1456(2)	69.6(15)
O004	-3293(6)	13023(5)	8137(2)	71.0(15)
N005	7596(6)	2079(6)	2191(2)	47.4(13)
N006	-2466(7)	8176(6)	7741(2)	51.3(13)
N007	3714(7)	5537(6)	4573(2)	52.1(14)
N008	1685(7)	6178(6)	5131(2)	58.0(15)
N009	2961(7)	3511(6)	4684(2)	53.2(15)
N00A	1704(7)	4562(6)	5619(2)	56.8(15)
C00B	9105(8)	4311(7)	1045(3)	44.7(14)
C00C	6416(8)	3663(7)	2681(3)	46.5(15)
C00D	5423(8)	3438(7)	3579(3)	48.0(14)
C00E	-3567(8)	6272(7)	9092(3)	46.1(14)
C00F	5710(8)	4090(7)	3124(3)	49.1(15)
C00G	-947(8)	8389(7)	7005(3)	48.9(16)
C00H	8106(8)	2865(7)	1816(3)	43.6(13)
C00I	6902(8)	2555(7)	2668(3)	48.2(14)
C00J	8712(9)	407(7)	1868(3)	50.8(16)
C00K	8308(8)	3202(7)	830(3)	45.7(15)
C00L	2968(9)	4713(8)	4785(3)	52.0(14)
C00M	8912(8)	3986(7)	2019(3)	45.5(15)
C00N	4592(8)	3903(7)	4026(3)	48.3(14)
C00O	-4444(8)	6873(7)	8825(3)	44.6(15)
C00P	7829(8)	2482(7)	1179(3)	44.8(15)
C00Q	-4029(9)	7455(7)	8374(3)	48.9(15)
C00R	7566(9)	793(7)	2009(3)	50.5(14)
C00S	8670(9)	-811(8)	1687(3)	54.3(16)
C00T	-1980(8)	6422(7)	7094(3)	50.4(16)
C00U	3799(8)	3136(7)	4278(3)	49.0(15)
C00V	-2335(8)	6362(7)	8925(3)	48.4(15)
C00W	-367(8)	6642(7)	6407(3)	50.3(15)
C00X	6643(8)	1980(7)	3140(3)	50.0(16)
C00Y	-1819(8)	7660(7)	7281(3)	47.6(14)
C00Z	9411(8)	4698(7)	1660(3)	44.0(15)
C010	-278(8)	7871(7)	6586(3)	51.3(16)

C011	-2517(9)	10161(7)	8391(3)	55.3(16)
C012	-2671(9)	9437(8)	7826(3)	55.3(14)
C013	-2864(9)	7520(7)	8203(3)	49.3(14)
C014	2062(9)	5185(8)	5207(3)	55.2(15)
C015	5929(8)	2410(7)	3577(3)	49.9(16)
C016	7570(10)	-1711(8)	1639(4)	62.2(16)
C017	6454(9)	-58(8)	1971(3)	59.9(17)
C018	-1278(8)	5886(8)	6662(3)	51.5(16)
C019	4537(8)	5117(7)	4195(3)	51.0(16)
C01A	10288(8)	6150(7)	853(3)	53(2)
C01B	6469(10)	-1263(8)	1794(3)	63.5(18)
C01C	468(9)	6115(8)	5958(3)	55.2(15)
C01D	-3104(9)	9924(8)	7352(3)	57.6(16)
C01E	-1968(9)	7015(7)	8489(3)	52.3(16)
C01F	871(9)	6631(8)	5518(3)	59.3(16)
C01G	-3090(10)	11841(8)	7993(3)	63.7(15)
C01H	904(9)	4996(8)	5989(3)	58.0(16)
C01I	-3260(9)	11115(8)	7430(3)	59.9(17)
C01J	-2737(9)	11310(8)	8485(3)	61.1(17)
C01K	-3254(9)	4960(8)	9761(4)	63(2)
C01L	6572(10)	-3806(8)	1418(4)	86(3)
C01N	-3543(10)	13579(8)	7643(4)	79(3

Table S3-11 Crystal data and structure refinement for **M7**.

Identification code	**M7**
Empirical formula	$C_{30}H_{21}F_6N_5O_2$
Formula weight	597.52
Temperature/K	150
Crystal system	triclinic
Space group	P-1
a/Å	10.1469(12)
b/Å	11.2785(14)
c/Å	25.924(3)
α /°	84.629(10)
β /°	84.957(9)
γ /°	63.007(9)
Volume/Å^3	2628.5(6)
Z	4
ρ_{calc}g/cm^3	1.510
μ /mm^{-1}	0.126
F(000)	1224.0
Crystal size/mm^3	? × ? × ?
Radiation	Mo Kα (λ = 0.71073)
2Θ range for data collection/°	4.446 to 50.052
Index ranges	$-11 \leqslant h \leqslant 12, -13 \leqslant k \leqslant 13, -28 \leqslant l \leqslant 30$
Reflections collected	21138
Independent reflections	9180 [R_{int} = 0.0451, R_{sigma} = 0.1063]
Data/restraints/parameters	9180/0/779
Goodness-of-fit on F^2	0.838
Final R indexes [I>=2σ (I)]	R_1 = 0.0434, wR_2 = 0.0849
Final R indexes [all data]	R_1 = 0.1008, wR_2 = 0.0940
Largest diff. peak/hole / e Å^{-3}	0.33/-0.30

Table S3-12 Fractional Atomic Coordinates ($\times10^4$) and Equivalent Isotropic Displacement Parameters ($Å^2\times10^3$) for **M7**. U_{eq} is defined as 1/3 of of the trace of the orthogonalised UIJ tensor.

Atom	x	y	z	U(eq)
F001	471.0(16)	2767.2(14)	1735.5(6)	46.9(4)
F002	5334.1(17)	-4503.7(14)	6207.7(6)	55.3(5)
F003	899.7(17)	1343.5(15)	1181.9(6)	60.8(5)
F004	5899.5(17)	-4165.3(15)	5417.2(6)	60.4(5)
F005	2310.1(17)	2286.7(16)	1187.1(6)	62.2(5)
F006	4807.9(18)	-5389.5(14)	5617.8(7)	66.2(5)
F007	1094(2)	4549.9(16)	5635.2(6)	69.8(6)
F008	3394(2)	-1565.3(17)	4452.2(6)	68.7(5)
O009	3269.8(19)	826.2(17)	-1885.0(7)	45.5(5)
F00A	3807.7(19)	-348.6(16)	4923.3(6)	66.4(5)
F00B	5554.9(19)	-1720.3(17)	4459.4(6)	73.5(6)
F00C	376(2)	3548.4(15)	5172.3(7)	81.9(7)
O00D	7270(2)	4890.2(18)	8424.7(7)	50.9(5)
N00E	3329(2)	-2019.8(19)	5890.3(7)	29.2(5)
N00F	2705(2)	107.9(18)	6478.4(7)	28.2(5)
O00G	-1457.2(19)	12206.7(16)	7222.3(8)	53.1(6)
N00H	2643(2)	1123.9(19)	2307.9(8)	30.3(5)
N00I	3817(2)	-255.9(19)	3567.2(8)	30.0(5)
N00J	4127(2)	-1112.3(19)	2606.2(8)	32.6(5)
N00K	1220(2)	1458.6(19)	5792.0(7)	30.8(5)
N00L	2160(2)	6737.9(18)	7341.0(8)	31.4(5)
F00M	-961(2)	4544.9(17)	5816.4(8)	88.7(7)
O00N	1614(2)	-6628.2(19)	-480.2(7)	58.9(6)
N00O	951(2)	-741.9(19)	5553.9(8)	33.1(5)

N00P	3027(2)	-2505(2)	-198.6(8)	37.0(6)
N00Q	3173(2)	1926(2)	3197.7(8)	36.9(6)
C00R	1994(2)	305(2)	6046.3(9)	26.4(6)
C00S	1762(2)	2492(2)	6453.6(9)	26.9(6)
C00T	2540(2)	1215(2)	6675.3(9)	29.1(6)
C00U	1990(3)	5733(2)	7116.4(9)	26.8(6)
C00V	2096(3)	-903(2)	5820.6(9)	26.8(6)
C00W	1198(2)	8107(2)	7294.1(9)	28.6(6)
C00X	1766(3)	3646(2)	6685.5(9)	28.6(6)
C00Y	3132(3)	3577(2)	6767.1(9)	30.3(6)
C00Z	3478(3)	6309(2)	7614.0(9)	27.9(6)
C010	3493(2)	650(2)	3173.2(9)	28.0(6)
C011	2542(3)	680(2)	1862.6(10)	30.7(6)
C012	3427(3)	195(2)	2660.1(9)	28.2(6)
C013	1147(3)	2536(2)	5993.4(9)	29.7(6)
C014	3239(3)	4598(2)	6975.5(9)	29.9(6)
C015	3251(3)	-642(2)	1746.0(9)	30.9(6)
C016	3399(3)	-3083(2)	5679.7(9)	30.9(6)
C017	3083(3)	-2077(2)	290.5(10)	32.5(7)
C018	610(3)	5808(2)	7047.4(9)	31.7(7)
C019	3113(3)	45(3)	-1473.7(10)	34.4(7)
C01A	337(2)	8699(2)	6875.7(9)	30.2(6)
C01B	519(3)	4771(2)	6832.3(9)	31.4(6)
C01C	3210(3)	-1156(2)	1243.7(10)	33.8(7)
C01D	3035(3)	-1656(2)	-642.0(10)	34.1(7)
C01E	3660(3)	5520(2)	8067.2(10)	32.6(7)
C01F	4575(3)	6647(2)	7431.9(10)	32.2(7)

C01G	3793(3)	177(3)	4029.0(10)	30.7(6)
C01H	1138(3)	8916(2)	7676.4(9)	32.9(7)
C01I	4937(3)	5053(2)	8326.7(10)	35.9(7)
C01J	4167(3)	-2083(3)	-1021.3(10)	35.3(7)
C01K	-573(3)	10068(2)	6833.6(10)	36.1(7)
C01L	4193(3)	-1244(2)	-1435.6(10)	34.6(7)
C01M	2280(3)	-3046(2)	5408.4(9)	36.1(7)
C01N	2728(3)	-3595(2)	-259.6(10)	33.1(7)
C01O	5880(3)	6183(2)	7685.0(10)	36.5(7)
C01P	6051(3)	5377(2)	8131.8(10)	35.8(7)
C01Q	-609(3)	10847(2)	7217.6(11)	36.6(7)
C01R	253(3)	10263(2)	7636.7(10)	38.6(7)
C01S	4032(3)	-1503(2)	2148.5(10)	34.4(7)
C01T	2460(3)	-1898(2)	1203.0(10)	36.1(7)
C01U	2036(3)	-5674(3)	-385.9(10)	39.2(7)
C01V	3919(3)	-882(3)	798.8(10)	40.0(7)
C01W	1548(3)	1772(3)	1491.9(11)	39.2(7)
C01X	2378(3)	-2341(2)	734.0(10)	37.1(7)
C01Y	2825(3)	-5724(2)	25.2(10)	38.7(7)
C01Z	1921(3)	-384(3)	-695.6(10)	42.7(7)
C020	3853(3)	-1346(2)	332.4(10)	38.7(7)
C021	3168(3)	-4695(3)	84.8(10)	40.8(7)
C022	423(3)	3784(3)	5651.4(12)	45.0(8)
C023	4131(3)	-859(3)	4462.8(11)	43.8(7)
C024	1074(3)	-1837(3)	5351.5(10)	37.4(7)
C025	4848(3)	-4293(3)	5732.8(11)	41.9(7)
C026	1973(3)	-3579(3)	-682.6(10)	40.4(7)

C027	3481(3)	1465(3)	4102.9(10)	41.4(7)
C028	1944(3)	478(3)	-1104.5(10)	41.7(7)
C029	1651(3)	-4617(3)	-744.2(10)	44.4(8)
C02A	3199(3)	2307(3)	3660.6(11)	44.6(8)
C02B	2290(3)	2212(3)	-1892.3(11)	54.0(8)
C02C	-2358(3)	12852(3)	6797.1(12)	62.5(9)
C02D	1699(4)	-7551(3)	-68.3(11)	62.6(9)
C02E	8552(3)	4906(3)	8185.1(13)	73.7(11)

Appendix IV Photophysical measurements

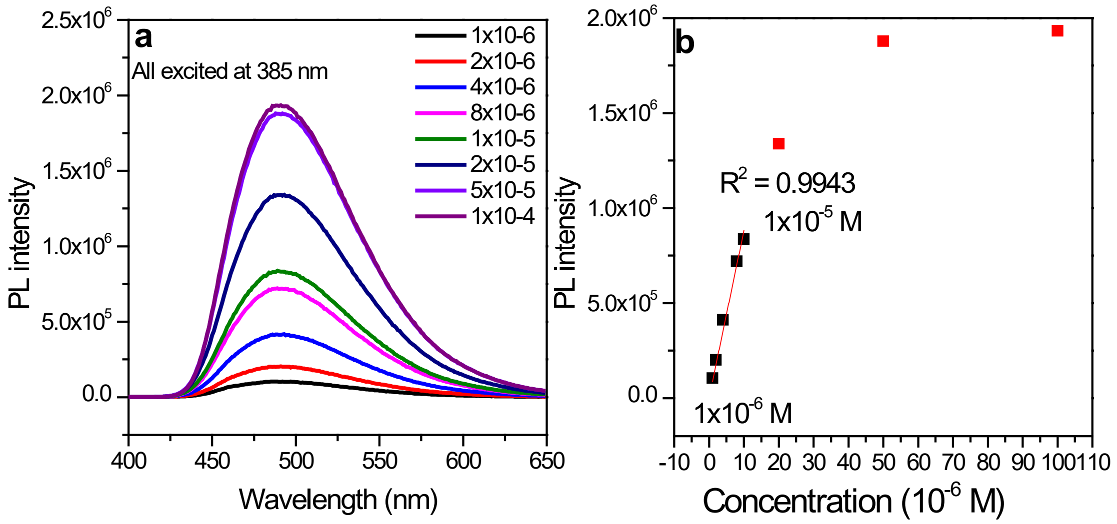

Figure S4-1 Determination of the linear domain for **M1** in chloroform, slit 2/2 nm.

Table S4-1 PLQY calculation of **M1** related to quinine sulfate.

k_{M1}[b] \ k_{qs}[a]	47277	48343	48708
9785	0.138[c]	0.135	0.134
9328	0.132	0.129	0.128
9152	0.129	0.127	0.126
Average	0.131	R^2	0.004

[a] The gradient value of fitting line for the graph of integrated emission intensity v.s. absorbance, when quinine sulfate is used as standard, λ_{exc} = 366 nm, 0.5 M sufuric acid as solvent, Φ_q = 0.546. [b] The gradient value of fitting line for the graph of integrated emission intensity v.s. absorbance of **M1** (chloroform solution), λ_{exc} = 366 nm. [c] Calculated value of PLQY.

Table S4-2 PLQY calculation of **M1** related to norharmane.

k_{M1}[b] \ k_{nh}[a]	53482	52734	52500
9785	0.134	0.136	0.137
9328	0.128	0.130	0.131
9152	0.126	0.128	0.128
Average	0.131	R^2	0.003

[a] The gradient value of fitting line for the graph of integrated emission intensity v.s. absorbance, when norharmane is used as standard, λ_{exc} = 366 nm, 0.5 M sufuric acid as solvent, Φ_n = 0.60. [b] The gradient value of fitting line for the graph of integrated emission intensity v.s. absorbance of **M1**

(chloroform solution), λ_{exc} = 366 nm. [c] Calculated value of PLQY.

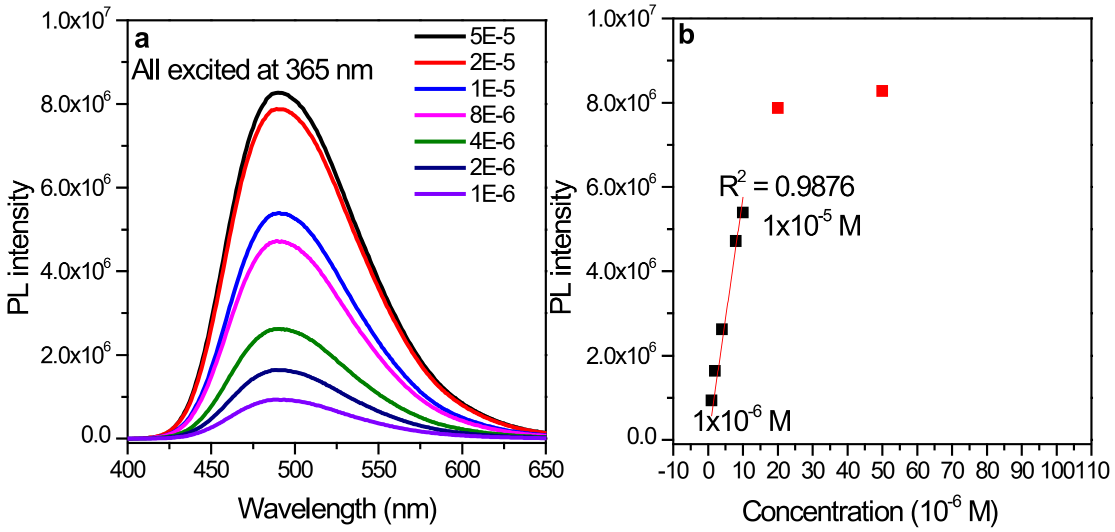

Figure S4-2 Determination of the linear domain for **M2** in chloroform, slit 2/2 nm.

Table S4-3 PLQY calculation of **M2** related to quinine sulfate.

k_{M2}^{b} k_{qs}^{a}	47277	48343	48708
51421	0.727	0.711	0.706
51664	0.731	0.715	0.709
52917	0.749	0.732	0.727
Average	0.723	R^2	0.008

[a] The gradient value of fitting line for the graph of integrated emission intensity v.s. absorbance, when quinine sulfate is used as standard, λ_{exc} = 366 nm, 0.5 M sufuric acid as solvent, $\Phi_q = 0.546$. [b] The gradient value of fitting line for the graph of integrated emission intensity v.s. absorbance of **M2** (chloroform solution), λ_{exc} = 366 nm. [c] Calculated value of PLQY.

Table S4-4 PLQY calculation of **M2** related to norharmane.

k_{M2}^{b} k_{nh}^{a}	53482	52734	52500
51421	0.707	0.717	0.720
51664	0.710	0.720	0.723
52917	0.727	0.738	0.741
Average	0.722	R^2	0.009

[a] The gradient value of fitting line for the graph of integrated emission intensity v.s. absorbance, when norharmane is used as standard, λ_{exc} = 366 nm, 0.5 M sufuric acid as solvent, $\Phi_q = 0.60$. [b] The gradient value of fitting line for the graph of integrated emission intensity v.s. absorbance of **M2** (chloroform solution), λ_{exc} = 366 nm. [c] Calculated value of PLQY.

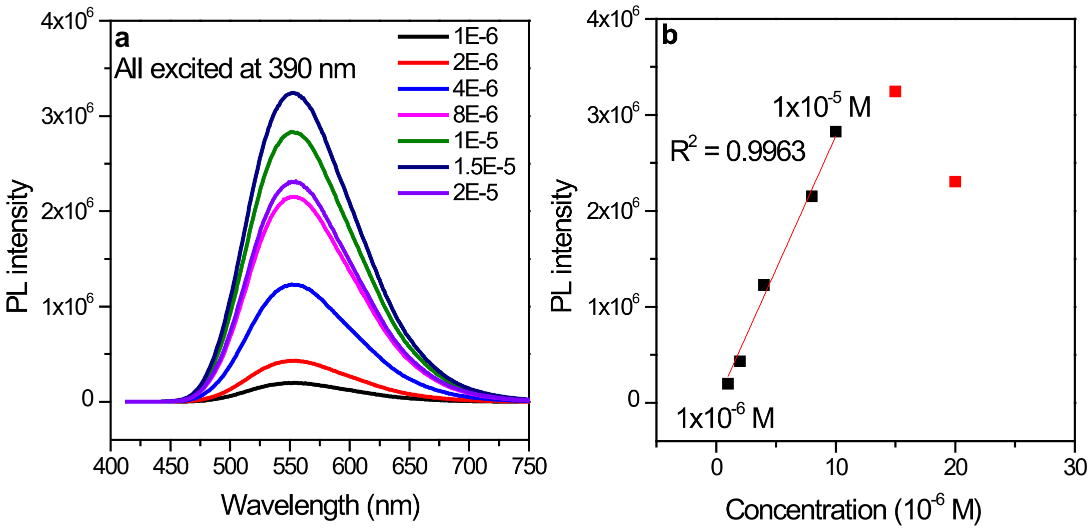

Figure S4-3 Determination of the linear domain for **M3** in DCM, slit 2/2 nm.

Table S4-5 PLQY calculation of **M3** related to quinine sulfate.

k_{M3}[b] k_{qs}[a]	47277	48343	48708
54981	0.778	0.761	0.755
55213	0.781	0.764	0.758
55514	0.785	0.768	0.762
Avergae	0.768	R^2	0.009

[a] The gradient value of fitting line for the graph of integrated emission intensity v.s. absorbance, when quinine sulfate is used as standard, λ_{exc} = 366 nm, 0.5 M sufuric acid as solvent, Φ_q = 0.546. [b] The gradient value of fitting line for the graph of integrated emission intensity v.s. absorbance of **M3** (chloroform solution), λ_{exc} = 366 nm. [c] Calculated value of PLQY.

Table S4-6 PLQY calculation of **M3** related to norharmane [a].

k_{M3} [b] k_{nh} [a]	53482	52734	52500
54981	0.756	0.766	0.770
55213	0.759	0.770	0.773
55514	0.763	0.774	0.777
Average	0.767	R^2	0.006

[a] The gradient value of fitting line for the graph of integrated emission intensity v.s. absorbance, when norharmane is used as standard, λ_{exc} = 366 nm, 0.5 M sufuric acid as solvent, Φ_q = 0.60. [b] The gradient value of fitting line for the graph of integrated emission intensity v.s. absorbance of **M3** (chloroform solution), λ_{exc} = 366 nm. [c] Calculated value of PLQY.

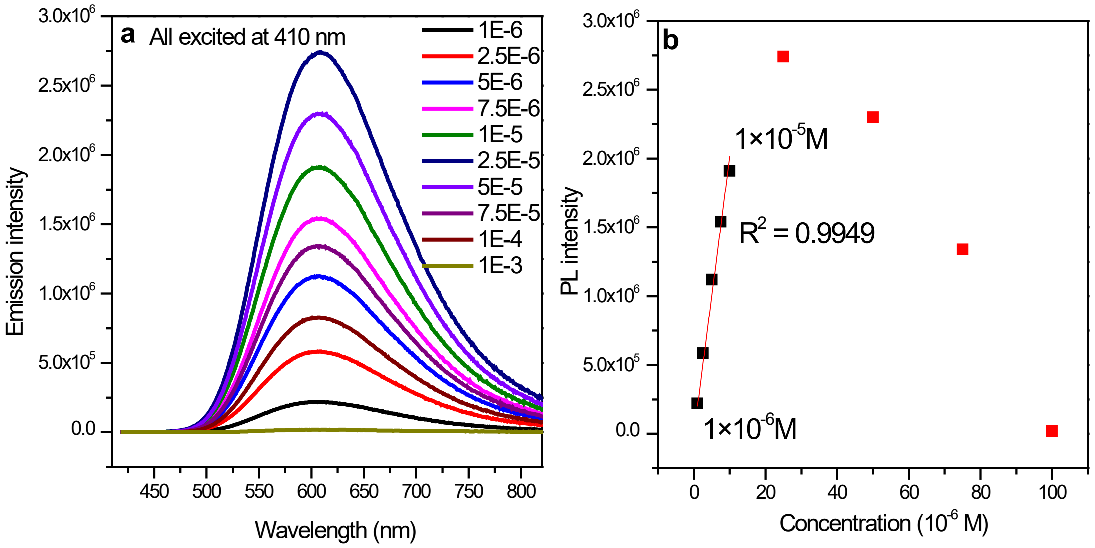

Figure S4-4 Determination of the linear domain for **M4** in chloroform, slit 2/2 nm.

Table S4-7 PLQY calculation of **M5** related to quinine sulfate [a].

k_{M3} k_{qs}	47277	48343	48708
25942	0.367	0.359	0.356
24452	0.346	0.338	0.336
24870	0.352	0.344	0.342
Avergae	0.349	R^2	0.009

[a] The gradient value of fitting line for the graph of integrated emission intensity v.s. absorbance, when quinine sulfate is used as standard, λ_{exc} = 366 nm, 0.5 M sufuric acid as solvent, Φ_q = 0.546. [b] The gradient value of fitting line for the graph of integrated emission intensity v.s. absorbance of **M5** (chloroform solution), λ_{exc} = 366 nm. [c] Calculated value of PLQY.

Table S4-8 PLQY calculation of **M5** related to norharmane [a].

k_{M3} k_{nh}	53482	52734	52500
25942	0.357	0.362	0.363
24452	0.336	0.341	0.342
24870	0.342	0.347	0.348
Average	0.349	R^2	0.008

[a] The gradient value of fitting line for the graph of integrated emission intensity v.s. absorbance, when norharmane is used as standard, λ_{exc} = 366 nm, 0.5 M sufuric acid as solvent, Φ_q = 0.60. [b] The gradient value of fitting line for the graph of integrated emission intensity v.s. absorbance of **M5** (chloroform solution), λ_{exc} = 366 nm. [c] Calculated value of PLQY.

Table 4-9 PLQY calculation of **M6** related to quinine sulfate.

k_{M3}[b] k_{qs}[a]	47277	48343	48708
17279	0.244	0.239	0.237
16918	0.239	0.234	0.232
16549	0.234	0.229	0.227
Avergae	0.235	R^2	0.004

[a] The gradient value of fitting line for the graph of integrated emission intensity v.s. absorbance, when quinine sulfate is used as standard, λ_{exc} = 366 nm, 0.5 M sufuric acid as solvent, $\Phi_q = 0.546$. [b] The gradient value of fitting line for the graph of integrated emission intensity v.s. absorbance of **M6** (chloroform solution), λ_{exc} = 366 nm. [c] Calculated value of PLQY.

Table 4-10 PLQY calculation of **M6** related to norharmane.

k_{M3}[b] k_{nh}[a]	53482	52734	52500
17279	0.237	0.241	0.242
16918	0.233	0.236	0.237
16549	0.227	0.231	0.232
Average	0.235	R^2	0.004

[a] The gradient value of fitting line for the graph of integrated emission intensity v.s. absorbance, when norharmane is used as standard, λ_{exc} = 366 nm, 0.5 M sufuric acid as solvent, $\Phi_n = 0.60$. [b] The gradient value of fitting line for the graph of integrated emission intensity v.s. absorbance of **M6** (chloroform solution), λ_{exc} = 366 nm. [c] Calculated value of PLQY.

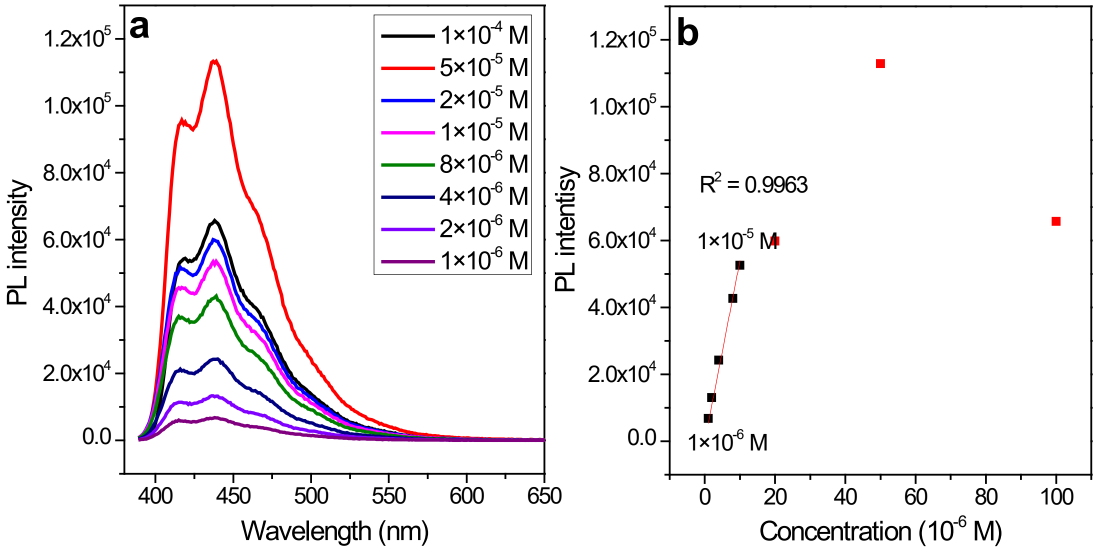

Figure S4-5 Determination of the linear domain for **M6** in chloroform, slit 1/1 nm.

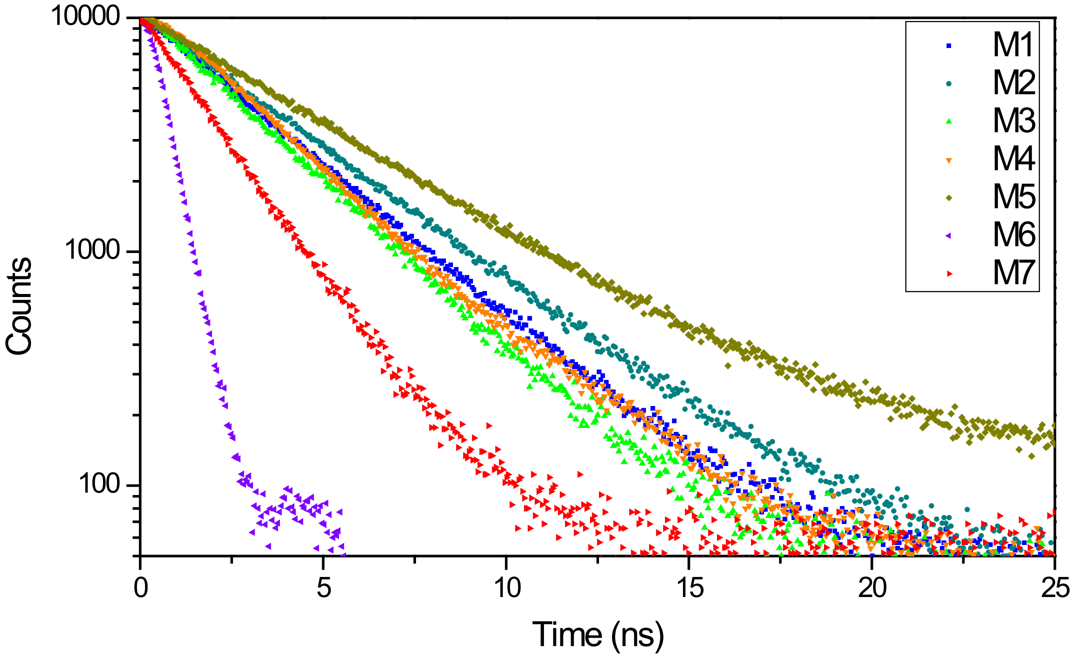

Figure S4-6 Fluorescence decay of **M3** in solution with different solvent.

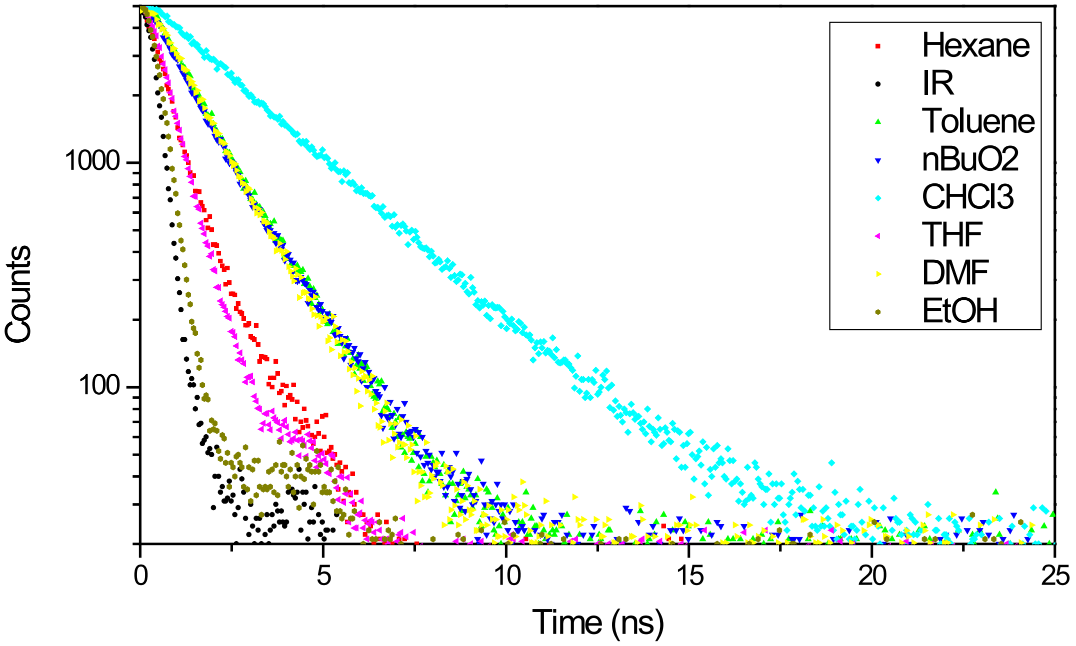

Figure S4-7 Fluorescence decay of **M3** in solution with different solvent.

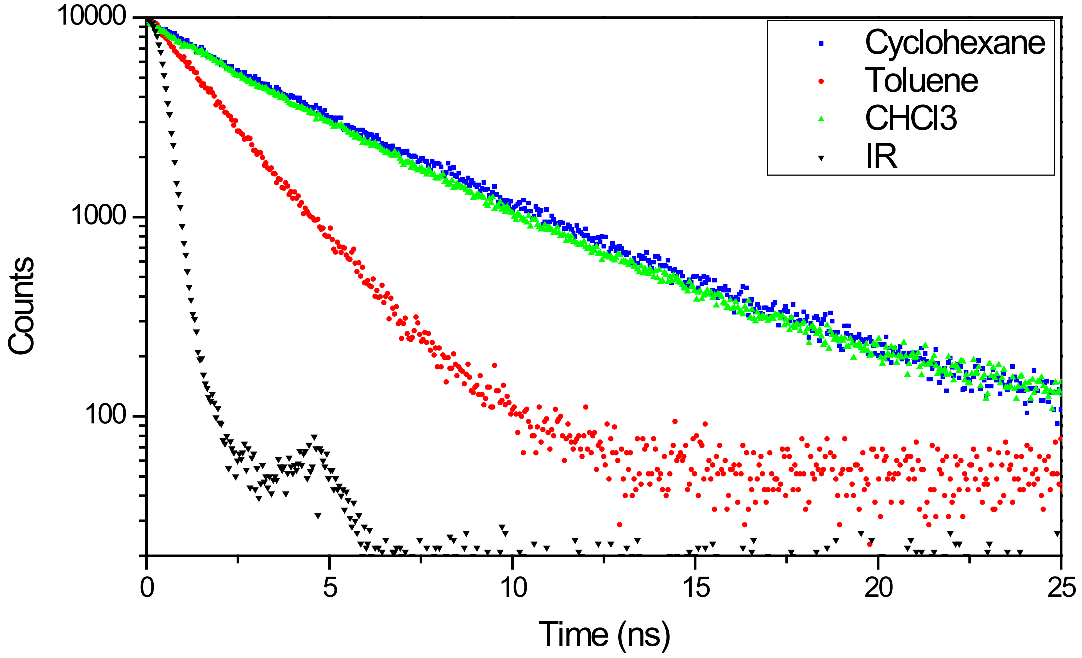

Figure S4-8 Fluorescence decay of **M7** in solution with different solvent.

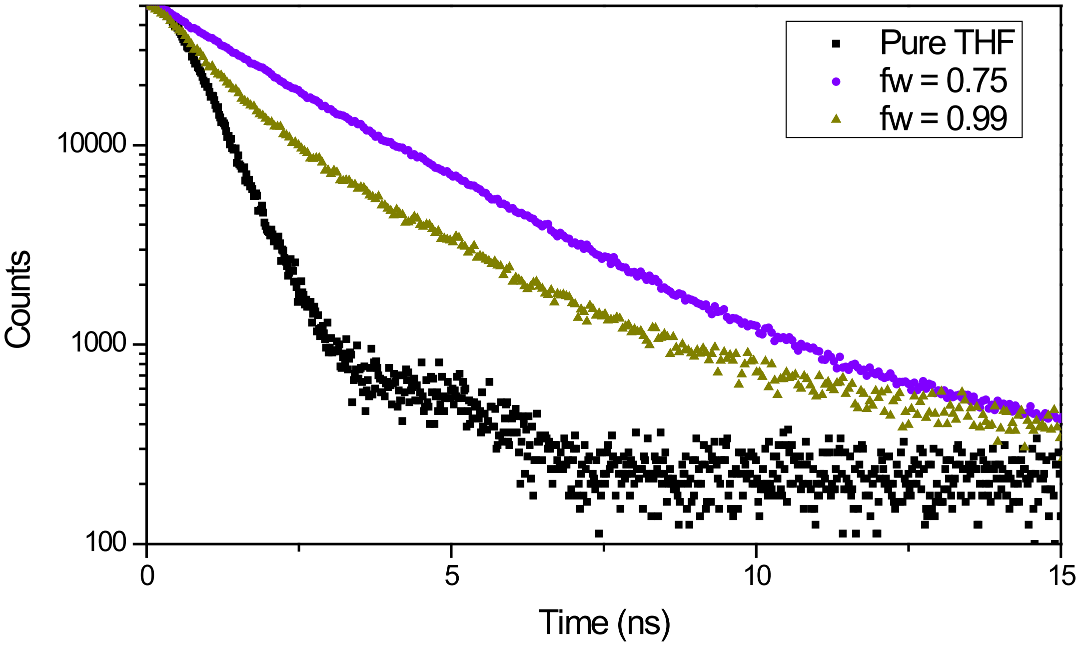

Figure S4-9 Fluorescence decay of **M4** in pure THF, 75% and 99% water/THF.

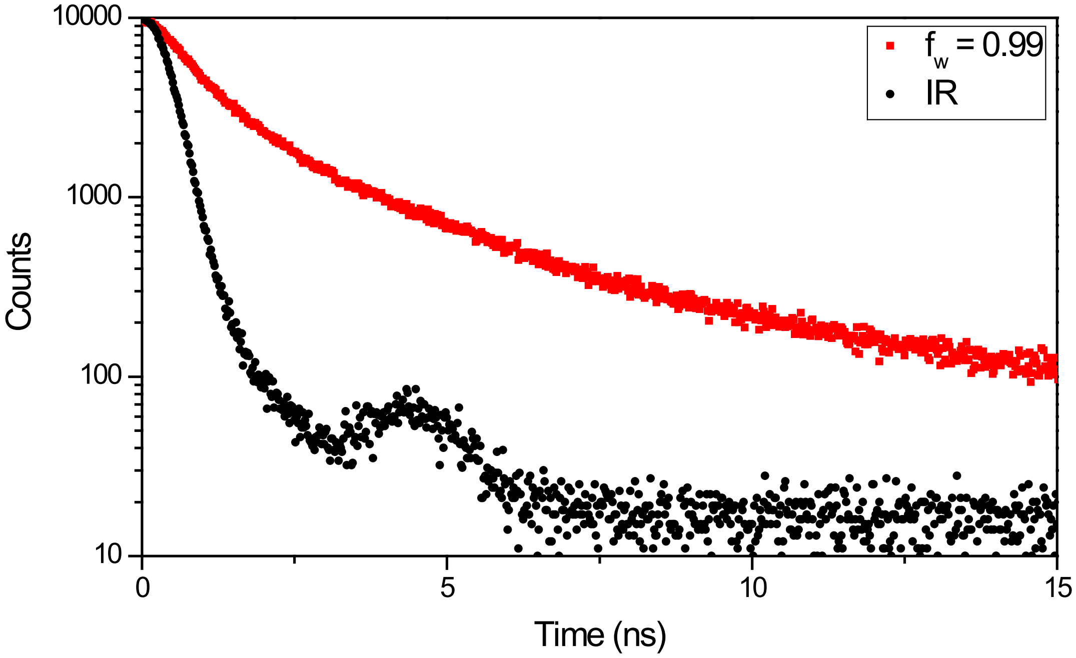

Figure S4-10 Fluorescence decay of **M3** in 99% water/THF.

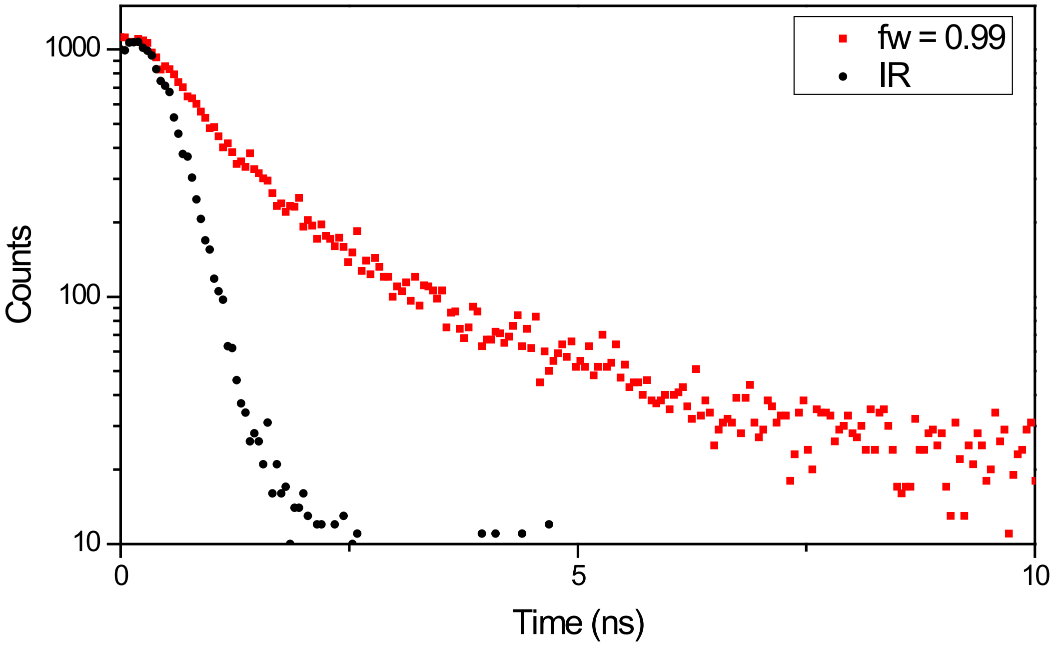

Figure S4-11 Fluorescence decay of **M7** in 99% water/THF.

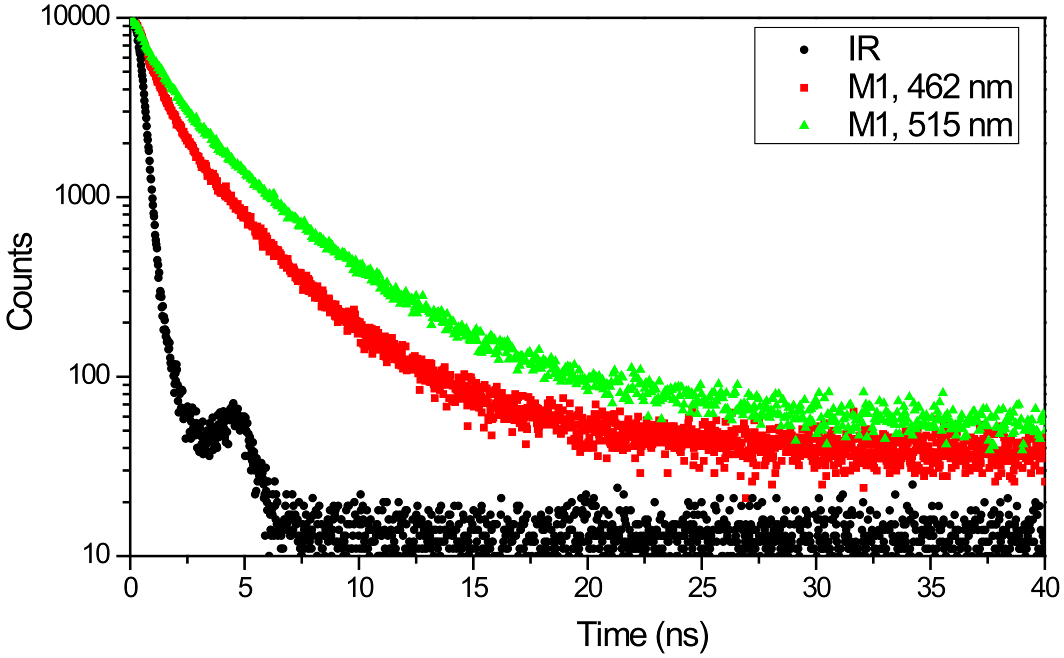

Figure S4-12 Fluorescence decay of **M1** in 10wt% spin-coated film at different emission wavelength.

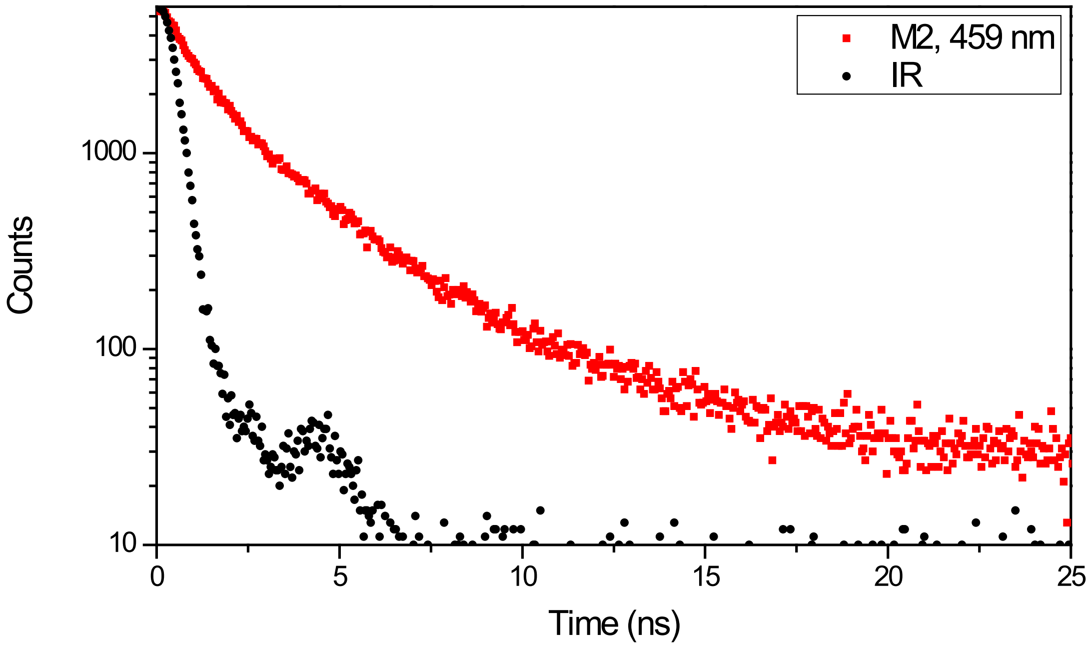

Figure S4-13 Fluorescence decay of **M2** in 10wt% spin-coated film at emission wavelength of 459 nm..

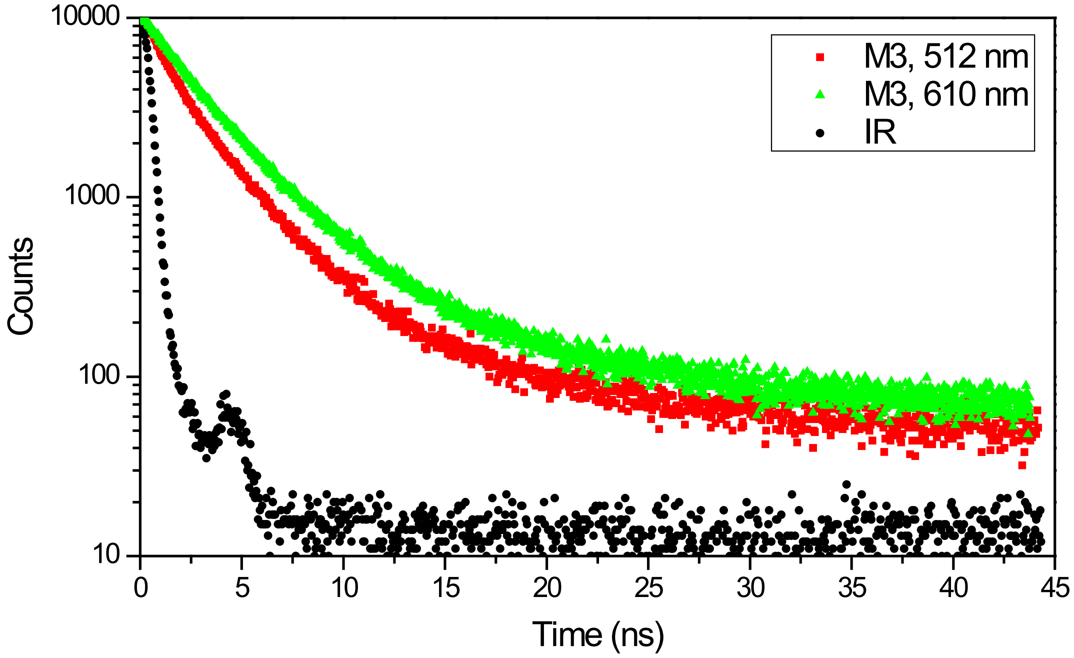

Figure S4-14 Fluorescence decay of **M3** in 10wt% spin-coated film at different emission wavelength.

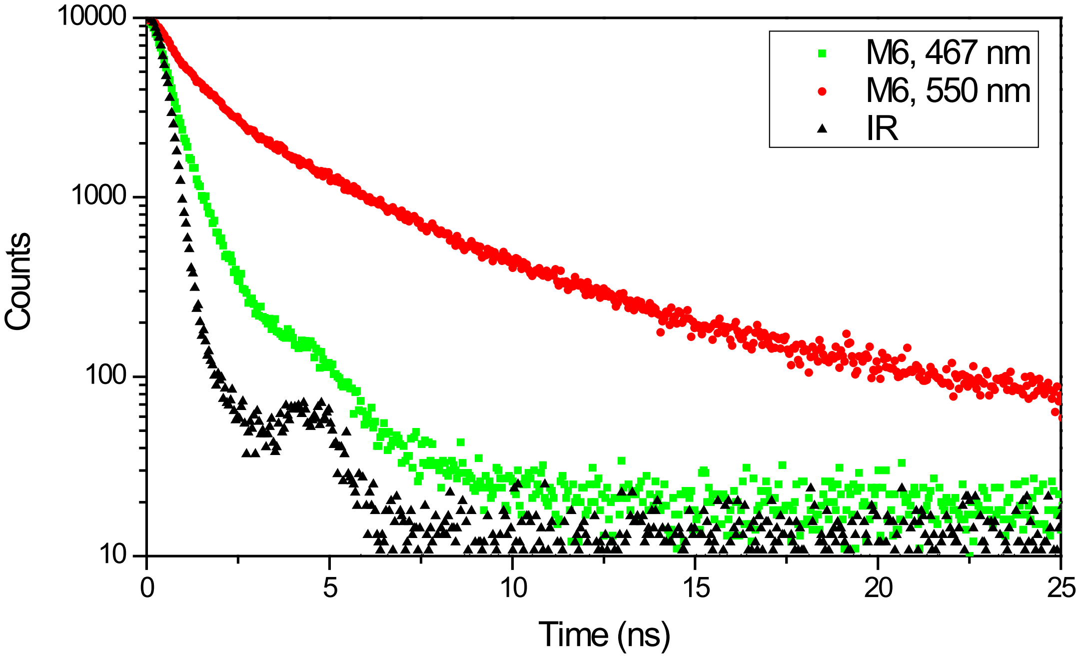

Figure S4-15 Fluorescence decay of **M6** in 10wt% spin-coated film at different emission wavelength.

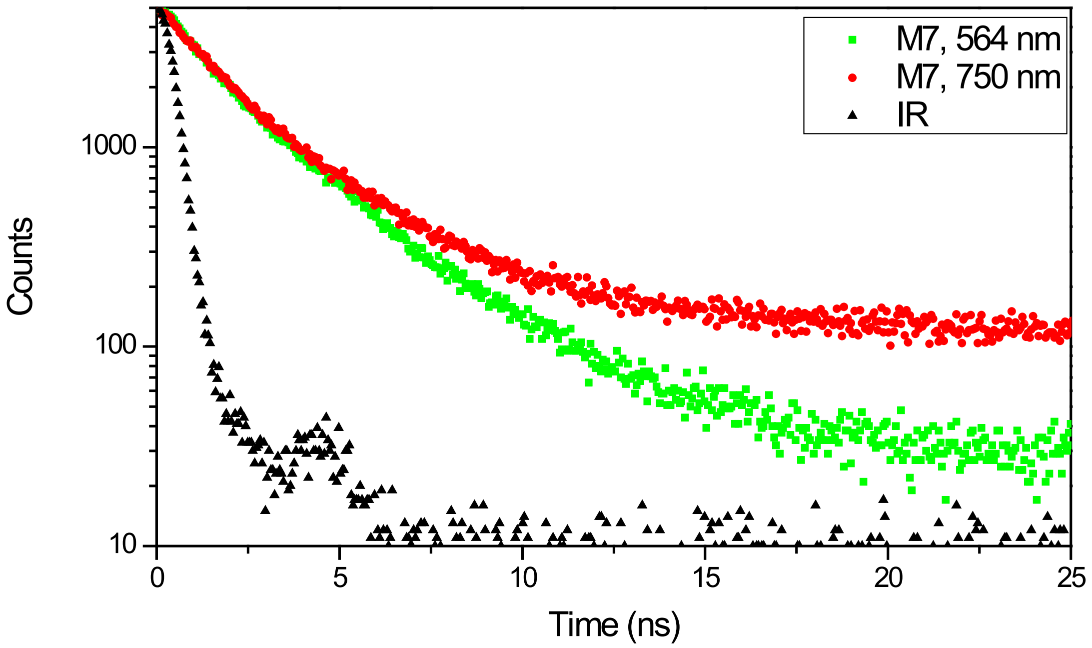

Figure S4-15 Fluorescence decay of **M7** in 10wt% spin-coated film at different emission wavelength.

Titre : Conception et synthèse de matériaux luminescents organiques avec une structure de 2,2′-bipyrimidine pour l'éclairage LED hybride

Mots clés : bipyrimidine, synthèse organique, diode électroluminescente hybride, luminescence.

Résumé : Les matériaux luminescents organiques présentent de nombreux avantages par rapport à leurs analogues inorganiques. En les concevant soigneusement, ils peuvent présenter une fluorescence efficace dans la région visible avec une couleur d'émission modulable et une absorption forte dans la région proche-UV et bleue. Grâce à cela, ils peuvent être fabriqués sous forme de films minces pour des dispositifs optoélectroniques légers. Ils peuvent être hautement solubles dans des solvants organiques, ce qui offre la possibilité de techniques de traitement en solution, telles que le dépôt par rotation et le revêtement par fente. Ils sont exempts de métaux, ce qui est souhaitable pour le développement durable. Pour ces raisons, le composés luminescents organiques pourrait constituer une alternative prometteuse au phosphore inorganique utilisé dans les diodes électroluminescentes (LEDs) blanches commerciales pour améliorer la qualité de la lumière.

Nous avons conçu et synthétisé une série de molécules donneur-accepteur **M1-M7** en utilisant de nouveaux accepteurs, des dérivés de 2,2′-bipyrimidine, comme bloc de construction. Elles ont été purifiées et soumises à des investigations photophysiques à la fois en solutions diluées et à l'état solide. Elles ont montré une couleur d'émission modulable couvrant presque tout le spectre visible, une forte fluorescence et absorption. Plus important encore, certaines d'entre elles présentent un taux de conversion élevé d'une source externe proche-UV ou bleue vers la lumière visible. Nous avons également examiné leurs photostabilités pour estimer leurs durées de vie. Des mélanges de différents émetteurs ont été réalisés pour générer de la lumière blanche. Enfin, des LED blanches hybrides ont été fabriquées à partir d'une LED inorganique bleue et d'un composé émetteur de lumière jaune.

Title : Design and synthesis of organic luminescent materials with a 2,2′-bipyrimidine scaffold for hybrid LED lighting

Keywords : bipyrimidine, organic synthesis, hybrid light-emitting diode, luminescence.

Abstract : Organic luminescent materials possess a lot advantages over the inorganic analogues. By carefully designing, they can exhibit efficiency fluorescence in visible area with tunable emission color and strong absorption in near-UV and blue region. Due to this, they can be made in thin films for light-weight optoelectronic devices. They can be highly soluble in organic solvent which provide the possibility for the solution-processing techniques, such as spin-coating and slot-die coating. They are metal-free, which is desired for the sustainable development. For these reasons, the organic luminescent compounds could be a promising alternative to the inorganic phosphors utilized in commercial white light-emitting diodes (LEDs) for the improvement of the light quality.

Herein, we designed and synthesized a series of donor-acceptor molecules **M1-M7** implementing new acceptors, 2,2′-bipyrimidine derivatives as building block. They were purified and taken to the photophysical investigations in both diluted solutions and solid state. They showed tunable emission color which can cover almost whole visible spectrum, strong fluorescence and absorption. More importantly, some of them exhibit high conversion rate from near-UV or blue external source to visible light. We also inspected their photostabilities to estimate their lifespans. The blenders of different emitters are made for generating white light. At last, the hybrid white LEDs were fabricated based on a blue inorganic LED and one yellow-emitting compound.